



**INSTITUTO POTOSINO DE INVESTIGACIÓN
CIENTÍFICA Y TECNOLÓGICA, A.C.**

POSGRADO EN CIENCIAS APLICADAS

**Síntesis y caracterización de materiales compuestos
polímero/nanotubo de carbono:
Impacto del injerto de polímero a la superficie de los CNx
MWNTs sobre las propiedades eléctricas y mecánicas de
los nano-compuestos**

Tesis que presenta

Benjamín Fragneaud

Para obtener el grado de

Doctor en Ciencias Aplicadas

En la opción de

Nanociencias y Nanotecnología

Director (Codirectores) de la Tesis:

Dr. Mauricio Terrones Maldonado

Dr. Jean-Yves Cavallé

Dr. Alfonso Gonzáles Montiel

San Luis Potosí, S.L.P., diciembre de 2006



Constancia de aprobación de la tesis

La tesis “**Síntesis y caracterización de materiales compuestos polímero / nanotubo de carbono: Impacto del injerto de polímero a la superficie de los CNx MWNTs sobre las propiedades eléctricas y mecánicas de los nano-compuestos**” presentada para obtener el Grado de de Doctor en Ciencias Aplicadas en la opción de Nanociencias y Nanotecnología fue elaborada por **Benjamín Fragneaud** y aprobada el **26 de octubre de 2006** por los suscritos, designados por el Colegio de Profesores de la División de Biología Molecular del Instituto Potosino de Investigación Científica y Tecnológica, A.C.

Dr. Mauricio Terrones Maldonado
(Director de la tesis)

Dr. Jean-Yves Cavallé
(Codirector de la tesis)

Dr. Alfonso Gonzáles Montiel
(Asesor de la tesis)



Créditos Institucionales

Esta tesis fue elaborada en el Laboratorio de (Nombre del Laboratorio) de la División de Materiales Avanzados para la Tecnología Moderna del Instituto Potosino de Investigación Científica y Tecnológica, A.C., bajo la codirección del Dr. Mauricio Terrones Maldonado, Dr. Jean-Yves Cavallé, Dr. Alfonso Gonzáles Montiel.



Instituto Potosino de Investigación Científica y Tecnológica, A.C.

Acta de Examen de Grado

El Secretario Académico del Instituto Potosino de Investigación Científica y Tecnológica, A.C., certifica que en el Acta 020 del Libro Primero de Actas de Exámenes de Grado del Programa de Doctorado en Ciencias Aplicadas en la opción de Nanociencias y Nanotecnología está asentado lo siguiente:

En la ciudad de San Luis Potosí a los 15 días del mes de diciembre del año 2006, se reunió a las 09:30 horas en las instalaciones del Instituto Potosino de Investigación Científica y Tecnológica, A.C., el Jurado integrado por:

Dr. Mauricio Terrones Maldonado	Presidente	IPICYT
Dr. Alfonso González Montiel	Secretario	CID-DESC
Dr. Fernando Jaime Rodríguez Macías	Sinodal	IPICYT
Dr. Leonardo Ríos Guerrero	Sinodal externo	IMP
Dr. Pedro Jesús Herrera Franco	Sinodal externo	CICY

a fin de efectuar el examen, que para obtener el Grado de:

**DOCTOR EN CIENCIAS APLICADAS
EN LA OPCIÓN DE NANOCIENCIAS Y NANOTECNOLOGÍA**

sustentó el C.

Benjamin Fragneaud

sobre la Tesis intitulada:

Síntesis y Caracterización de Materiales Compuestos Polímero/Nanotubo de Carbono: Impacto del Injerto de Polímero a la Superficie de los CNx MWNTs sobre las Propiedades Eléctricas y Mecánicas de los nano-compuestos

que se desarrolló bajo la dirección de

Dr. Mauricio Terrones Maldonado
Dr. Alfonso González Montiel (CID-DESC)

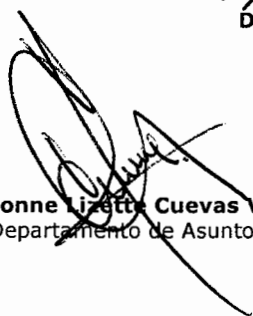
El Jurado, después de deliberar, determinó

APROBARLO

Dándose por terminado el acto a las 12:00 horas, procediendo a la firma del Acta los integrantes del Jurado. Dando fé el Secretario Académico del Instituto.

A petición del interesado y para los fines que al mismo convengan, se extiende el presente documento en la ciudad de San Luis Potosí, S.L.P., México, a los 15 días del mes diciembre de 2006.


Dr. Marcial Bomilla Marín
Secretario Académico


L.C.C. Ivonne Lizette Cuevas Velez
Jefa del Departamento de Asuntos Escolares



Dedicatorias

à mes parents,

Agradecimientos

En primer lugar, quisiera agradecer profundamente mis directores de tesis: Dr. Mauricio Terrones Maldonado (IPICYT, San Luis Potosí, México), Dr. Jean-Yves Cavaillé (GEMPPM, Lyon, Francia), Dr. Alfonso González Montiel (CID, Lerma, México) por el tiempo y el apoyo que me han dedicado durante esa tesis de doctorado.

No podría olvidar el apoyo y la paciencia de Karine Masenelli Varlot, que interactuó como co-asesor de tesis y que también dedicó mucho de su tiempo sin contarlo.

Obviamente, agradezco los laboratorios CID, GEMPPM y IPICYT por haberme dado la oportunidad de realizar esos trabajos de investigación.

Finalmente, a un nivel personal y afectivo mando mis agradecimientos a mi esposa: Mitzi Natalia Hernandez Cruz, quien contribuyó a mantenerme animado, sobre todo cuando el tiempo parecía una eternidad. También supo escucharme y ayudarme a tener una mirada mas critica en cuanto a mis resultados.

Mis padres y mi hermana son también unas personas a quien quisiera mandar unos reconocimientos. Ellos siempre me apoyaron durante mi carrera, y contribuyeron a que me sintiera lo suficiente capaz para asumir la responsabilidad de un proyecto de investigación.

Es necesario mandar agradecimientos a muchas personas perteneciendo a cada uno de los laboratorios involucrados en este proyecto:

CID:

Edgar, Luis, Oscar, Mariamne, Pablito, Lorena, Manuel, Loli, Lety (sistemas), Lety (química), chela etc...

GEMPPM: Alex, Dan, souhail, Stéphanie, Rafael, julien (cazenave), Julien Ramier, Florent etc...

Quisiera mandar un agradecimiento especial a Etienne Munch (GEMPPM). Su amistad, apoyo incondicional (en todos sentidos) y paciencia fueron mas que esencial en la realización de una parte de este trabajo

IPICYT: Julio, Ana Laura, pepe, lalo etc...

Resumen

Síntesis y caracterización de materiales compuestos polímero / nanotubo de carbono: Impacto del injerto de polímero a la superficie de los CNx MWNTs sobre las propiedades eléctricas y mecánicas de los nano-compuestos:

Unos nuevos materiales híbridos, proviniendo del injerto de poliestireno a la superficie de unos nanotubos de carbono dopados con nitrógeno (CNx MWNT), fueron sintetizados y usados en la elaboración de nano-compuestos a matriz polimérica. En esos trabajos hemos estudiado el impacto de esos nanotubos injertados sobre las propiedades mecánicas y eléctricas de unas matrices de poliestireno (PS) y poli (butadieno-co-estireno) (PSBS). Los nanotubos injertados presentan una mejor dispersión en una matrice de PS en comparación con los nanotubos sin tratamiento químico. Sin embargo ese tipo de funcionalización no permite bajar el umbral de precolación eléctrica dado que el injerto aísla eléctricamente los CNx MWNTs. Por otra parte, el refuerzo mecánico de matrices poliméricas (PS) es mejor con injerto, sobre todo cuando los nano-compuestos están sometidos a grandes deformaciones mecánicas. En el caso particular de una matriz nano-estructurada (PSBS), observamos un refuerzo mecánico mucho más importante. La conexión, vía los CNx MWNTs injertados, de los nano-dominios de PS de la matriz, permitió llevar a cabo la aparición de una red percolante rígida con umbral de percolación muy bajo ($P_c < 0.05 \text{ vol.}\%$).

Título de la Tesis: Síntesis y caracterización de materiales compuestos polímero / nanotubo de carbono: Impacto del injerto de polímero a la superficie de los CNx MWNTs sobre las propiedades eléctricas y mecánicas de los nano-compuestos

PALABRAS CLAVE: modificación química, ATRP, modificación de superficie, materiales híbridos, nanotubos de carbono, materiales compuestos, propiedades eléctricas, propiedades mecánicas, copolímero bloque

Abstract

New hybrid materials from the grafting of polystyrene on the surface of nitrogen doped carbon nanotube were synthesized. These chemically modified nanotubes were further used in the fabrication of polymer based nanocomposites. In these works, we studied the impact of the polymer grafted nanotubes on the electrical and mechanical properties of a polystyrene (PS) and a poly (butadiene-co-styrene) (PSBS) matrices. The grafted nanotubes have a better dispersion in a PS matrix as compared to the as received ones. Nevertheless, this kind of functionalization does not lower the percolation threshold since the grafted polymer layer electrically isolates the nanotubes each others. On the other hand, the mechanical reinforcement (PS matrix) increases when the nanotubes are polymer grafted. Furthermore, a stronger mechanical reinforcement is observed for large strain deformation. Concerning the nano-structured PSBS matrix, we observed a stronger mechanical reinforcement as compared to the PS matrix. The PS grafted nanotubes permit to connect the PS nano-domains of the matrix and consequently forms a percolating rigid network with a very low threshold ($PC < 0.05$ vol.%).

Thesis title: Synthesis and characterization of polymer/carbon nanotubes composites: Impact of polymer grafting on the surface of CNx MWNTs on the electrical and mechanical properties of the nanocomposites.

KEY WORDS: chemical functionalization, ATRP, surface modification, Hybrid materials, carbon nanotubes, composite materials, material electrical properties, material mechanical properties, block copolymer.

Introduction

Nowadays the material industry focuses a considerable part of its investigation on composite materials. A composite material is defined as a material that is constituted of two or more phases. Generally, the continuous phase is named the matrix; this phase being surrounded by the other(s) phase(s), named filler(s). The fillers exhibit physical (mechanical, electrical, magnetic, etc...) or physico-chemical properties (flame retardant, gas barrier, oxidant properties) very dissimilar to those of the matrix. The aim of the introduction of fillers is to modify the main bulk properties of the matrix. This kind of materials exists in various forms: metal / metal composites, metal / ceramic composites, ceramic / ceramic composites. Nevertheless, most of the industrial applications are found in polymer-based composites. Polymer matrices are attractive due to in their low weight (density $\approx 1 \text{ g.mol}^{-1}$), nevertheless some of their physical properties are not satisfactory, and thus it is necessary to modify them by adding specific fillers.

The last few years, the scientific community has focused on nanometer scale fillers. Indeed, nanometer scale fillers are advantageous because they could exhibit enhanced binding forces with the matrix. Moreover, as compared to a micrometer scale filler, the distance between nano-particles within the matrix is lower, and thus becomes comparable to the gyration radius of a macromolecular chain (amorphous matrix) or to a crystalline domain (semi crystalline matrix). However, the modification of the filler surface results in an increase of the attraction force between nano-particles (i.e, electrostatic force, van der Waals forces) and finally a novel problem arises: the nanoparticle dispersion.

When the filler process enhanced mechanical properties when compared to the matrix it is named reinforcing filler. In the area of polymer-based composites we should mention the use of glass particles (spherical particles or fibers) or carbon black, highly representative of the interest of the scientific community. Both types of fillers have been used as a reinforcing agent: modulus enhancement, change in plastic deformation, modification of the fracture mechanism. We should point out that carbon black, as well as carbon nanotubes, can be

considered as conductive fillers. These materials could modify at least two physical characteristics of the matrix (multifunctional filler).

Few years ago, in 1991, S.Iijima [1] identified the structure of the carbon nanotubes. Due to their fascinating physico-chemical properties, carbon nanotubes still remain an important subject that is being investigated worldwide. In particular, academic and industrial researchers still consider that these long fibers could be good candidates to enhance simultaneously the mechanical and electrical properties of polymers even better than carbon black.

One of the most important problems found in the literature when using nanofillers in a polymer matrix is to reach good dispersions and a strong interfacial adhesion. Indeed, non bonding interactions like van der Waals forces make those particles to aggregate easily. In order to take advantage of the nanotube aspect ratio (the ratio between their mean length and mean diameter), it is necessary to disperse them uniformly within the matrix. From our point of view, many techniques could be used, but the one that should be the most efficient and the better controlled would be to graft a polymer onto the nanotube surface.

The subject of this PhD thesis is to study the mechanical and electrical properties of various polymers filled with Nitrogen-doped Multiwalled Carbon Nanotubes (CNx MWNTs). CNx MWNTs are very unique multiwalled carbon nanotubes. Indeed, unlike conventional MWNTs, CNx MWNTs find their originality in their nitrogen content and their characteristic bamboo-like morphology. This bamboo-like structure seems to be particularly attractive for the enhancement of the mechanical properties of polymers, since concentric sheets cannot slide one on another. Furthermore, the nitrogen doping induces a very distinct physico-chemical nature through the presence of electron-donor defects (the nitrogen atoms), which enhances the surface chemical reactivity.

An important outcome of this work is devoted to polymer grafting on the surface of CNx MWNTs using a recent controlled free radical polymerization named Atomic Transfer Radical Polymerization (ATRP). The PS-grafted CNx MWNTs are then used as mechanical and electrical fillers in two different polymers. In

this PhD thesis we will study their role on the mechanical and electrical properties of polystyrene and poly (butadiene-co-styrene).

The comparison of all the results with those obtained on the same polymers filled with as-produced CN_x MWNTs will permit us to understand how the physico-chemistry of the system, and particularly the presence of the grafted polymer layer, influences the mechanical and electrical behavior of the nanocomposites.

After a brief review related to nanotubes and polymer composites (chapter 1), the second chapter reports some theoretical elements on which we based our work. The first theoretical point deals with the carbon nanotube chemistry and on the ATRP polymerization technique. The second relevant theoretical point is related with the morphology of block copolymers and the adhesion between carbon nanotubes and polymer matrices. The third point describes percolation theories and the evolution of the electric conduction for small fibers embedded in composites. Finally, we present the mechanical properties of the polymer composites, emphasizing the state of the art concerning carbon nanotubes / polymer composites.

The third chapter describes the experimental techniques used to synthesize the different polymer composites.

The fourth chapter concerns the study of the nano-composite properties. The first part presents the grafting of polystyrene on the CN_x MWNTs surface. The second part gives microstructural analysis of the nano-composites. The third part, present the electrical properties of the same composites, and finally in the fourth part it is presented the mechanical properties of the nanotube filled composites. Here we will compare our results with those presented in the literature.

Finally, conclusions will be draw and perspectives will be discussed in chapter five.

Table of contents

Chapter I General introduction 17

A.1 Generalities on polymers.....	18
A.1.1 Characteristic temperatures of polymers:	19
A.2 Nanotubes	20
A.2.1 Generalities: Discovery of other allotropic forms of carbon (C ₆₀ and identification of carbon nanotubes)	20
A.2.2 Nanotube synthesis processes	21
A.2.3 Physico-chemical properties of Multiwalled Carbon Nanotubes	24
A.2.3.1 Electrical Properties of carbon nanotubes	25
A.2.3.2 Mechanical properties of carbon nanotubes	26
A.2.4 Nitrogen Doped Multiwalled Carbon Nanotubes (CN _x MWNTs)	27
A.2.4.1 Chemical properties and structure of the CN _x MWNTs	27
A.2.4.2 CN _x MWNTs might be more chemically reactive:.....	28
A.2.4.3 CN _x MWNT are electrically conductive.....	28
A.2.4.4 Nitrogen doping, bamboo-like tubular structures and mechanical properties	29
A.3 Carbon nanotubes-polymer composites	29
A.4 Conclusions	31

Chapter II Theoretical part and hypotheses 32

Part A Chemical modification of carbon nanotubes 33

A.1 Chemical modification of carbon nanotubes.....	35
A.1.1 Surface modification of CNTs by physico-chemical interactions	35
A.1.2 Covalently linked chemical modification	36
A.1.2.1 Carboxylation of carbon nanotubes	36
A.1.2.2 Carbon nanotube structure and chemical reactivity.	38
A.1.2.3 Addition reactions	42
A.1.3 Polymer grafting: “grafting to” or “grafting from” techniques	44
A.1.4 Chemical structure and reactivity of CN _x MWNTs	45
A.1.5 Hypothesis about carbon nanotubes chemical reactivity	46
A.2 Atomic Transfer Radical Polymerization (ATRP)	46
A.2.1 Generalities	46
A.2.2 Hybrid material synthesis using ATRP	48
A.2.3 ATRP initiator	49

A.2.4	ATRP catalyst	49
A.2.5	ATRP ligand	50
A.2.6	Kinetics and molecular weight : theoretical elements	50
A.2.6.1	Kinetic	50
A.2.6.2	Molecular weight.....	51
Part B Microstructure of the polymer/ carbon nanotubes composites		53
B.1 Polymers morphology		54
B.1.1	Physico-chemistry of the polymer miscibility	54
B.1.1.1	Atomistic and molecular interactions	54
B.1.1.2	Polymer miscibility	55
B.1.2	Structural changes in the morphology of block copolymers	56
B.2 Chemical functionalization and filler / matrix interfacial adhesion strength: pull out phenomenon		58
Part C Percolation theory and electrical behaviour of polymer / carbon nanotube nanocomposites		60
C.1 Introduction to the percolation theory.		61
C.1.1	History and general concept.	61
C.1.2	Link percolation	61
C.1.3	Percolation statistical representative values	62
C.1.3.1	Quantity of s sized clusters normalized by the quantity of possible network links.	63
C.1.3.2	Probability to belong to the infinite cluster	63
C.1.3.3	Size of finite length clusters.	64
C.1.3.4	The characteristic length.....	65
C.1.4	Scale law	65
C.2 Application of percolation theory to carbon nanotubes nanocomposites electrical properties		66
C.2.1	Electrical properties below the percolation threshold	68
C.2.2	Electric properties above percolation threshold	68
Part D Mechanical properties of polymer composites and polymer / carbon nanotubes composites		70
D.1 Nanotube composites: A review		72
D.1.1	Mechanical behavior of polymers:	72
D.1.2	Generalities of composites materials	73
D.1.3	Importance of the matrix-carbon nanotube interfaces	74
D.1.4	Elastic mechanical properties of two-phase composites	75
D.1.4.1	Mean field theory.....	76
D.1.4.2	Mechanical percolating network theory	78
D.1.4.3	Entangled fibers and impact on nanocomposites properties.	80
Part E Conclusions of chapter II		81

Chapter III Materials and experimental techniques 83

Part A Matrix and CN_x MWNTs: synthesis and characteristics 84

A.1	CN _x MWNTs	84
A.2	Polystyrene	85
A.3	Poly (butadiene-co-styrene)	86

Part B CN_x MWNT Chemical modification 87

B.1	Chemical modification of CN_x MWNTs: chemical mechanisms	87
B.1.1	Synthesis route for Surface Phenyl Grafted CN _x MWNT	87
B.1.2	Atomic Transfer Radical Polymerization Macroinitiator grafted CN _x MWNTs	88
B.1.3	In-situ PS polymerization of CN _x MWNTs using ATRP	89
B.2	Experimental protocol for Polystyrene grafted CN_x MWNTs	90
B.2.1	Phenyl Grafted CN _x MWNTs synthesis	90
B.2.2	Macroinitiator-grafted CN _x MWNT synthesis	91
B.2.3	Synthesis of PS grafted CN _x MWNTs	92
B.3	Chemical analysis tools	94
B.3.1	Fourrier Transformed Infra Red (FTIR)	94
B.3.2	Coupled gas Chromatography / Mass Spectrometer (GC-MS)	95
B.3.3	Thermogravimetric Analysis	97
B.3.4	Electron Energy Loss Spectroscopy / Energy Dispersing Spectroscopy (EDS)	97
B.3.5	Raman Spectroscopy	98
B.3.6	Electron Spin Resonance (ESR)	98

Part C Polymer / CN_x MWNT composite : synthesis and microstructural characterization 100

C.1	Polymer / CN_x MWNT nanocomposite synthesis.....	100
C.2	Electronic microscopy characterization	102
C.2.1	Transmission Electronic Microscopy (TEM)	102
C.2.2	Scanning Electronic Microscopy (SEM)	102
C.3	Differential Scanning Calorimetry (DSC).....	102

Part D Electrical and mechanical analysis tools 104

D.1	Dielectric measurements	104
D.2	Dynamic Mechanical Analysis.....	105
D.3	Tensile tests	107

D.4	Compression tests:.....	107
-----	-------------------------	-----

Chapter IV Experimental results and discussions 109

Part A Efficient coating of N-doped carbon Nanotubes with PS using Atomic Transfer Radical Polymerization (ATRP). 110

A.1	Phenyl grafted nanotubes and ATRP macroinitiator grafted nanotubes	113
A.1.1	Identification of the phenyl grafted molecules	114
A.1.2	Proof of the grafting by Raman spectroscopy	115
A.1.3	Quantification of the grafting (TGA)	117
A.1.4	Coupled gas chromatography / mass spectrometer	118
A.1.5	Operating grafted ATRP macroinitiator: Electron spin resonance (ESR)	119

A.2 Polystyrene grafted CN_x MWNTs..... 121

A.2.1	HRTEM of Polystyrene grafted CN _x MWNTs	121
A.2.2	EELS and EDS Analysis of the PS grafted layers	122

A.3 Conclusion about Efficient coating of N-doped carbon Nanotubes with polystyrene using Atomic Transfer Radical Polymerization..... 124

Part B Morphology and interfacial adhesion of the CN_x MWNT / polymer nanocomposites 125

B.1 Dispersion of the CN_x MWNTs in a polymer matrix 126

B.1.1	Dispersion of the CN _x MWNTs in a polystyrene matrix	126
B.1.2	Dispersion of CN _x MWNTs in a poly (butadiene-co-styrene) matrix.	127
B.1.3	Polymer / CN _x MWNTs interfacial adhesion	128

B.2 Effect of the CN_x MWNTs on the PSBS copolymer microstructure.... 134

B.2.1	PSBS Morphology	134
B.2.2	CN _x MWNT / PSBS nanocomposite microstructure	135
B.2.2.1	As received CN _x MWNT / PSBS	135
B.2.2.2	PS grafted CN _x MWNTs in a PSBS matrix.....	136
B.2.2.2.1	Small tubes	137
B.2.2.2.2	Large tubes	138

B.3 Glass transition temperature of the CN_x MWNT / PS nanocomposites. 140

B.4 Conclusion about the morphology and adhesion of CN_x / Polymer composites 144

Part C Electrical properties of the CNx MWNT / polymer composites 145

C.1 Electrical behavior of CNx MWNT / polymer nanocomposites.....	147
C.1.1 Nanocomposites using as produced CNx MWNTs	147
C.1.2 Nanocomposites using PS-g-CNx MWNTs	151
C.2 Conclusion	155

Part D Mechanical properties of the CNx MWNT polymer nanocomposites 156

D.1 Nanocomposites using PS matrix: mechanical properties.....	156
D.1.1 Compression tensile test: elastic mechanical behavior	156
D.1.1.1 Experimental Results	156
D.1.1.2 Comparison with the Halpin Kardos Model.....	158
D.1.2 Dynamic Mechanical analysis: above the glass transition temperature	161
D.1.2.1 α Transition temperature	164
D.1.2.2 Pseudo plateau characteristics	164
D.1.2.3 Pseudo plateau characteristics: storage modulus.....	166
D.1.3 Large strain deformation	168
D.2 Nanocomposites using SBS matrix.....	171
D.2.1 Dynamic Mechanical analysis	171
D.2.1.1 α Transition temperature	174
D.2.1.2 Storage shear modulus.....	174
D.2.2 Tensile test	176
D.2.2.1 Linear Viscoelastic behavior	176
D.2.2.1.1 a-CN _x	177
D.2.2.1.2 PS-g-CN _x	178
D.2.2.2 Large strain deformation	181
D.3 Conclusions	184

Chapter V Conclusions and perspectives 185

Part A Conclusions 186

A.1 synthesis of polystyrene grafted CNx MWNTs.....	186
A.2 Morphology and adhesion of the CNx MWNTs composites	186
A.3 Electrical properties of CNx MWNT polymer composites.....	187
A.4 Mechanical properties of the CNx MWNT polymer composites	188

Part B Further works and perspectives 189

B.1	Carbon nanotubes chemical modification.....	189
B.2	Morphology of PS grafted carbon nanotubes	189
B.3	Electrical behavior of polymer grafted carbon nanotubes	190
B.4	Mechanic properties of polymer carbon nanotubes composites	190
Annex I.a	191
Annex I.b	192
Annex II	193
Bibliography	194

Table of figure:

Figure 1: Schematic representation of a) a homopolymer b) a statistical copolymer c) a block copolymer	19
Figure 2: Molecular model of the C ₆₀ structure	20
Figure 3: Theoretical structures of two particular types of chiral single walled nanotubes a) zig-zag structure b) armchair structure [3]	21
Figure 4: carbon nanotubes produced by different methods; a) MWNTs produced by spray pyrolysis methods [14], b) overview of the carbon concentric carbon shells on the micrograph (a) ; c) carbon nanotubes produced in hydrogen arc discharge conditions [15], and d) carbon nanotubes produced using a CVD process [16]	22
Figure 5: Different growth mechanisms occurring in CVD processes A) growth mechanism postulated by Baker et al. [17] for the formation of carbon filaments by pyrolysis of acetylene on metal particles; B) growth mechanism proposed for carbon fibers and filaments by pyrolysis of benzene over metallic particle [15] and C) growth mechanism proposed for carbon filament synthesis from Fe-Pt / C ₂ H ₂ system [16,17].	23
Figure 6: HRTEM micrograph of a multiwalled Carbon nanotube. The graphene sheets are visible when observed edge-on and appear in black. The distance between two consecutive graphene sheets is 0.34 nm [21].	24
Figure 7: Different electronic properties depending on the helicity.....	25
Figure 8: Theoretical representation of pyridine (pink atoms) and tertiary amine (green atoms) nitrogen sites in a CN _x MWNT.....	27
Figure 9: Representation of different defects observed in CNTs: defect A are heptagonal or pentagonal rings in the framework that lead to a bend in the tube (topological defects); B defects are sp ³ hybridized defects (with hanged molecules); C are holes produce by strong oxidative conditions that leave -COOH groups and D are opened ends oxidized by a strong acid treatment.	36
Figure 10: Summary of diverse second step reactions done after an oxidizing treatment (first step) [60]	38
Figure 11: Representation of the chemical structure of CNTs	39
Figure 12: on the left sp ² carbon hybridation, on the right sp ³ carbon hybridation	40
Figure 13: Orbital structure of the CNT external layer, a) transversal representation of the overlap of the carbon Z orbitals in CNTs; b) representation of the angle induced by the pyramidalization due to a sp ³ hybridization compared to a trigonal configuration (sp ² hybridization) [62]; c) representation of the misalignment between carbon z-orbitals in SWNTs.....	41
Figure 14: side wall addition chemical reaction on SWNTs or MWNTs [60].....	43
Figure 15: General mechanism of ATRP process	47
Figure 16: schematic presentation of hybrid materials produced by ATRP process [97].	48
Figure 17: Representation of the behavior of a liquid drop on a solid substrate. θ is the contact angle, and is representative of the compatibility of the chemical substances.	54
Figure 18: Representation of a structured di-block copolymer (A-B), which blocks are composed of immiscible polymers.	57
Figure 19: Transition phase diagram for conformationally symmetric block copolymer, where χ_N is a function of f [130]	57

Figure 20: a) Computer simulations permitting to calculate the work necessary to completely pull out a SWNT from a polystyrene matrix [134]; b) Computer simulation demonstrating the effect of the tubes form defects on the pull out phenomenon (“interlocked tubes”) [136].	59
Figure 21 : Schematic of a link percolating network	62
Figure 22 : Simulated statistical dimension in a 3D cubic site percolating network, $P_{\infty}(p)$ is the probability for a site to belong to an infinite cluster, $X^A(p)$ is the portion of active sites that belong to the infinite cluster, $X^B(p)$ is the portion of active sites that belong to the back bone, $X^I(p)$ the portion of isolated active sites.	65
Figure 23 : a) Definition of the waviness of a fiber between 2 contacts [70], b) evolution of the percolation threshold in a 2D network against the waviness of the fiber	67
Figure 24 : Electrical conductivity against frequency next to the percolation threshold	69
Figure 25: a) Evolution of the compliance during a creep test, J_{el} is the elastic compliance, J_{an} is the anelastic compliance, J_{vp} is the viscoplastic compliance; b) representation of the strain behavior against stress for thermoplastic polymer tensile tests.	72
Figure 26: Representation of the upper and lower limit of the mean field theory	76
Figure 27: 4 Halpin Tsai layer used model to generate Halpin-Kardos Model.	77
Figure 28: Model of Takayanagi adapted to percolating system.	79
Figure 29: schematic snap shot for the spray pyrolysis to synthesize CN _x MWNTs.	84
Figure 30: growth mechanism for CN _x MWNTs.	85
Figure 31: bamboo-like structured CN _x MWNTs TEM photomicrograph [176].	85
Figure 32: Styrene monomer.	86
Figure 33: Butadiene monomer	86
Figure 34: BPO free radical liberation mechanism	87
Figure 35: Chemical mechanism of free radical addition on the CN _x MWNT external layer	88
Figure 36: CN _x MWNT covered by phenyls groups	88
Figure 37: Chemical reaction equation of the proton aromatic ring substitution.	89
Figure 38: CN _x MWNT following the ATRP process.	90
Figure 39: Experimental scheme of the addition of BPO to CN _x MWNTs.	91
Figure 40: Scheme depicting the solvent drying process	92
Figure 41: Experimental scheme of the ATRP line.	93
Figure 42: Harmonic oscillator model for a bi-atomic system.	94
Figure 43: Experimental schematic of an FTIR analyzer.	95
Figure 44: Experimental scheme of the GC-MS spectrometer	96
Figure 45: Polymer / CN _x MWNT composite synthesis process.	101
Figure 46: Experimental scheme of DSC device	103
Figure 47: Skeme of the Shear Dynamic Mechanical Analysis device used.	106
Figure 48: Compression tensile test device used in this work.	108
Figure 49: Theoretical schematic diagram showing the different stages of the functionalization process of CN _x MWNTs. First the grafting of aromatic rings takes place, subsequently the bromination of such rings occurs. These brominated molecules then act as macroinitiators during the ATRP reaction of PS.	114
Figure 50: FTIR spectra of: As-produced CN _x nanotubes, and phenyl grafted CN _x MWNTs.	115
Figure 51: TGA plots for different types of modified CN _x nanotubes, carried out under a N ₂ atmosphere.	118

Figure 52: TEM micrographs of: a) as produced CN _x MWNT showing the external surface of the tube and the lack of amorphous carbon deposited around the outer layer; b) PS-grafted CN _x MWNT exhibiting a homogenous layer of PS coating the CN _x nanotubes; c-d) HRTEM micrographs of PS grafted CN _x MWNT showing the morphology of the amorphous layer and the “graphitic” walls of the tubes (shown by white lines); the PS coating is also indicated in figures (c) and (d)...	121
Figure 53: a) Low loss EELS spectra of as-received CN _x -MWNTs (top spectrum), the ATRP reacted CN _x MWNT (middle spectrum) and polystyrene (bottom spectrum); b) EDX spectrum of the tube ATRP reacted CN _x MWNT coated with PS (also shown in Fig. 4c). It is clear the presence of Br, which was attached to the phenyl groups prior to polymerization. Therefore, the ATRP reaction took place efficiently. Note that Cu signal comes from the TEM grid and the Si signal from the quartz tube where the tubes were produced.....	122
Figure 54: SEM photomicrographs at a low magnification of a) PS-g-CN _x / polystyrene nanocomposites and, b) a-CN _x / polystyrene nanocomposites.	126
Figure 55: SEM photomicrographs of a) and b) PS-g-CN _x / PSBS nanocomposites; c) and d) a-CN _x / PSBS nanocomposites after cryogenic fracture.	128
Figure 56: SEM micrographs of the CN _x MWNTs / PS nanocomposites after breaking at ambient temperature; a) PS-g-CN _x / PS nanocomposite with white circles indicating cut tubes, b) a-CN _x / PS nanocomposite. The black circles indicate holes or pulled out tubes. On the right side is represented the proposed mechanisms of fracture.....	129
Figure 57: TEM micrographs of an ultramicrotomic cut of a-CN _x / PS nanocomposites. The white circles on the photomicrograph a) indicate tubes pulled-out from the matrix. b) depict a white circle probably indicating a hole left by a pull-out effect during the preparation process.....	130
Figure 58: TEM photomicrographs of the PS-g-CN _x / PS nanocomposites.....	131
Figure 59: TEM micrographs of the PS-g-CN _x / PS nanocomposites low and high magnification showing the cross-section of a PS-g-CN _x that is well attached to the PS matrix	132
Figure 60: TEM micrograph of the PSBS matrix (after ruthenium staining). The dark regions correspond to the butadiene blocks and the bright ones to the styrene blocks.....	134
Figure 61: TEM micrographs of a-CN _x / PSBS nanocomposites. The bright regions of the copolymer are the polystyrene phase, and the dark areas represent the polybutadiene phase.	135
Figure 62: TEM micrograph of the 2.5 vol. % PS-g-CN _x / PSBS nanocomposite. The bright regions of the copolymer are the polystyrene phases, and the dark regions are the polybutadiene phases. The white circles indicate PS-g-CN _x encapsulated in PS cylinders.	137
Figure 63: Morphology details of the PS-g-CN _x in the PSBS matrix.	138
Figure 64: Proposed structure of the CN _x MWNTs / PSBS matrix next to the tube surface; a) the tube is small enough to act as a PS block cylinder, b) the PS grafted layer interacts with the PSBS matrix and induces aligned PS block cylinders along the CN _x MWNT axis, c) the PS grafted layer interacts with the PSBS matrix and induces PS block cylinder perpendicular to the CN _x MWNT axis.....	139
Figure 65 : Glassy transition temperatures determined by DSC of the PS matrix, a 2.5 vol. % a-CN _x / PS nanocomposite, a 2.5 vol. % PS-g-CN _x / PS nanocomposite, pure PS-gCN _x	140

Figure 66: Glass transition temperature of polystyrene against its molecular weight [192].	141
Figure 67: A) For the composites with a-CN _x , the matrix have the same glass transition than pure PS; B) For the composites with PS-g-CN _x the PS matrix next to the PS grafted layer ($T_g < T_g$ pure PS) has a lower glass transition: the low molecular weight PS grafted layer act as a plasticizer.	142
Figure 68 : Complex conductivity modulus $\sigma(\omega)$ of nanocomposites containing a-CN _x at different volume fractions: a) PS matrix and b) PSBS matrix.....	148
Figure 69 : Experimental conductivity results and fitted scaling law for a-CN _x polymer nano-composite a) with PS matrix and b) with PSBS matrix.....	150
Figure 70 : Complex conductivity modulus of the Ps-g-CN _x nano-composites against the frequency at different volume fractions of filler; a) PS matrix, b) PSBS matrix.	152
Figure 71: Young modulus experimental results for a-CN _x nanocomposites: (-★-); PS-g-CN _x nanocomposites (-■-); theoretical results calculated from Halpin Kardos theory (—).....	159
Figure 72: DMA results for the a-CN _x / PS composites, a) storage shear modulus as a function of the temperature and b) tangent of the loss angle as a function of the temperature	162
Figure 73: DMA results for the PS-g-CN _x / PS composites, a) storage shear modulus as a function of the temperature and b) tangent of the loss angle as a function of the temperature	163
Figure 74: representation of the possible contacts behavior between carbon nanotubes: a) schema of simple contact; b) schema of entangled contact [70]	166
Figure 75: Experimental shear storage modulus at 420 K of PS filled with a-CN _x MWNTs (...○...) or PS-g-CN _x MWNTs (-■-), and shear modulus from Halpin Kardos calculation (—).	166
Figure 76: $T \gg T_g$ matrix; when the filler volume fraction lower than the percolation threshold the tubes do not have any interaction and may be modeled by the Halpin Kardos model. For volume fraction of filer higher than the percolation threshold, the interaction between tubes should be considered as strong interaction compared to the shear modulus of the matrix.	167
Figure 77: Compression tensile test curves of: a) a-CN _x , b) PS-g-CN _x	168
Figure 78: DMA results for the a-CN _x / PSBS composites, a) storage shear modulus as a function of the temperature and b) tangent of the loss angle as a function of the temperature	172
Figure 79: DMA results for the PS-g-CN _x / PSBS composites, a) storage shear modulus versus temperature and b) tangent of the loss angle versus temperature.....	173
Figure 80: SEM micrograph of the a-CN _x in PSBS; a) original SEM micrograph and, b) treated micrograph to highlight the disorder in the PSBS matrix	175
Figure 81: TEM micrograph that represents the hexagonal packed structure preserved when using PS-g-CN _x and how PS-g-CN _x link the matrix PS domains.	176
Figure 82: Experimental measured Young modulus of a-CN _x / PSBS (-■-), Prediction of Halpin Kardos mean field approach: $f = 150$ (—),	178
Figure 83: Modulus of PSBS composites as a function of the filler volume fraction: Young Modulus of PS-g-CN _x / PSBS composites (-■-), (—) Mechanical percolating model and (- - -) Halpin-Kardos Model.....	179
Figure 84: Room temperature tensile test of CN _x MWNT composites using a PSBS matrix, a) a-CN _x composites, b) PS-g-CN _x composites.....	182

Table of abbreviations:

a-CNx: As received CNx MWNTs
ATRP: Atomic Transfer Radical Polymerization
BPO: Benzoin Peroxide
CNTs: Carbon Nanotubes
CNx MWNTs: Nitrogen doped Multiwalled Carbon Nanotubes
CNx MWNTs-BPO: Phenyl grafted CNx MWNTs
CNx MWNTs-BPO-Br: ATRP macroinitiator grafted CNx MWNTs
CVD: Chemical Vapor Deposition
DMA: Dynamic Mechanical Analysis
DSC: Differential Scanning Calorimetry
E: Young's modulus
EDS: Energy Dispersing Spectroscopy
EELS: Electron Energy Loss Spectroscopy
ESR: Electron Spin Resonance
f: aspect ratio
FTIR: Fourier Transform Infra Red spectroscopy
G: Shear modulus
GC/MS: Coupled Gas Chromatography / Mass Spectroscopy
H.K: Halpin Kardos
 M_n : Molecular Weight
MWNTs: Multi-Walled Nanotubes
 P_c : percolating threshold volume fraction
PS: Polystyrene
PSBS: poly (styrene-co-styrene)
PS-g-CNx: PS grafted CNx MWNTs
SEM: Scanning Electron Microscopy
STM: Scanning Tunneling Microscopy
STS: Scanning Tunneling Spectroscopy
SWNTs: Single-Walled Nanotubes
 $T\alpha$: Principal relaxation in dynamic mechanical analysis
t: percolation critical exponent
 $\text{Tan}(\delta)$: Tangent of the loss angle during DMA experiments

TEM: Transmission Electron Microscopy

Tg: Glassy Temperature

TGA: Thermogravimetric Analysis

Chapter I

General introduction

A.1 Generalities on polymers

Polymers can be defined as macromolecules composed of long chains of one (homopolymer) or various (co-polymer) elementary units named monomers. The polymer synthesis belongs to the organic chemistry area. The reactions consist in assembling molecules. It can be instanced the most famous processes known: addition, radical propagation. From these processes, it can be generated a lot of polymer types, among which: homopolymers, statistical co-polymers and block co-copolymers. A homopolymer is constituted of long macromolecular chains composed of the same monomer (C.f. Figure 1 a.). The most characteristic parameters which define this kind of materials are the glass transition temperature and the molecular weight. In the following paragraph we will summarize the physical meaning of these parameters. If the macromolecular chains contain several types of monomers, we define it as a co-polymer. Co-polymers can be either statistical or block co-polymers. Figure 1 b) and c) is a schematic representation of a co-polymer macromolecular chain. It is named statistical co-polymer when the monomer units (type A or type B in Figure 1) are randomly assembled along the macromolecular chain. On the contrary to statistical copolymers, the monomer units constitute larger units of the same composition (the so-called blocks) within the block co-polymer macromolecular chain. Typically these materials have properties of both polymers A and B (on Figure 1 c.). Moreover, the physical behavior of block co-polymers is function of the molecular weight and molecular weight polydispersity of each block. It is detailed later in the chapter IV part B (morphology and interfacial adhesion of CNx MWNT composites) that the microstructure is deeply dependent of those parameters too.

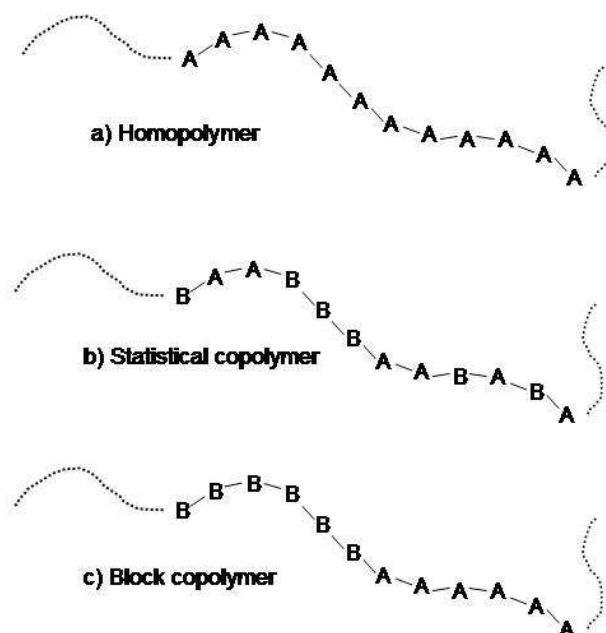


Figure 1: Schematic representation of a) a homopolymer b) a statistical copolymer c) a block copolymer

A.1.1 Characteristic temperatures of polymers:

From the liquid state to lower temperatures, the thermodynamic dimensions of a polymer will change because of the structural evolutions that occur in the bulk material. In some cases, a decrease of the temperature permits a rearrangement of the structure and a partial crystallization of the system occurs. Those materials, named semi-crystalline materials, have a typical response in differential scanning calorimetry tests, represented by an endothermic peak at a given temperature (crystallization temperature). Most of the monomers generate purely amorphous chains that do not offer this opportunity.

The glass transition (at a temperature T_g) represents the variation from a metastable state into an out of equilibrium state, and is always observed in amorphous materials (amorphous polymer or amorphous phase of a semi-crystalline polymer). When the temperature decreases from the liquid state, at a given temperature value named glass transition temperature (T_g) the molecular mobility is not high enough to maintain the material in the liquid state. Consequently, molecules pass into a glassy state. T_g is usually determined by Differential Scanning Calorimetry (DSC) and is a function of the temperature scan rate. At the glass transition temperature (T_g), the structural rearrangement

is comparable to the experience time. On the contrary, below T_g the material evolves slowly to its equilibrium state. This phenomenon is known as physical aging and could be responsible for changes in the mechanical behavior.

Commonly confused with the glass transition, the α relaxation represents a cooperative movement in the material. It occurs at a temperature T_α , defined as the temperature of the maximum energy dissipated by mechanical dynamical sollicitation. T_α is function of the sollicitation frequency.

A.2 Nanotubes

A.2.1 Generalities: Discovery of other allotropic forms of carbon (C_{60} and identification of carbon nanotubes)

In 1985 the journal Nature [2] published the discovery of a new material which constitutes the starting point of a new era in carbon materials. These materials consist of carbon cage molecules known as fullerenes. C_{60} is the most stable fullerene molecule and consists of 60 carbon atoms exhibiting hexagonal and pentagonal faces (sp^2 -like hybridization) similar to a “soccer-ball” (Figure 2).

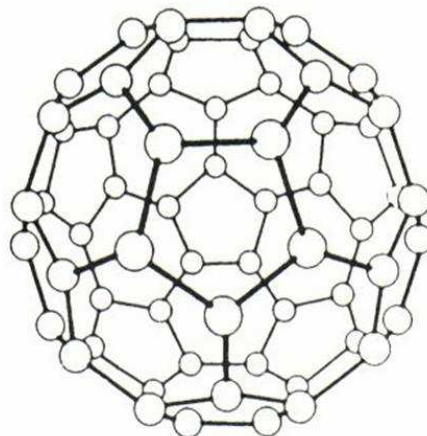


Figure 2: Molecular model of the C_{60} structure

Later, in 1991, Sumio Iijima, while he was working on producing C_{60} by arc-discharge, found nested graphene cylinders on the cathode deposit [1]. These structures are known as nanotubes. Carbon nanotubes (CNTs) are thus composed of rolled-up co-axial graphene sheets closed by fullerene

hemispheres. The main body of a perfect Carbon Nanotube tube (CNT) is composed of carbon atoms exhibiting sp^2 hybridization, whereas the end caps have the structure of fullerenes (sp^3 -like hybridization). CNTs can exist in two main forms: Single-Walled Carbon Nanotubes (SWNTs) and Multi-Walled Carbon Nanotube (MWNTs), depending on the number of coaxially rolled-up graphene sheets. Moreover, SWNTs can exist in several chiral forms, depending on the way the graphene sheets are rolled-up, see Figure 3.

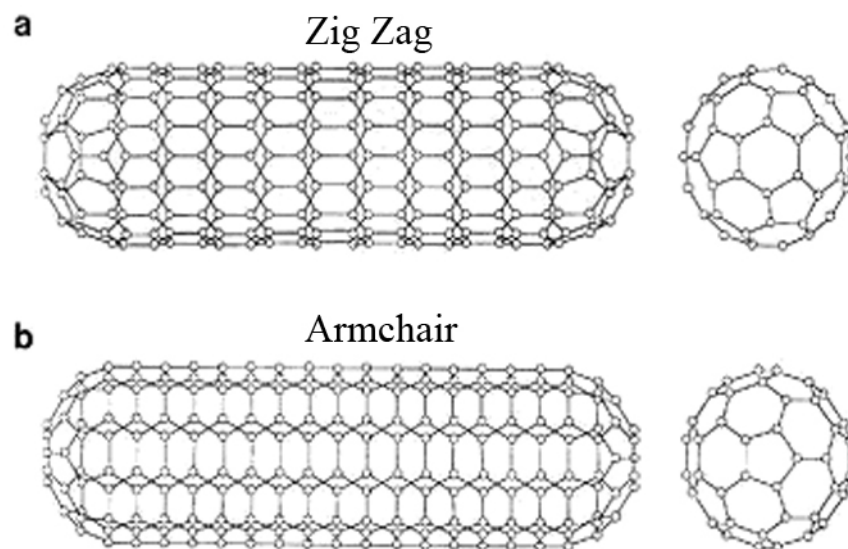


Figure 3: Theoretical structures of two particular types of chiral single walled nanotubes a) zig-zag structure b) armchair structure [3]

CNTs rapidly attracted the interest of the scientific community. Indeed, many physicists and chemists were fascinated by their incredible physico-chemical properties. The electronic properties of SWNTs [4, 5] appear to be dependent on the chirality and the diameter of the tubes, and they can exhibit either a metallic or a semiconducting behavior, contrarily to MWNTs which always display conducting properties. More interestingly, both SWNTs and MWNTs have an incredible longitudinal Young's modulus [6, 7] combined with a large transversal flexibility [8] and an extremely high aspect ratio (length to diameter ratio). This explains why the composite material community is very interested in using the CNTs as nanofillers.

A.2.2 Nanotube synthesis processes

As mentioned above, nanotubes could be found in the carbon soot of a graphitic cathode after an arc evaporation experiment [1]. However, these quantities did not allow complete investigations of this type of nanotubes. The first gram production was performed when the pressure of Helium in the arc evaporation method was increased [9]. Nowadays, other processes are used to produce carbon nanotubes: pyrolysis of hydrocarbons on metal particles, laser vaporization of a graphite target [10, 11], solar carbon vaporization [12, 13], and electrolysis of graphite electrodes in molten ionic salts [12]. We will describe below the process of pyrolysis of hydrocarbons on metal particles because this process can be modified to produce nitrogen-doped MWNTs (CN_x MWNTs).

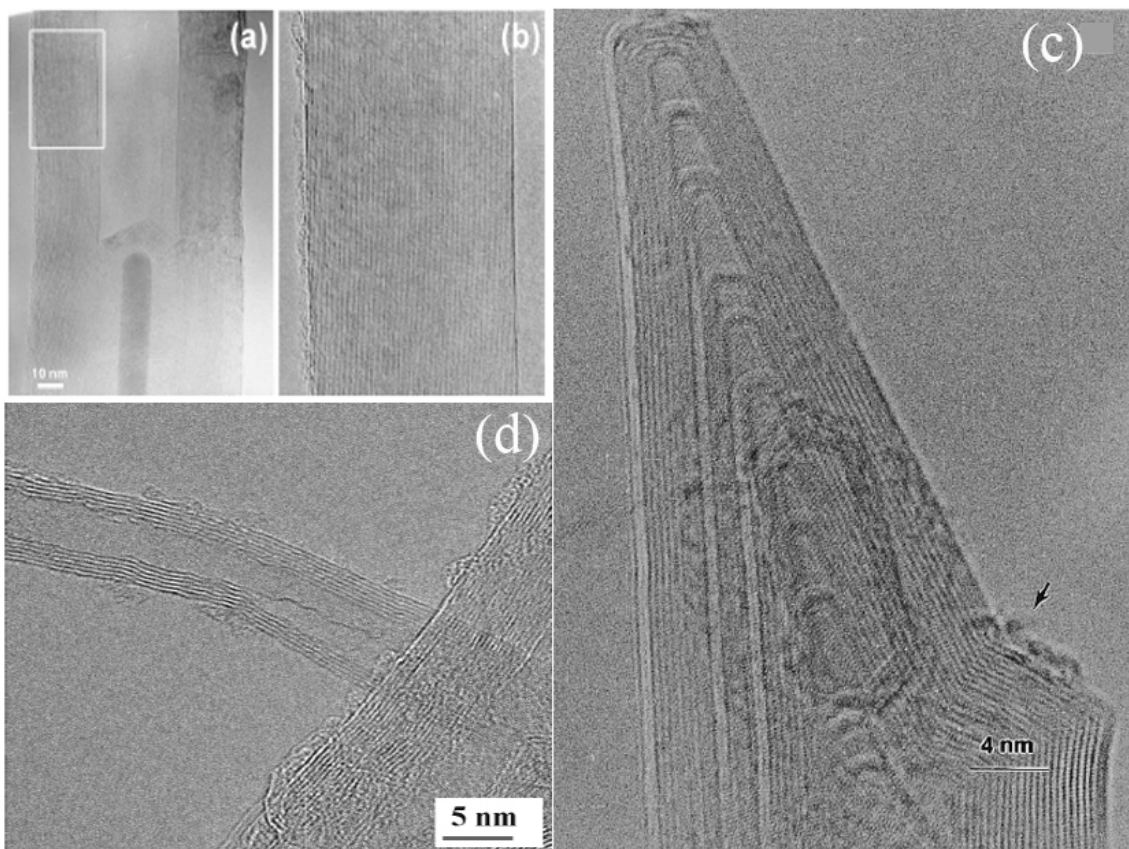


Figure 4: carbon nanotubes produced by different methods; a) MWNTs produced by spray pyrolysis methods [14], b) overview of the carbon concentric carbon shells on the micrograph (a) ; c) carbon nanotubes produced in hydrogen arc discharge conditions [15], and d) carbon nanotubes produced using a CVD process [16]

In Figure 4 it is shown carbon nanotubes produced by different synthesis process. The process of pyrolysis of hydrocarbons over metal particles, also known as Carbon Vapor Deposition (CVD), consists of the pyrolysis of hydrocarbon gases over a metal catalyst (Co, Ni, Fe, and Pt). It generates

nanotubes, C_{60} , and different nanotubes-like structures. Many works have been performed in order to describe and understand the growth of CNTs. Three important models exist: carbon diffusion through the catalytic particles [17], the top carbon diffusion on catalytic particles [18], and the bottom carbon diffusion through catalytic particles [18, 19].

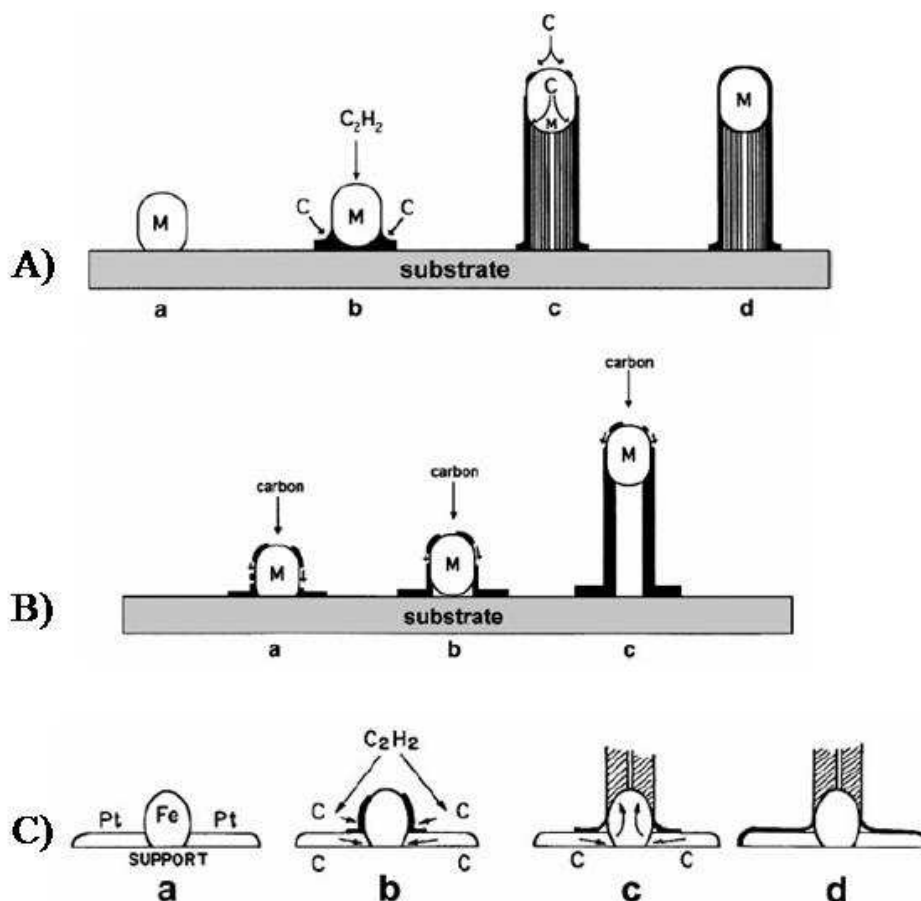


Figure 5: Different growth mechanisms occurring in CVD processes A) growth mechanism postulated by Baker et al. [17] for the formation of carbon filaments by pyrolysis of acetylene on metal particles; B) growth mechanism proposed for carbon fibers and filaments by pyrolysis of benzene over metallic particle [15] and C) growth mechanism proposed for carbon filament synthesis from Fe-Pt / C_2H_2 system [16,17].

Figure 5 illustrates the differences among the different growth models. The carbon diffusion through the catalytic particle is depicted in Figure 5 A); here carbon fragments diffuse through the catalytic particle and precipitate at the other side of the particle as graphene sheets (colder zone). This process was proposed to explain the formation of CNTs from acetylene on metal particles. Figure 5 B) sketches the mechanism of top carbon diffusion on catalytic particles. This model postulates that the carbon diffuses on the end of the catalytic particle as solid carbon (graphite) and precipitates at the other side.

Finally, Figure 5 C) represents the bottom carbon diffusion through catalytic particles. In this case, the carbon diffusion occurs from the bottom to the top of the catalytic particle. On the contrary to the other models, the catalytic particle remains at the bottom of the substrate.

It has been shown that a vapor composed of a metal catalyst and carbon atoms can also be pyrolysed in order to produce carbon nanotubes. The metal carbon vapors are usually produced by heating metallocenes with organic molecules (for example: ferrocene/benzene [20]). The structure of the carbon nanotubes can be controlled via different experimental parameters: pressure of the inert gas, temperature of the furnace, carbon gas source, and metallocene type.

A.2.3 Physico-chemical properties of Multiwalled Carbon Nanotubes

The nature and form (size) of the catalyst particle allows to synthesize either SWNTs or MWNTs. In the following section, we will describe essentially MWNTs, since they were used in this thesis work because of their lower fragility during chemical functionalization. MWNTs are characterized by the presence of concentric cylinders of graphene (C.f. Figure 6). The number of layers that composes the MWNT depends on various parameters that include the synthesis route, the carbon source, the catalyst type, etc.

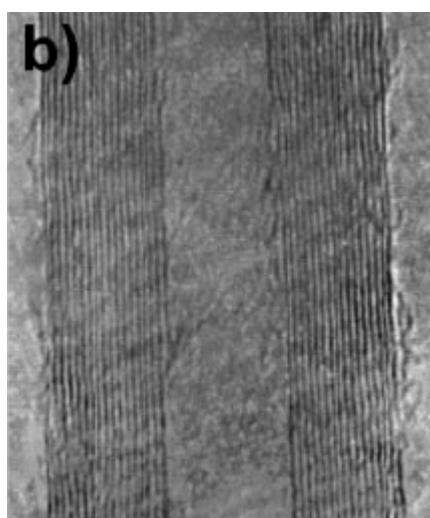


Figure 6: HRTEM micrograph of a multiwalled Carbon nanotube. The graphene sheets are visible when observed edge-on and appear in black. The distance between two consecutive graphene sheets is 0.34 nm [21].

A.2.3.1 Electrical Properties of carbon nanotubes

CNTs belong to the family of fullerenes. Different electronic properties can be observed, depending on the nanotube helicity (c.f. Figure 7).

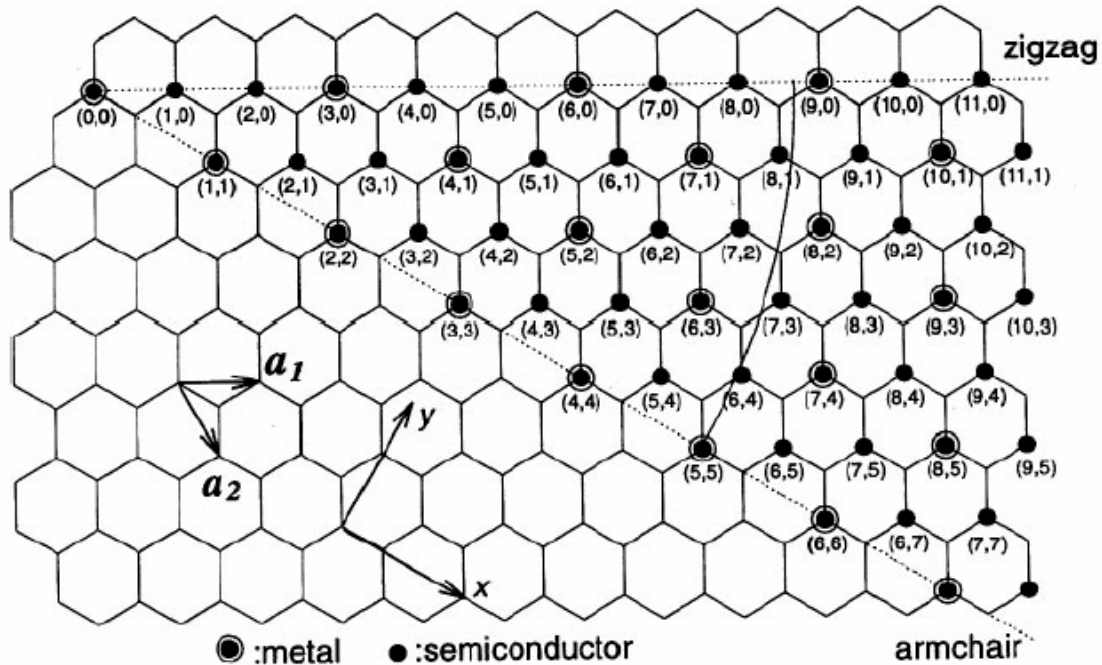


Figure 7: Different electronic properties depending on the helicity

The electronic behavior of CNTs has been largely investigated from the theoretical point of view. Recent experimental studies on the conductivity of the nanotubes (measured on aligned bundles) show that nanotubes as conducting rods [22-25]. Scanning Tunneling Microscopy (STM) and Scanning Tunneling Spectroscopy (STS) are two powerful techniques that are used to characterize the transport phenomenon in CNTs. Thanks to these equipments, it is possible to observe the local electronic density and conclude about their metallic or semi-conducting character. Using these techniques, it has for example been shown that SWNTs behave as metals or semiconductors depending on their helicity. Bulk transport measurements moreover indicate that the conducting behavior of nanotubes is temperature dependent [25], but the values are different when compared to SWNTs [26]. It can therefore be concluded that each nanotube has its own electronic behavior [26], which depends on its chirality, diameter, defect concentration, number of layers, cristallinity.

Defects in the structure of the tubes can largely modify their electronic behavior [11, 27]. For example the introduction of hexagonal and pentagonal rings can change the chirality and thus the conducting or semi-conducting character of the CNTs. It is also predicted that nanotubes with periodic arrangements of pentagons, hexagons and heptagons can behave as metals or even superconductors[28].

A.2.3.2 Mechanical properties of carbon nanotubes

One of the main advantages of carbon nanotubes is their outstanding longitudinal Young's modulus. It was indeed expected that CNTs have at least the modulus of graphene sheets (1.03 TPa). Because of their nanometric size it is quite difficult to measure accurately the modulus of CNTs. Direct measurements on SWNTs using a bending force with an Atomic Force Microscope (AFM) revealed a Young's modulus between 0.32 and 1.47 TPa [29]. Indirect measurements of the MWNT Young's modulus from their vibrational energy provide a narrower range of values: 1-1.8 TPa [6].

Most of the moduli measured in the literature are presented in Table 1. The parameters explaining the differences between the measured Young's moduli of the CNTs are their diameter, crystallinity, and helicity [30-32].

Reference	Kind of tube tested	
Treacy et al.[6]	MWNT	$E = 1.8 \pm 1.4$ TPa
Wong et al.[7]	MWNT	$E = 1.28 \pm 0.59$ TPa
Krishnan et al.[33]	SWNT	$E = 1.25 \pm 0.45$ TPa
Pan et al.[34]	MWNT	$E = 1.72 \pm 0.64$ TPa
Walter et al [35].	SWNT	$E = 45 \pm 7$ GPa
Poncharal et al.[36]	MWNT	$E = 1$ TPa
Salvetat et al.[37]	MWNT	$E = 810 \pm 410$ GPa
Salvetat et al.[38]	SWNT	$E = 1$ TPa
Yu et al. [29]	SWNT	$13 < E < 52$ GPa
Yu et al. [39]	MWNT	$270 < E < 950$ GPa
Zhu et al.[40]	SWNT	$49 < E < 77$ GPa
Demezyk et al.[41]	MWNT	$E = 0.91 \pm 0.18$ TPa
Qi et al.[42]	MWNT	$E = 0.91 - 1.24$ TPa

Table 1: Young's moduli of several SWNTs and MWNTs reported in the literature.

A.2.4 Nitrogen Doped Multiwalled Carbon Nanotubes (CNx MWNTs)

A.2.4.1 Chemical properties and structure of the CNx MWNTs

Figure 29 shows the experimental equipment used to synthesize nitrogen doped MWNTs. Using this process it is possible to produce large quantities of material (g/day). In addition the nitrogen concentration varies from 1 to 7 at.% using this technique. Nitrogen atoms can be introduced in the graphitic structure into two forms. It can be present as substitutional atoms, where nitrogen acts in the structure as a carbon does: substitutional nitrogen atoms are bound with the adjacent carbon atoms of the network by three covalent bonds. In the second possible structure, nitrogen atoms can form pyridine-like groups, as shown in Figure 8. Moreover, it was also shown that nanotubes sometimes encapsulated gaseous nitrogen. It indeed appears that nanotubes synthesized using this process are also good gas containers [43].

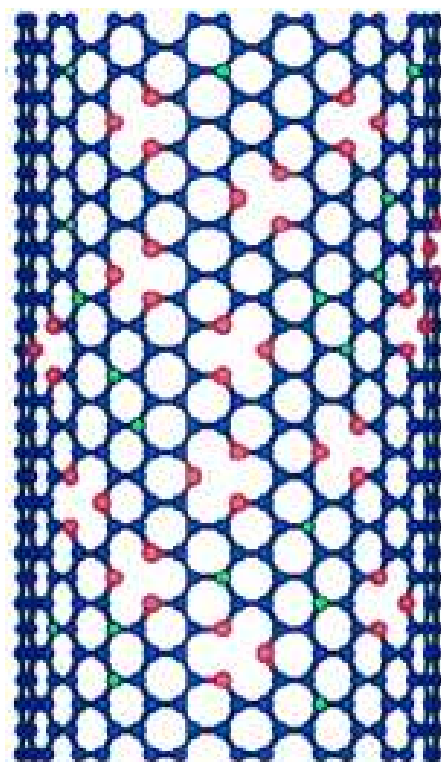


Figure 8: Theoretical representation of pyridine (pink atoms) and tertiary amine (green atoms) nitrogen sites in a CNx MWNT

On the contrary to boron doped nanotubes, nitrogen seems to be homogeneously distributed along these tubes [44]. In reference [45], it is mentioned that the presence of nitrogen in the graphene plane tends to lower the crystalline order of the network [46]. A Recent work, using Raman spectroscopy analysis [47] demonstrated that doping nanotubes with nitrogen increases the D-band intensity. D-band is associated to the disorder on the contrary to the G band, which represents the graphitic level of the carbon material. As a consequence, the higher nitrogen concentration is, the lower the crystallinity of the tubes becomes [44]. Last results, bamboo-type structures are always observed in CNx MWNTs.

A.2.4.2 CNx MWNTs might be more chemically reactive:

It is well known that pure graphite is chemically inert. So, the reduced crystallinity of the CNx MWNTs let us expect that the presence of nitrogen will promote the formation of anchoring sites. The grafting of chemical groups on the CNx MWNT surface might thus be more efficiently performed on CNx MWNTs rather than on undoped nanotubes.

A.2.4.3 CNx MWNT are electrically conductive

One advantage of the CNx MWNTs is that they are always electrically conductive. Nitrogen is an electron donor dopant; which is a key point for grafting molecules on their surface (c.f. Chapter II part A. 1.4: chemical structure and reactivity of CNx MWNTs). M. Terrones [45] provides references related to the electronic behavior of CNx MWNTs. STEM and STS analysis on N-doped nanotubes revealed that they are purely metallic [45]. Considering that substitutional nitrogen is an electron-donor doping atom, electrons are present in the conduction band [45]. This leads to a negative thermoelectric power (TEP) response characteristic of an electron-like conduction. The same work revealed a value of the conductivity equal to about 10 S.m^{-1} .

A.2.4.4 Nitrogen doping, bamboo-like tubular structures and mechanical properties

Theoretical calculation [45] have been performed to estimate the Young's modulus of CNx MWNTs [48]. They revealed that the modulus should be inferior to that of undoped MWNTs because of the presence of defects (nitrogen atoms) within the carbon network. The calculated Young's modulus was indeed estimated to be 0.5-0.8 TPa, instead of 1 TPa for undoped MWNTs. Another published work reports measurements of the CNx MWNT modulus [49]. The results confirmed a drastic decrease in the Young's modulus; the experimental value being equal to 30 GPa. The very low value obtained was attributed to the very high concentration of nitrogen defects ($\approx 2-5\%$). It is thus expected that lower concentrations of nitrogen atoms will not alter significantly the Young's modulus.

However, unlike pristine MWNTs [50], the bamboo type structure of the tubes permits an increase in the interaction between all concentric layers. They have a bamboo-like structure that avoids telescopic sliding of concentric cylinders within each tube upon tensile tests; therefore we should expect a better mechanical reinforcement for large strains.

A.3 Carbon nanotubes-polymer composites

The fabrication of polymer-based composites involves more and more nano-scale materials as fillers. Indeed, by reducing the dimensions of the fillers, it is possible to increase the surface/volume ratio. Indeed, as compared to micron scale fillers the nanoscale fillers exhibit a higher contact surface with the matrix. Thus, they are expected to improve the mechanical reinforcement by increasing the load transfer (C.f: Chapter II mechanical behavior of the polymer composites). In particular, carbon nanotubes are excellent candidates for fabricating nanocomposites. Indeed, the carbon nanotubes are not only rigid fillers (longitudinal modulus ≈ 1 TPa) but they are also good for producing electrically conductive fillers. In addition, carbon nanotubes exhibit a very high aspect ratio. As a consequence, they are expected to form an electric percolating network at very low volume fractions.

Nevertheless, when nanoparticles are added to the matrix the number of contacts among particles increases, and consequently enhances attractive interactions among them (e.g. via van der Waals or electrostatic forces). This effect induces agglomeration of nanoparticles that do not lead to good dispersions in the matrix. Many researchers have tried to achieve good dispersions of the carbon nanotubes in different matrix. First, we should mention the use of different physico-chemical processes in the fabrication of polymer / carbon nanotubes nano-composites in order to enhance the dispersion of nanotubes in polymer matrices. For example, P. Pötschke [51], using melt mixing to disperse MWNTs in polycarbonate, reached the electric percolation threshold at 1 wt.%. Moreover, the work by M. K. Seo and co-workers [52] should be mentioned, in which they used the same technique to disperse MWNTs in a polypropylene matrix and observed an electric percolation threshold in the range of 1-2 wt.%. As a consequence, we can deduce that the physico-chemistry of the matrix / carbon nanotube interface has an important influence on the dispersion efficiency. Other groups preferred to use the solvent casting technique, which generally consists of dispersing nanotubes in a solvent by ultrasonication and finally maintaining the dispersion with a vigorous mechanical stirring during the solvent evaporation. For example, J. K. W. Sandler et. al [53] dispersed MWNTs in an epoxy matrix and found a very low electric percolation threshold, at 0.0025 wt.%. On the contrary, S. Barrau [54] reported an electric percolation threshold at 0.3 wt.% for a dispersion of SWNTs in an epoxy matrix. The difference observed between these results could be attributed to an aggregation phenomenon of the tubes. Finally, as it will be detailed in chapter IV, chemical functionalization has been used to modify their surface in order to improve their dispersion. It has been shown [55] that grafting aromatic rings on the carbon nanotube surface permits to reach a better dispersion in benzenic solvents such as toluene or benzene. We should also mention the works of J. Chen [56], who obtained a specific dispersion in polar solvents by grafting -OH groups using strong acid treatments. Finally, it was demonstrated [57] that grafting macromolecules on the surface of carbon nanotubes should decrease their cohesive forces in a particular media.

A.4 Conclusions

In this chapter, we summarized the important concepts related to the fabrication of nano-composites. We have presented the principal physical properties of the CNTs. It appears that their high aspect ratio associated to their electrical and mechanical properties make them good candidates as polymer modifiers. SWNTs are difficult to use in the synthesis of nanocomposites. Indeed, they generally contain many impurities. Consequently we prefer to use MWNTs in this work.

We have shown that the CNTs tend to aggregate when dispersed in a polymer matrix. Furthermore, it appears that they have a low interfacial adhesion with polymers. As a consequence, we decided to carry out the grafting of polymer on the CNT surface. In this chapter, we have also detailed the chemical properties of MWNTs. We have shown that they tend to be chemically inert (graphene sheets). Since the nitrogen doping induce defects in the structure of MWNTs, we believe that they are more chemically reactive. Moreover, the bamboo-like structure resulting from the nitrogen doping, might avoid the sliding of concentric tubular sheets when working under longitudinal stress. As a consequence, the nanotubes we have used in this works are CNx MWNTs.

Finally, in a first part we will focus our works on the grafting of polystyrene on the external layer of CNx MWNTs. Thus, these chemically modified CNTs will be used in the fabrication of nanocomposites. Then, we will study and discuss the mechanical and electrical properties of these nanocomposites. The polymer matrix, we choose are: polystyrene, and a poly (styrene-co-butadiene). The first one has the same nature than the grafting, and the second one will permit to observe the effect of the grafting on its microstructure.

Chapter II

Theoretical part and hypotheses

Part A Chemical modification of carbon nanotubes

The chemical addition of functional groups, on nanotube surfaces, modifies their chemical environment, allowing selective dispersions of nanotubes in a particular media. The literature is abundant regarding the modification or functionalization of carbon nanotubes [57-60]. For example non-covalent modifications [61] (i.e, physical adsorption) could change the nanotube electronic and surface properties. Also, by using non-ionic surfactants in the polymers fabrication processes, it has been shown [62, 63] that the introduction of 1 wt. % of carbon nanotubes results in notable effects on the mechanical characteristics of the composite material. Many efforts have been carried out in order to disperse nanotubes in solvents. However, the mechanical and electrical properties of the composite materials highly depend on the dispersion of the nanotubes in the polymer matrix. Unmodified nanotubes tend to aggregate due to high Van der Waals forces. This phenomenon is not desired in the modification of polymers with carbon nanotubes (either SWNTs or MWNTs). As mentioned earlier, functionalization of the nanotube surface helps to overcome this problem. For example carboxylic groups have been chemically bonded to the nanotube surface in order to permit the dispersion in polar solvents [40] or to allow other reactions on the tube surface such as esterification [64]. It can also be mentioned that, hydrothermal treatments at high pressures and temperatures modify the chemistry of the nanotube surface [65]. A more classical process such as Bingel Reactions has demonstrated that SWNTs could be surface modified [66]. Other authors have demonstrated much higher efficiency to modify the surface of nanotubes by novel processes: free solvent organic modification [67]. However, one should emphasize that graphite is chemically inert and similarly large diameter nanotubes are expected to have similar inertness.

One should also note that CNx MWNTs are a special kind of carbon nanotubes. The defects induced by nitrogen doping are expected to improve the chemical reactivity of carbon nanotubes. Moreover these nanotubes always display a bamboo-like structure that ensures that all layers of CNx MWNT are interconnected and will not slide telescopically. We believe that this structure could have a major effect on the mechanical properties of nanocomposites when compared to classical rested cylinders.

A.1 Chemical modification of carbon nanotubes.

These last few years the interest in chemical modifications on the external layer of carbon nanotubes has increased. These surface modifications are important for enhancing the tube reactivity and produce reinforced nanocomposites.

Recent reviews point out the importance of chemical modifications of nanotubes [57-60]. In this section we will try to point out the chemical path of the nanotube chemical reactions discussed in these reviews. The chemical reactions can be classified in: thermally activated, electrochemical or photochemical processes [59]. Other researchers preferred the terms “covalent” and “non-covalent” processes [57]. Finally, some reports focused their works on the localization of the chemical modification: end caps, on defect sites or side nanotube walls [60].

A.1.1 Surface modification of CNTs by physico-chemical interactions

Non-covalent interactions between carbon nanotubes and organic molecules have the main advantage that they preserve the intrinsic sp^2 hybridized structure of the material, and as a consequence it permits to retain their electric and mechanical properties. It has been reported that poly(vinyl pyrrolidone) and poly(styrene sulfonate) can wrap up nanotubes [68]. This phenomenon has been attributed to π -stacking or should need van der Waals interactions between the carbon nanotube surface and organic molecules. It has also been reported that it is possible to immobilize biological molecules on the nanotube surfaces. In 1998, Z.J. Guo and co-workers reported [69] that peptides nucleic acids, and proteins can be attached to nanotubes surfaces by a “**wrapping**” phenomena. It is also important to mention the use of surfactants to modify the surface of nanotubes [70]. As mentioned above, all these references point out that this kind of processes are effective to reach good dispersions of carbon nanotubes in polymer matrices and preserve the structure of the CNTs. Nevertheless, pure CNTs display a lack of adhesion with the polymer matrix when compared with covalently bonded functionalized CNTs.

A.1.2 Covalently linked chemical modification

A.1.2.1 Carboxylation of carbon nanotubes

It is reported [60] that end capped carbon structures, such as fullerenes, have a higher reactivity due to the presence of pentagons (highly curved structures). Highly curved nanotubes induce the formation of sp^3 hybridization and makes easier the opening of the carbon bonds (either σ or π bonds) [62]. Opened MWNTs demonstrated their capacity to react with carboxylic acid due to the sp^3 hybridized carbon atoms that hanged at the end of the tubes. Figure 9 shows the results of a strong acid treatment initially performed to open SWNTs (D), and the following oxidation of the carbon covalent σ bond (C).

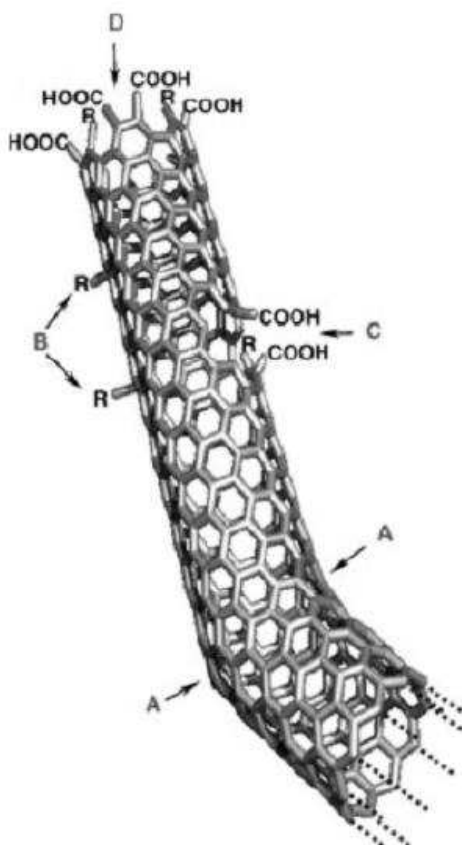


Figure 9: Representation of different defects observed in CNTs: defect A are heptagonal or pentagonal rings in the framework that lead to a bend in the tube (topological defects); B defects are sp^3 hybridized defects (with hanged molecules); C are holes produce by strong oxidative conditions that leave $-COOH$ groups and D are opened ends oxidized by a strong acid treatment.

As a consequence defects are favourable sites that are able to react chemically. Indeed, it was shown that side wall defects, which are defined as non-hexagonal structures (pentagonal sites named Stone Wales defects, hanged

particles, vacancies in the structure [71] C.f. Figure 9 A., B), would have a lower resistance to oxidation [72]. Generally, chemical reactions on defects are carried out using strong acid treatments, and they involve a two step (or more) surface transformation followed by the grafting of new functional groups by esterification, amidisation, substitution etc...

Figure 10 summarizes different secondary reactions obtained after strong acid treatments. There are numerous treatments that permit the oxidation of CNTs : it can be mentioned the use of HNO_3 , $\text{KMnO}_4 / \text{H}_2\text{SO}_4$, Oxygen gas, $\text{K}_2\text{Cr}_2\text{O}_7 / \text{H}_2\text{SO}_4$ or OsO_4 [73-75]. According to S. Barnajee [60] it has been shown that using strong acid treatments on the surface of the carbon nanotubes permits further chemical modification. For example it was possible to attach molecular moieties, particles and quantum dots, bio inspired moieties, and macromolecular moieties [76, 77]. The attachment of molecular moieties has shown its efficiency to improve the solubility of CNTs in a particular solvent (i.e. tetrahydrofuran (THF), chloroform, toluene, CHCl_3)[78, 79]. As an example we can mention the reaction of oxidized nanotubes with thionyl chloride to generate acyl chloride groups [72]. Moreover, quantum dots such as Au or Ag metal particles have been anchored to oxidized CNTs that were previously treated with 1 - ethyl - 3(3 - dimethylaminopropyl) carbodiimide hydrochloride (EDC) [80]. Finally, it should be mentioned that calculations predict a loss of 15% of the SWNT buckling force at 1% carbon functionalization [81].

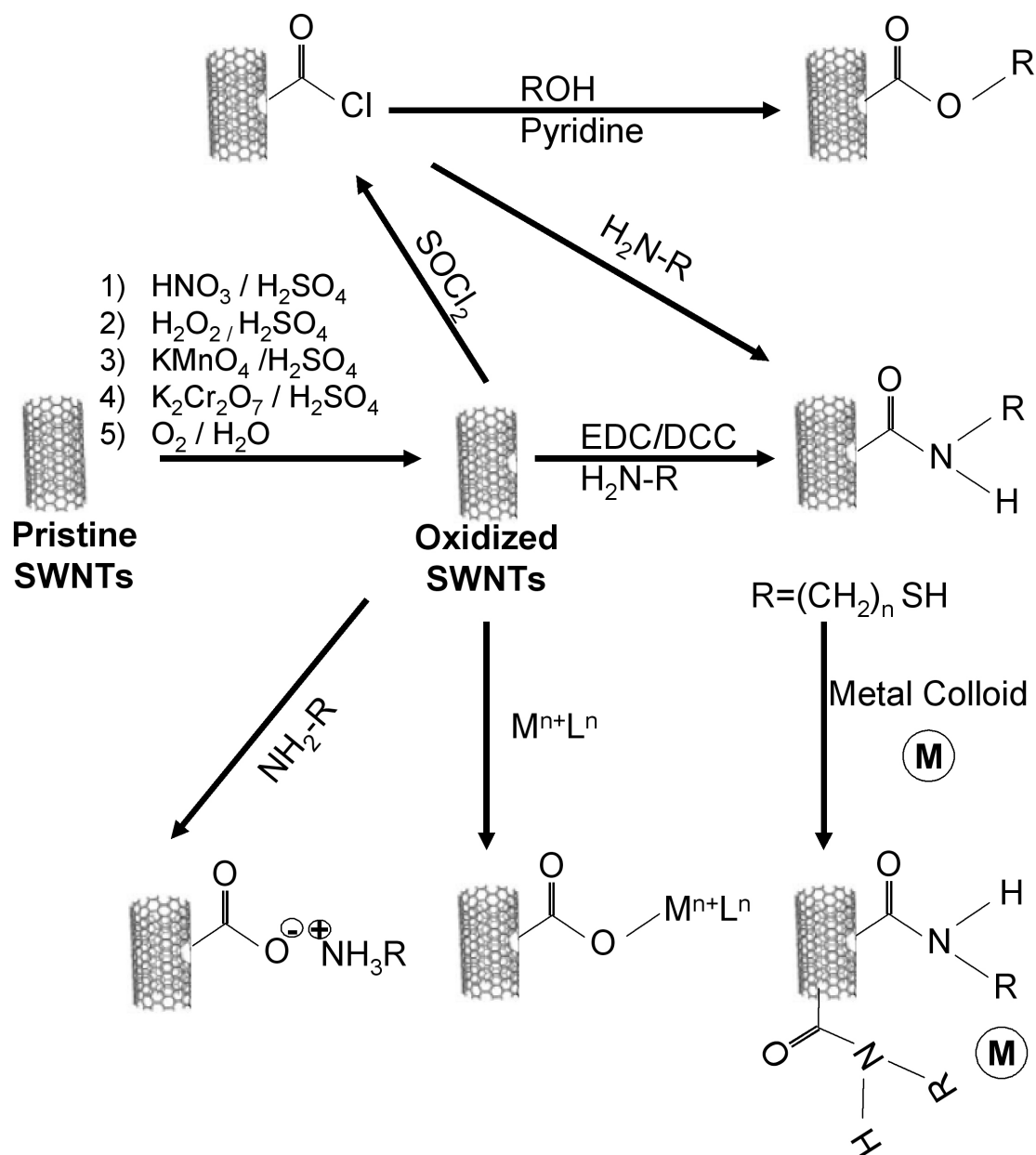


Figure 10: Summary of diverse second step reactions done after an oxidizing treatment (first step) [60]

A.1.2.2 Carbon nanotube structure and chemical reactivity.

As shown in Figure 11, CNTs are comparable to a graphene sheet: all carbons in the CNT structure exhibit a theoretical sp^2 hybridization. Consequently, carbon atoms have two σ bonds in the xy plan, with a π bond corresponding to the overlap of the Z -axis orbitals. In a first approximation, for a time infinitely

short, the external layer of CNTs can be represented as that shown in Figure 11:

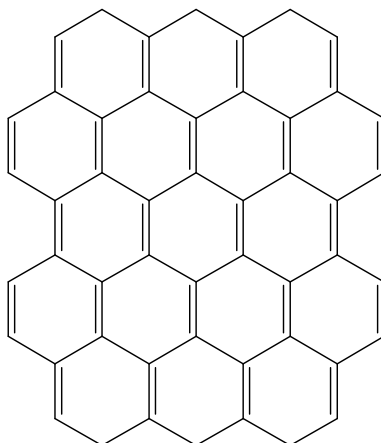


Figure 11: Representation of the chemical structure of CNTs

It is well known that graphite is quite difficult to modify because of its crystalline form: hexagonal compact symmetry. The C-C single bond is one of the strongest bonds in nature; as a consequence it is very difficult to open this hexagonal network. Moreover the opening of the C-C single bond would generate defect in the main carbon structure of the CNTs. A highly modified CNT could lead to the collapsing of the nanotube.

In order to modify CNTs external layer, it should be interesting to open the C=C double bond. The opening of the carbon double bonds presents the advantage to preserve part of the tube structure. Indeed, chemical reactions should be carried out with the electrons of the π bonds; consequently the σ bonds remain intact. Thus it should be possible to preserve the tube structure of a grafted external layer.

It should be pointed out that this hypothesis implicates that the diameter of CNTs has an effect on the multiwalled carbon nanotubes reactivity. A rapid geometry analysis of the system allows us to understand this phenomenon. Indeed, by attacking the carbon/carbon double bonds it is possible to transform sp^2 hybridized sites into sp^3 hybridized areas. But as shown in the Figure 12 sp^3 carbon has a tetragonal form and occupies three space dimensions, whereas sp^2 carbon is a planar configuration. This suggests that the external layer has to be deformed, and the CNTs crystalline order is broken.

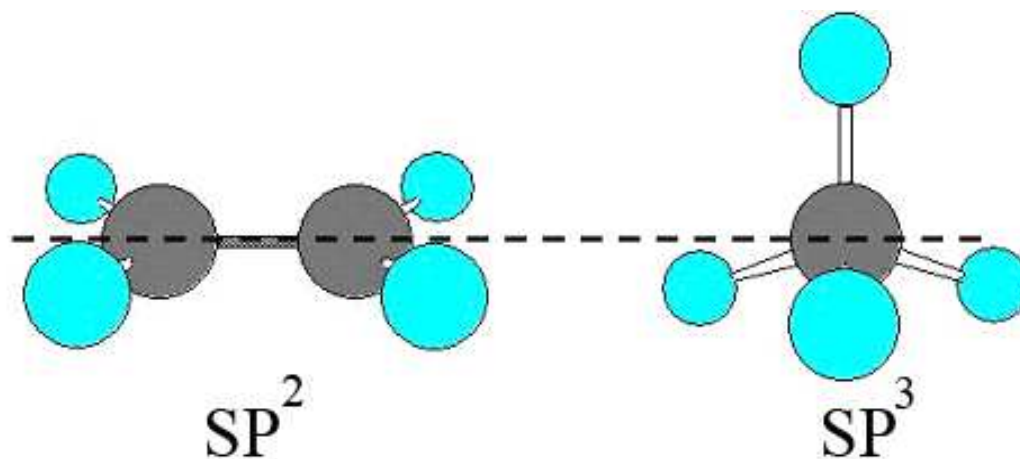


Figure 12: on the left sp^2 carbon hybridization, on the right sp^3 carbon hybridization

The geometry of nanotubes shows that as the diameter of the tubes increases the pyramidalization angle: θ becomes less acute (cf. Figure 13). Thus, as mention previously, the external layer of the MWNT can be considered as a planar graphitic sheet: chemically neutral. Consequently, small diameters CNTs (more reactive) tend to induce a sp^3 like hybridization. Moreover Figure 13 a) shows that the Z orbitals overlap is lower for smaller diameters tubes. As a consequence, the C=C double bond for small diameter CNTs is weaker and easier to break. Some published articles about nanotube modification mention that when the diameter increases, the reactivity of nanotubes decreases [82]. Moreover, it has been reported that the tube ends are easier to functionalize due to the presence of pentagons, responsible of highly curved surfaces [83]. The same work shows that sonication is able to bend the tubes and induces a sp^3 hybridization; these authors concluded that the reactivity of nanotubes is higher when sonication is used. Finally, considering that large diameters induce lower reactivity in the tubes, MWNTs are less reactive than SWNTs. It should be mentioned that the functionalization of the external layer of MWNTs needs to be highly energetic due to the change in carbon hybridization: sp^2 - sp^3 transformation. Moreover, it has been reported [62, 78] that misalignment of the Z-orbitals is a important factor in the stability of the π carbon double bond (C.f. Figure 13 c).

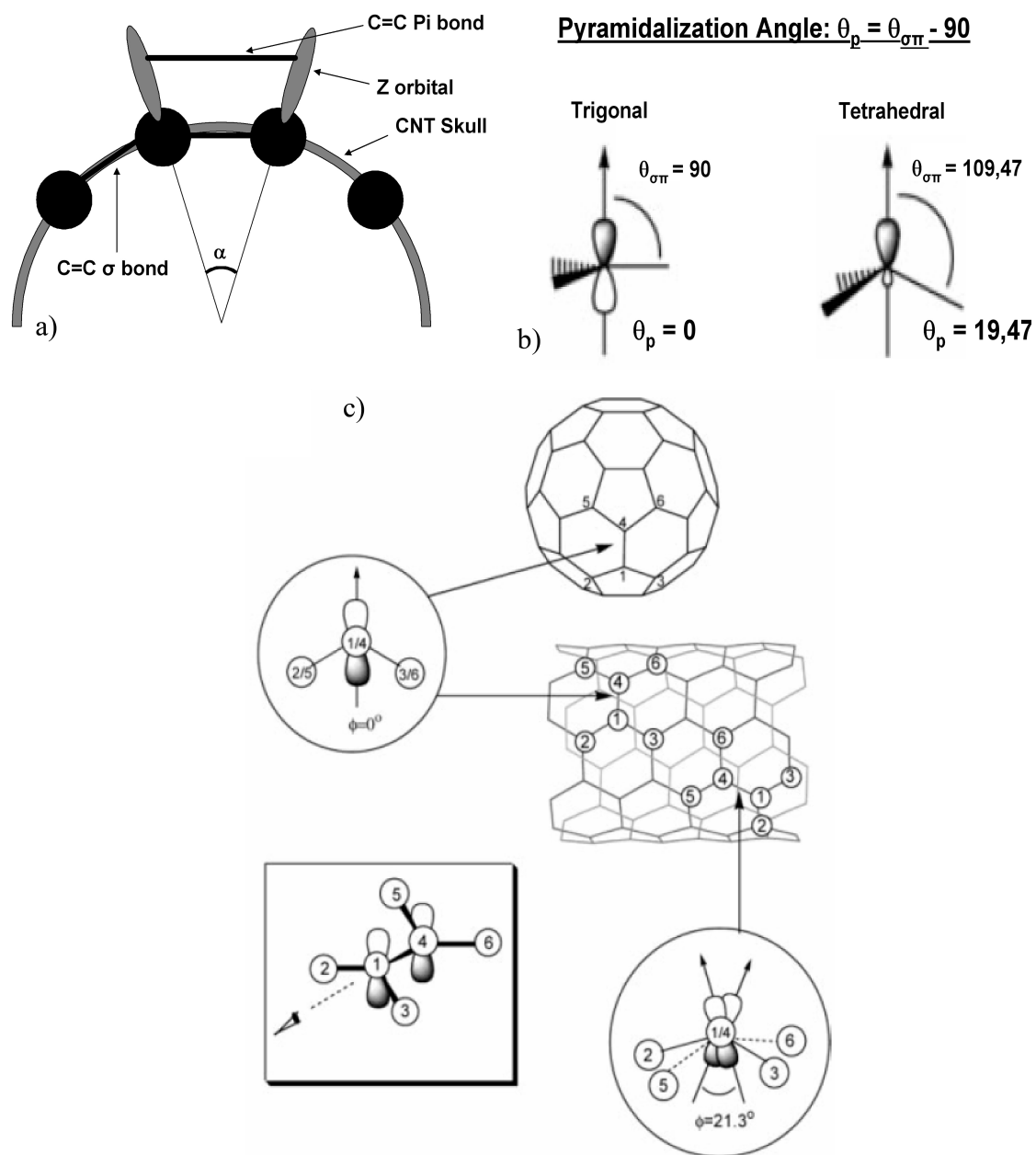


Figure 13: Orbital structure of the CNT external layer, a) transversal representation of the overlap of the carbon Z orbitals in CNTs; b) representation of the angle induced by the pyramidalization due to a sp^3 hybridization compared to a trigonal configuration (sp^2 hybridization) [62]; c) representation of the misalignment between carbon z-orbitals in SWNTs.

Indeed, the misalignment between carbon z-orbitals observed in SWNTs, generates torsional strains and the relief of these strains will control the chemical reactivity of carbon nanotubes. Finally, the pyramidalization as well as the misalignment of the carbon z-orbitals, are inversely proportional to the diameter of the nanotubes [71]. Therefore, MWNT are indeed less reactive when compared to SWNTs or fullerenes.

A.1.2.3 Addition reactions

As mentioned earlier, in order to functionalize the external layer of MWNTs it is possible to open the sidewall C=C π conjugated bond by chemical addition. The chemical addition consists in opening the π carbon double bond by a homolytic or heterolytic cleavage in order to covalently link moieties, whereas acid treatments generally disrupt the carbon σ single bond. The chemical addition can be a polar addition (nucleophilic addition) or neutral (homolytic cleavage of the carbon π double bond). Finally, the chemical addition, as compared to acid treatments, presents the advantage to react with unsaturated carbon atoms, and consequently it does not generate vacancies in the hexagonal framework. For end-closed CNTs, the addition on the carbon double bond has to be in the cis position.

Figure 14 summarizes the possible addition reactions on SWNTs or MWNTs according to S. Barnajee [60]. As an example of the chemical addition on CNTs external layer, it can be mentioned the fluorination of the CNTs side wall at 150-325°C [84]. The C-F bond instability permits secondary reactions such as allylic displacement when fluorinated CNTs react with alkyllithium precursors to generate side wall alkylated CNTs [85]. Interestingly, alkylated CNTs recover their original structure (pristine CNTs) when oxidized in airflow. Other addition processes such as 1,3-dipolar-cycloaddition have been reported in the addition of ozone [86] or nitrile imine [87]. The reaction of CNTs with diazonium compounds using a thermal activated free solvent process, permits to highly functionalize CNTs [67]. Chemical addition reactions appear to be very interesting to select semi-conductors and metallic nanotubes. It can be pointed out that free radical addition is one of the reactions depicted in the Figure 14. Many of these chemical reactions are very useful to disperse CNTs in a particular media or to carry out particular secondary reactions.

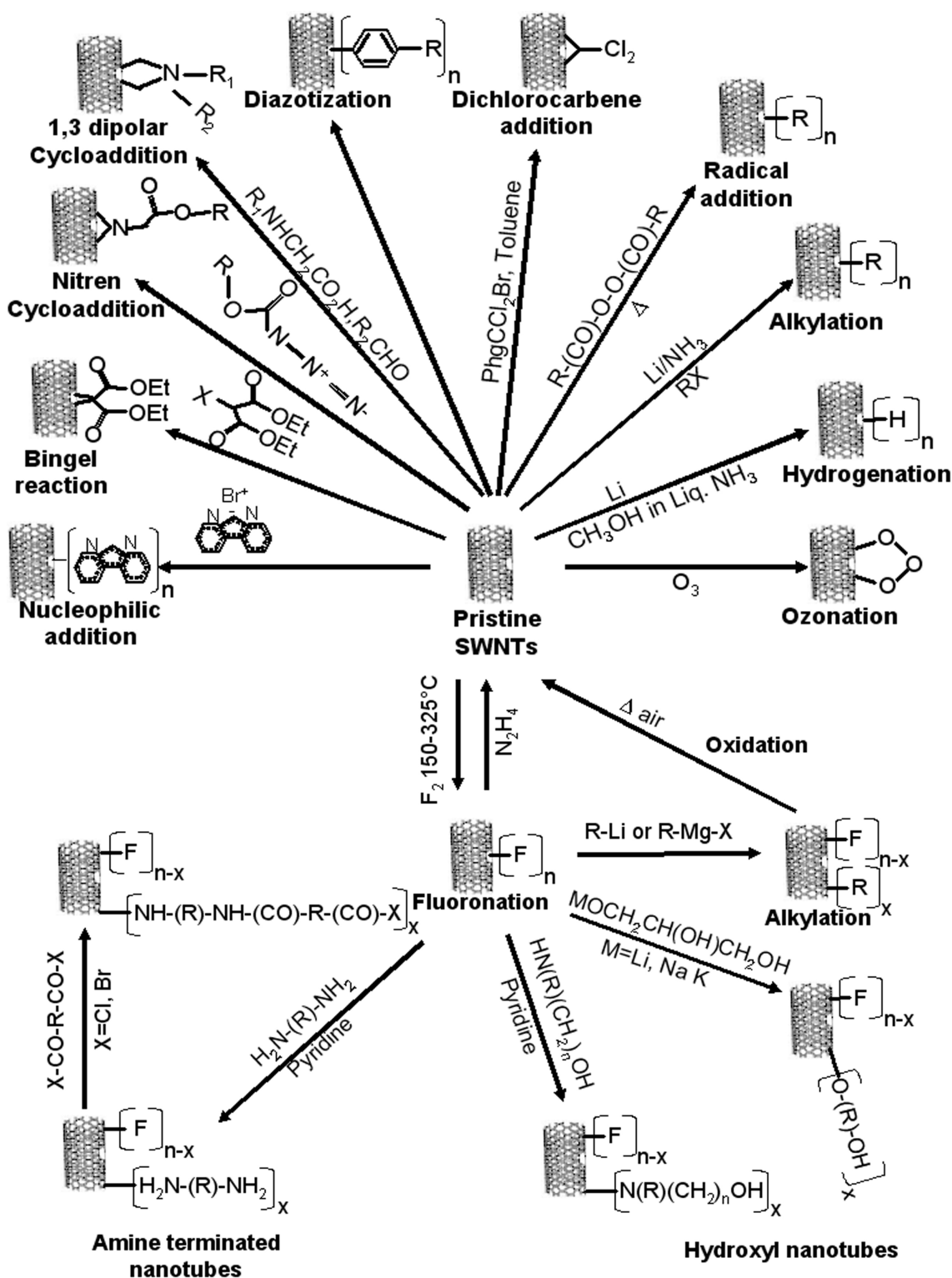


Figure 14: side wall addition chemical reaction on SWNTs or MWNTs [60]

Unlike to carboxylation of CNTs by acid treatment, the chemical addition reactions can initiate on the intact parts of the CNTs sidewall [59]. Thus,

defects in CNTs should lower the overlapping of the z-orbitals making, easier the cleavage of different moieties.

The additions of organic molecules based on the opening of the carbon π double bonds generally tend to “catch” electrons that are involved in the electrical conduction process. Based on this, any chemical modification of the external layer of the CNTs should modify significantly their electric properties. Furthermore, when carbon nanotubes begin to lose their graphitic structure, the mechanical properties are also altered and it is observed changed in their mechanical properties [81]. As a conclusion, the chemical addition on CNTs should improve their dispersion in a particular solvent, but it results in altered electrical and mechanical properties.

A.1.3 Polymer grafting: “grafting to” or “grafting from” techniques

We can distinguish two forms of polymer grafting on the nanotubes: “grafting to” and “grafting from”. The “**Grafting to**” method corresponds to a double step reaction where polymers are grafted to the nanotube surface occurring due to a chemical function previously attached to the CNT. Most reports concerning the “grafting to” method, the carbon nanotubes have been functionalized with an acid that reacts with a functional group in a polymer leading to esterification or amidification reactions. In the review by Liu [57] there is an indication of several polymers and copolymers grafted using the “grafting to” method: poly (propionylethylenimine-co-ethylenimine) (PPEI-EI) [88], poly (styrene-co-aminomethylstyrene) (PSN) [89], poly (ethylene oxide) (PEO) [90], poly (styrene-co-hydroxymethylstyrene) (PSA) [72], poly (styrene-co-p-(4-(4'-(vinylphenyl)-3-oxobutanol)) (PSV) [64], poly vinyl alcohol (PVA) [91], etc...

There are also reports on “grafting to” using a free radical chemical addition process. A living polystyrene controlled by 2,2,6,6-tetramethylpiperidine-1-oxide (TEMPO) has been grafted to MWNTs by a polymer termination step according to a radical process [92].

“**Grafting from**” is an alternative way to graft polymers on the external layer of MWNTs. In this particular technique the CNT contains the polymerization

reaction initiator grafted on its surface. The reactional groups on the surface will react with monomers. The macromolecules grow-up from the surface through a polymerization reaction. As an example, Liu [57] reports reactions by Atomic Transfer Radical polymerization (ATRP) brushes based on the polymerization of Methyl Methacrylate (MMA) [93] monomer, styrene monomer [92] or Polystyrene-*b*-Poly (acrylic acid) (PS-*b*-PAA) [94]

There are other reports on controlled polymerization on the nanotube surface such as the ring open polymerization and anionic polymerization [57, 95]. In general all the routes using the “grafting from” in-situ polymerization are living controlled polymerizations.

A.1.4 Chemical structure and reactivity of CNx MWNTs

This work focuses on the use of CNx MWNTs as the basis for the chemical grafting of polymers. As described in the first chapter, CNx MWNTs exhibit a bamboo-like structure due to the introduction of nitrogen atoms in the carbon structure of the nanotubes [45]. The bamboo-like structure could help to prevent the telescopic sliding of the concentric shells of MWNTs during mechanic stretching, but also could allow easier chemical modifications due to the presence of N atoms containing additional electrons useful to improve reactivity. Kamalakaran et al. [14] reported Raman spectra which demonstrated that CNx MWNTs containing 2% mol. of nitrogen display a D-band peak more intense than classical pure MWNTs. D-Band represents the disorder in the carbon nanotube structure. As a consequence, we can think that nitrogen atoms break the symmetry of the hexagonal carbon framework implying a higher reactivity of the nanotubes shell. Furthermore, nitrogen atoms are introduced in the carbon structure in two ways: Substitutional tertiary amine nitrogen (three coordinated N), or pyridinic functions (two coordinated N). The substitutional tertiary amines represent nitrogen atoms that replace C atoms, whereas the pyridinic nitrogens make a double bond with a carbon atom [45]. These chemical functionalities are responsible of the disorder because they cause a hole in the structure. As an example M. Terrones and co-workers reported some chemical modifications of

CNx MWNT using acid treatment [96], able to decorate CNx MWNTs with Au nanoparticles.

A.1.5 Hypothesis about carbon nanotubes chemical reactivity

As a first approximation we should consider that the main structure of MWNTs is comparable with alkenes: all carbons are composed of two σ single bonds and one π double bond. However, CNTs can be modified only in the **cis** addition way. Indeed, just one side of the double bond is accessible (because of the tubular geometry of the material). It means that the addition reaction that can be carried out on nanotubes follows the anti-Markovnikov rule.

In 1870, Markovnikov, thanks to experiments, described an empirical rule that permitted to conjecture the position of the addition on alkene molecules. The anti Markovnikov rule generally represents the additions to an alkene that adopt the CIS configuration. If we consider that nanotubes have an alkene-like structure, it should be expected that all addition reactions following the anti-Markovnikov rule will react chemically with CNTs. For, example free radical addition, carbene addition, epoxydation, cis hydroxylation etc...Most of these reactions are mentioned in the literature (C.f. Figure 14) [60].

A.2 Atomic Transfer Radical Polymerization (ATRP)

A.2.1 Generalities

The Atomic Transfer Radical Polymerization (ATRP) belongs to the class of polymerization reactions named controlled radical polymerization, and it is a pseudo living type of polymerization. Let us define the meaning of this expression term by term.

Controlled means that the growth is regulated by specific processes that permit to reduce and almost eliminate the termination step of the polymerization

reaction. The molecular weight of the resulting macromolecular material is a function of time.

Living means that the reaction, generally thermally activated, can be stopped and initiated repeatedly. The expression “dormant” chains will be used when referring to a non reactive (but potentially thermally activated reactive) molecule.

Radical refers to growth polymerization mechanism. This process is based on the propagation of a free radical by adding a monomer to the end of the macromolecular chain that will transfer the free radical.

Figure 15 describes the general mechanism of Atomic Transfer Radical Polymerization [97].

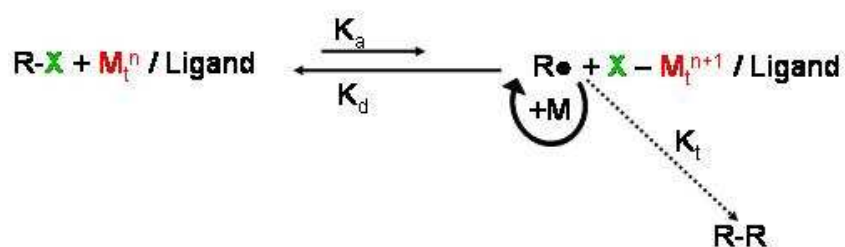


Figure 15: General mechanism of ATRP process

The free radicals are generated through a reversible redox catalyzed process. The initiator is generally an alkyl halide: R-X (where X is a halogen atom), which oxidizes the catalyst complex transition metal (M_t^n / ligand), from its lower oxidation state (n) to the next state (n+1), thus generating a free radical. The presence of this free radical permits the growth of the polymer chain, due to a free radical propagation process [97].

Because the redox reaction equilibrium is displaced on the dormant species side, the catalyst goes back to its reduced state and the free radical is caught by the halogen atom. Once the free radical is deactivated, a dormant polymer chain is obtained that still continues growing once it is activated. The oscillation frequency between active / dormant species is one of the most important parameters of the control process. Indeed, if the halogen-containing molecule remains for long times in the dormant specie state, the probability to oxide the catalyst with the impurities in the solution increases, and the reaction can be permanently inhibited. On the other extreme, if the reaction keeps active for a

long time, the probability for the polymer living chains to find each other and go through a termination step is higher. So, in order to find the best reaction control, it is necessary to investigate about the activity of initiator with a particular catalyst complex. The nature of the metal and the nature of ligand are crucial parameters that define the redox reaction equilibrium constant.

A.2.2 Hybrid material synthesis using ATRP

ATRP technique has been used in the past to graft polymers on an inorganic surface. Several cases have been reported of in-situ controlled polymerization on inorganic surfaces (C.f. Figure 16)

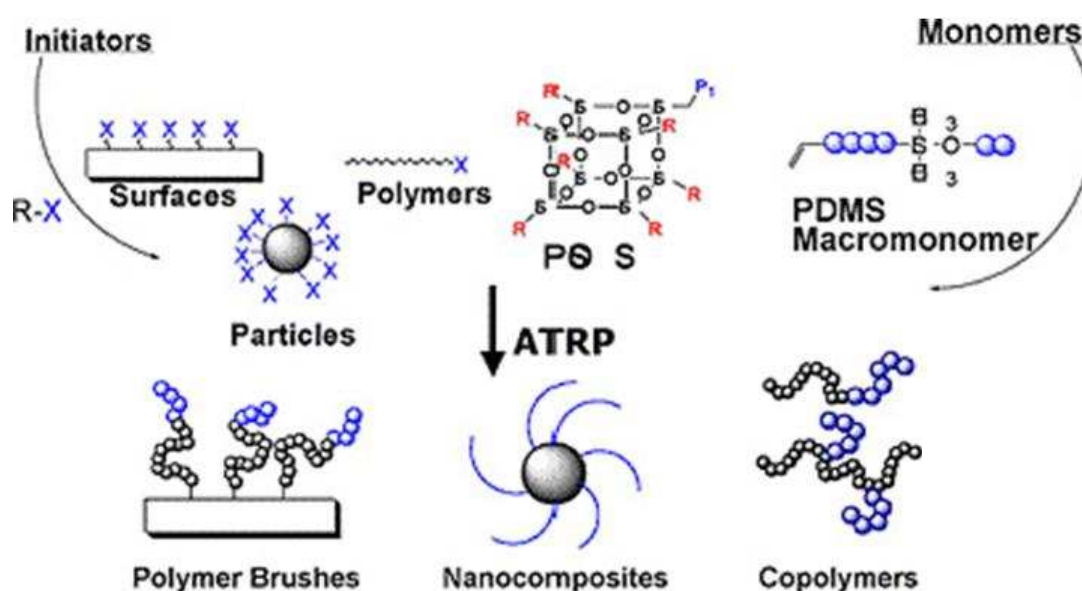


Figure 16: schematic presentation of hybrid materials produced by ATRP process [97].

For example, silica nano-particles have been grafted with different monomers using ATRP [97, 98]. Other nano-particles functionalized with silane halogenated molecules permit the polymerization of benzyl acrylate, styrene, and homo or block copolymers [99]. The interest in using this technique is the control of the polymer interface size. The functionalized surface acts as macro-initiator, the controlled reaction allows a good definition of the polymer layer thickness [100].

A.2.3 ATRP initiator

As mentioned previously, alkyl halides are effective initiators for ATRP. Many compounds have been used for this purpose such as: halogenated alkanes [101, 102], benzylic halides [103, 104], α -haloesters [105, 106], α -haloketones [107, 108], α -halonitrile [109, 110] and sulfonyl halides [111, 112].

The stabilization of the radicals depend on the functional group next to the alkyl halide, for example a tertiary alkyl halide is a better initiator than a secondary, and a secondary is more efficient than a primary [113, 114]. The halogen species (F, Cl, Br or I) used is also important. Depending on the bond strength (R-X), the system will be more or less active. Generally only Br and Cl are used in ATRP systems. The polarity of the F atom is too high and the chemical bond (R-F) is too stable to be reduced. Iodine on the contrary is more reactive but the unusual reactivity of iodine with metals or metal atoms complicate the control of the reaction [115].

To carry out a successful reaction, the initiation has to be faster than the propagation in order to reduce side reactions that can occur.

A.2.4 ATRP catalyst

The catalyst is certainly the key element of ATRP processes. Generally that is a transition metal in its oxidation state (n) that is oxidized to a state (n + 1). "The ideal catalyst should be highly selective for atom transfer and should not participate in other reactions" [97]. Transition metals are highly sensitive to oxidation, and therefore need high purity conditions during the polymerization process. Each polymerization needs its equilibrium constant and for this reason, many metals have been investigated for the different monomer system. The following metals have been reported in the study of ATRP catalysts: Molybdenum and chromium (group 6) [98, 99], rhenium (group 7) [100, 101], ruthenium and iron (group 8) [101, 116], rhodium (group 9) [117], nickel and palladium (group 10) [118, 119] and copper (group 11) [120]

A.2.5 ATRP ligand

The ligand is used to solubilize the transition-metal catalyst in an organic solvent, and to adjust the redox potential for a given reaction [97]. The two main categories of ligands are the nitrogenated and phosphorus containing macromolecules. In the copper mediated systems nitrogen ligands are often used [110, 121], while phosphorus ligands have been used with the other transition metals mentioned in the precedent paragraph. Moreover, it is reported that steric effects belonging to the ligand can reduce the activity of the transition-metal and as a consequence the type of ligand is adjusted depending on the monomer used [121].

A.2.6 Kinetics and molecular weight : theoretical elements

A.2.6.1 Kinetic

Figure 15 shows a general mechanism for ATRP, from this equilibrium equation, we established an equilibrium constant K_{eq} of the redox reaction:

$$\text{Eq. 1} \quad K_{eq} = \frac{k_a}{k_d},$$

Where k_a is the activation rate constant and k_d is the deactivation rate constant.

Following this argument, if we express k_a and k_d in function of the reactant concentrations, K_{eq} can be written:

$$\text{Eq. 2} \quad K_{eq} = \frac{[R^\bullet][\text{ligandCu(II)X}]}{[R-X][\text{ligandCu(I)X}]}$$

The polymerization rate (R_p) is giving by substituting each term by its equivalent in concentration in the following equation:

$$\text{Eq. 3} \quad R_p = \frac{-d[M]}{dt}:$$

$$\text{Eq. 4} \quad R_p = k_p [M][R^\bullet] = k_p K_{eq} [M][R-X] \times \left(\frac{[\text{Ligand Cu(I)}]}{[\text{Ligand Cu(II)X}]} \right)$$

We can reduce this mathematical expression in a simple way:

$$\text{Eq. 5} \quad R_p = k_p^{app} [M],$$

Where k_p^{app} is defined as:

$$\text{Eq. 6} \quad k_p^{app} = k_p K_{eq} [R-X] \times \left(\frac{[\text{Ligand Cu(I)}]}{[\text{Ligand Cu(II)X}]} \right)$$

k_p^{app} represents the apparent propagation rate. These equations show how important is to preserve the ratio $[\text{Cu(I)}] / [\text{Cu(II)}]$ to control the reaction. In a semi-logarithm graph, if $[\text{Cu(I)}] / [\text{Cu(II)}]$ is constant, the conversion against time would be linear, a result that is consistent with a first order reaction. Any deviation could indicate that Cu(II) species are generated and the control on the chain size is lost.

A.2.6.2 Molecular weight

ATRP presents inherent advantage to the “living” character of the polymerization such as low polydispersity: $M_w / M_n < 1.5$ [97].

M_n can be defined in the following equation:

$$\text{Eq. 7} \quad M_n = \left(\frac{\Delta[M]}{[R-X]_0} \right) \times (M_w)_0$$

In equation 7, $\Delta[M]$ represents the concentration of consumed monomer, $[R-X]_0$ the initial concentration of initiator and $(M_w)_0$ the molecular weight of monomer.

The polydispersity is defined by:

$$\text{Eq. 8} \quad M_w / M_n = 1 + \left(\frac{[R-X]_0 k_p}{k_{deact} [D]} \right) \times \left(\frac{2}{p} - 1 \right)$$

Where $[D]$ represents the concentration of deactivator and p the monomer conversion [97]. Eq. 8, shows that if the concentration of the initiator is constant, a representative plot of M_n against conversion is linear. Moreover, Eq. 8

explains that when the conversion increases, the polydispersity decreases. However it can be deduced that if the rate of propagation is high, the polymer will have a broader M_w dispersion. Consequently, if the radical propagation rate is too high between each redox process, the control on polymer polydispersity will be lost. If this is the case, then k_{deact} is too high.

Part B Microstructure of the polymer/ carbon nanotubes composites

In this section we will emphasize the physico chemical properties of polymers and polymer composites. Indeed, the use of a structured block polymer in the fabrication of carbon nanotube composites involves complex nanostructural changes. Therefore, the physico-chemical phenomena such as molecular electrostatic interactions will be described. We will summarize the basic knowledge necessary to understand how CNx MWNT interacts with the polymer matrix (either PS than PSBS).

It has been shown that carbon nanotubes have a poor adhesion with most polymer matrices [122-125]. This lack of adhesion between the polymer matrix and the carbon nanotube is observed by a pull-out phenomenon[122-125].

We will discuss on the behavior of the carbon nanotubes in a polymer matrix when subjected to mechanical stresses. It is clear that the chemical functionalization of the CNx MWNTs might influence the matrix / filler adhesion and consequently the fracture of the composites upon deformation

B.1 Polymers morphology

B.1.1 Physico-chemistry of the polymer miscibility

B.1.1.1 Atomistic and molecular interactions

In order to describe the miscibility of two chemical components, let us explain a conventional example of a liquid penetrating a solid surface. When a drop of liquid is deposited on a solid surface, the adhesive forces of the solid tend to attract the molecules of the liquid, whereas the cohesive forces of the liquid tend to maintain the liquid molecules together. In Figure 17, the equilibrium state of the drop of liquid on the solid surface is represented. At the equilibrium between the liquid cohesive forces and the solid attractive forces, the contact angle θ represents the wetting of the drop on the substrate. If the substrate attractive forces are largely superior to the liquid cohesive forces, the angle θ is close to zero. In the opposite case (liquid cohesive forces largely superior to the substrate attractive forces), θ is close to π .

The same experiment with two liquids can well account for the miscibility or the phase separation of the solvents. This experiment is a good representation of the interpenetration of two chemical substances.

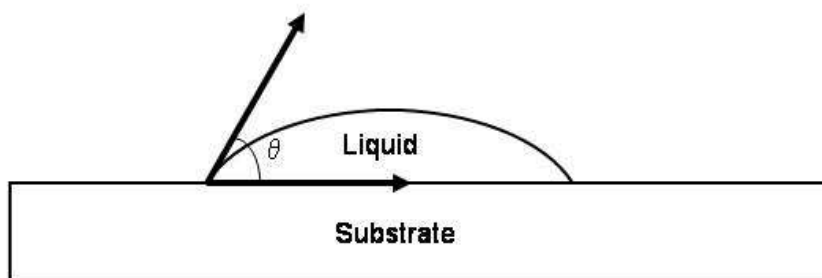


Figure 17: Representation of the behavior of a liquid drop on a solid substrate. θ is the contact angle, and is representative of the compatibility of the chemical substances.

The cohesive and attractive forces between two substances originate from electrostatic forces, van der Waals forces or steric repulsions, but it is easier to speak about attractive and repulsive forces. Repulsive forces generally originate from the electrostatic interactions or steric repulsion forces, whereas attractive forces are essentially the results of the van der Waals forces [126].

a. Electrostatic interactions

The electrostatic interactions result from ion-ion, ion-dipole or dipole-dipole interactions. The dipole can be induced or permanent. The ion-ion interactions are predominant at large distances. This kind of interaction can be attractive or repulsive, depending on the sign of the electric loads involved.

b. Van der Waals forces

The van der Waals forces exist between non polar molecules, and are the result of interactions between the non permanent induced-induced dipoles or permanent-induced dipoles. The asymmetric position of an atom electronic cloud around the nucleus can induce a dipolar moment. This instantaneous dipole can induce on the neighboring molecules a dipolar moment. Finally, the resulting force is an attractive force.

c. Dispersion London Forces

The oscillation of electrons around the nucleus can induced dipolar moments due to the distortion of the electronic cloud. Even if the temporal average of the dipolar moment is equal to zero, it can punctually induce a dipolar moment in the neighboring molecules.

d. Steric repulsion

When two atoms are very close, the electron clouds generate a repulsive force that prohibits their interpenetration. This force drastically increases when the distance between the atoms is lower than their radii. The steric repulsion forces involved between non spherical molecules also depend on their orientation. For example, a ramificated molecule will exhibit a lower boiling point than the same linear molecules, since the ramifications prohibit their alignment and consequently the intermolecular interaction decreases.

e. Hydrophobic interactions

The non polar molecules, when they are introduced in an aqueous media become isolated from each other because the polar water molecules tend to form tetrahedral structures by hydrogen bonds (polar interactions). This description of the molecular interactions allows our understanding of the physical fundamental phenomenon involved in the miscibility of two liquids.

B.1.1.2 Polymer miscibility

On the contrary to matricial solution theories, the Flory-Huggins theory is able to describe the behavior of polymer solutions [127, 128]. It was the first model that gave a mathematical expression of the combinatory entropy for mixtures of macromolecules with different lengths. This model takes into account the fact that the polymers are long flexible chains, where the positions of the segments are dependent on each others. The Flory-Huggins model cannot describe with good precision the thermodynamic properties of a polymer mixture; nevertheless, it provides a good prediction of the solution stability.

In order to describe the solutions with a non-charge mix enthalpy, the parameter χ (called the Flory-Huggins parameter) was introduced in the original Flory-Huggins theory [129]. The Flory-Huggins parameter is expressed by the following mathematical expression:

$$\chi = \frac{w}{kT}$$

Where w is the energy necessary to interchange the segment positions (J . segment⁻¹).

The sign of the Florry-Huggins parameter permits the prediction of the miscibility of polymers. Indeed, a positive χ indicates the presence of a repulsive force between the molecules (either electrostatic or steric repulsive forces), and consequently the polymers are not miscible. If the repulsion is strong enough, this should lead to a phase separation. On the other hand, if χ is negative, the polymers are miscible.

B.1.2 Structural changes in the morphology of block copolymers

When a block copolymer is composed of two immiscible blocks, the molecules have to rearrange their structure in order to minimize the energy of the system. Figure 18 depicts how a di-block copolymer will order its chains so as to respect the immiscibility of each block. Indeed, the chains A of a copolymer will orient towards the A chains of on other copolymer (the same for B chains), thus leading to a structured material.

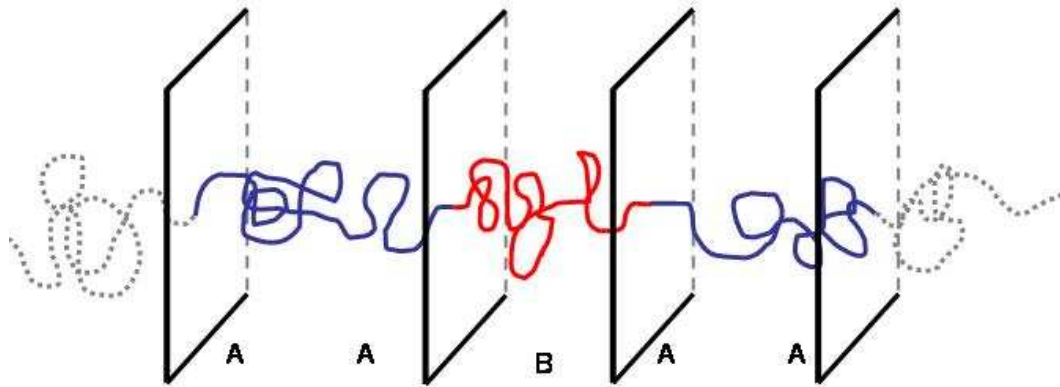


Figure 18: Representation of a structured di-block copolymer (A-B), which blocks are composed of immiscible polymers.

Miscibility and organization of polymer chains in a block copolymer are generally described by a phase transition graph, where the phase changes depending on thermodynamic dimensions like “ f ” or χN . “ f ” represents the volume fraction of a block.

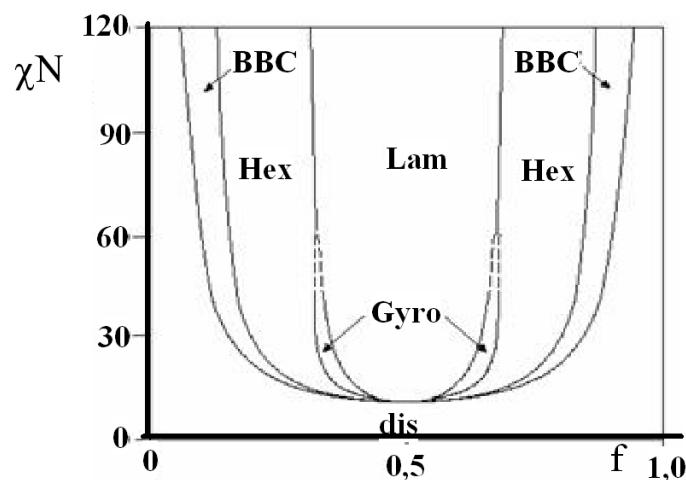
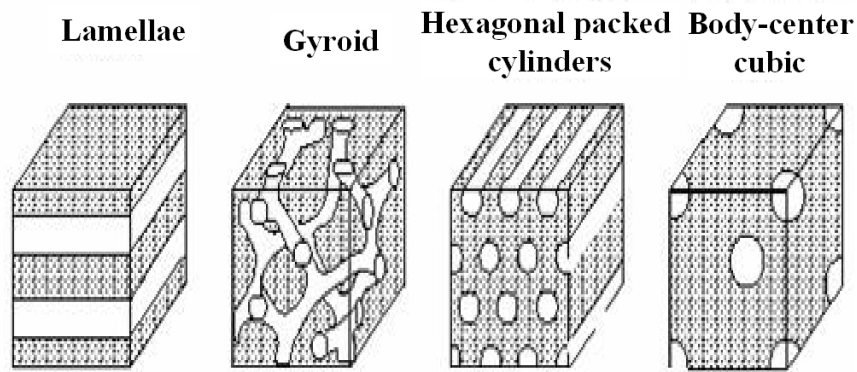


Figure 19: Transition phase diagram for conformationally symmetric block copolymer, where χN is a function of f [130]

As mentioned previously, χ is the Flory-Huggins parameter that reflects the interactions between each block. Finally N is the degree of polymerization. When the product χN exceeds a critical value (order-disorder critical value), the system separates itself into separated organized micro-phases (5-500 nm). The diagram observed in Figure 19 is a computed diagram using the self-consistent mean field theory [131, 132]. It represents the different possible morphologies for a symmetric di-block copolymer, such as poly (styrene-co-butadiene) (PSBS). The structures that exist for a linear diblock copolymer are: body centred cubic, gyroid, lamellae, and hexagonal packed.

B.2 Chemical functionalization and filler / matrix interfacial adhesion strength: pull out phenomenon

It is commonly accepted that high interfacial adhesion strength between the filler and the matrix would increase the reinforcement by enhancing the load transfer. Nonetheless, a good interfacial adhesion of the filler within the matrix should induce different fracture behaviour of the composite. The literature reports numerous papers about pull-out effects in carbon nanotubes during the breakage of the composite [122-125]. As an example we can mention the work by M. Wong [133] and co-workers on polystyrene / MWNTs composites, where the fracture propagated along the nanotube surface. In the same paper, it is mentioned that the nanotubes, without any chemical treatment (chemical bond functions), do not have a good interfacial adhesion with polymers. Indeed, it has been shown elsewhere by computer simulations that the interaction forces between carbon nanotubes and a polymer matrix essentially originates from electrostatic interactions and van der Waals forces [134]. The energy necessary to extract a nanotube from the polymer matrix has been calculated by considering the work necessary to pass from a fully embedded carbon nanotube to a totally pulled-out tube (C.f. Figure 20a.). It has been shown that depending on the polymeric matrix used, the stress necessary to completely pull out a tube will depend on the system studied, being equal to: 186 MPa for

SWNT / PS [133], 138 MPa for SWNT / Epoxy [133] and 500 MPa for SWNT / polyurethane [135]. Finally, it has been shown theoretically that the defects in the structure of carbon nanotubes can lead to an increase of this value [136] (C.f. Figure 20 b.).

As far as functionalized CNTs / polymer composites are concerned, the few reports published demonstrate that the increase of the interface cohesion results in a good adhesion matrix / filler, and consequently the breakage of the tubes during fracture tests, instead of pull-out phenomenon [137, 138].

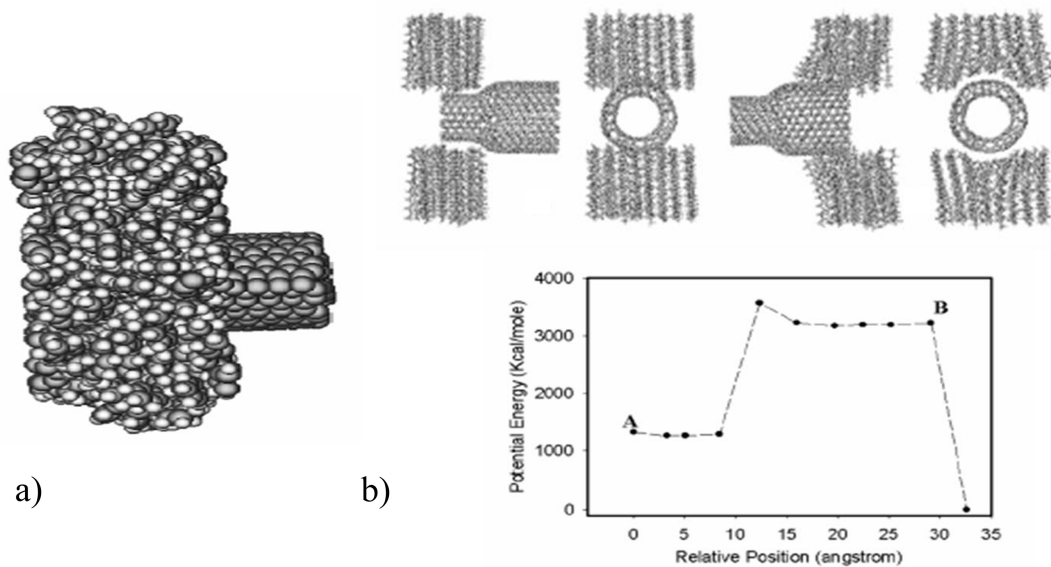


Figure 20: a) Computer simulations permitting to calculate the work necessary to completely pull out a SWNT from a polystyrene matrix [134]; b) Computer simulation demonstrating the effect of the tubes form defects on the pull out phenomenon (“interlocked tubes”) [136].

Interestingly, G.L. Hwang and co-workers studied the effects of grafting poly (methyl metacrylate) on the surface of MWNTs by studying PMMA-grafted MWNTs in a PMMA matrix by TEM in-situ tensile tests, and compared their behaviour to that of pristine MWNTs non-grafted in the same matrix [138]. First, they showed that the grafted tubes did not pull out of the matrix, whereas the pristine tubes did. They also found that a high cohesion between matrix and filler could result in an alignment of the tubes during the tensile test.

Part C Percolation theory and electrical behaviour of polymer / carbon nanotube nanocomposites

The literature contains numerous papers related to the electrical behavior of carbon nanotubes polymer nanocomposites (with either SWNTs or MWNTs). For example, it can be mentioned the work J.N Coleman et. al in 1998 who observed a percolation threshold at 8.5 wt. % of nanotubes in PMPV matrix [139]. This percolation threshold is very high and far from those expected by theory. Subsequently, other papers were published on CNT / polymer nanocomposites electrical behavior using different polymer matrices: Epoxy [53, 54], Poly (methyl metacrylate) [51], Polystyrene and Polycarbonate [51]. These papers, depending on the polymer matrix used, reveal percolation thresholds at different volume fractions of filler, as well as different critical exponents. This indicates that the physico-chemistry of the system has an effect on the nanotube dispersion. Moreover the dissimilar results reported using the same matrix (i.e. [51] or [53, 54]), clearly indicate that the processes involved in the synthesis of carbon nanotubes polymer / nanocomposites are crucial.

C.1 Introduction to the percolation theory.

C.1.1 History and general concept.

The concept of percolation appears in 1954 with Broadbent and J.M. Hammersley when they were studying the water penetration in a labyrinth composed of open / closed doors.

From the definition of Roussenq, the percolation concept can be described as a communication problem on a large distance, where locally there are some sites that can relay the information. Below a given concentration of links between each site, the information will not cross through the domain (supposed infinite) because it does not exist any continuous path. Above a given critical threshold value (p_c) of links, the active sites can cross-link and the probability to transmit the information becomes equal to 1. In other words, the percolation theory permits to describe critical phenomenon due to the random dispersion of a phase A in a phase B. Numerous studies have used this concept: disease propagation in a population (stemmed / propagated), composite materials (conductors / insulators), flow of liquids in a porous media (local humidity, flow trough the system), etc...

The concept requirements to study a system using percolation theory are:

- The dimensions of the domain are very large compared to the dimensions of link elements.
- The relation (contact) between links is local.
- This relation (between links) relies on random phenomenon.

C.1.2 Link percolation

In the percolation theory, elementary sites can be categorized either as: percolation sites, or percolation links. In this research, we will focus on the link percolation: we postulate that nanotubes, when they are dispersed in a polymer matrix, can be considered as links.

From the percolation theory, linked networks can be visualized as a network in which each link can be active with the probability p , or inactive with the

probability $1-p$. P defines the fraction of active sites. In Figure 21 a percolating link network with a fraction of active elements p lightly superior at the critical fraction p_c is represented. We observe the presence of an infinite cluster that links both parts of the domain. We can easily imagine that by lowering the fraction p this cluster will break due to the absence of links called “sensible links” (Figure 21 link B).

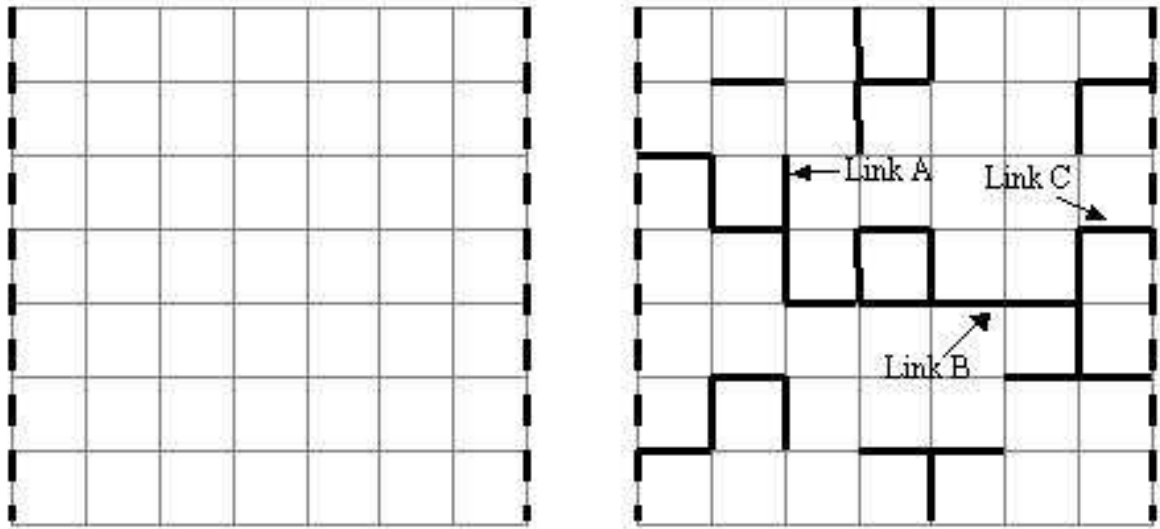


Figure 21 : Schematic of a link percolating network

An increase of the active fraction p will multiply links such as link C, which increase the “communication” path through the sample. Finally, we can notice the presence of “dead arms” branches, represented by link A, that do not participate in the communication phenomenon.

Percolation threshold: definition

In a network X where links are active with a probability p , the percolation threshold p_c is defined as the concentration p at which an infinite cluster appears. If $p > p_c$, there is a pathway between the two sides of the network. If $p < p_c$ such a pathway does not exist.

C.1.3 Percolation statistical representative values

In a percolating problem there are some statistical fundamental values that permit monitoring the evolution of the system as a function of the fraction of active links (p): (a) the quantity of s length normalized clusters, (b) the probability to belong to an infinite cluster, (c) the average length of finite clusters and (d) the critical lengths.

C.1.3.1 Quantity of s sized clusters normalized by the quantity of possible network links.

The quantity of possible links will be named n_s , where n_s represents the networks containing N sites. Therefore, the average value of clusters which length is s could be described as:

$$n_s = \frac{\text{Total of } n_s \text{ length clusters}}{N}$$

The probability of s sites to be active is p^s . In order to describe a cluster of size s , we have to mention that all the sites around this cluster are inactive. So it is defined by the letter u , the perimeter of the cluster which not only physically represents the inactive sites around the active sites cluster, but also holes in the cluster. Consequently, the inactive perimeter of the s sized cluster has the probability $(1-p)^u$ to occur. We define g_{su} as the quantity of clusters with length s and a perimeter u . The mathematic expression of n_s normalized by the quantity of sites can be written as [140]:

$$n_s = \sum_u g_{su} p^s (1-p)^u$$

As a consequence the total number of sites is the sum of all s length sites:

$$G(p) = \sum_s n_s$$

C.1.3.2 Probability to belong to the infinite cluster

The probability $P_\infty(p)$ that a link belongs to an infinite cluster can be expressed as:

$$p_{\infty}(p) = \frac{\text{Quantity of links in the unfinite cluster}}{\text{Quantity of active sites}}$$

Before the percolation there are no infinite clusters. So the probability of a site to belong to this cluster is zero. Above the percolation threshold, the probability $P_{\infty}(p)$ increases drastically. We will describe later that this value increases following an exponential tendency, and $P_{\infty}(p)$ is the parameter that described the order of the percolation transition. In fact, at the percolation threshold $[dP_{\infty}/dp](p)$ exhibits a vertical tangent [141].

$$p_{\infty}(p) = 0 \text{ if } p < p_c$$

$$p_{\infty}(p) = 1 \text{ if } p > p_c$$

C.1.3.3 Size of finite length clusters.

In the same way we defined the infinite cluster, we can calculate the probability to belong to a finite cluster. The probability to belong to a finite cluster of length s is $s \cdot n_s$. Consequently, the probability for a site to belong to any cluster of any length s is $\sum_s s \cdot n_s$.

$$\sum_s s n_s = \frac{\text{Quantity of links in the finite cluster}}{\text{Total quantity of links (active, inactive)}}$$

So, in order to calculate the length of a finite cluster, we define w_s as the probability for a cluster to have s active sites.

$$w_s = \frac{n_s s}{\sum_s n_s s}$$

Finally, the average length of a finite cluster can be expressed as:

$$S(p) = \sum_s w_s s = \sum_s \frac{n_s s^2}{\sum_s n_s s}$$

$S(p)$ is adimensional, it does not represent a physical distance in the analyzed system.

C.1.3.4 The characteristic length

$\xi(p)$ is the characteristic length; it is representative of the distance between two sites of the same cluster. The correlation function $C(p, r)$ is defined as the probability to find an active site to be at distance r from another site being active, and belonging to the same cluster. This value is normalized so that: $C(p, r) = 1$ for a distance $r = 0$.

$$\zeta^2(p) = \frac{\sum_r r^2 C(p, r)}{\sum_r C(p, r)}$$

C.1.4 Scale law

We have mentioned that the percolation behavior was assimilated to a phase transition. The percolation occurs by observing a drastic change of the quantities $S(p)$, $G(p)$, $P(p)$ and $\xi(p)$. Figure 22, illustrates how those values evolve.

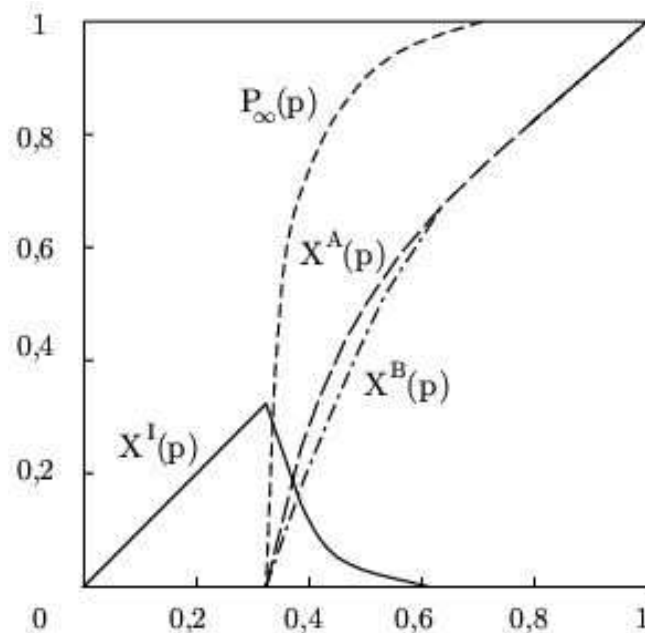


Figure 22 : Simulated statistical dimension in a 3D cubic site percolating network, $P_\infty(p)$ is the probability for a site to belong to an infinite cluster, $X^A(p)$ is the portion of active sites that belong to the infinite cluster, $X^B(p)$ is the portion of active sites that belong to the back bone, $X^I(p)$ the portion of isolated active sites.

The probability for a site to belong to an infinite cluster quickly increases to 1. The portion of active sites that belong to an infinite cluster increases dramatically above p_c . These important changes can be expressed with the following scale law:

$$X \propto (p - p_c)^{\pm \text{exp}}$$

The exponent is a function of the dimension of the system in space and is named universal exponent. Table 1 summarizes the values of the critical exponents in different space dimensions.

Size	Exponent	Scale law	1D	2D	3D
P(p)	β	$(p-p_c)^\beta$	0	5/36	0.4
S(p)	γ	$ p-p_c ^{-\gamma}$	1	43/18	1.8
G(p)	α	$ p-p_c ^{2-\alpha}$	1	-2/3	-0.6
$\xi(p)$	ν	$ p-p_c ^{-\nu}$	1	4/3	0.89

Table 1: value of the universal critical exponents for different parameter in function of the space dimension.

In this work, as demonstrated by De Genne [142], we will focus our attention on the backbone effects, which has been demonstrated to be responsible of most of the physical changes in combined systems.

C.2 Application of percolation theory to carbon nanotubes nanocomposites electrical properties

The introduction of carbon nanotubes in a polymer matrix generates changes on its physical properties. It has been shown that for a given volume fraction of CNTs, it is observed an electrical percolation [51, 53, 54, 143]. This phenomenon can be modeled by a scale law described by Stauffer [140]:

$$\frac{\sigma}{\sigma_0} = (p - p_c)^\gamma \quad \text{pour } p > p_c$$

Where σ_0 is the conductivity when the material has 100% of the filler, and t is a new critical universal exponent.

p_c highly depends on the filler dispersion, and the filler aspect ratio. The low percolating volume fractions reported are generally attributed to the high aspect ratio of nanotubes. The aspect ratio is define by: $f=d/L$, where d is the diameter of the nanotube (≈ 50 nm for MWNTs), and L the length of the tube (≈ 1 μm for MWNTs).

It has been reported the influence of the aspect ratio of the fiber on the value of the percolation threshold. Favier [144] calculated the influence of the aspect ratio on the percolation threshold using Monte Carlo simulations in a 3D network. It has been demonstrated that one should expect the percolation to occur at 0.1% vol. for $f \cong 10$, whereas for $f \cong 100$ it is expected a percolation at: $P_c < 0.01\%$ vol.

Furthermore, as shown in the first chapter, carbon nanotubes have a low flexion modulus. It results in highly twisted tubes when introduced in a polymer matrix. Some works studied the influence of the fiber waviness in a 2D network [145]. As shown in Figure 23, they calculated the evolution of the percolation threshold value against the curvature of the fiber, and demonstrated that the percolation threshold should increase when the fibers are very twisted.

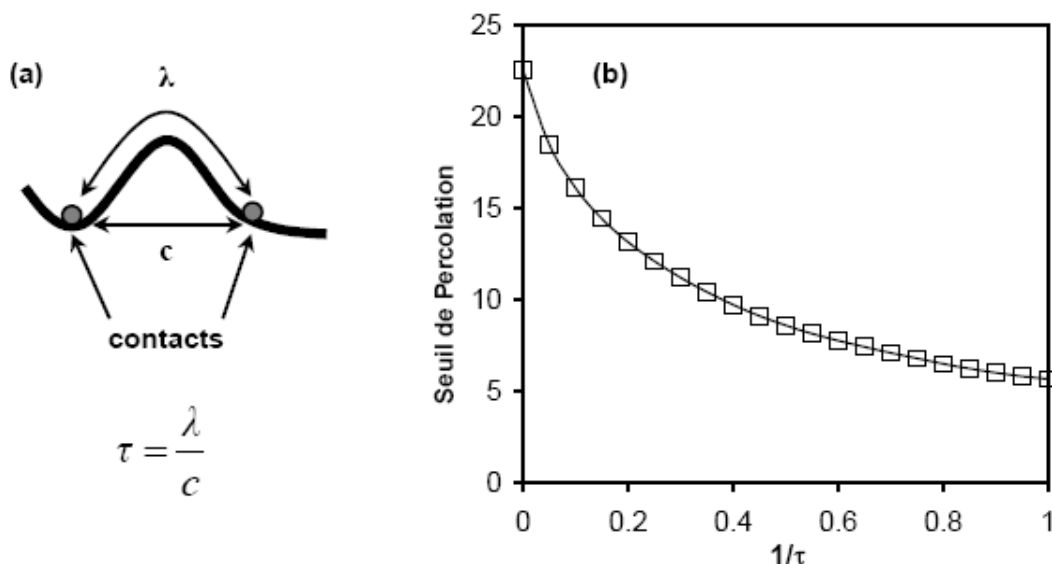


Figure 23 : a) Definition of the waviness of a fiber between 2 contacts [70], b) evolution of the percolation threshold in a 2D network against the waviness of the fiber [145]

The literature [140, 146, 147] reported that the theoretical critical exponent ranges between 1.6 and 2.0. However, published experimental results showed that critical exponents can occur between 1.2 to 3.1. A Recent works by F. Dalmas et. al [148], have shown that the contact resistance between nanotubes is function of the volume fraction of nanotubes. This hypothesis considers that the higher the volume fraction, the lower the contact resistance. As a consequence it is observed an effect on the critical exponent t . Moreover, in this work, it is reported numerical calculations considering the effect of the waviness angle of the fiber. Using a constant contact resistance between the tubes, it is shown that the critical exponent is higher for tubes that are more twisted.

C.2.1 Electrical properties below the percolation threshold

The introduction of metallic particles in an insulator matrix results in a local polarization between each filler. These type of materials can be modeled by a serie-parrallel network of capacities and resistances [149]. Thus below the percolation threshold the material conductivity is frequency dependent. The higher the frequency is, the higher the conductivity: $\sigma = \omega \cdot \epsilon'' \cdot \epsilon_0$. If the quantity (volume fraction) of fillers is increased, an increase in the quantity of local capacity is expected, thus the material is more capacitive. It has been reported that metallic filled polymers near to the percolation threshold reveal a change in the electrical properties following a power law rule: $\sigma(\omega, p_c) \propto \omega^x$.

C.2.2 Electric properties above percolation threshold

The percolation threshold is represented by the existence of a continuous conductive path through the material. Carbon nanotubes are physically in contact. Because the contact is not perfect, the continuous path should be modeled with series of resistors, where each resistor represents a contact between tubes. Thus, the conducting phenomenon is essentially ohmic, and as a consequence frequency independent [149].

Nevertheless, close to the percolation, dead arms or isolated tubes still remain in the material. These particles are acting as local nano-capacitors. Thus the

behavior observed is the sum of an electrical capacity and an ohmic electrical transport [149]. As shown in Figure 24, for a given frequency (namely the critical frequency), the capacitive effect exhibits a higher value than the ohmic effect. For higher filler volume fractions, the resistance of the system dramatically falls and the capacitive transport is dominated by the ohmic conduction.

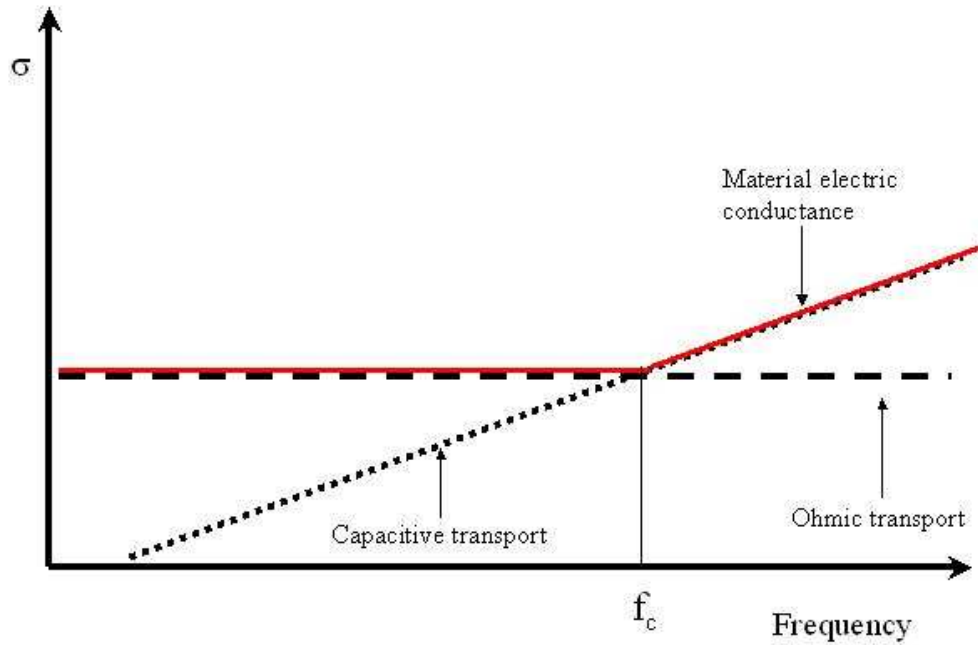


Figure 24 : Electrical conductivity against frequency next to the percolation threshold

Part D Mechanical properties of polymer composites and polymer / carbon nanotubes composites

The literature presents numerous papers dealing with the mechanical properties of polymer / carbon nanotubes composites. By adding carbon nanotubes to a polymer matrix, it is expected an increase of the Young's modulus and the tensile strength of the nanocomposite. Nevertheless, results obtained are very dependent on the volume fraction, the kind of matrix, the synthesis process, and other parameters. The Young's modulus enhancement ranges from some percents to a factor 3 [45, 58, 124, 137, 143, 150-154]. For example Y. Breton et al. [137] have investigated the effect of the MWNTs on the mechanical properties of epoxy / MWNT nanocomposites. They reported an increase of the Young modulus of 16% with 3% of $\text{Co}_x\text{Mg}_{(1-x)}\text{O}$ catalytically grown MWNTs; whereas using a Co/NaY catalyst, the Young modulus of the composite increases by 32%. Other works [125] demonstrated that the composite synthesis process used (i.e, resin infiltration method or melt mixing) permits to reach a highly entangled nanotube network. It resulted in materials with different mechanical properties (increase of 50% using infiltration method, and 40% using melt mixing method). Depending on the chemical nature of the matrix involved, the physical-chemical bonding between nanotubes and the matrix changes, and subsequently the load transfer seems to be affected by a poor adhesion between the matrix and nanotubes [58, 124, 150, 154]. It has been also reported, that in semicrystalline polymeric matrices, nanotubes can act as nucleant agent. The matrix increases its crystalline level, which in turn results in

an increase of the load transfer because of the better adhesion between the matrix and filler [155]. However, the Young's modulus increase (by about 2 for 0,01% vol. fraction) can be attributed to the higher content of crystallites rather than the amorphous phase. Finally, each system, depending on its physical-chemical properties, seems to have its own mechanical reinforcement behavior. Some theoretical calculations explained the phenomenon involved in the mechanical reinforcement of carbon nanotubes composites. Halpin-Tsai rule of mixtures predicts results in good agreement with experimental data for low volume fractions of aligned carbon nanotubes (<2.5%) [155, 156]. Nevertheless, the load transfer is lower than the predicted value. The lack of dispersion as well as the poor matrix / filler adhesion are involved in the low mechanical properties observed experimentally [151, 157]. Other molecular dynamics or molecular mechanics calculations applied to a pull out experiment confirmed these results [158]. As a consequence, we should expect that the chemical functionalization or the grafting of polymeric chains on the carbon nanotube surface would be a solution to prevent the aggregation phenomenon as well as to improve the physical interactions between matrix and fillers.

In this part, we will briefly recall the basic knowledge necessary to understand the mechanical behavior of polymers, block copolymers and polymer-based composites. These elements are necessary to understand the mechanisms involved in the deformation of CNx MWNTs / Polymer nanocomposites.

We will discuss in this section the effect of the introduction of rigid fillers on the mechanical behavior. Several issues from the literature will be presented in order to understand the properties of the composites which are studied in this work.

D.1 Nanotube composites: A review

D.1.1 Mechanical behavior of polymers:

The response to a mechanical deformation of an amorphous polymer is a highly complex viscoelastic / viscoplastic behavior. As a first approximation, we can divide the deformation mechanism into three components. The **elastic** behavior takes place in the beginning of the mechanical test. The strain is instantaneous, reversible and proportional to the stress [159, 160]:

$$\sigma = E.\varepsilon$$

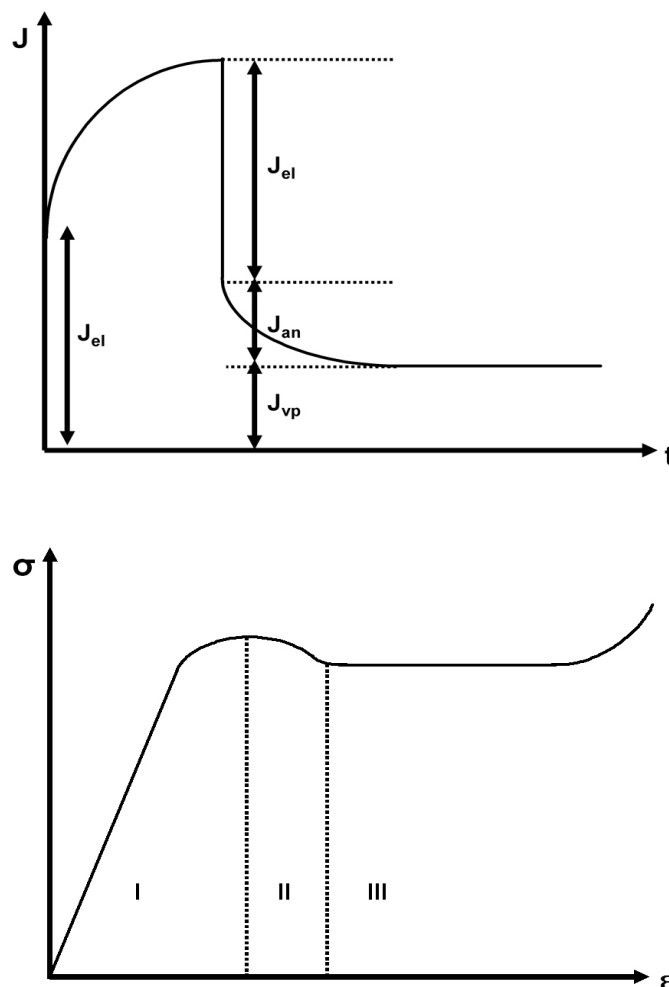


Figure 25: a) Evolution of the compliance during a creep test, J_{el} is the elastic compliance, J_{an} is the anelastic compliance, J_{vp} is the viscoplastic compliance; b) representation of the strain behavior against stress for thermoplastic polymer tensile tests.

For a longitudinal stress, E is commonly called the Young's modulus. At the same time, it is observed an anelastic component, which characterizes the fact that the strain is reversible with time or temperature, and that the stress is a function of the strain rate. At higher strains, a viscoplastic component appears and gradually increases, which is non-reversible with time or temperature (at least for temperatures below the glass transition temperature) [159, 160].

Figure 25:a) illustrates the creep behavior of a polymeric material. In this scheme the evolution of the compliance J (defined as the ratio strain/stress, under linear conditions) is represented versus the experimental time. When a deformation is applied to a polymer, it is usual to observe three compliance components. The elastic compliance J_{el} is instantaneously recovered when the deformation is annealed. The anelastic compliance (J_{an}) is recovered below T_g within a time which strongly depends on temperature. The third component, the viscoplastic compliance (J_{vp}) cannot be recovered below T_g (and is usually recovered above T_g due to entropic forces) [159, 160].

Figure 25b) presents the behavior of a polymer during a tensile test at constant strain rate. The three domains displayed in the Figure correspond (i) to the elastic and anelastic response, (ii) to a softening of the material, and (iii) to a steady state corresponding mainly to the viscoplastic response. It is classically followed by a hardening due to the macromolecules stretching; occurring at high strains. However, the evolution of the three components permits the analysis of the deformation mechanism [159, 161]. Zone I: The elastic strain starts at the beginning of the tensile test to reach a maximum at the yield stress (σ_y). The slope at the origin is close to the Young's Modulus. At the same time, the anelastic strain gradually increases. Zone II: The elastic strain reaches a constant value. At the same time, the anelastic strain still increases gradually and the viscoplastic strain starts to appear. The resulted stress decreases to reach an almost constant value against the deformation. Zone III is representative of the the plastic deformation. This leads to a hardening of the material due to the elongation of the macromolecular chains until the fracture of the bulk material occurs.

D.1.2 Generalities of composites materials

A composite material can be defined as a material which contains two or more distinct phases. The interest in introducing a dispersed phase (filler) in a continuous phase (matrix) is to modify the properties of the original material (matrix). The literature on composite materials based on a polymeric matrix is abundant. Among other things, it is reported various mechanical effects as a function of the filler: high impact behavior (HIPS) for fillers softer than the matrix, whereas for fillers stiffer than the matrix, increase of the Young's modulus, shifts of the glassy temperature, etc... Moreover, the fillers can have other effects on the physical behavior of the matrix like flame retardation, modification of the electrical properties (conductors), modification of the magnetic properties (paramagnetic, ferromagnetic etc.), bio-sensitive behavior, etc. Obviously, the effects of the filler rely on its physical properties and chemical nature. A review by Péla Kunkánszky [162] summarizes the effects of the surface nature of the filler, its size and the state of the fabrication of composite materials.

D.1.3 Importance of the matrix-carbon nanotube interfaces

The use of nano-scale fillers is important because an increase of the area in contact with the matrix occurs. By increasing this area, interfacial effects can be amplified. The fraction of interphase (zone surrounding the filler where the properties of the matrix differ from that of the bulk) in the bulk material may also be increased. Finally, compared to microscopic fillers using the same volume fractions, the use of nano-scale fillers permits a decrease in the filler-filler distances, which may become of the same order of magnitude as the gyration radius of a macromolecule. All these effects may enhance the mechanical reinforcement [155]. However, the presence of nanoparticles aggregates may lower the developed area and thus the reinforcing effects. Indeed, Y. Wang [163] reported that nanotubes aggregate at high concentrations. Consequently, he observed a reduced mechanical reinforcement.

As mentioned above, the matrix may have a different behavior near the interface with the nano-filler. It has been reported that the polymeric chains may be wrapped (physical interaction) to the surface of the nano-filler, so that

the molecular mobility of the macromolecule can be reduced. In some cases, an increase of the glass transition temperature is observed. But the literature reports also some examples where it seems that the molecular mobility is increased close to the filler surface.

Y.T. Sung et al.[143], carried out experiments with polycarbonate / carbon nanotubes composites. They observed by dynamic mechanical analyzes the presence of a double peak of $\tan(\delta)$. The higher transition corresponded to the glass transition of the polymer that has partly lost its mobility near the carbon nanotube surface. Indeed, it has been shown that the amorphous polycarbonate develops a semicrystalline behavior in presence of MWNTs [164]. In the same paper [143] it was shown by X-ray diffraction analysis and DSC, that polycarbonate exhibits a more regular structure next to MWNTs. Other references [152] have used ionic surfactants to disperse carbon nanotubes and observed a similar phenomenon. We should mention that the addition of surfactants may have an effect of plasticizer on the polymeric matrix, so that in this case, it is difficult to attribute the change in the glass transition temperature (T_g) to carbon nanotubes. Finally, up to the date there is no clear evidence of an increase of T_g due to the presence of carbon nanotubes reported in the literature.

In a semicrystalline polymeric matrix, carbon nanotubes can act as nucleating agents [155, 165, 166]. The presence of crystallites at the interface has a drastic impact on the elastic modulus of the polymer, especially for temperatures above T_g .

Finally, it has been reported that during tensile tests, at high strains, pull out phenomenon occurs due to sliding of the nanotubes and the polymeric matrix at the interface [167]. As a consequence, we should expect to avoid the pull-out phenomenon and observe a higher reinforcement effect at high deformations if a good adhesion between the nanotubes and the matrix is achieved (for example by a chemical treatment).

D.1.4 Elastic mechanical properties of two-phase composites

The Reuss and Voigt limits describe the two extremes for the mechanical behavior of two-phase composites. The series model, namely Reuss model, which is the lower limit, consists of series associations of two materials. Most of the strain is supported by the soft component, and thus the elastic modulus evolution with the volume fraction of the rigid phase is weak. The parallel model, namely Voigt model, which is the upper limit, supposes that the strain is homogeneous in the material, and the stress is mainly due to the hard phase. Such a situation may occur when very strong interactions between stiff fillers lead to the formation of a continuous network, forming a continuous rigid phase through the matrix.

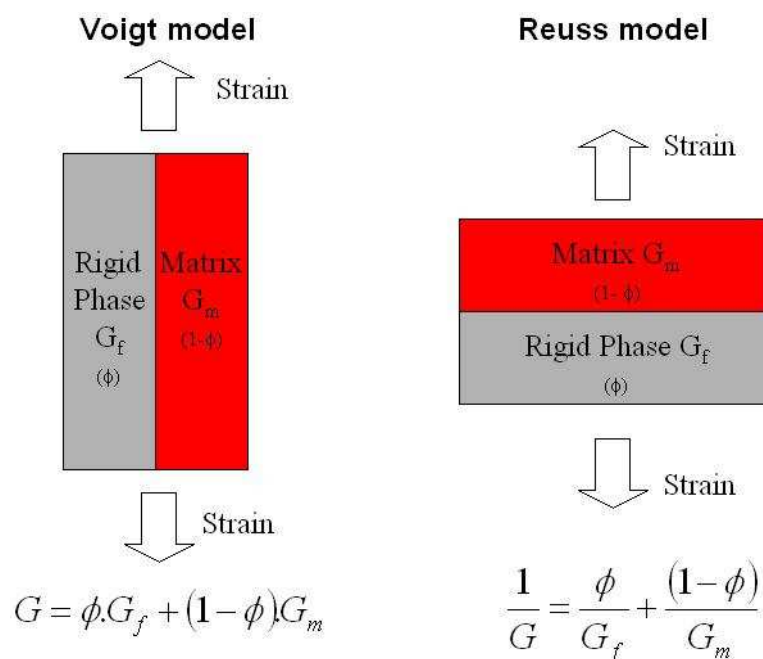


Figure 26: Representation of the upper and lower limit of the mean field theory

From Figure 26 G is the modulus of the composite, G_f the modulus of the fiber, G_m the modulus of the matrix, ϕ is the volume fraction of filler. This figure describes the theoretical differences between Voigt and Reuss models. The equations showed in this figure permit to calculate the resulting modulus of the composite as a function of the filler volume fraction. These two models are generally far from reality and are not representative of the reinforcement caused by fibers in a polymer matrix.

D.1.4.1 Mean field theory

In 1956 Kerner [168] proposed a self consistent model of three phases where the fillers (phase 1) are surrounded by the matrix (phase 2), these phases being in turn embedded in a phase (3) which has the properties of the composite itself. This model takes into account the connectivity of the matrix. Nevertheless it does not take into account the geometry of the filler. Halpin and Tsai (1969) [169] developed a model for unidirectional short-fibers composites based on equations similar to those described by Kerner. The advantage of this model is that it takes into account the aspect ratio of the fiber. Finally, Halpin and Kardos extended this result to isotropic short fiber composites in 1972. In the Halpin-Kardos approach [170], the authors reformulate the Halpin-Tsai equation considering four layers oriented at 0° , $+45^\circ$, 90° , -45° (Cf. Figure 27). We have to point out that the Halpin-Kardos model considers that there is no interaction between the fibers. However, it has the particularity to take into account the aspect ratio and the anisotropy of the mechanical properties of the fillers.

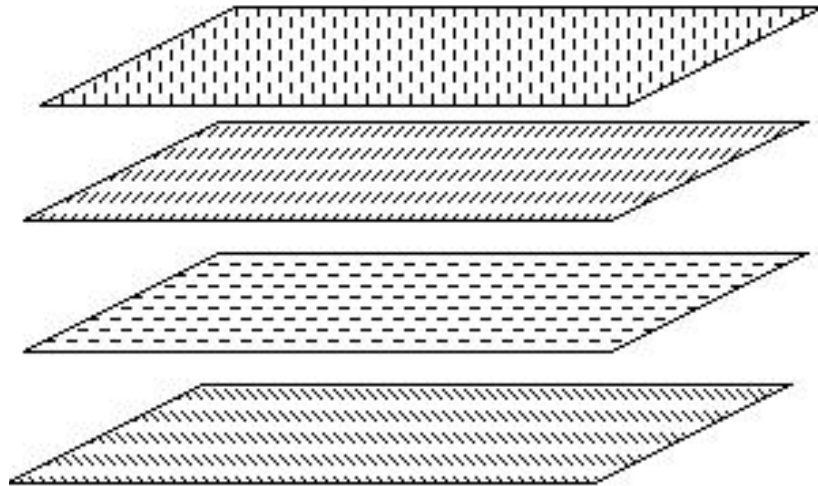


Figure 27: 4 Halpin Tsai layer used model to generate Halpin-Kardos Model

Parameters of each layer are given by the Halpin-Tsai equation:

$$\frac{E_{ii}}{G_m} = \frac{2E_{f_{ii}}(1+\nu_m) \cdot (1 + \xi_{ii} X_f) + 4\xi_{ii}(1+\nu_m)^2 \cdot (1 - X_f)G_m}{E_{f_{ii}}(1 - X_f) + 2(\xi_{ii} + X_f)(1+\nu_m)G_m}$$

$$\frac{G_{12}}{G_m} = \frac{G_f(1 + \xi_{12}X_f) + \xi_{12}(1 - X_f)G_m}{G_f(1 - X_f) + (\xi_{ii} + X_f)G_m}$$

where, E_{fii} is the Young's modulus of the fiber in the direction i ($i=1,2$). G_f and G_m are the shear modulus of the fiber and the matrix, respectively. X_f is the fiber volume fraction. γ is the matrix Poisson's factor. ξ_{ii} represents the geometry of the fiber:

$$\xi_{11} = 2\left(\frac{L}{e}\right) \quad \xi_{22} = 2\left(\frac{l}{e}\right) \quad \xi_{12} = \left(\frac{l}{e}\right)^{\sqrt{3}}$$

L , l , e are respectively the length, the width and the thickness of the fiber.

Finally the calculation gives the equation of Halpin-Kardos (laminates description):

$$G = \frac{E_{11} + E_{22}(1 - \nu_{12})}{8(1 - \nu_{12}\nu_{21})} + \frac{G_{12}}{2}$$

Where ν_{12} and ν_{21} are obtained by the following equations, ν_f being the fiber Poisson's factor:

$$\nu_{12} = X_f\nu_f + 9(1 - X_f)\nu_m$$

$$\nu_{21} = \nu_{12} \frac{E_{22}}{E_{11}}$$

D.1.4.2 Mechanical percolating network theory

The percolation concept, previously described in the Chapter II part C, has been extended to their mechanical properties in order to explain the drastic changes observed in a material for a given rigid phase volume fraction [142, 171]. In this model, strong interactions between the fillers are considered. Ouali et al. [172], in a study of polymer blends, implemented the percolation concept to the series-parallel model of Takayanagi [173]. Figure 28 represents the Takayanagi

series – parallel model adapted to the mechanical percolation concept. On this scheme $P(\psi)$ represents the volume fraction of the percolating rigid phase.

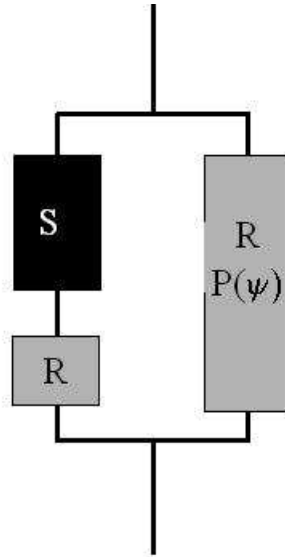


Figure 28: Model of Takayanagi adapted to percolating system.

This model has been successfully used to describe the mechanical behavior of cellulose fiber polymer nanocomposites, where fibers have strong OH interactions between each other [149].

The percolation theory defines the volume fraction of the infinite percolating cluster P . In this case, P can be calculated as a function of the filler volume fraction (ψ) [172, 174]:

$$p(\psi) = 0 \quad \text{if } \psi < \psi_c$$

$$P(\psi) = \left(\frac{\psi - \psi_c}{1 - \psi_c} \right)^b \quad \text{if } \psi > \psi_c$$

where ψ_c is the percolation threshold and b is the critical exponent.

Finally, we have to consider a soft phase “S” in series with a rigid phase “R”, and on the other branch we represent the percolating rigid phase. Then the shear modulus can be defined by the following equation:

$$G = \frac{(1 - 2P(\psi) + P(\psi) \cdot \psi)G_s G_r + (1 - \psi) \cdot P(\psi)G_r^2}{(1 - \psi)G_r + (\psi - P(\psi))G_s}$$

where G_s and G_r are the shear moduli of the soft phase and the rigid phase, respectively.

D.1.4.3 Entangled fibers and impact on nanocomposites properties.

In chapter I, we described the physical properties of nanotubes. One of the most important properties of carbon nanotubes is their very high aspect ratio. As a consequence we should expect that the entangled fibers would behave as a rigid network, and thus one should observe a mechanical reinforcement similar to those of cellulose whiskers in a polymer matrix [149]. Nonetheless, the literature does not relate such a behavior of the composites. Most of the reinforcement mechanisms are attributed to a load transfer phenomenon [122, 137].

It has been reported that entangled nanotubes are able to increase the temperature at which the polymeric composite starts to flow [70, 148]. Moreover, using tensile tests coupled with electrical measurements, the authors demonstrated that depending on the preparation method of the composite, the nanotubes could be entangled or not. In the same work, they described the existence of two kinds of contact: simple contacts between different nanotubes forming coils, and contacts at the entanglement between two nanotubes. For the sake of simplicity, we will call these two types of contacts, simple contacts and entangled contacts. On the other hand, O. Meincke [175] studied the effects of the carbon nanotubes in polyamide-6. Using rheological analysis and plotting the loss tangent versus the frequency, he demonstrated that a mechanical percolation threshold can be observed by the presence of a liquid-solid transition such as gelation ($\tan(\delta)$ is frequency independent).

Part E Conclusions of chapter II

In the previous sections, we summarized the state of the art concerning the chemical modification of the carbon nanotubes. It was shown that one can distinguish the chemical modification of CNTs from a destructive point of view. The strong acid treatment is considered as a highly destructive process and should be avoided to preserve the properties (conductivity, Young's modulus, etc...). Grafting polymers on nanotubes might be an alternative route to functionalize nanotubes without inducing extended damage. However, the nanotubes may be as inert as graphite and it may be difficult to carry out grafting on their surface. On the contrary, CNx MWNTs might be more chemically reactive. Indeed the defects induced in the carbon graphene sheet by the nitrogen atom might lower the stability of the π carbon double bonds. We have shown that few papers used the ATRP as an in-situ polymerization to graft polymers on carbon nanotube surfaces. Furthermore, the literature has shown that this polymerization technique is a suitable process to generate homogeneously grafted hybrid materials.

It was presented the basic knowledge concerning the physico chemistry of a two phase mixtures. We expect that the polymer grafting can be a solution to lower the aggregation of carbon nanotubes when dispersed in a polymer matrix. A description of micro-structured block copolymers was done by describing atomic interactions between macromolecules. Indeed we are interested in studying the effect of the polymer grafting on the block copolymer microstructure. Finally, we emphasize on the effects of the matrix / filler interaction during a mechanical test. It appears that the polymer grafting on the surface of the CNx MWNTs might avoid the pull out phenomenon. Therefore, we expect that the plastic deformation and the fracture properties of the nanocomposites will be largely affected when using polystyrene grafted CNx MWNT as a mechanical reinforcement.

Concerning the electrical properties of carbon nanotube polymer composites, we did a review on the percolation theory basic knowledge and its applications with nanocomposites polymer /carbon nanotubes. It appears that the electrical percolation can be described by using two main parameters: the percolation threshold (p_c) and the critical exponent (t). p_c is a function of the filler: dispersion, aspect ratio, and waviness. On the other hand t is dependent of the waviness and the contact resistance between carbon nanotubes when introduced in a matrix. Then we decided to study the effect of the carbon nanotube polymer grafting on these parameters.

Finally, we presented the basic knowledge concerning the mechanical properties of polymers composites and its applications to carbon nanotube composites. The literature has demonstrated that when added carbon nanotubes in a polymer matrix, it increases the composite Young's modulus (when increasing the carbon nanotube volume fraction). In order to understand the elastic behavior of our composites we described two theoretical models: Halpin-Kardos model, and mechanical percolating model. The Halpin-Kardos equations permit to calculate the elastic modulus for composites using homogeneously dispersed short straight rigid fibers. In this model the fibers are considered without interactions between each other. On the contrary the percolating mechanical model permits to describe the reinforcement for composites where the fibers have strong interactions as compared to the matrix modulus. The grafted nanotubes are a special case where the fibers are long, flexible and the grafting can modify the interactions. Thus, we will study which of both models is more adapted to describe our system.

Chapter III

Materials and experimental techniques

Part A Matrix and CNx MWNTs: synthesis and characteristics

A.1 CNx MWNTs

The CNx MWNTs were given by the IPICYT. As shown in Figure 29 the process to synthesize CNx MWNTs consists in pyrolyzing a mixture of ferrocene $\text{Fe}(\text{C}_5\text{H}_5)_2$ and $\text{C}_6\text{H}_5\text{CH}_2\text{NH}_2$ (0.2 g of $\text{Fe}(\text{C}_5\text{H}_5)_2$ in 2 mL $\text{C}_6\text{H}_5\text{CH}_2\text{NH}_2$) at 850-900 °C (0.2 g of $\text{Fe}(\text{C}_5\text{H}_5)_2$ in 2 mL $\text{C}_6\text{H}_5\text{CH}_2\text{NH}_2$). The decomposition of the organic compounds takes place above/below 350°C. The organic residues are transported in a gas carrier stream (e.g., Ar) and precipitate as CNx MWNTs in the pyrolysis zone [176].

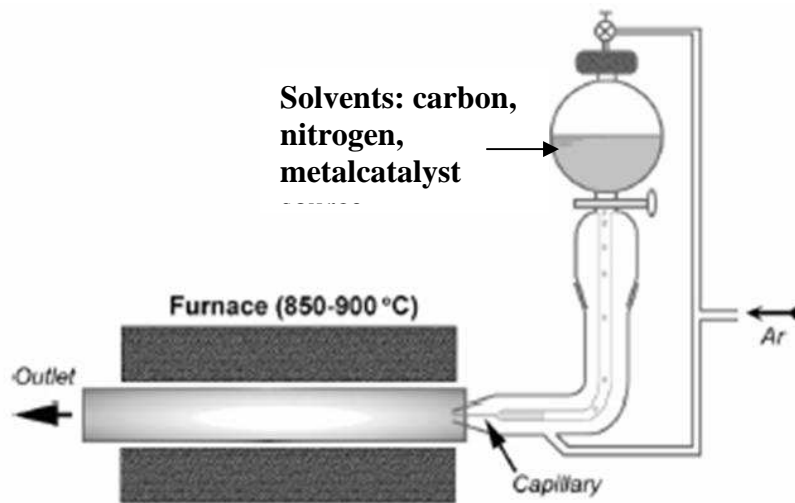


Figure 29: schematic snap shot for the spray pyrolysis to synthesize CNx MWNTs.

In Figure 30 it is represented the growth mechanism for CNx MWNTs during gas pyrolysis. A) The CN species liberated from the solvent mixture pyrolysis further fragment on the surface of the metal catalyst creating CN radicals, gaseous N_2 and carbon. B) and C) The carbon and possibly the nitrogen precipitate on or diffuse through the metal catalyst, forming nanotubes or fibers. D) Nanotubes growth until the leading catalytic particle is deactivated [176].

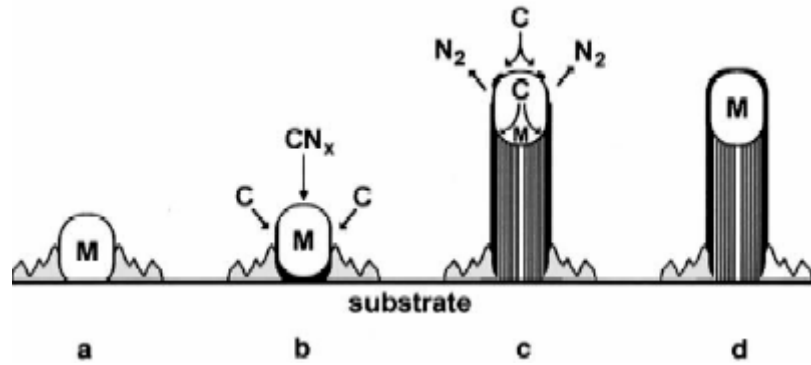


Figure 30: growth mechanism for CN_x MWNTs

As shown in Figure 31 the CNTs obtained are bamboo-like structured. The nanotubes we observed by SEM are 20 μm long and have a diameter about 50 nm [177]. It leads to an aspect ratio (length diameter ratio) of 400.

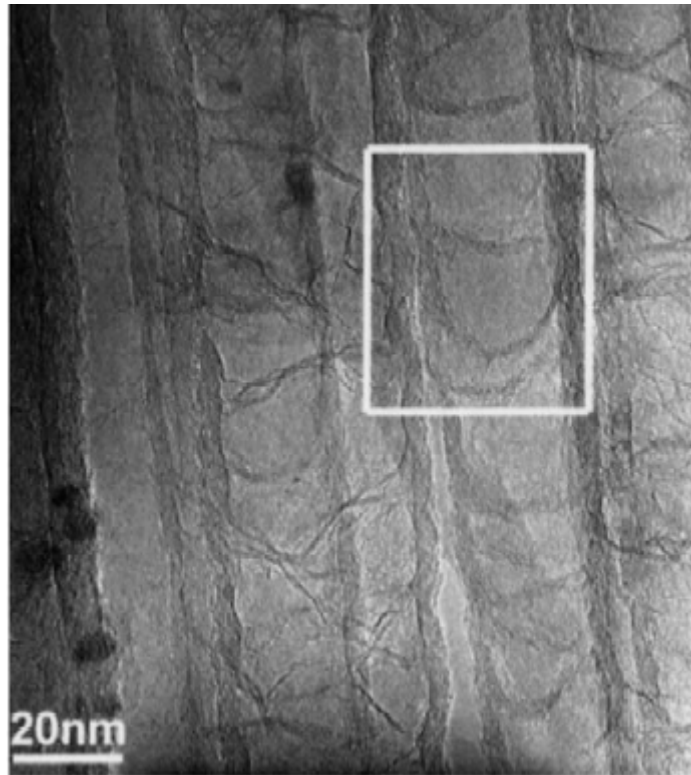


Figure 31: bamboo-like structured CN_x MWNTs TEM photomicrograph [176].

A.2 Polystyrene

The polystyrene is an amorphous polymer which glassy temperature is about 100°C. The polymer is generally obtained by radical propagation of styrene monomers (C.f. Figure 32). The PS matrix was obtained from Resirene (model HH-104).

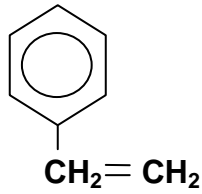


Figure 32: Styrene monomer.

A.3 Poly (butadiene-co-styrene)

The PSBS used was produced by anionic polymerization in an industrial reactor; the butadiene monomer is described in Figure 33. Its glassy transition is about -90°C. The polymer we used was provided by resirene (model 1205). This polymer is a linear block copolymer.

The PSBS molecular weight is $M_n = 100,000$. The PS block has a molecular weight $M_n = 10,000$.

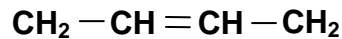


Figure 33: Butadiene monomer

Part B CN_x MWNT

Chemical modification

B.1 Chemical modification of CN_x MWNTs: **chemical mechanisms**

B.1.1 Synthesis route for Surface Phenyl Grafted CN_x MWNT

In the previous section we defined that in ATRP the chemical form of a macro-initiator has to be an alkyl halide [97]. Furthermore, it has been reported that free radicals are able to chemically react with SWNTs [178]. Authors report that mixing benzoic peroxide with SWNTs under heating, lead to the grafting of aromatic rings on the nanotube external layer. One of the aims of this section is to demonstrate that even if MWNTs are less reactive (because of their diameter) it is possible to make them chemically active.

Based on this report, we carried out a reaction mixing Benzoyl Peroxide (BPO) and CN_x MWNTs in a solvent at high temperature. Indeed, BPO is composed of an aromatic ring and has styrene-like structure; and consequently it is a good candidate to be used as an ATRP macroinitiator. Previous studies reveal that a 70% percent of benzoic peroxide initiates benzoic free radicals, and some 30% liberate phenyl free radicals with CO₂ gas (C.f. Figure 34). For the sake of simplicity, we will further refer to phenyl radicals, even though benzoic peroxide radicals are present.

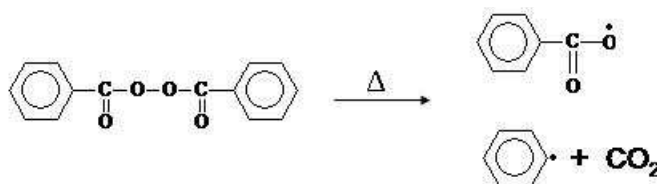


Figure 34: BPO free radical liberation mechanism

As depicted in Figure 35, in the presence of CN_x MWNTs, we expect that π double bonds of the carbon structure will be attacked by the free radicals. The homolytic opening of the carbon double bond would allow the stabilization of a free radical. The other electron of the π double bond should resonate in the carbon structure of the CN_x MWNT until it becomes stabilized by another free radical in solution or by an impurity.

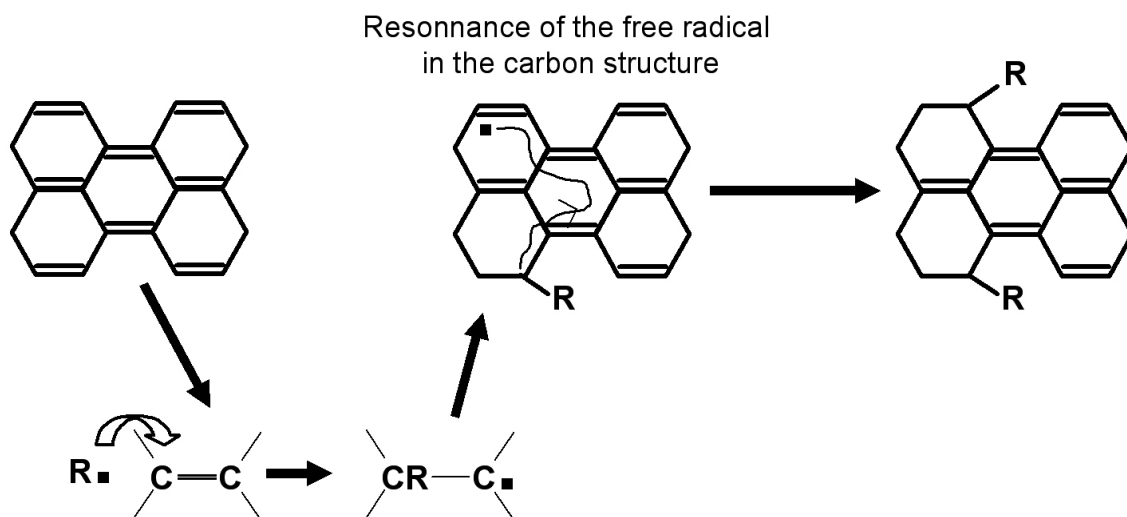


Figure 35: Chemical mechanism of free radical addition on the CN_x MWNT external layer

The product of this reaction is expected to be CN_x MWNTs covered by phenyl groups (Cf. Figure 36)

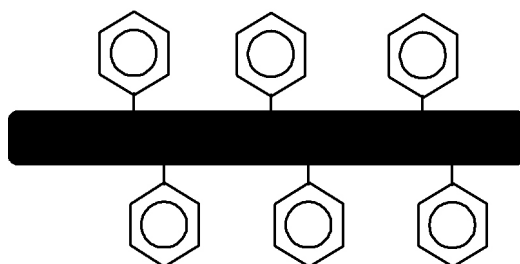


Figure 36: CN_x MWNT covered by phenyls groups

B.1.2 Atomic Transfer Radical Polymerization Macroinitiator grafted CN_x MWNTs

After CNTs have been grafted with aromatic rings they are subjected to a process where a proton of the aromatic rings is substituted for a Bromine atom.

It has been reported that proton aromatics rings can be substituted by bromine in presence of FeBr_3 and molecular Br_2 at 55°C (Cf. Figure 37).

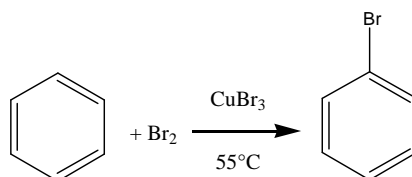


Figure 37: Chemical reaction equation of the proton aromatic ring substitution

Then, the halogenated radical exhibits all the characteristics to initiated ATRP in the presence of CuBr (ATRP catalyst reaction).

B.1.3 In-situ PS polymerization of CNx MWNTs using ATRP

CNTs containing macroinitiator molecules for ATRP will then be used to carry out a polymerization on the CNTs surfaces. The modified nanotubes will serve to make a polymer chain grow by propagation of the free radical using a controlled redox process. In

Figure 38, we can observe that the reaction is composed of three parts. The first part corresponds to the initiation of the redox mechanism that will permit the liberation of controlled free radicals. Subsequently, it is represented the addition of the monomer (styrene in this study), by free radical propagation. The mechanism that will control the chain growth is the oscillation of the Br element from the end of the chain to the catalyst. The temperature will permit to adapt this oscillation, and as a consequence control the polydispersity of the polymer molecular weight. After some time, nanotubes will be highly coated with a layer of PS.

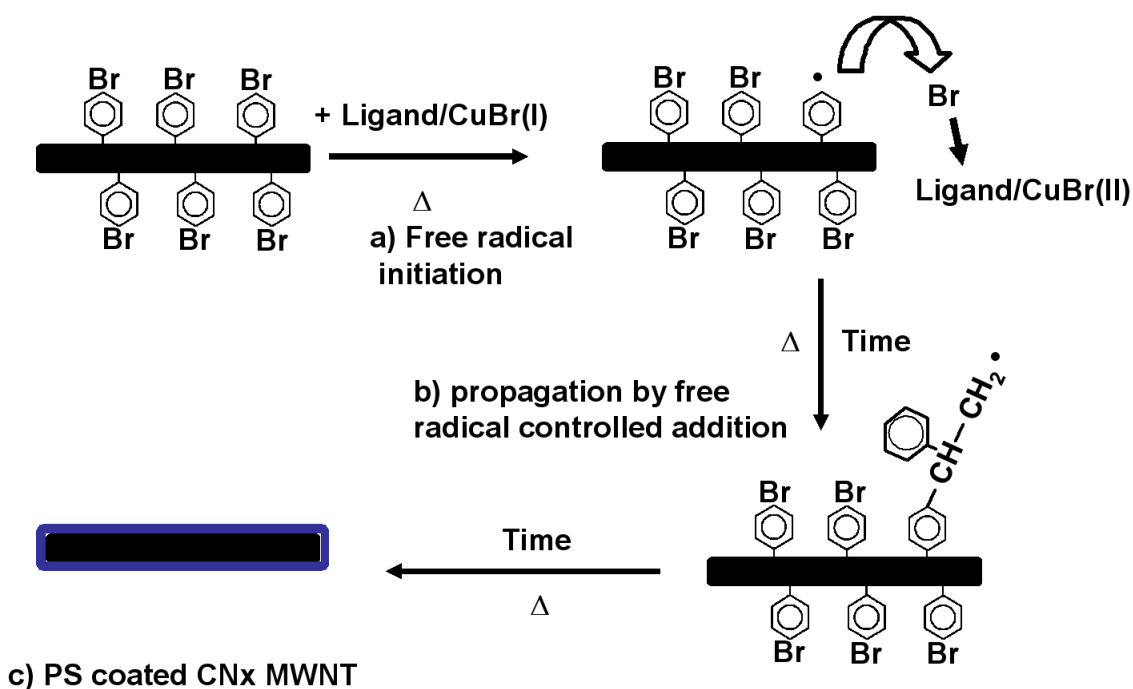


Figure 38: CNx MWNT following the ATRP process

B.2 Experimental protocol for Polystyrene grafted CNx MWNTs

B.2.1 Phenyl Grafted CNX MWNTs synthesis

Nanotubes were functionalized by a free radical process using Benzoin peroxide. 10 mg of CNx MWNTs were dispersed in reactive grade toluene (98,5% purity) by sonication for 30 min. This first treatment permits to remove residual silica and metal catalysts resulting from the CNx MWNT growth. Then, the solution was filtered with a whatman 500 nm porous paper filter. We believe that most of metal and silica nanoparticles (≈ 50 nm) will pass through the filter and that the MWNTs (≈ 20 μm length) will be kept on the paper. The paper is kiln-drained at 120°C . 10 mg of dried CNx MWNTs were then dispersed using sonication for additional 30 minutes. The suspension was mixed with 1% solution in weight of BPO and finally heated at 105°C for five hours, with vigorous agitation in a sealed flask (Cf. Figure 39).

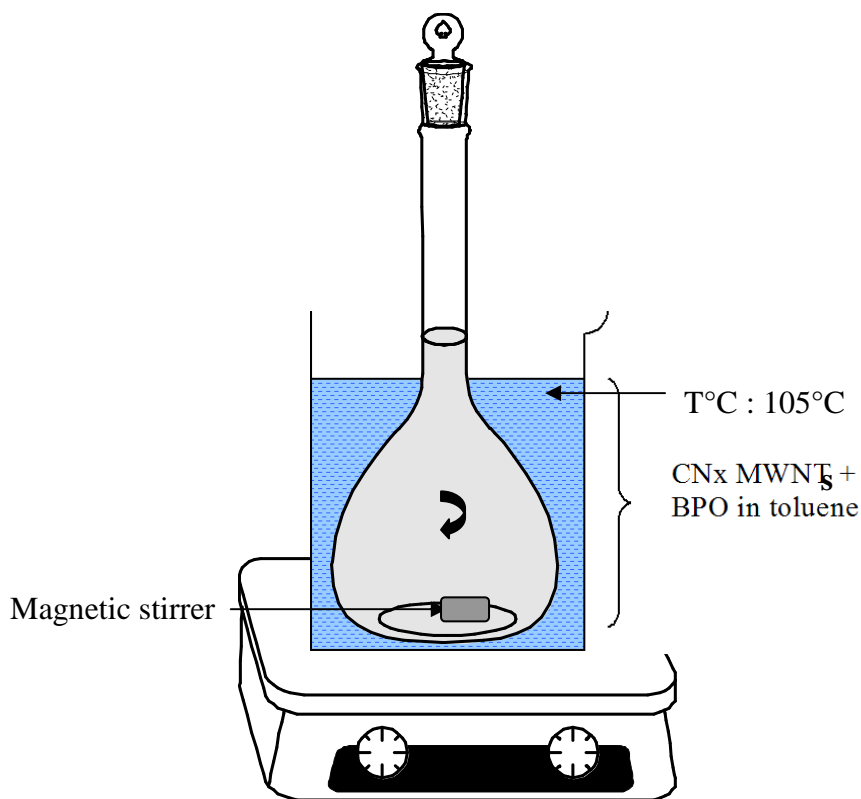


Figure 39: Experimental scheme of the addition of BPO to CN_x MWNTs

Subsequently, the CNTs were collected by filtering in an ashless whatman filter, and washed with reactive grade toluene. The residual solvent was removed by evaporation at 90°C under reduced pressure.

B.2.2 Macroinitiator-grafted CN_x MWNT synthesis

CN_x MWNTs from the previous step (grafted with phenyls) were chemically modified in order to attach a bromine atom in the para position. A proton of the grafted benzoil was substituted by a Bromine atom, at 55°C with Aldrich 98% purity Br₂, and FeBr₃ (Aldrich, 98%) as catalyst. CCl₃ was used as the solvent, since the C-Cl bond has a higher electronegativity compared to C-Br and thus it is not possible for it to affect the reaction.

10 mg of previously phenyl grafted CN_x MWNTs were dispersed in 20 mL of reactive grade solvent (99% purity) CCl₃ using sonication for 30 minutes. The proportions of catalyst CuBr₃ and molecular Br₂ added to the reactive solution are described in Table 2.

mole of grafted BPO	mole of Br ₂	mass of CuBr ₃
n	1.1 n	≈ 1 mg

Table 2: Proportion of reactants used during the bromine / proton aromatic ring substitution.

The reaction was carried out for 3 hours under vigorous stirring. Finally, CN_x MWNTs were filtered on an ashless whatman filter and washed with an excess of diverse solvents: CCl₃, Tetra Hydrofuran (THF) in order to perfectly wash the sample and eliminate impurities (neutral or more electronegative). Lastly, collected macroinitiator grafted MWNTs were dried at 80°C under reduced pressure for 24 hours.

B.2.3 Synthesis of PS grafted CN_x MWNTs

A requirement to carry out a successful ATRP reaction is that all reactants are dried, and oxygen free. Reactive grade Toluene (98,5% purity) was dried over silica in a chromatographic column (C.f. Figure 40). The Inhibitor was removed from Reactive grade Styrene (99% purity) with 10% weight NaOH solution. Then, it was dried over silica in a chromatographic column. Lastly, oxygen diluted in the solvent is removed by passing N₂ through for 30 minutes.

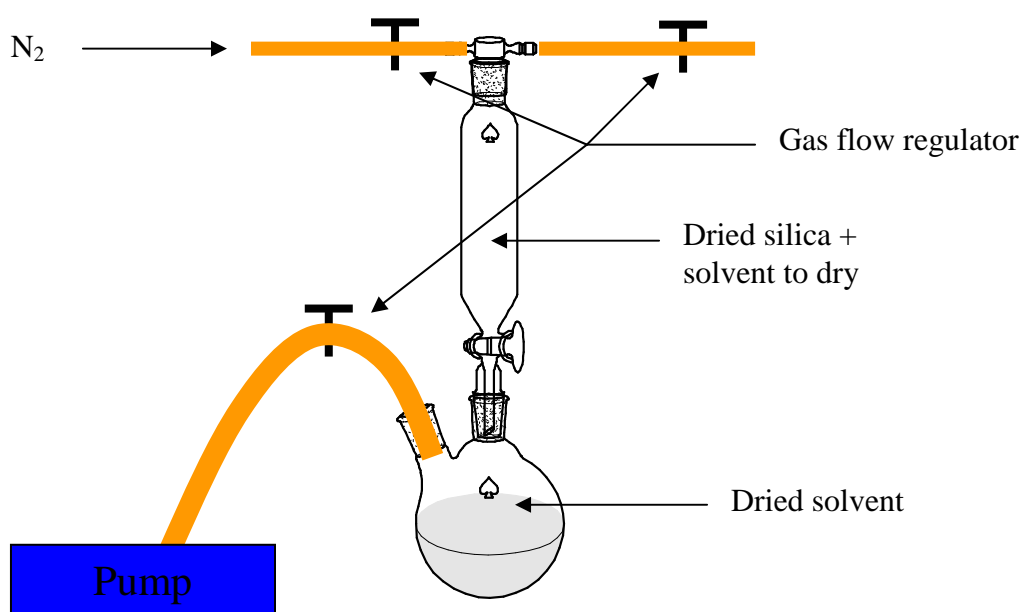


Figure 40: Scheme depicting the solvent drying process

All these reactants were preserved in a sealed bottle container.

To carry out ATRP reaction CuBr(I) was stirred for 24 hours in glacial acetic acid to remove CuBr(II). Then, CuBr(I) (98%, Aldrich) was dispersed in a solution of dinonyl bipyridine (Aldrich, 98% purity) in dried toluene, and strongly stirred for several hours to disperse all CuBr(I) molecules. The mixture was prepared under a N₂ atmosphere (in a glove box) to avoid water and oxygen catalyst oxidation. The proportion ligand / catalyst is respectively 2:1. Shlenk reactors were connected to a special line where a switch offers primary vacuum or N₂ gas (Figure 41). Reaction mixture: toluene / styrene, is vacuumed and nitrogen filled three times to assure the absence of any oxidation agent (H₂O, O₂) during the polymerization. The reaction was conducted in diluted media: 50/50% (volume), toluene/styrene, using vigorous stirring at 120°C. The same proportion of nanotube / total volume of reactant is preserved: 10 mg → 20 mL.

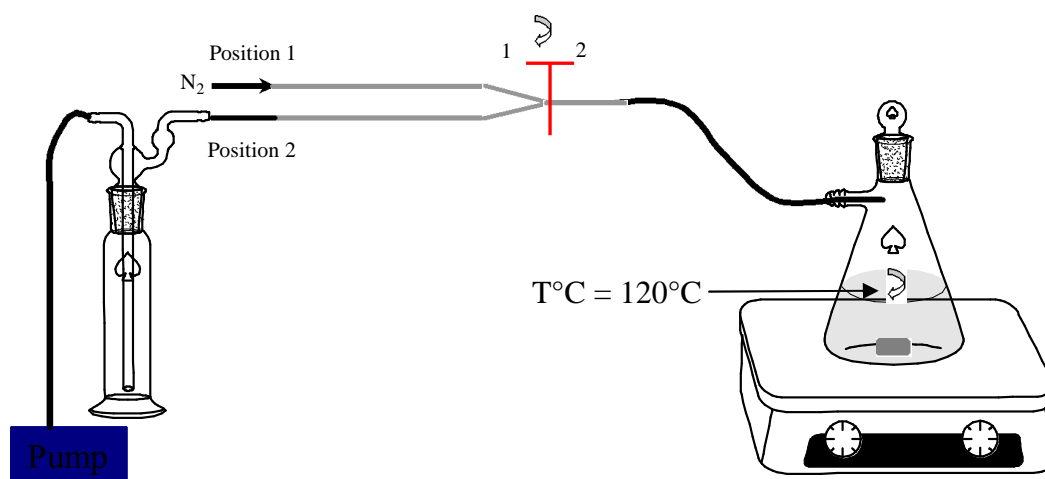


Figure 41: Experimental scheme of the ATRP line

After completing the reaction, the samples were filtered three times through a ceramic filter (50 nm porous large), and washed with an excess of reagent grade toluene.

B.3 Chemical analysis tools

B.3.1 Fourier Transformed Infra Red (FTIR)

A molecule exposed to infrared rays can absorb photons with a wavelength corresponding to functional vibration of its chemical functional groups. On Figure 42, it is represented the classical harmonic oscillator, which can model the behavior of a chemical bond between two different atoms. If we consider two atoms A and B, and μ the reduced mass of the A-B atom system, k the bond force constant bond force of the equivalent hairspring, we can define the adsorption frequency by:

$$\bar{\nu} = \frac{1}{2\pi c} \sqrt{\frac{k}{\mu}}$$

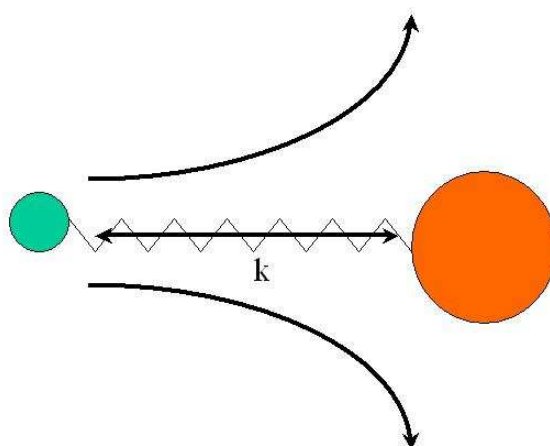


Figure 42: Harmonic oscillator model for a bi-atomic system

This simple model permits us to understand that each chemical bond will have its specific absorption frequency. Nevertheless, infrared spectroscopy is not so simple. This technique is accurate enough to distinguish most of the organic molecules, depending on their polarity or their chemical nature of the covalent bond. Depending on the polarity of the chemical bond, the absorption peak will vary in intensity or in line-width. In order to be IR active, a molecule needs to have a changing dipole.

Figure 43 represents the experimental scheme of an FTIR analyzer. The process to obtain FTIR spectra consist in irradiating the sample with IR waves. Then, the absorbed IR beam passes through a NaCl prism that permits to spatially separate the different wavelengths. The reference beam (background) is subtracted to the previous information, thus permitting the elimination of noise from the analyzer box. Finally, an analyzer (computer) constructs the FTIR spectrum.

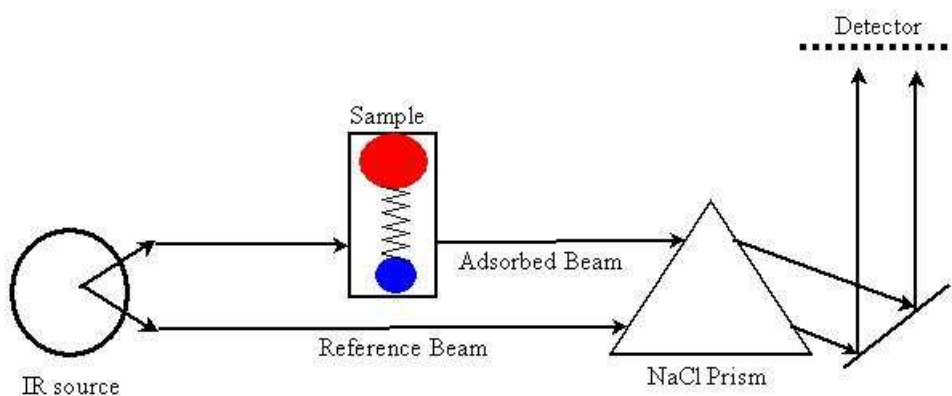


Figure 43: Experimental schematic of an FTIR analyzer

B.3.2 Coupled gas Chromatography / Mass Spectrometer (GC-MS)

This technique is the combination of two chemical analytical techniques: gas chromatography and mass spectrometry. The first one consists in separating the different organic elements in time from the material that is being studied. Organic molecules, depending on their chemical properties will pass more or less quickly through the chromatographic column. The gas spectrometer ionizes molecules due to the electron beam, and the fragmented molecular ions obtained can be analyzed as a function of their weight and electric charges. The combination of these two techniques is a powerful tool to study complex compositions and low concentration materials (some ppm). An experimental scheme is depicted in Figure 44.

- Gas chromatography

Chromatography is a physico-chemical test which separates the different components of a mixture (gas, liquid) by passing it over a stationary phase (in our case a solid) using a mobile phase (gas in this work). The sample can be sublimated by an electric discharge and subsequently introduced in the gas chromatography column. Consequently, every component is subjected to a retention force due to the stationary phase and a mobile force. There are numerous types of chromatographic tests, in this thesis we used a gas/ solid chromatography. This kind of tests can be defined as an adsorption chromatography. Indeed, the stationary phase retains the different components by physical interactions like dipole - ion bonding, dipole - dipole bonding or van der Waals interactions. Finally, we obtain spectra of the separated organic components in time.

- Mass spectrometry

The material that is analyzed is introduced in the mass spectrometer and ionized by an energetic ion beam (generally 70 eV). The ions produced are called molecular ions, and permit to determinate the molecular mass of a given molecule. Subsequently, these fragments are selected by the ratio mass / electric charge due to an electric or magnetic field, and finally collected by a detector. The fragments constitute the mass spectra which analyze permits to define the molecular composition of the original molecule.

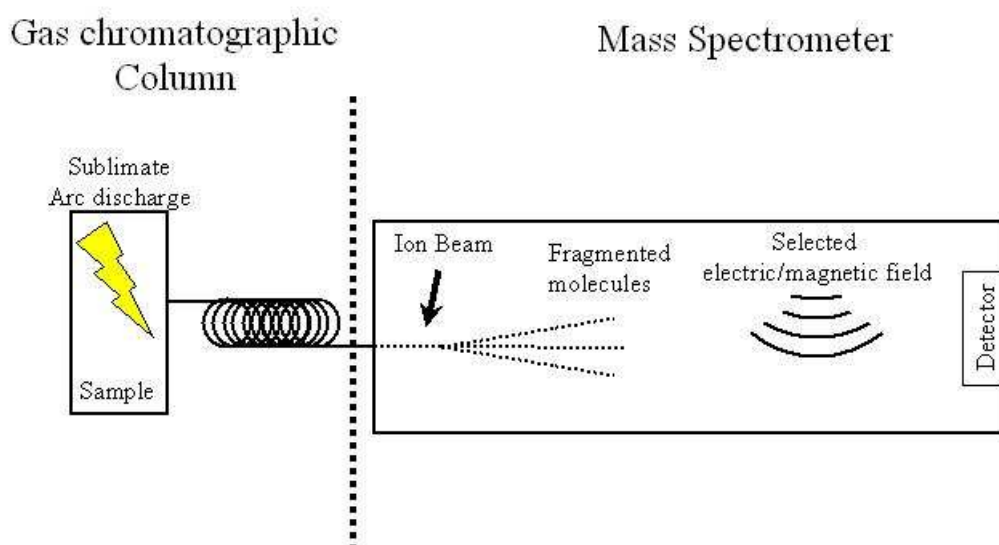


Figure 44: Experimental scheme of the GC-MS spectrometer

B.3.3 Thermogravimetric Analysis

The thermogravimetric analyses (TGA) consist in measuring the mass loss during heating treatment. Because molecules fracture during a heating process, this technique does not permit to do qualitative analyses. However, it should reveal very accurate quantitative measurements. The gas injected in the furnace should permit to select the degradation process. For example, oxygen will generate oxidation and nitrogen permits a simple thermal degradation of organic molecules in the material. In this work, TGA has permitted to calculate the quantity of molecules grafted on the carbon nanotube surface.

B.3.4 Electron Energy Loss Spectroscopy / Energy Dispersing Spectroscopy (EDS)

- *EELS*

An electron beam of a few hundred of keV which passes through a material causes different excitations that can be observed by different microanalyses techniques. An EELS signal corresponds to the transmitted electrons which have lost an energy ΔE . EELS analyses are very adequate to study organic systems because it permits to analyze light elements like carbon, nitrogen.

EELS spectra are obtained from inelastic interactions between the incident electrons and the material. The energy losses are characteristic not only of the elements present in the material but also of their chemical environment. The energy losses less than 50 eV come from inelastic interactions with the external layers of the electronic clouds, whereas energy losses superior to 50 eV come from transitions of an electron from a core level to an antibonding orbital. In both cases, informations can be obtained about the nature and the valence of the analyzed species. K. Varlot [179] has demonstrated that it was possible to distinguish many organic bonds such as σ c-c, σ c=c, σ o-c in polymers and consequently distinguish two different polymers using EELS.

Concerning this work, EELS was a powerful technique that permitted to study the composition of the grafted layer on the CNx MWNTs.

- *Energy Dispersing Spectroscopy (EDS)*

After the excitation of the materials atoms by the electron beam, a radiative desexcitation may occur, and the material emits x-ray photons which energies are characteristic of the elements present in the material.

In these works, the very low detection threshold of EDS permitted to confirm the presence of brome in the PS grafted CNx MWNTs.

B.3.5 Raman Spectroscopy

Raman spectroscopy relies on the inelastic scattering of monochromatic light with a material. In Raman scattering, the energies of the incident beam and scattered photons are different. If IR modes are due to changes in the dipole moment, Raman activity is due to a change of the polarizability. As a consequence, Raman spectroscopy is highly sensitive to the material crystallinity, orientation and temperature. Raman spectroscopy is useful for analyzing molecules without a permanent dipole moment which would not show up on an IR spectrum. For example in carbon nanotubes, this technique can be used to determine the graphitic level of the material. It is commonly accepted that it exists a G band that represents the graphitic level of the tubes, and a D-band that is responsible for the introduction of disorder in the system (sp^3 , defects, etc...).

In this work, we used this technique to analyze the disorder induced in the graphene layers by grafting organic molecules on the surface of the CNx MWNTs. It should be mentioned that the most common light source used with this technique is a tunable Ar-ion laser.

B.3.6 Electron Spin Resonance (ESR)

Electron Spin Resonance, known as well as Electron Paramagnetic Resonance (EPR), is a spectroscopic technique that permits to detect unpaired electrons.

Unlike to nuclear magnetic resonance (NMR), which excites the spin of the atom nucleus, ESR excites electron spins. As a consequence ESR is useful to detect free radicals in organic molecules or oxidation state transitions in inorganic metal complexes. An unpaired electron has a magnetic moment μ_B . This magnetic moment, when introduced in a magnetic field B_0 with a specific frequency, will resonate for a certain energy defined as:

$$\Delta E = h\nu = g_e\mu_B B_{\text{eff}}$$

where g_e is the gyromagnetic ratio of the electron. $B_{\text{eff}} = B_0(1-\sigma)$, so the precedent equation can be written as: $\Delta E = h\nu = g_e\mu_B B_{\text{eff}} = g\mu_B B_0$. Because free electrons are sensitive to their environments, g factor is representative of each chemical component.

Two ESR acquisition processes are possible. The first one consists in scanning the absorbance frequency with a constant external field. In the second process or alternatively the external field changes with a constant frequency radiation.

This technique has permitted to confirm that the brominated phenyl grafted CNX MWNTs could initiate the ATRP redox process in the presence of CuBr (I), and it also confirmed that the process was temperature reversible.

We carried out ESR experiments at different temperatures. In order to carry out this kind of experiment, we mixed in reagent grade toluene, CN_x MWNT-BPO-Br, CuBr(I) and 4,4'-dinonyl 2,2'-bipyridine (dNbpy) in the molecular proportion 1:1:2. The solution was heated at different temperatures (90°C to 130°C) during ESR measurements.

Part C Polymer / CN_x MWNT composite : synthesis and microstructural characterization

C.1 Polymer / CN_x MWNT nanocomposite synthesis

Four types of nanocomposites were synthesized. Table 3 summarizes the conditions and reactants used for the different composites. Two kinds of matrices were used in this work. The PS matrix was obtained from Resirene (model HH-104). The PSBS matrix is a linear block copolymer styrene-butadiene-styrene (30% styrene, 70 % butadiene) was provided by Resirene (model 1205).

Figure 45 shows the process used to synthesize the nanocomposites. Ungrafted CN_x MWNTs were sonicated for 30 minutes in reagent grade toluene. Subsequently, the polymer (PS or PSBS) was added to the solution and magnetically stirred for a couple of hours in order to disperse the materials. The magnetic stirring was maintained while the solvent was evaporated using an air flow over the solution. Finally, when the preparation became viscous, the residual solvent was evaporated under vacuum and heat for 48 hours.

PS grafted CN_x MWNTs were dispersed by stirring in solvent for 8 hours. Sonication was not used in this process to avoid damaging the grafted layers. Subsequently, the same process as described above was used to prepare the nanocomposites with PS grafted CN_x MWNTs.

Details of the solvent sonication time and evaporation temperatures used are contained in Table 2.

Filler	Matriz	Solvent	Prior nanotube sonication time	Evaporation temperature
CNx MWNT	PS	Toluene	30 min	110°C
CNx MWNT	SBS	Cyclohexane	30 min	80°C
PS-CNx MWNT	PS	Toluene	none	110°C
PS-CNx MWNT	SBS	cyclohexane/toluene	none	80°C

Table 3: Synthesis conditions for preparing composites with PS or PSBS.

Films of about 0.6 mm to 0.8 mm thickness were obtained by pressing the solvent-free nanocomposites for 15 minutes over their glassy temperatures, i.e: 150°C for the PS matrix, and 85°C for the SBS matrix.

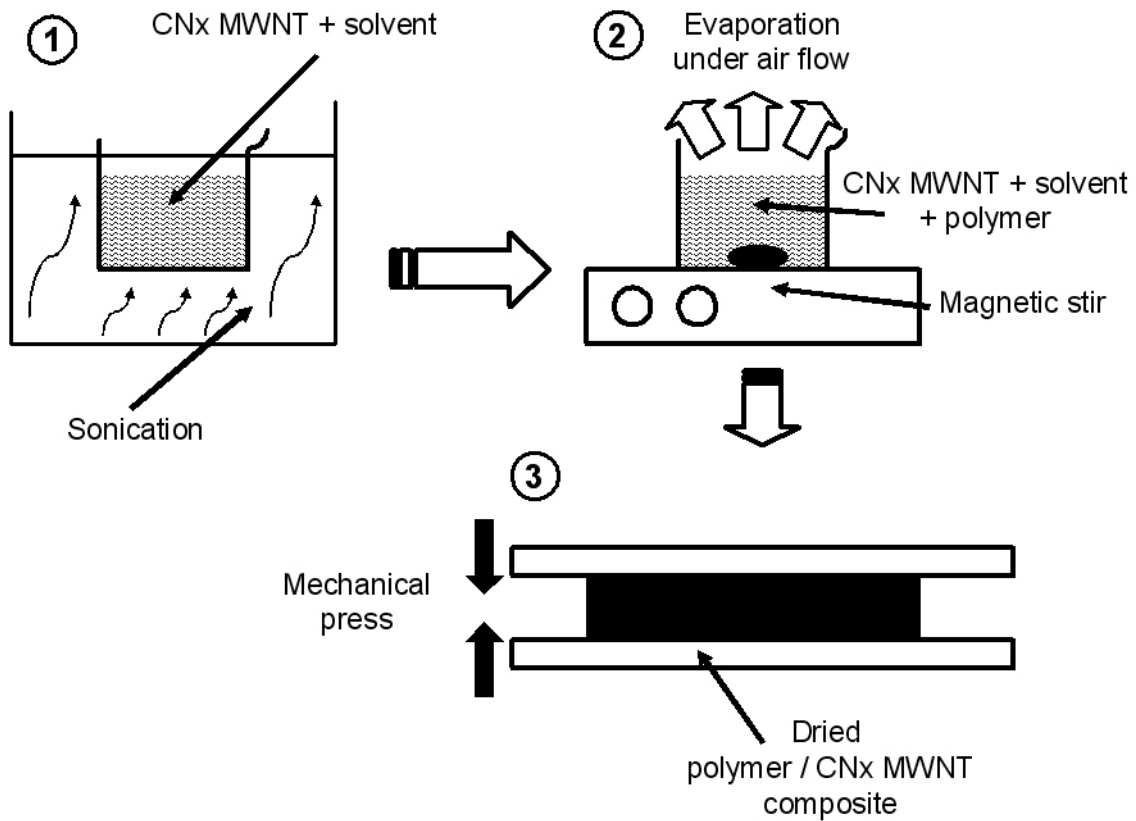


Figure 45: Polymer / CNx MWNT composite synthesis process

C.2 Electronic microscopy characterization

C.2.1 Transmission Electronic Microscopy (TEM)

A droplet of the polystyrene grafted CNx-MWNTs suspension was deposited on a microscopy copper grid (300-mesh) covered with a holey carbon film. HRTEM observations were carried out on nanotubes that were passing over the holes of the carbon film. For these observations we used a JEOL 2010F microscope, equipped with a Field Emission Gun, and operating at 200 kV. Micrographs were acquired with a Gatan Slow Scan CCD camera.

C.2.2 Scanning Electronic Microscopy (SEM)

The produced nanocomposites were fractured at room temperature. The fracture surfaces were observed without any metal coating with a field emission SEM (model FEI XL30) under high vacuum. The accelerating voltage was set to 800 V. Secondary electrons were used to form the images.

C.3 Differential Scanning Calorimetry (DSC)

As shown in Figure 46, the differential scanning calorimeter consists of two sealed pans: a sample pan and a reference pan. During the experiment, the instrument detects differences in the heat flow between the sample and the reference. This information is treated and results in a plot of the differential heat flow between the reference and sample cell as a function of the temperature. When there is no thermodynamic physical or chemical process during measurement the heat flow should slightly increase or decrease: the baseline. An exothermic or endothermic process within the sample results in a deviation in the difference between the two heat flows. Glass transitions may occur as the temperature of an amorphous solid is increased. These transitions appear as a step in the baseline of the recorded DSC signal. This is due to the sample undergoing a change in heat capacity; no formal phase change occurs. To ensure that the sample is all the time at the quasi-thermodynamic equilibrium we have to use a very low temperature ramp rate. In this work the temperature

ramp rate was chosen about $1^{\circ}\text{C}\cdot\text{min}^{-1}$. The sample pans were aluminium pans. All the experiments were run under a nitrogen flow ($60\text{ mL}\cdot\text{min}^{-1}$)

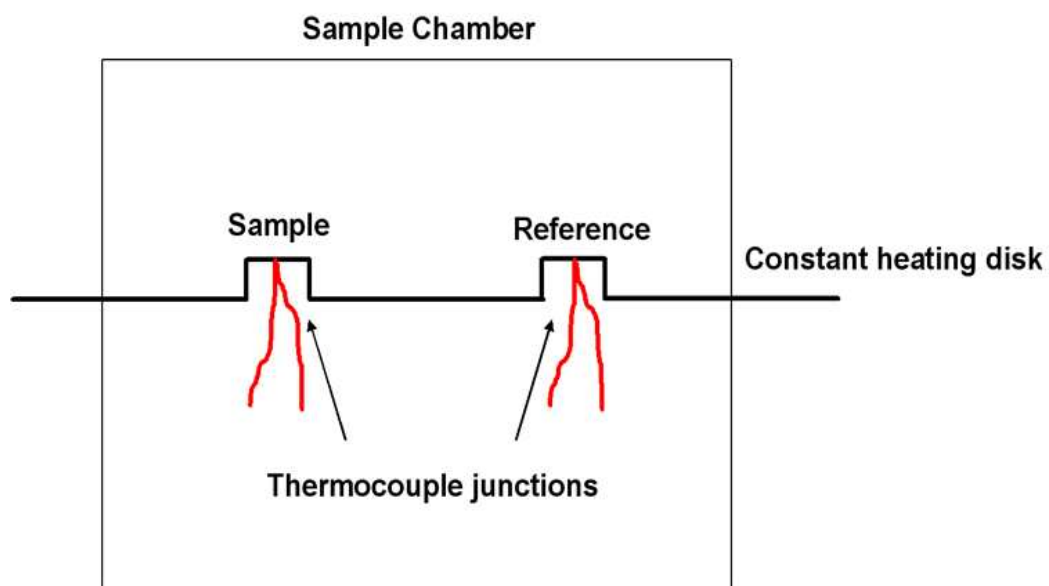


Figure 46: Experimental scheme of DSC device

Part D Electrical and mechanical analysis tools

D.1 Dielectric measurements

The complex conductivity measurement consists in applying an alternative tension to the sample:

$$U = U_0 \sin(\omega t)$$

and measuring the resulting intensity. This intensity is shifted in phase (angle ϕ) with the tension:

$$I = I_0 \sin(\omega t + \phi)$$

The electric field used is weak, thus ensuring the proportionality between polarization and conductivity. The conductivity is deduced by calculating the I^*/U^* ratio and expressing it as: $\sigma^* = \sigma' + i\sigma''$. The real and imaginary part of the complex conductivity can be calculated using the following mathematical expressions:

$$\sigma' = |\sigma^*| \cos \phi \quad \text{and} \quad \sigma'' = |\sigma^*| \sin \phi$$

Finally, the phase shift between the real and the imaginary part of the complex conductivity ($\tan \phi$) represents the energy loss in the material caused by Joule effects.

- **Dielectric measurements**

All AC measurements were performed with a solartron 1226 bridge. The frequency analysis ranged from 10 mHz to 1 MHz, and the AC voltage amplitude was set to 1 V. Before measurements, the nanocomposite extremities were coated with a silver paint in order to ensure a good electrical contact between the electrode and the nanocomposite.

D.2 Dynamic Mechanical Analysis

Dynamic Mechanical Analysis (DMA), also known as Dynamic Mechanical Spectroscopy, is a useful tool that permits the determination of the viscoelastic properties of the material. The test consists in applying a sine wave mechanical force to the sample in the linear domain (elastic or viscoelastic domain), and in measuring the response of the system versus temperature (isochronal measurements) or versus frequency (isothermal measurements).

The sine wave force can be described either by its strain or by its stress

$$\begin{aligned}\sigma_a^* &= \sigma_0 e^{(i\omega t)} \\ \varepsilon_a^* &= \varepsilon_0 e^{(i\omega t)}\end{aligned}$$

The response of the sample to this mechanical force is out of phase with an angle δ :

$$\begin{aligned}\sigma_r^* &= \sigma_0 e^{(i\omega t - \delta)} \\ \varepsilon_r^* &= \varepsilon_0 e^{(i\omega t - \delta)}\end{aligned}$$

Then, the complex modulus (shear modulus in our experiments) can be deduced:

$$\begin{aligned}G^* &= G' + iG'' \\ \text{where} \\ G' &= \frac{\sigma_0}{\varepsilon_0} \cos(\delta) \\ \text{and} \\ G'' &= \frac{\sigma_0}{\varepsilon_0} \sin(\delta)\end{aligned}$$

Tan (δ) is a very useful parameter often called “internal friction coefficient”, that represents the energy dissipated as heat during an excitation cycle. Variations of G^* or $\tan(\delta)$ against temperature (as well as against frequency) are representative of various relaxation phenomena. In polymeric materials, the α relaxation (or main relaxation) is representative of long distance motions of the macromolecular chains. When the experiment is performed in the isochronal mode and measured at 1Hz, it is generally considered that the G'' peak temperature (T_α) is close to the glass transition. However, T_α also depends on

the mechanical coupling between the matrix and the filler. It is thus preferable to determine the glass transition temperature by differential scanning calorimetry.

The equipment we used is a home made device built at the GEMPPM (France) and commercially available (Metravib SA). A schematic representation of the apparatus is given in Figure 1. A magnet between two Helmholtz coils where an alternative current is injected creates the shear stress. The torque is transmitted to the sample by a metallic hard stick. The material strain is detected by a reflected laser diode and transmitted to the computer interface for calculation. The particularity of this device is its ability to measure the complex mechanical modulus with a very high accuracy, and the sample thickness section dimensions can range from 100 μm to few mm. All the measurements were carried out at 1Hz, using a heating rate of 3 K/min.

Description of the equipment:

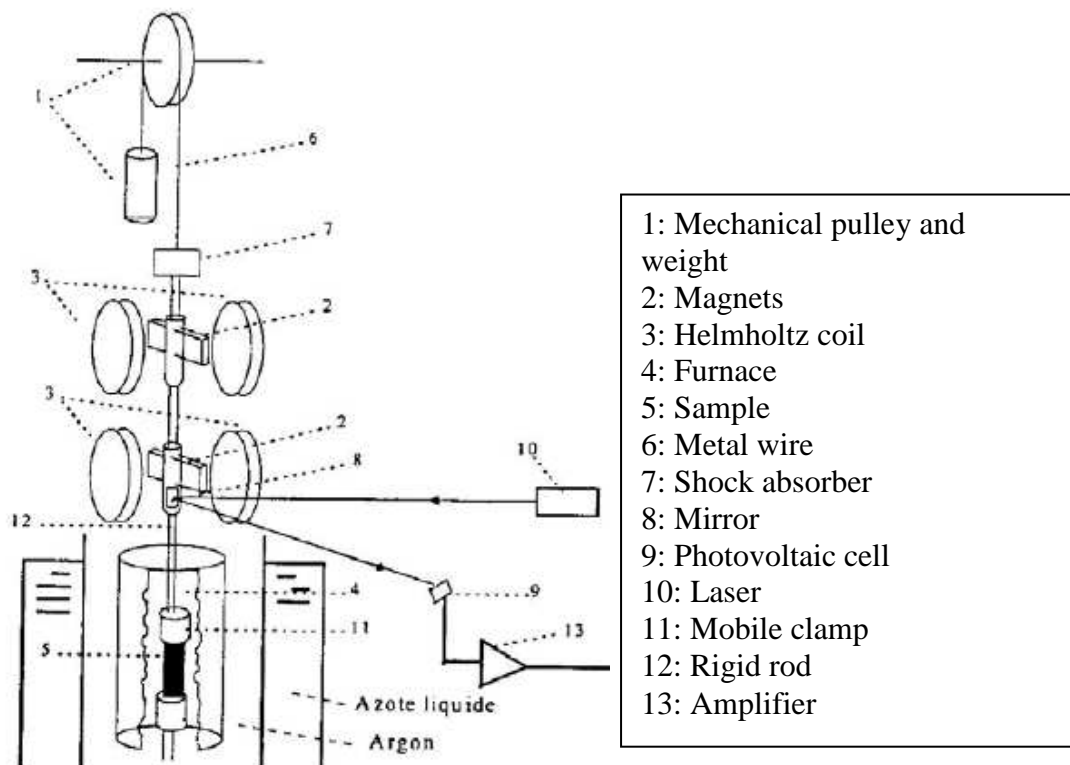


Figure 47: Skeme of the Shear Dynamic Mechanical Analysis device used.

D.3 Tensile tests

Tensile tests were performed at room temperature, on a MTS 1/ME tensile test device. The equipment permits to measure the force induced by the machine on the sample with a constant strain rate. The strain rate was about 0.4 s^{-1} for the PSBS matrix. The samples used were of barbell type, with $L = 9.60 \text{ mm}$, $l = 3.00 \text{ mm}$, $0.50 \text{ mm} < e < 0.75 \text{ mm}$. For all the samples the tensile tests were carried out five times. The extremities of each sample were glued to the grips in order to avoid any sliding what would create measurement errors.

These data permit to calculate the stress in the sample against strain. Nominal stress and nominal strain can be defined by the following expressions:

$$\sigma = \frac{F}{S_0}$$
$$\varepsilon = \frac{\Delta L}{L_0}$$

Where S_0 and L_0 represent the initial section and the initial length of the sample, ΔL and F correspond to the measured length and force at a given time respectively.

The true stress and true strain take into account the evolution of the section dimensions during the tensile test, and can be defined as:

$$\sigma = \frac{F}{S}$$
$$d\varepsilon = \frac{dL}{L}$$

D.4 Compression tests:

Some polymers like PS have a highly brittle mechanical behavior. If this kind of material is studied by tensile test, a rapid break of the sample would prohibit the analysis of its mechanical behavior under large stress conditions (plastic behavior). On the contrary, compression tensile test is known to allow higher deformations than tensile tests.

The compression tests were performed using an INSTRON standard mechanical testing machine equipped with parallel plateaus. The samples we used consisted of cylinders with a diameter of 4.5 mm and a length of 8 mm. The diameter/length ratio allows us to eliminate undesirable deformations such as the “flambage”. Furthermore, in order to restrain “tonneau” deformation mechanism, the contact surfaces of the sample were polished and lubricated with molybdenum disulphide (MoS_2).

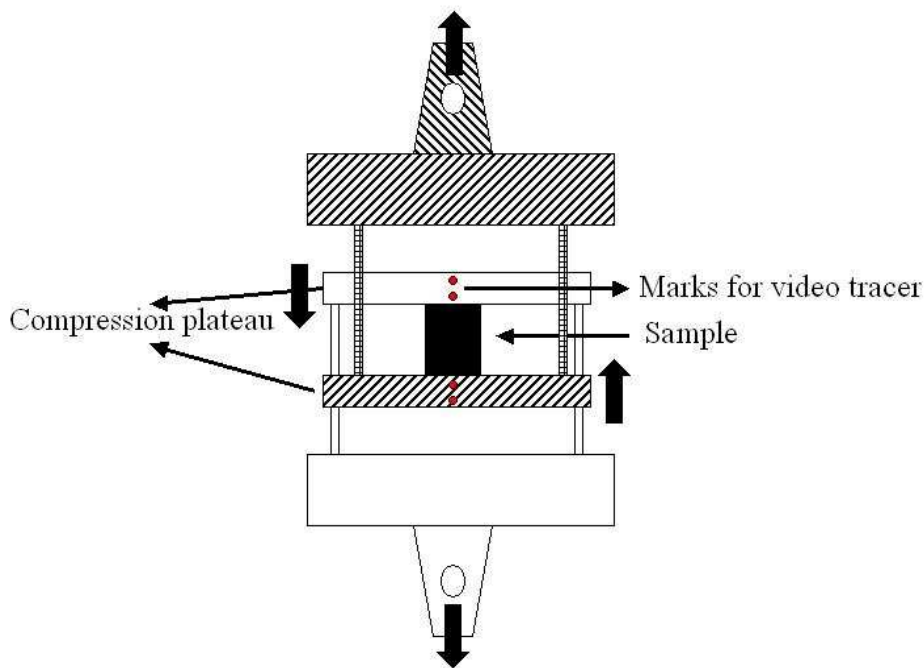


Figure 48: Compression tensile test device used in this work.

To ensure an accurate measurement of the stress, we used a video device which is able to follow the deformation of the samples because reference marks were etched previous to experiment (Figure 48). A first step for measuring the stress consists of determining the distance between the marks when the compression plateaus are in contact (zero reference). Then a simple calculation using the data collected during the experiment permits an accurate measurement of the nominal stress. Finally, we found that the strain rate was about 10^{-4} s^{-1} for the PS matrix.

Chapter IV

Experimental results and discussions

Part A Efficient coating of N-doped carbon Nanotubes with PS using Atomic Transfer Radical Polymerization (ATRP).

Soon after the identification of the carbon nanotubes [1], various researchers focused their efforts on the nanotube synthesis and their applications. Nanotubes (single- and multi-walled) possess fascinating physico-chemical properties [41, 45, 180]. In particular, the surface of multi-walled carbon nanotubes (MWNTs), which usually exhibit large diameters (e.g. 10-50 nm), is similar to that of neutral graphite (planar). An additional and inherent characteristic of nanotubes (single- and multi-walled) is that they tend to form aggregates when dispersed in an aqueous medium due to the presence of van der Waals interactions. This phenomenon is not desired when fabricating polymer composites containing carbon nanotubes because the tube dispersion is not homogenous within the matrix. Therefore, in order to modify the inert surface of MWNTs, making them chemically reactive, nanotube functionalization is required [66, 181]. This process modifies the surface of the carbon nanotubes and makes them prone to a selective dispersion in a particular medium. The literature related to modified or functionalized carbon nanotubes is abundant [58, 60]. For example non-covalent modifications [61] (i.e. physical adsorption) have shown to alter their electronic and surface properties. It has also been demonstrated that when carboxylic groups are chemically bonded to the nanotube surface (tube ends or tube waist), these groups promote a uniform dispersion in a polar solvent [182] that could be then used to fabricate composites. Alternatively, non-ionic surfactants could be employed in the production of carbon-nanotubes/polymer composites [63, 183]. Here, the introduction of 1 wt % of carbon nanotubes in a polymeric matrix has

proved to have significant effects on the glass transition temperature and the mechanical characteristics of the material [63, 183]. Unfortunately, the presence of non-ionic surfactants around the nanotube does not maximize the interaction between the nanotubes and the polymer matrix. One way of maximizing this interaction when fabricating a nanocomposite, consists of grafting covalently polymer chains on the outer surface of CNTs [91, 184]. In this context, a recent and novel approach, known as Atomic Transfer Radical Polymerization (ATRP) has been reported [97]. This redox process is thus able to grow polymer chains from solid surfaces. In this process, the initiator is a halogenated organic molecule (with Br or Cl) that allows the synthesis of polymers via an open-close mechanism. Recently, Peng Liu [57] reviewed “grafted from” processes used in nanotube polymer grafting. ATRP has been recently used for modifying the surfaces of SWNTs or *pure carbon* MWNTs [93, 185-187]. Different kinds of monomers were involved in these polymerization reactions: Methyl Methacrylate, n Butyl Methacrylate, Styrene and ter Butyl Acrylate. One advantage of such polymerizations consists in controlling the relative size and architecture of the synthesized polymer (e.g. block copolymer, alternate copolymer, random copolymer). The grafting of polystyrene by ATRP on CN_x MWNTs external layer is a new investigation area. Indeed, few papers report the grafting of polymer by free radical controlled process. Furthermore, most of them reported in-situ polymerization SWNTs (since they appear to be more chemically reactive).

In this chapter, we describe a controlled free radical synthesis route that is able to functionalize CN_x MWNTs. These functionalized tubes could then be used to grow uniformly PS chains on their surface using ATRP reactions. We used CN_x MWNTs because they exhibit an intrinsic bamboo-like structure. Such stacked-cone morphologies are expected to provide enhanced mechanical properties if embedded in polymers, due to the absence of pull-out telescopic effects observed when stretching the composites; the telescopic effect is a common drawback experienced by co-axial MWNTs (undoped). Moreover, we believe that the presence of nitrogenated defects in the graphitic structure of CN_x MWNTs promotes the stabilization of free radicals on the nanotube surface, and therefore could improve the efficiency of the ATRP reaction. Unlike conventional functionalization techniques, our chemical route does not require any acid

treatment, and the tubes are subjected to a process in which the surface is first modified with organic molecules containing aromatic rings. Subsequently, each of these aromatic rings is modified by the substitution of a "hydrogen atom" by Br. The resulting material is then used as a macroinitiator in styrene living polymerization via ATRP.

Many techniques were used to analyze different chemical synthesis steps. The first two steps, which consist in the grafting of an ATRP macro initiator on the CN_x MWNT surface, were quantified and confirmed by Fourier Transformed Infra Red (FTIR) spectroscopy, Thermo Gravimetric Analysis (TGA), coupled gas chromatography / mass spectrometry (GC/MS) and Raman Spectroscopy. These techniques permit to confirm that the ATRP initiator was covalently bonded to the CN_x MWNT external layers. Electron Spin Resonance (ESR) was used to confirm the ability of the ATRP initiator to generate controlled free radicals that allowed us to control the addition of monomer by free radical propagation (polymerization). Finally, the grafted nanotubes, were observed by High Resolution Transmission Electron Microscopy (HRTEM) which confirmed the presence of an amorphous polymer coating on the external layer of CN_x MWNTs. Complementary information was obtained by Electron Energy Loss Spectroscopy (EELS), and EDS in order to confirm that the amorphous layer observed consist of polystyrene polymerized by in-situ ATRP process.

A.1 Phenyl grafted nanotubes and ATRP macroinitiator grafted nanotubes

The literature supplies numerous examples of addition reactions on nanotube surfaces [60]. One of those processes concerns the free radical addition. Ying et al. reported the grafting of aromatic rings on the side walls of SWNTs [178]. In the present chapter, we carried out a kindred reaction onto CN_x MWNTs and verified that conjugated π carbon double bonds and various defects could react efficiently with free radicals in order to graft aromatic rings. The theoretical reaction process is described in Figure 49. At 105°C, benzoic peroxide decomposes into free radicals. These free radicals open the conjugated π carbon double bond, and could also react with defective sites within the CN_x MWNTs surface in order to stabilize them on the side walls of CN_x MWNTs. The second step of the chemical surface modification consists in substituting a proton from the aromatic ring by a Br atom. This process was accomplished by reacting phenyl grafted CN_x MWNT with molecular Bromine at 55 °C in the presence of $FeBr_3$. The brominated phenyl molecules can then act as macroinitiators for the ATRP polymerization in the presence of a complex catalyst-ligand ($CuBr(I)$ -dnBpy in this case), and styrene at 110°C [97].

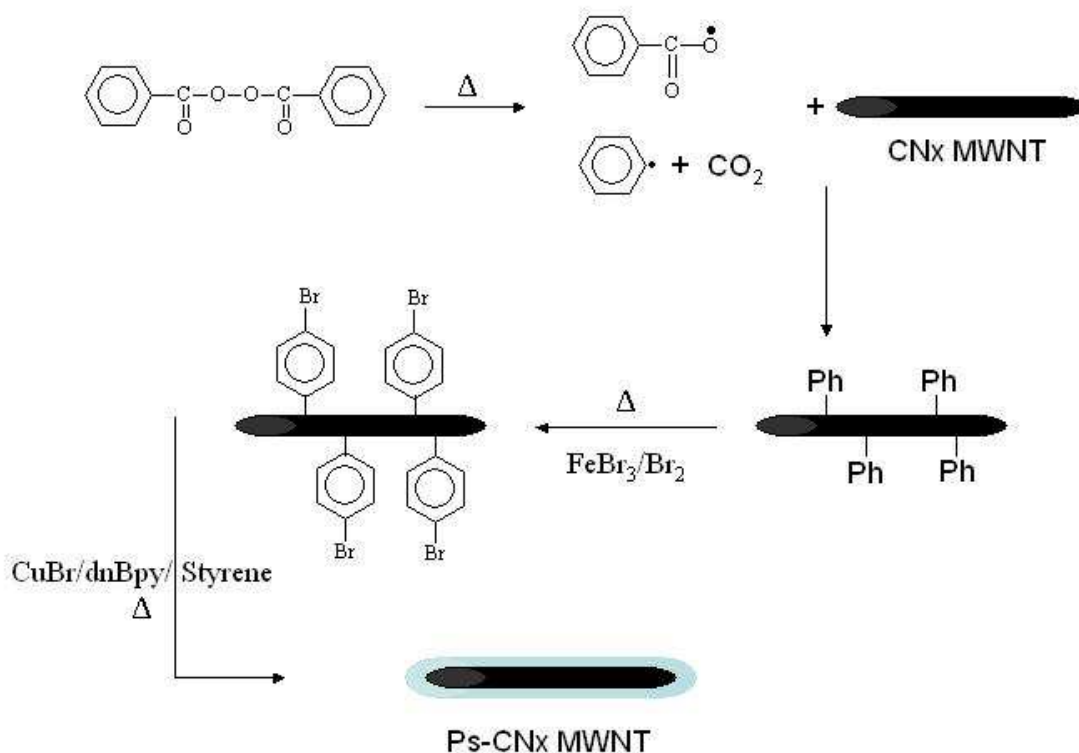


Figure 49: Theoretical schematic diagram showing the different stages of the functionalization process of CN_x MWNTs. First the grafting of aromatic rings takes place, subsequently the bromination of such rings occurs. These brominated molecules then act as macroinitiators during the ATRP reaction of PS.

A.1.1 Identification of the phenyl grafted molecules

The phenyl grafted CN_x MWNTs were analyzed by FTIR and the spectrum compared with that of as-produced CN_x MWNTs. The FTIR spectra are depicted in Figure 50. The spectrum corresponding to as-produced CN_x MWNTs (Figure 50), shows bands between 1400 - 1800 cm⁻¹ that arise from the contributions of the ambient gas (noise), and a wide shoulder located between 800 cm⁻¹ and 1200 cm⁻¹ could be attributed to the “graphitic” structure of the nanotubes. The signal is very weak and does not allow us to observe substituted nitrogen elements present within the graphene layers [45]. However, after the reaction with BPO, the spectrum of the nanotubes is clearly different. This indicates that the external layers of CN_x MWNTs were modified. The band located at 1730 cm⁻¹ is usually associated with the stretching of C=O bonds. The band at 1270 cm⁻¹ can be assigned to the stretching of C-O covalent bonds. The association of these two bands implies that ester groups are present in the functionalized material. The upshift witnessed for the

$C-O$ stretching band could indicate that these ester groups are linked to aromatic rings. Finally, the presence of aromatic rings (phenyl groups) is confirmed by the weak signal placed at 735 cm^{-1} , representing the resonance of 5 adjacent hydrogen atoms. Therefore, it is possible to conclude that these aromatics groups are chemically attached to the CN_x MWNTs after reaction with BPO.

In addition, tertiary amine groups linked to two radicals R, and a phenyl group is characterized by the presence of a band at 1376 cm^{-1} . Phenylic tertiary amines could arise from pyridinic nitrogen sites, which are chemically reactive. In addition, the band at 1457 cm^{-1} is representative of the $C-H$ covalent bond stretching. This signal indicates that the external layer of the CN_x MWNT could be distorted due to the sonication process used prior to the reactions.

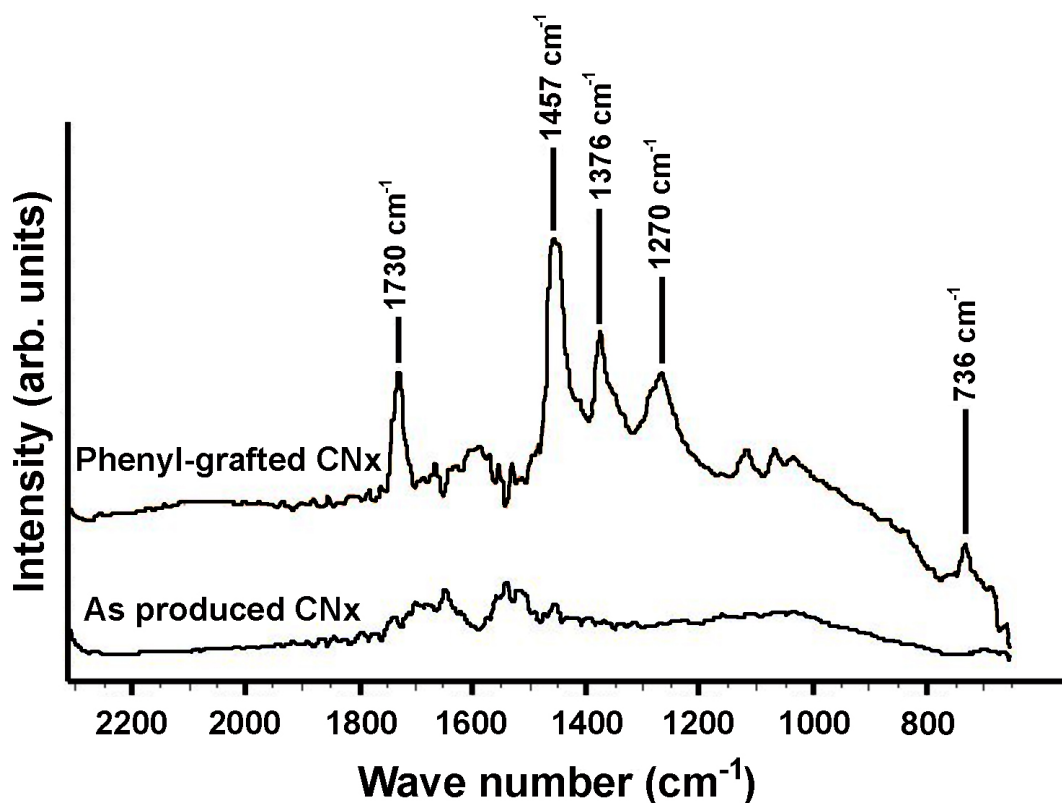


Figure 50: FTIR spectra of: As-produced CN_x nanotubes, and phenyl grafted CN_x MWNTs.

A.1.2 Proof of the grafting by Raman spectroscopy

We reported before that Raman spectroscopy is a very powerful test that allowed the measurement of the graphitic level of nanotubes. It is reported [188, 189] that the existence of the graphitic peak, G-line, located at 1590 cm^{-1} . The

G-line peak is generally decomposed in three peaks G(+), G(-1), G(-2)), which could represent the level of graphitization of the carbon nanotubes. On the other hand it exists an additional peak, namely D-line, centered at 1390 cm^{-1} that represent the disorder in the graphitic structure. It was reported, that the side wall functionalization of CN_x MWNT tend to transform sp^2 carbon-carbon bond into sp^3 . As a consequence, the modification of the external layer of CN_x MWNT might be observed by the relative increase of the D-line against the G-line. Annex I shows the results we obtained for as produced CN_x MWNT and BPO chemically reacted CN_x MWNT. Spectra were normalized and fitted by three gaussian curves: G-line centered at 1590 cm^{-1} , D-line at 1390 cm^{-1} and finally amorphous carbon broad peak ($1100\text{-}1500\text{ cm}^{-1}$).

The fitted-normalized spectrum of as produced CN_x MWNTs (annex I.a.), reveals the presence of a peak at 1590 cm^{-1} (graphitic G-line), representing a high graphitization level of the material. Nevertheless the presence of the D-line at 1360 cm^{-1} means that the nitrogen doping of CN_x MWNTs induce disorder in the hexagonal carbon lattice. Similar results were obtained for aromatic rings grafted CN_x MWNTs (annex I.b.) Nevertheless the fitted curve data demonstrate a relative increase of the D band for BPO CN_x MWNTs. The ratios between areas of D-line and G-line are respectively 0.43 for as produced CN_x MWNT, and 0.475 for aromatic rings grafted CN_x MWNTs. All results are summarized in Table 4. These results imply that Benzoic free radicals chemically react with CN_x MWNTs.

	Peak	center gravity (cm-1)	Peak area (%)
<i>As produced CN_x MWNT</i>	D-line	1354	9.32
	G-line	1590	21.62
	amorphous carbon	1401	69
<i>BPO-CN_x MWNT</i>	D-line	1353	11.43
	G-line	1587	24.08
	amorphous carbon	1404.5	64.48

Table 4: Raman Spectroscopy data obtained from CN_x MWNTs and BPO- CN_x MWNTs.

We could point out that the weight of the amorphous peak is lower for BPO-CN_x MWNTs. We think that sonication, and filtering process during functionalization should influence the loss of amorphous carbon. Indeed, sonication should blastoff some amorphous carbon layer present on the external cap of CN_x MWNTs. This observation led us to sonicate as produced nanotubes before reacting with BPO or before being introduced in the polymer matrix.

A.1.3 Quantification of the grafting (TGA)

Thermogravimetric analyses (TGA) of the products, from the different stages of the reaction, are shown in Figure 51. It is clear that as-produced CN_x MWNTs exhibit a good stability at high temperatures, i.e. up to 650°C. They do not lose weight, so they are not destroyed while heating under nitrogen. However, BPO-reacted CN_x MWNTs have a different thermal behavior. At around 200°C, there is an initial loss of weight that continues until the temperature reaches 425°C; the weight mainly loss is about 6 % of the sample's total weight. The weight loss occurs around 350°C (4% of the total weight loss). This loss could be attributed to the release of phenyl groups. TGA experiments on BPO-reacted CN_x MWNTs are in agreement with FTIR analyses because the weight loss observed for the phenyl grafted nanotubes appears to be a combination of grafted side wall aromatic rings, and the distorted fragments of the external tube layers produced after functionalization (2% of the weight loss). CN_x MWNTs containing grafted brominated aromatic rings (CN_x MWNTs-BPO-Br), undergo a slightly larger weight loss when compared to those that are simply grafted with BPO (CN_x MWNTs-BPO). The maximum weight loss is about 8 % of the total weight, thus the molecules released could have a higher molecular weight. It can be therefore concluded that the bromination of aromatic rings was efficient. This 2% increase of the weight loss is then attributed to the Br substitution. Finally, after polymerization (CN_x MWNTs-PS), the weight loss indicates that the amount of PS grafted on the nanotubes side walls is about 40% of the total mass.

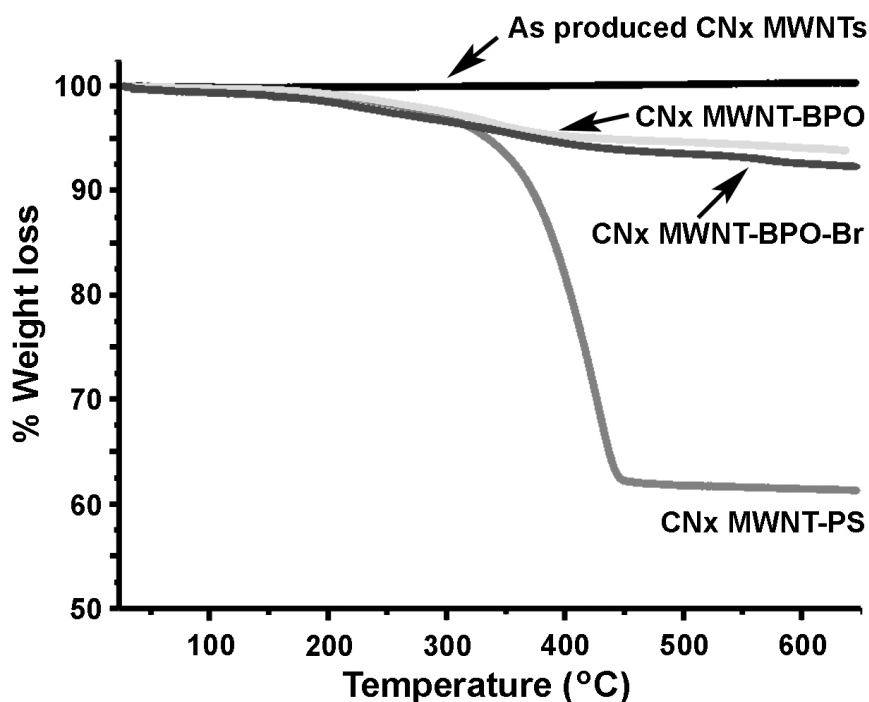


Figure 51: TGA plots for different types of modified CN_x nanotubes, carried out under a N₂ atmosphere.

A.1.4 Coupled gas chromatography / mass spectrometer

The analyses of the composition of the gases released during TGA experiments were carried out using a couple gas chromatograph/mass spectrometer. The results obtained are presented in Table 5. The table shows the chemical composition of the released gases during heating. TGA experiments revealed that grafted chemical functionalities are released above 300 °C.

The schematic diagram shown in Figure 49, shows the way aromatic rings are anchored to the nanotube surface, and this scheme could be confirmed in our mass spectrometry experiments. For example, molecules containing aromatic rings (Benzoic acid, Benzaldehyde and Toluene Benzene) comprise about 60% (mol.) of the gas released. Most of these grafted molecules originate from the reaction between CN_x MWNTs and BPO. The presence of CO₂ is attributed to the fragmentation of benzoic acid during pyrolysis. Benzantracene, biphenyl, naphthalene and other molecules may arise from fragments detached from the carbon nanotube skeleton. The latter molecules represent about 30% (mol.) of the total weight loss observed. Similar results (not shown here) were obtained

on brominated phenyl grafted nanotubes (CN_x MWNTs-BPO-Br). The presence of bromated aromatic rings, about 30% (mol.) of the pyrolyzed gas, ensures that the generation of ATRP macroinitiators on the nanotube side walls was successfully achieved. We also find amine molecules in the residues (<1-2%) that could be related to nitrogenated sites within the functionalized CN_x tubes; this value is consistent with the N content of as-produced CN_x MWNTs (ca. 2 % at.).

Molecules detected	% mol.
CO ₂	9.3
Benzoic acid	34.4
Benzaldehyde	3.2
Toluene Benzene	23.9
Naphtalene	1.6
Biphenyl	5
Benzantracene	7.3

Table 5: Molecules detected by mass spectrometry during the pyrolysis of BPO modified CN_x MWNTs (CN_x MWNTs-BPO).

A.1.5 Operating grafted ATRP macroinitiator: Electron spin resonance (ESR)

Literature [97] reported the trace of ATRP reaction kinetics as a function of time. We mentioned that the catalyst (metal transition) is oxidized by the macroinitiator (halogenated organic molecule) in order to liberate a free radical. This free radical oscillates between its dormant state and active state, which allows to control the radical polymer chain growth (Cf. Figure 15: General mechanism of ATRP process). ESR is able to detect unpaired electrons like free radicals and complex metal transition atoms. Thus, this technique permits to detect and measure the quantity of free radicals generated during the ATRP reaction as well as the quantity of oxidized free catalyst. Because both element concentrations are linked together by the equation described in Figure 15, ESR might help to find the efficiency of the CN_x MWNT macroinitiator we

synthesized. In this study, the use of ESR confirmed the capacity of CN_x MWNT-BPO-Br system to initiate the ATRP reaction, and consequently obtain the ideal working temperature during polymerization.

ESR spectra are presented in Annex II. Spectrum A), shows the results obtained for pure oxidized catalyst: CuBr(II) at ambient temperature. We obtained a peak attributed to CuBr(II) for $g = 2.1426$, what will be used as reference. The catalyst in its oxidized state is ESR sensitive because of its unpaired electrons. It means that when the equilibrium reaction is highly displaced on the dormant species side, we should not observe any ESR signal. However, at specific temperatures the reaction might start and generates free radicals that will appear by the presence of the CuBr(II) peak. More over, we described before that ATRP reaction is a thermally activated livingness controlled free radical polymerization. As a consequence, the system should initiate and inhibit polymerization several times, meaning that the polymerization reaction is controlled. Spectrum B in annex II shows the experimental results we obtained at 120°C . We observed a peak for $g = 2.1953$ what is representative of CuBr(II). Finally, spectrum C of the annex II, which is the system at ambient temperature, confirmed the absence of CuBr(II), implying that the redox process is reversible and the system returns-back to equilibrium.

ESR experiments were very useful to confirm that the CN_x MWNT ATRP macroinitiator was able to generate controlled free radicals and as consequence in-situ Polystyrene chains. Nevertheless, the experimental protocol did not allow us to make more accurate measurements, for example about kinetics, macroinitiator turnout, etc... The first point was that the ebullition temperature of the solvent (toluene) is about 120°C , meaning that while running the experiments, the concentration of the reactant was changing as well as the reaction kinetics. Consequently, we could not observe equilibrium polymerization states that permit the kinetic calculation. More over, when CN_x MWNTs are not polymer grafted, the tubes tend to aggregate (not homogeneous). Finally, because the experiment tube is not sealed, we would have expected that for long time measurements, the catalyst would have been oxidized and the polymerization would have been inhibited.

A.2 Polystyrene grafted CN_x MWNTs

A.2.1 HRTEM of Polystyrene grafted CN_x MWNTs

Figure 52 depicts HRTEM micrographs of as-produced CN_x MWNT (a), and PS-grafted CN_x MWNT (b-d). Figure 52a. shows the external layers of a typical CN_x MWNT without any treatment. We observed that the CN_x MWNTs exhibit external diameters ranging between 20 and 50 nm. We also notices that the surface of the as produced CN_x nanotubes is composed of a well graphitized layer (no amorphous carbon layer coating the nanotubes). In contrast, after the ATRP reaction, the CN_x MWNTs exhibit an amorphous layer (identified as PS from EELS; see below) that could be clearly seen (Figure 52 b-d).

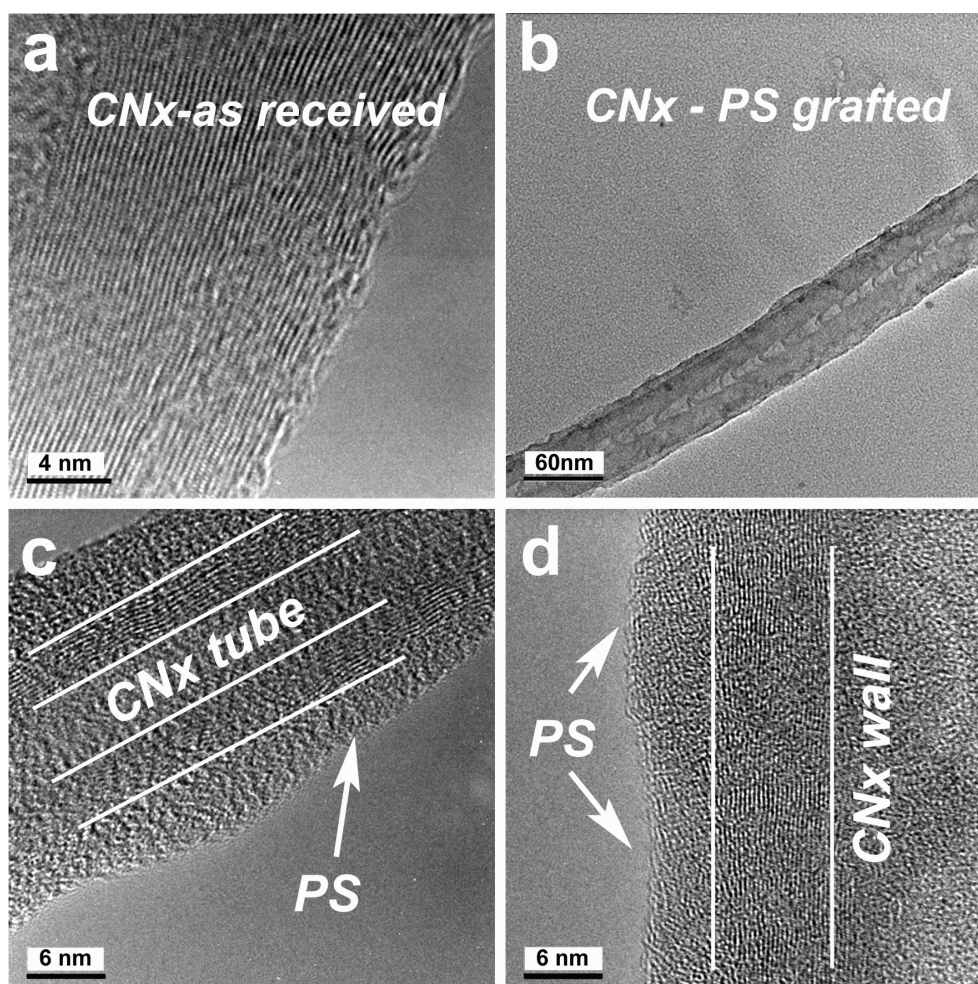


Figure 52: TEM micrographs of: a) as produced CN_x MWNT showing the external surface of the tube and the lack of amorphous carbon deposited around the outer layer; b) PS-grafted CN_x MWNT exhibiting a homogenous layer of PS coating the CN_x nanotubes; c-d) HRTEM micrographs of PS grafted CN_x MWNT showing the morphology of the amorphous layer and the “graphitic” walls of the tubes (shown by white lines); the PS coating is also indicated in figures (c) and (d).

Polymers synthesized by ATRP usually have very low polydispersity (<1.5), meaning that the polymer chains should exhibit similar lengths. The fact that the amorphous layer is relatively uniform on the surface of the tube (Figure 52 b.) leads us to conclude that the polymer chains efficiently grew from the nanotube surface. The average thickness of the PS amorphous layer was estimated to be about 3-5 nm. HRTEM images of the polymer/CN_x MWNT interface are shown in Figure 52 c-d. These images confirm that the graphitic-like walls of the CN_x-MWNTs were preserved after the ATRP polymerization process. It is noteworthy that both the external graphitic cylinders and the bamboo structure of CN_x MWNTs were not affected after polymerization.

A.2.2 EELS and EDS Analysis of the PS grafted layers

EELS analyses are able to efficiently distinguish different carbon/carbon bonds [179]. In Figure 53 a., low-loss EELS spectrum of as-produced CN_x MWNTs exhibits a peak located at 5.4 eV, which corresponds to the $\pi \rightarrow \pi^*$

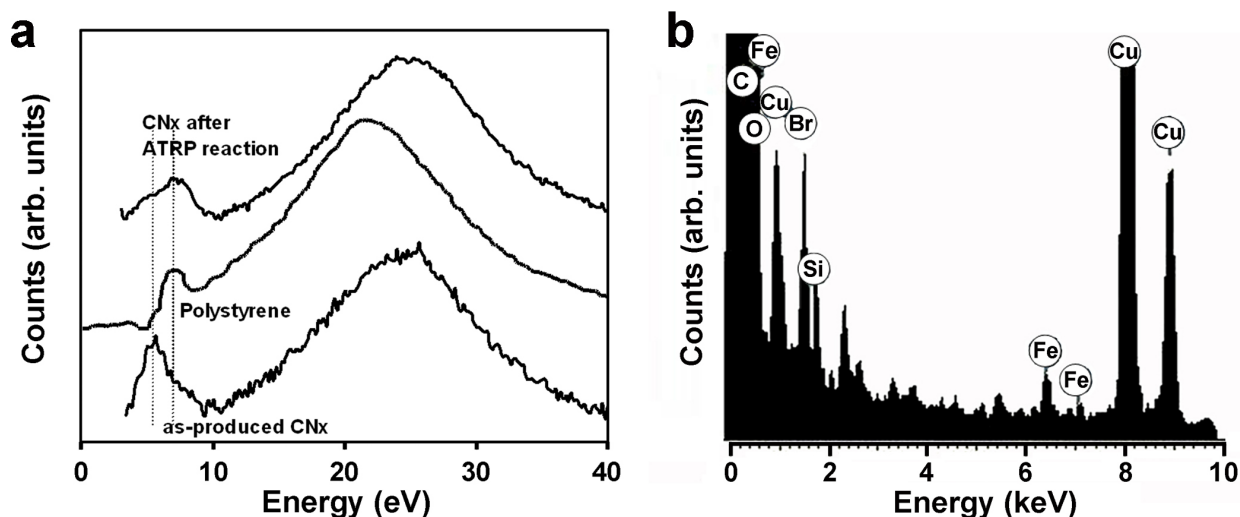


Figure 53: a) Low loss EELS spectra of as-received CN_x-MWNTs (top spectrum), the ATRP reacted CN_x MWNT (middle spectrum) and polystyrene (bottom spectrum); b) EDX spectrum of the tube ATRP reacted CN_x MWNT coated with PS (also shown in Fig. 4c). It is clear the presence of Br, which was attached to the phenyl groups prior to polymerization. Therefore, the ATRP reaction took place efficiently. Note that Cu signal comes from the TEM grid and the Si signal from the quartz tube where the tubes were produced.

transition in conjugated C=C bonds (e.g. graphitic-like structure of the CN_x-MWNTs). The spectrum of pure commercial PS exhibits a peak at 6.9 eV which correspond to the $\pi \rightarrow \pi^*$ transition of aromatic rings [179]. Interestingly, the EELS spectrum of PS-grafted nanotubes exhibits both peaks at 5.4 and 6.9 eV. It is thus confirmed that the amorphous layer coating the CN_x MWNT contains aromatic rings and is related to PS grown by in-situ ATRP polymerization.

Finally, Figure 53 b. represents an EDX spectrum showing the elements found in the same tube studied by EELS (see tube from Figure 53 c). Copper clearly comes from the microscopy grid and from the specimen holder. The presence of nitrogen arises from the CN_x MWNTs. Carbon and oxygen can also arise from the holey carbon film. Iron is present due to the catalyst used during the synthesis of the CN_x nanotubes. Silicon are impurities that may have come from the quartz tube used to prepare the CN_x material. Interestingly, a peak characteristic of bromine is observed. This is attributed to the Br atoms that are attached on all polymer chain ends that coat the CN_x MWNTs. This analysis confirms that the polymer layer was grown by the redox of ATRP. Thus, meaning that the ATRP open/close mechanism, responsible of growing polymer chains, is possible with the grafted macro-initiator that we synthesized.

A.3 Conclusion about Efficient coating of N-doped carbon Nanotubes with polystyrene using Atomic Transfer Radical Polymerization.

Our results demonstrate that it is possible to use a free radical reaction to chemically modify the CN_x MWNTs surface. An ATRP reaction was used to efficiently graft PS chains on CN_x -MWNTs by an in-situ reaction (“graft from” method). It is noteworthy that the tubes did not require any acid treatment prior to the functionalization or ATRP reaction. Although some minor degradation was found by FTIR and TGA during sonication, we confirmed by HRTEM that the main body of the nanotubes remained almost intact, and the tubes were homogeneously covered with an amorphous layer of PS (3-5 nm thick). Our ATRP approach is able to wet completely the surface of the doped nanotubes. We expect these grafted tubes to be efficient fillers for the fabrication of reinforced polymer, as the presence of grafted polystyrene should increase the polymer-nanotube interactions, thus ensuring an excellent load transfer.

Part B Morphology and interfacial adhesion of the CN_x MWNT / polymer nanocomposites

In order to observe the quality of the CN_x MWNTs dispersion in polymer matrices, Transmission Electron Microscopy (TEM) and Scanning Electron Microscopy (SEM) [124, 125] are commonly used. Moreover, SEM is a very useful tool to observe the fracture surfaces of the composites [124, 125, 137], thus permitting to obtain information related to the adhesion of the fillers within the matrix. Nevertheless, it is very difficult to quantify the dispersion from either TEM or SEM images. Other techniques, such as conductivity measurements should permit to obtain information related to the dispersion. Nevertheless, in chapter IV part C, we will show that the electric percolation threshold is highly dependent on the process used to fabricate composites, on the matrix morphology and on the tubes aspect ratio; consequently it is only able to provide a comparative evaluation of the dispersion. Finally, the observation of the sedimentation rate in glass vials is also used to estimate the stability of the dispersion in a solvent [60].

In this chapter, we will focus our discussion on the grafting effects on CN_x MWNTs dispersion. We will demonstrate that the adhesion of the nanotubes within the matrix is highly increased when the CN_x MWNTs are PS covalently grafted. Lastly, we will discuss about the influence of CN_x MWNTs on the structure of a di-block copolymer (Poly (butadiene-co-styrene)).

For the sake of simplicity, we will further refer to a-CN_x for as received CN_x MWNTs, and PS-g-CN_x for PS grafted CN_x MWNTs.

B.1 Dispersion of the CNx MWNTs in a polymer matrix

B.1.1 Dispersion of the CNx MWNTs in a polystyrene matrix

Unfortunately, there is no technique able to provide quantitative data on the nanotube dispersion in a polymer matrix. As a consequence, in order to study the effect of the polystyrene grafting on the nanotube dispersion and, we decided to perform a comparative (qualitative) description of the composites synthesized, using electron microscopy.

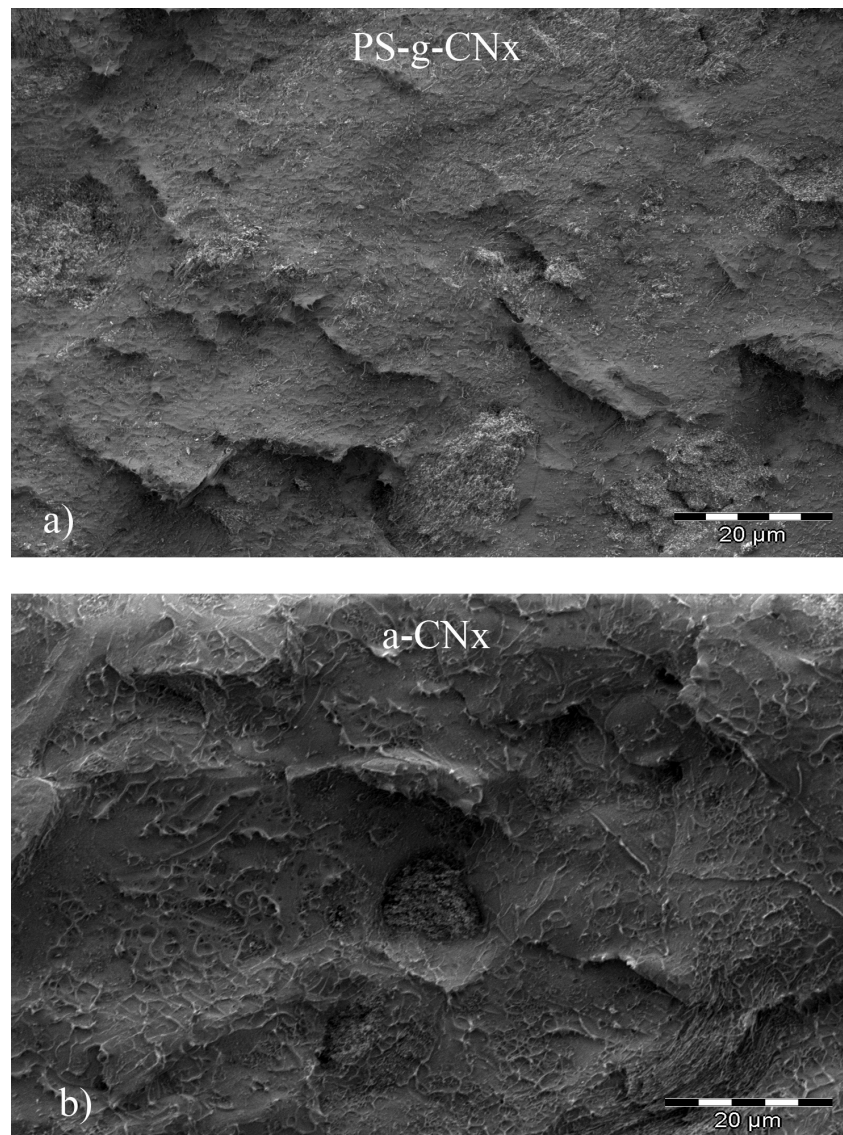


Figure 54: SEM photomicrographs at a low magnification of a) PS-g-CNx / polystyrene nanocomposites and, b) a-CNx / polystyrene nanocomposites.

Figure 54 represents SEM photomicrographs of the nanocomposites using a PS matrix using either a- CN_x or PS-g- CN_x . We observed these systems after fracture the material at ambient temperature. The low magnification permits a clear an overview of the samples.

In Figure 54a., we can observe the PS-g- CN_x / PS nanocomposites at 2.5 vol.% nanotubes (weight of carbon nanotubes without the PS layer). As compared to the a- CN_x / polystyrene at 2.5 vol. % (Figure 54b); the polystyrene grafting seems to lead to a better dispersion of the nanotubes within the PS matrix. Indeed, only small heterogeneities could be seen within PS-g- CN_x composites, whereas bigger agglomerates (about 10 microns) are observed with composites containing a- CN_x for example at the center of the Figure 54 b. Those agglomerates may be groups or bundles of CN_x MWNTs that were not separated by ultrasonication

Finally, it should be mentioned that there are aggregates in both composites, even with PS-g- CN_x MWNTs. Y. Wang et al. [163] reported that above 1 vol. % of randomly dispersed nanotubes, the nanotubes should saturate the matrix, and consequently start to form aggregates. This could explain the presence of small aggregates even in PS-g- CN_x / PS composites (C.f. Figure 54a.), although the dispersion seems quite homogenous.

B.1.2 Dispersion of CN_x MWNTs in a poly (butadiene-co-styrene) matrix.

Similar results are obtained when CN_x MWNTs are introduced in a PSBS matrix: the dispersion of PS-g- CN_x seems to be more homogeneous than that of a- CN_x (see Figure 55, obtained on nanocomposites after cryogenic fracture) This comparative description of the CN_x MWNTs dispersions in both polymeric matrices tends to confirm that grafting of PS on the carbon nanotube external layer lowers the cohesive forces (van der Waals, electrostatic forces) among carbon nanotubes. Therefore, it means that the solvent (as well as the polymer) increases its cohesive forces (lowering the interface energy) with the nanotubes, thus resulting in a better adhesion between the polymeric matrix and the carbon nanotubes.

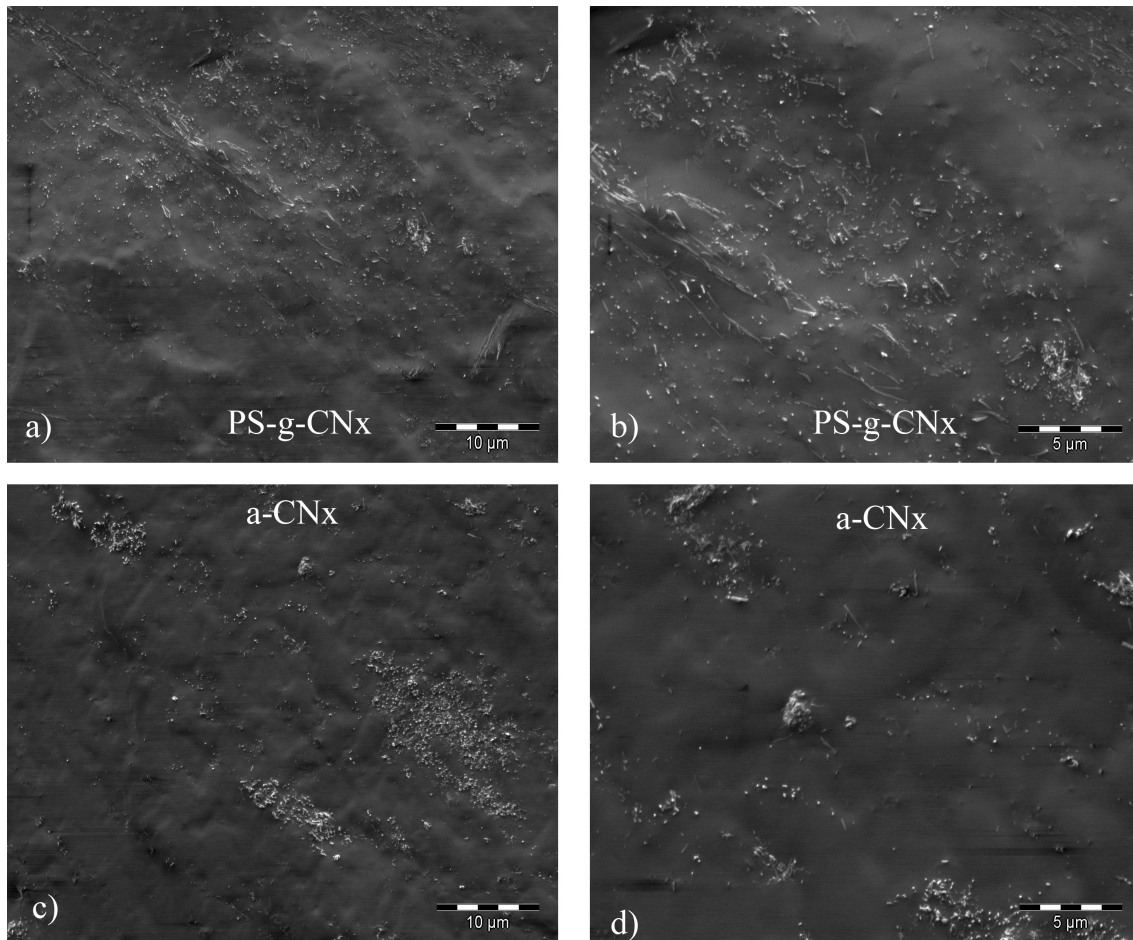


Figure 55: SEM photomicrographs of a) and b) PS-g-CN_x / PSBS nanocomposites; c) and d) a-CN_x / PSBS nanocomposites after cryogenic fracture.

Nevertheless, we should mention that the density of carbon nanotube is twice more important than the density of the polymer solution. As a consequence, the polymer grafting may be a good way to enhance the dispersion of nanotubes, but it does not avoid the sedimentation of the carbon nanotubes due to gravity. Thus, it is necessary to maintain vigorous stirring during the composite fabrication process in order to avoid sedimentation of the nanotubes.

B.1.3 Polymer / CN_x MWNTs interfacial adhesion

As mentioned above, the grafting of polystyrene on the external layer of CN_x MWNTs seems to increase the cohesive forces between the nanotubes and the matrix. It is expected that the increase of the cohesive forces between the matrix and the filler also results in a better interfacial adhesion. G.L. Hwang and co-workers found that the important cohesion forces between the matrix and the fillers result in an alignment of the carbon nanotubes in the strain direction

during a tensile test [138]. On the contrary, other authors who used untreated nanotubes reported that the fracture should propagate through the weak interface between the carbon nanotubes and the matrix [190]. In Figure 54, we observe a large view of the CNx MWNTs/PS nanocomposites. There we see that a-CN_x are parallel to the fracture and seem to have propagated the fracture, whenever PS-g-CN_x are perpendicular to the fracture and cut.

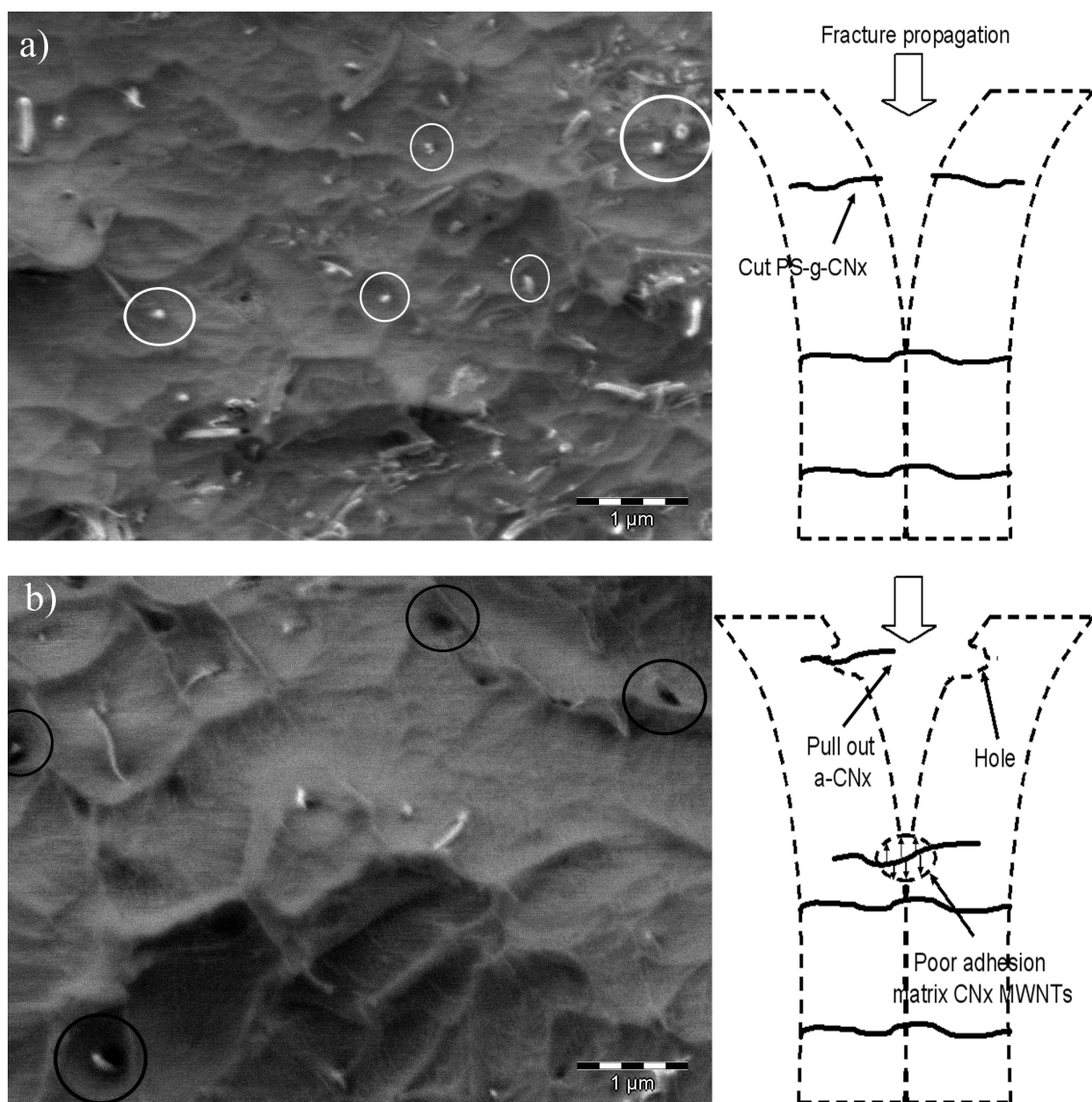


Figure 56: SEM micrographs of the CN_x MWNTs / PS nanocomposites after breaking at ambient temperature; a) PS-g-CN_x / PS nanocomposite with white circles indicating cut tubes, b) a-CN_x / PS nanocomposite. The black circles indicate holes or pulled out tubes. On the right side is represented the proposed mechanisms of fracture.

Figure 56 a) also depicts the fracture surface of the PS-g-CN_x / PS nanocomposites after breaking the composite at ambient temperature at higher

magnification. We can observe that the tubes were cut (see white circles) meaning that the adhesion at the PS-g-CN_x / PS interface is strong enough to propagate the fracture through the nanotube and not along the tubes. On the contrary in Figure 56 b) depicts the fracture surface of a-CN_x / PS nanocomposites. The black circles indicate the presence of pulled-out tubes and holes, what should be representative of a poor adhesion between a-CN_x and PS. Indeed, the black circle at the bottom of the photomicrograph indicates that the matrix released the stress during the fracture by nanotubes sliding. Finally, the holes are representative of the tubes that slide within the matrix (poor adhesion). Schemes representing the fracture mechanisms are represented in Figure 56.

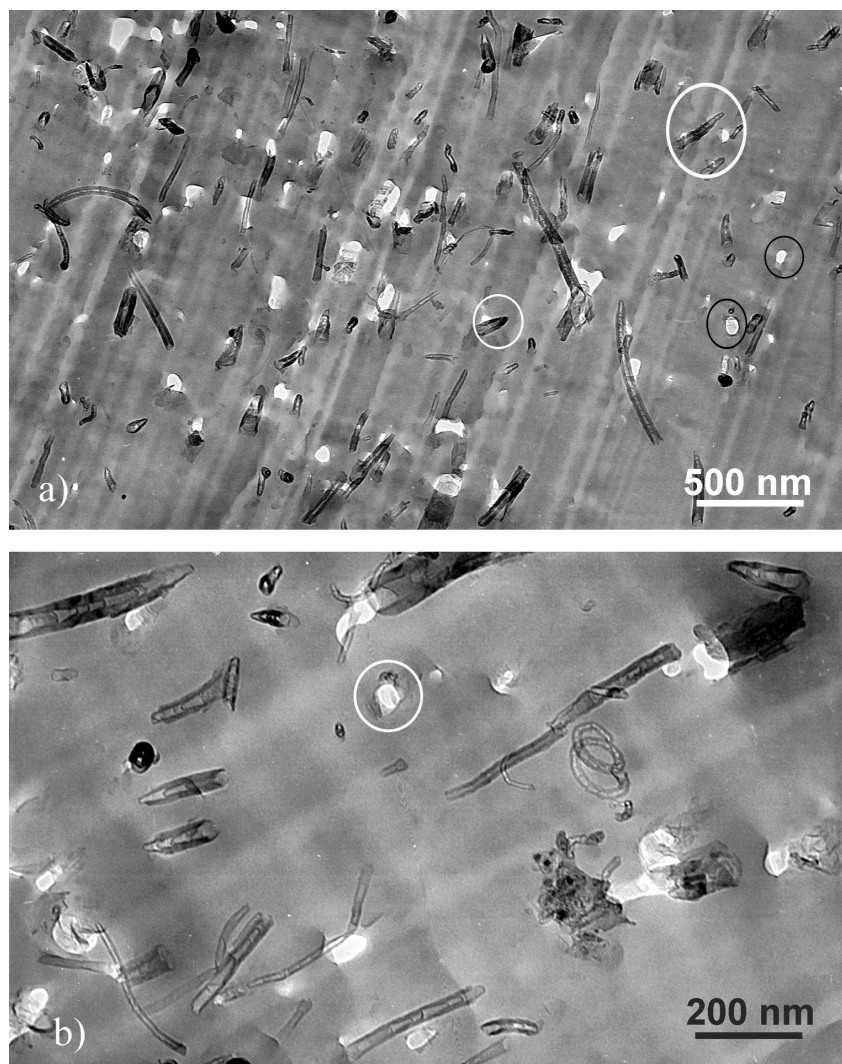


Figure 57: TEM micrographs of an ultramicrotomic cut of a-CN_x / PS nanocomposites. The white circles on the photomicrograph a) indicate tubes pulled-out from the matrix. b) depict a white circle probably indicating a hole left by a pull-out effect during the preparation process.

TEM analyses were performed to better describe the nanocomposites materials. They permit to confirm that untreated tubes have a lower adhesion within the matrix. Indeed, Figure 57 a) and b) show TEM micrographs obtained from a-CN_x MWNT / PS nanocomposites. The white circles in Figure 57 a) represent the tubes that are coming out of the material surface plane, indicating that they were pulled out from the matrix during the ultramicrotome preparation process. On the other hand, Figure 57 b) reveals the presence of a hole which is highlighted by a white circle, which could be a piece of evidence of the pull-out phenomenon. These observations are representative of a lack of adhesion between the matrix and the a-CN_x.

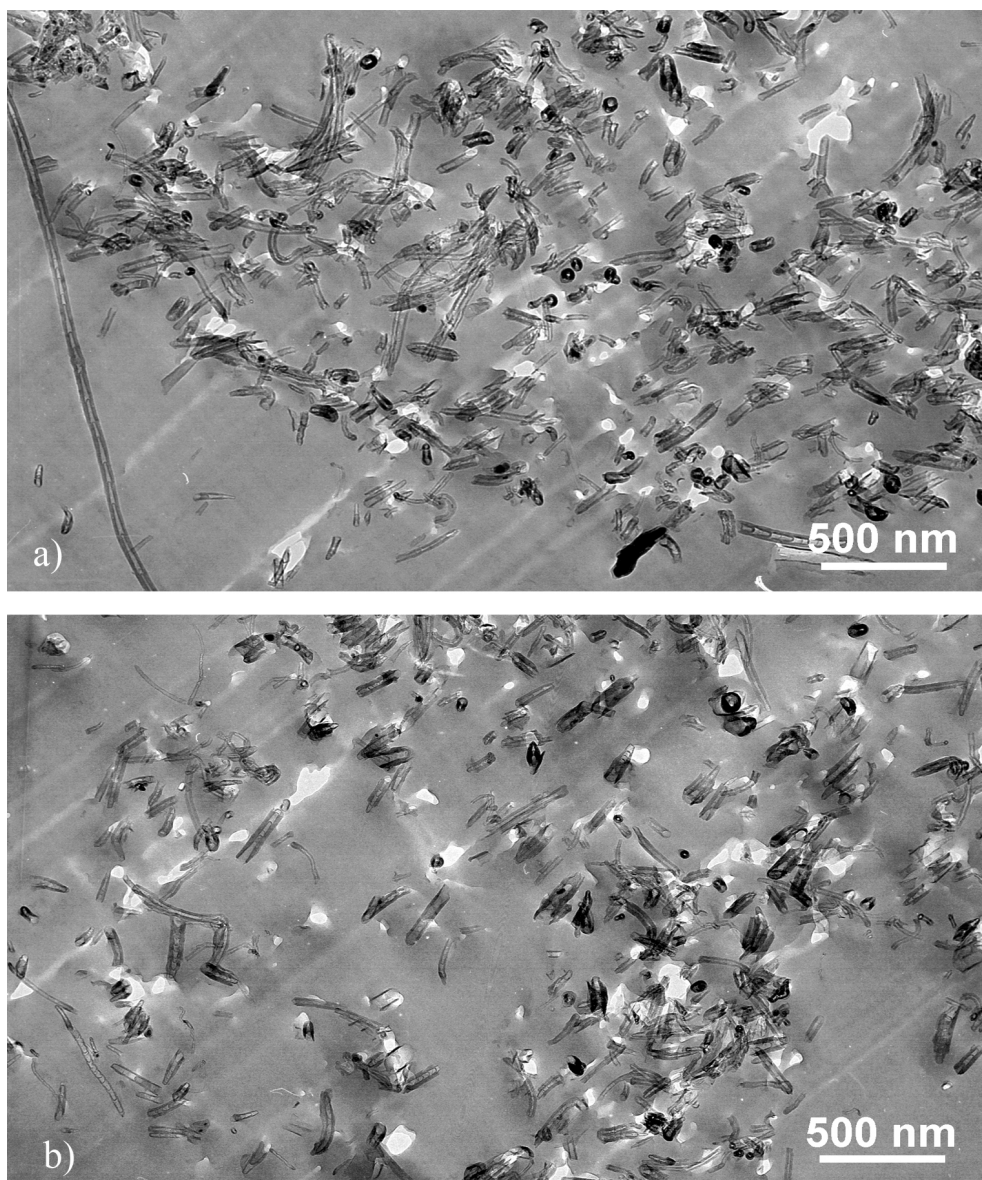


Figure 58: TEM photomicrographs of the PS-g-CN_x / PS nanocomposites.

Figure 58 a) and b) show TEM photomicrographs obtained from the PS-g-CN_x / PS nanocomposites. On the contrary to as-received carbon nanotubes, most of the tubes are cut and not pulled out from the matrix (during the ultramicrotome preparation process). This reveals a better adhesion to the matrix.

Finally, in order to confirm the idea that grafting of PS on the external layers of CN_x MWNTs leads to an increase of the cohesive forces between the nanotubes and the matrix, a micrograph of a cut tube was acquired at higher magnification (see Figure 59).

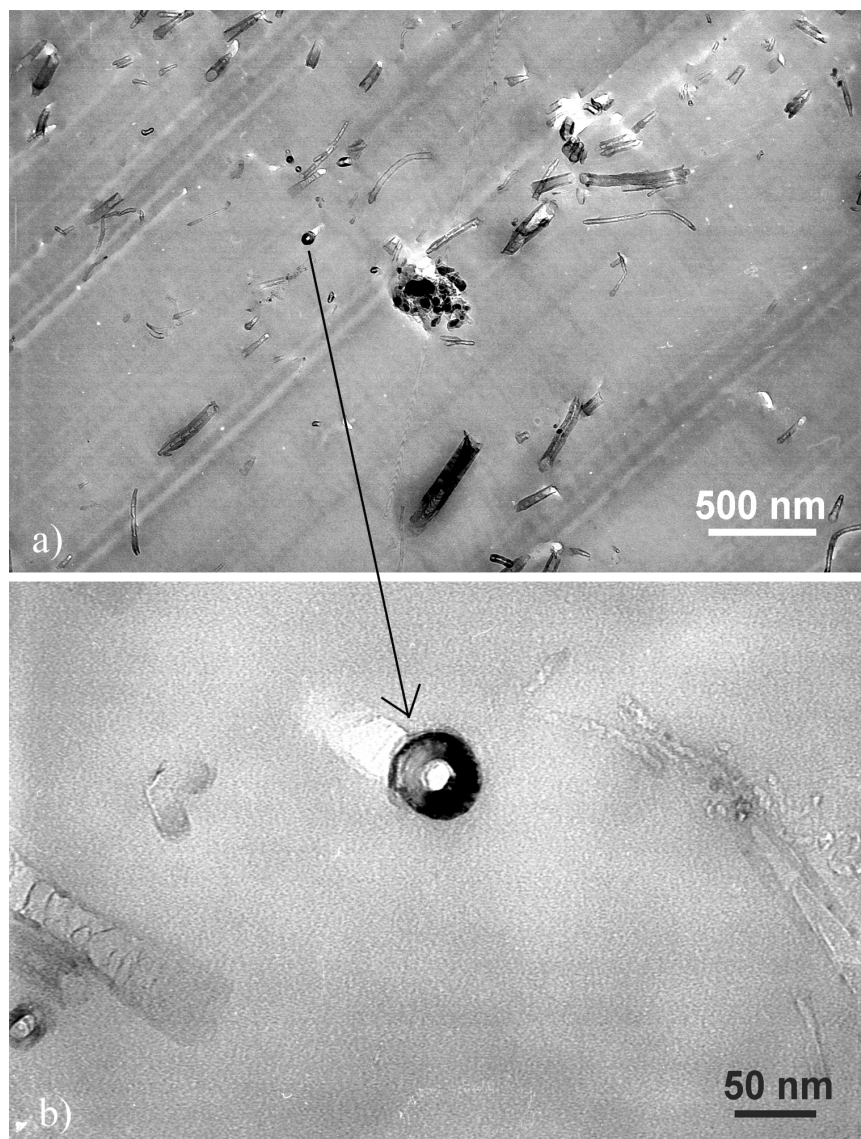


Figure 59: TEM micrographs of the PS-g-CN_x / PS nanocomposites low and high magnification showing the cross-section of a PS-g-CN_x that is well attached to the PS matrix

This micrograph shows a PS grafted nanotube cut perpendicularly to its axis. A hole was created during the preparation by ultramicrotomy. Despite the presence of this hole neither ultramicrotomy induced pull-out of the nanotube nor its displacement is observed, which confirms that the adhesion of the nanotube with the matrix was improved. Note that a darker layer surrounding the nanotube can be observed. This may be attributed to the grafted PS layer, which density would be higher than that of the PS matrix.

B.2 Effect of the CNx MWNTs on the PSBS copolymer microstructure

B.2.1 PSBS Morphology

From the structure of the SBS macromolecule and the styrene to butadiene ratio, the expected structure of the poly (butadiene-co-styrene) used exhibits a hexagonal packed structure. Indeed, it is well known that polybutadiene and the polystyrene are not miscible due to London dispersive forces [191]; it means that the product χN exceeds the order–disorder critical value. Therefore, we expect that the block copolymer we will tend to arrange into ordered phases and more particularly into the hexagonal packed cylinder structure.

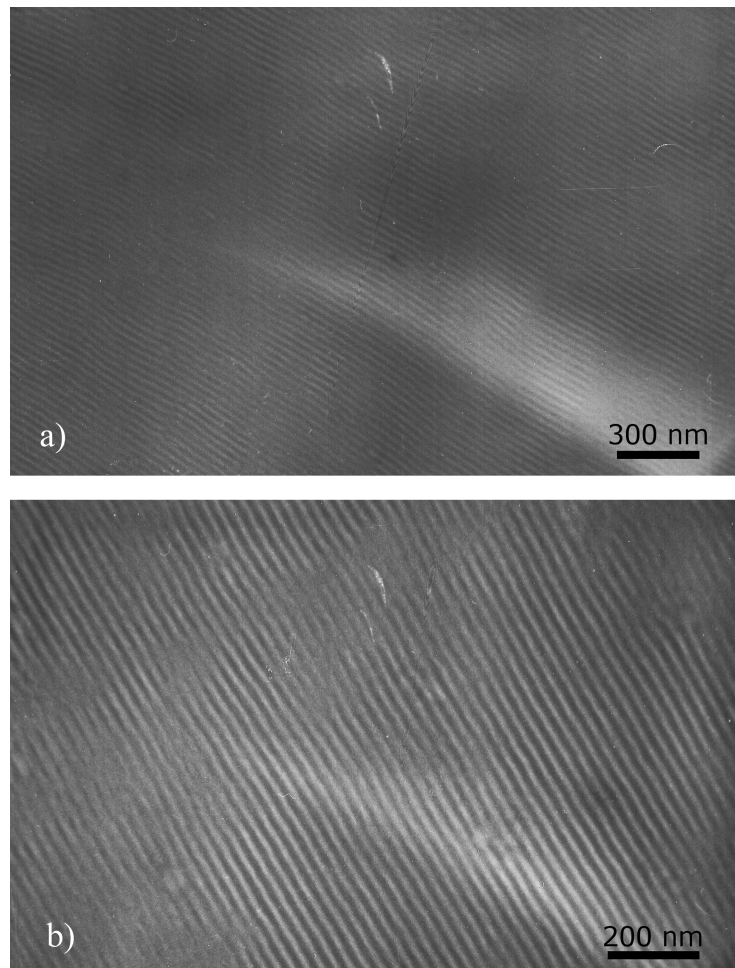


Figure 60: TEM micrograph of the PSBS matrix (after ruthenium staining). The dark regions correspond to the butadiene blocks and the bright ones to the styrene blocks.

Figure 60 a) and b) display TEM micrographs of the PSBS. Due to ruthenium staining, the dark regions represent the polybutadiene blocks, and the bright ones the polystyrene blocks. The photomicrograph is representative of either lamellae or hexagonal packed cylinders. Knowing that the expected structure is the hexagonal packed cylinder structure, the observation of lamellae would mean that the film of pure PSBS exhibits a uniform morphology. If we consider that the hexagonal packed cylinder structure is observed, the polystyrene cylinders that lie in the observation plane would be highly oriented and each domain of hexagonal packed copolymer would be greater than $3 \mu\text{m}^2$.

B.2.2 CN_x MWNT / PSBS nanocomposite microstructure

B.2.2.1 As received CN_x MWNT / PSBS

The introduction of long fibers such as carbon nanotubes may induce a modification of the block copolymer microstructure.

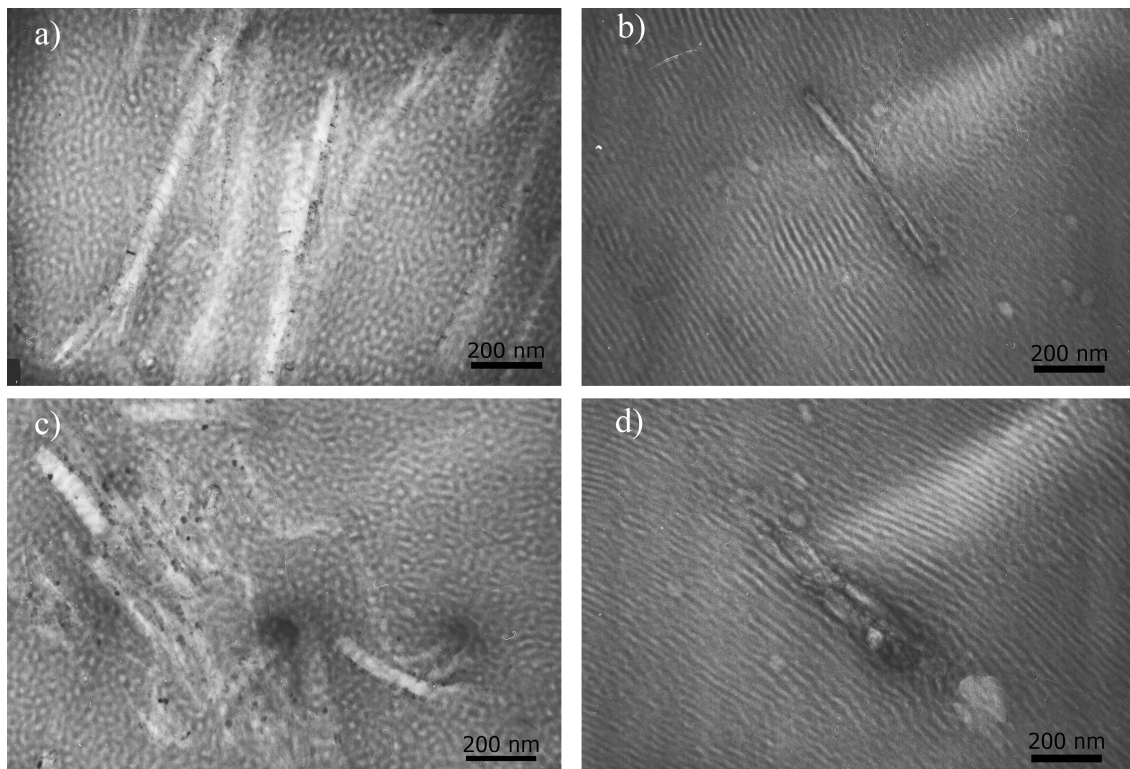


Figure 61: TEM micrographs of a- CN_x / PSBS nanocomposites. The bright regions of the copolymer are the polystyrene phase, and the dark areas represent the polybutadiene phase.

In Figure 61 four micrographs of the PSBS-based nanocomposites with 2.5 vol. % a-CN_x are displayed. Due to staining with ruthenium tetroxide, the bright regions in the copolymer are the polystyrene phase, and the dark ones are the polybutadiene phases. A lot of carbon nanotubes can be seen in Figure 61 a), and they largely disturb the microstructure of the PSBS matrix. Indeed, we did not observe the hexagonal packed structure anymore but a disordered bi-phased material. Figure 61 c) also displays a region with several nanotubes, forming an aggregate. We also observed a kind of disordered bi-phased material induced by the presence of the carbon nanotubes. On the contrary, Figure 61 b) and d) present the cases of isolated tubes in the PSBS matrix. On these micrographs, it can be observed that the hexagonal packed structure is not largely affected by the presence of the CN_x MWNTs. Next to the surface of the tube, the disorder is more important than far from the tube (≈ 100 nm). Moreover, it seems that a-CN_x have a preferential interaction with one of the blocks of the copolymer, which locally perturbs its hexagonal packed order. Indeed, on Figure 61 d), local changes in the microstructure of the copolymer appear on the surface of CN_x MWNTs, with the appearance of PSBS micelles. This phenomenon is certainly caused by the locally higher attractive forces between the CN_x MWNTs and one part of the block copolymer (namely the P.S blocks), which may result in a higher concentration of this block at a given point. These microstructural changes can result from an increase of the local electro-negativity due to the presence of amine, or bipyridine sites in CN_x MWNTs.

B.2.2.2 PS grafted CN_x MWNTs in a PSBS matrix

In Figure 62 a) and b) are represented TEM micrographs of the PSBS-based nanocomposite with 2.5 vol. % PS-g-CN_x. In this case, the introduction of CN_x MWNTs has a very different impact on the microstructure of the PSBS matrix. On the contrary to the composites synthesized with a-CN_x, the hexagonal structure is well preserved. Nonetheless, we should mention the hexagonal packed domains are smaller than those of pure PSBS matrix. Figure 63 shows undoubtedly that the PS-g-CN_x has a preferential interaction with the PS block. It clearly appears that the PS grafted layer interacts with the PS block in order to induce new hexagonal packed domains. Consequently, the morphologic

interaction between the PS-g-CN_x and the matrix depends on the diameter of the carbon nanotube. Thus, we will distinguish the cases of small and large nanotubes in the following discussion.

B.2.2.2.1 Small tubes

In Figure 62, white circles are drawn in order to indicate the presence of small tubes that are embedded in a PS cylinder of the hexagonal packed structure. This phenomenon is not observed for larger tubes. We can imagine that the smallest tubes are small enough to behave as PS block cylinders.

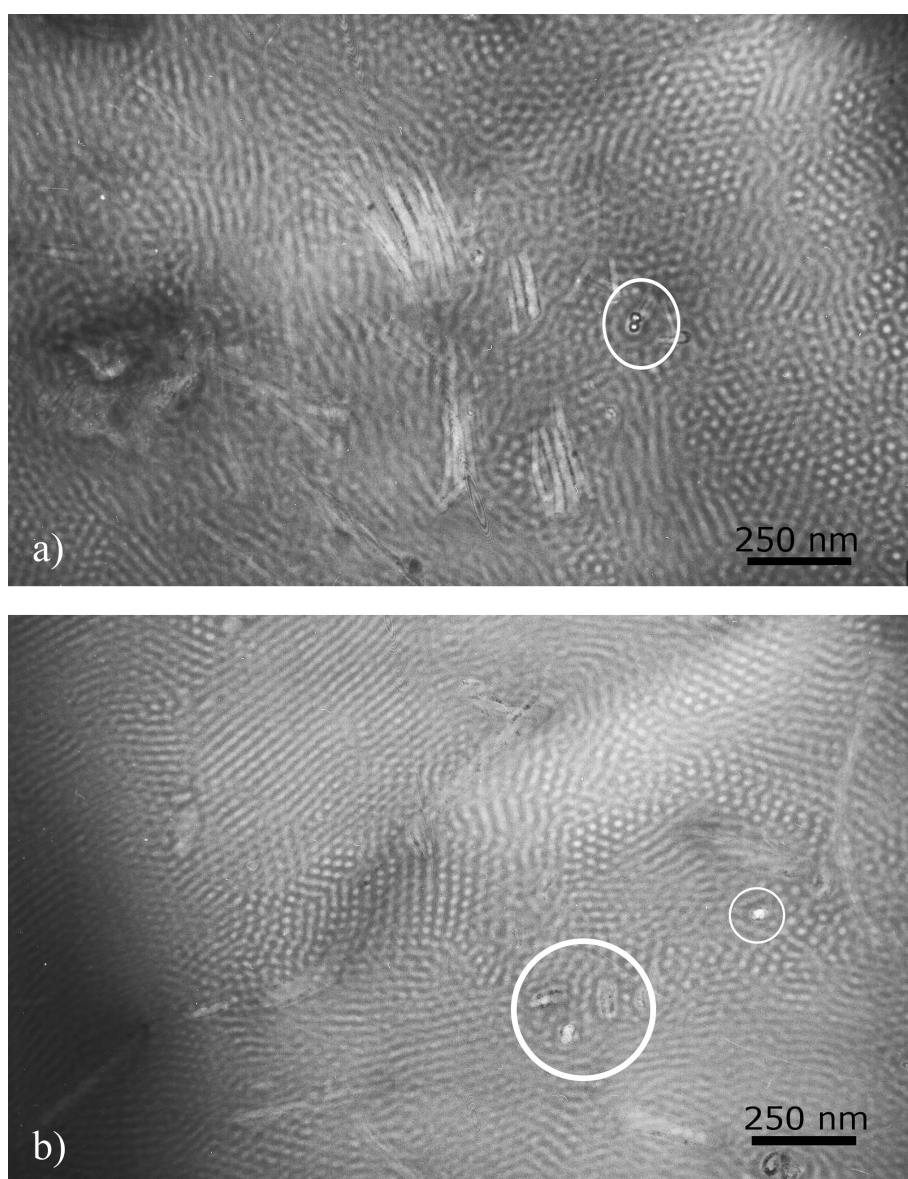


Figure 62: TEM micrograph of the 2.5 vol. % PS-g-CN_x / PSBS nanocomposite. The bright regions of the copolymer are the polystyrene phases, and the dark regions are the polybutadiene phases. The white circles indicate PS-g-CN_x encapsulated in PS cylinders.

Therefore, on Figure 62 a) and b) it is possible to distinguish a group of two or three tubes that are aligned in the cylinder axis. For higher diameters of CN_x MWNTs, the radius of the hybrid material would be too large to behave as a PS block cylinder.

B.2.2.2.2 Large tubes

In the case of large tubes, their diameters prohibit them to act as if they were a cylinder of the hexagonal packed structure. Thus, as shown in Figure 62 b), the PS-g- CN_x can be crossed over by the hexagonal packed structure. On the other hand, we observed that they can be aligned in the axis of the PS cylinder direction (C.f. Figure 62 b).

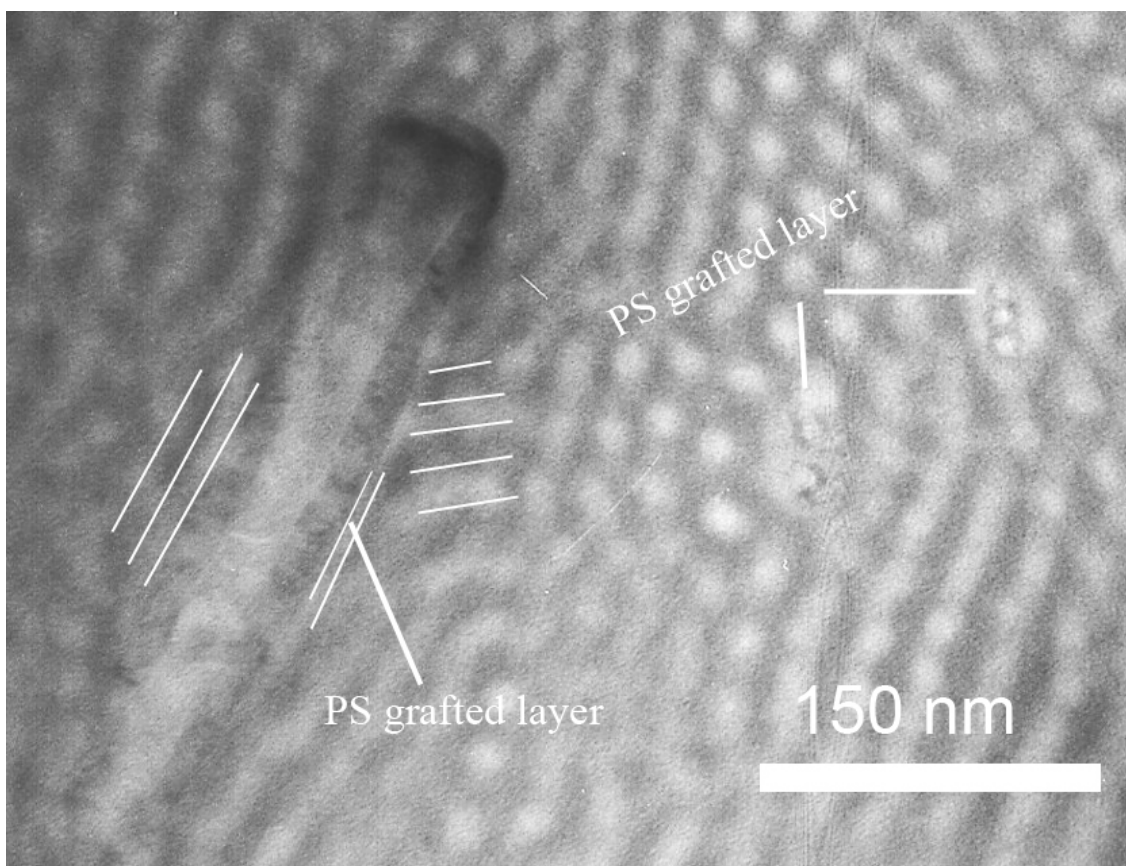


Figure 63: Morphology details of the PS-g- CN_x in the PSBS matrix.

The image displayed in Figure 63 is a very useful micrograph that explains how the PS grafted layer interacts with the matrix. On the contrary to a- CN_x , the PS-g- CN_x have a constant interaction with the PS blocks all along the tube (due to

the PS grafted layer). The copolymer seems to be oriented in a radial form all along the PS-g-CN_x, as the PS grafted chains are.

Figure 64 a) describes the proposed orientation of the block copolymer around the small diameter PS-g-CN_x, which might result in a hexagonally packed structure, where the nanotubes act as if they were PS block cylinders. Based on the structure observe on Figure 63, Figure 64 b) indicates how the PS grafted layer induces aligned PS cylinders in the axis of the CN_x MWNTs. Finally, Figure 64 c) represents another structure which can describe the formation of PS block cylinders perpendicular to the CN_x MWNT axis (miscellaneous like structure). This structure could explain the observation of PS cylinders that seems to cross over the CN_x MWNTs (Figure 62; top-right of the micrograph).

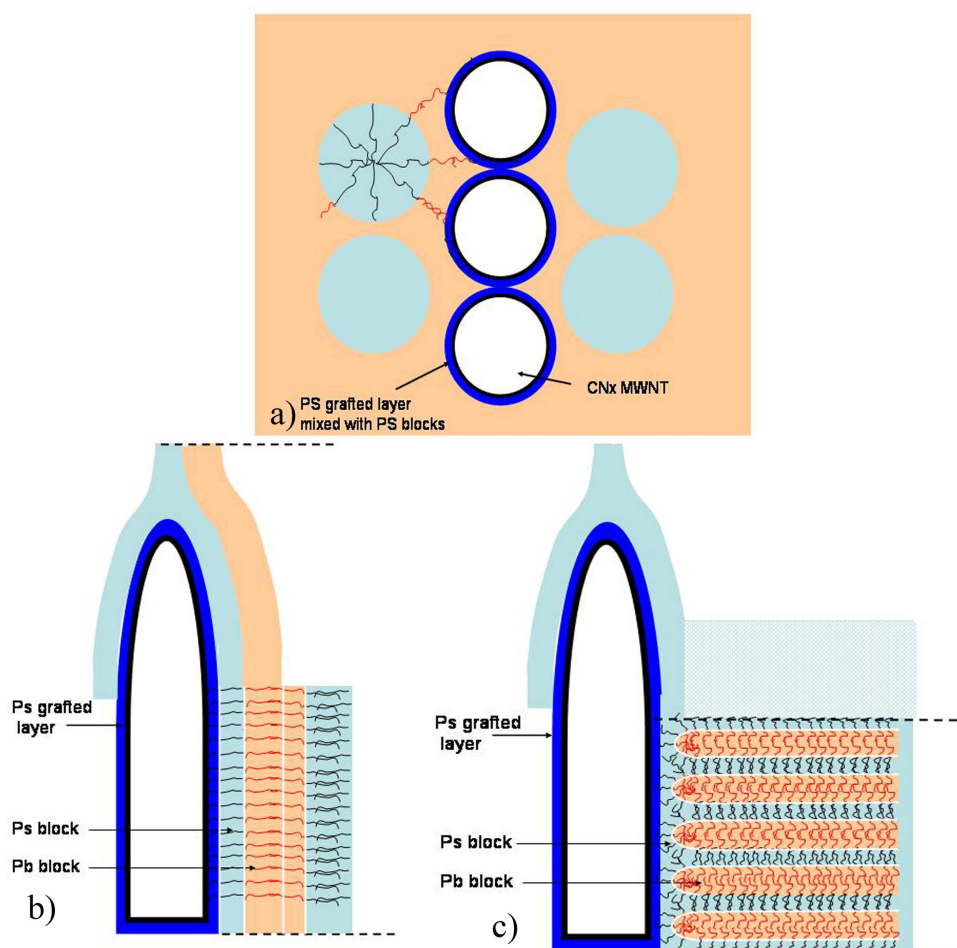


Figure 64: Proposed structure of the CN_x MWNTs / PSBS matrix next to the tube surface; a) the tube is small enough to act as a PS block cylinder, b) the PS grafted layer interacts with the PSBS matrix and induces aligned PS block cylinders along the CN_x MWNT axis, c) the PS grafted layer interacts with the PSBS matrix and induces PS block cylinder perpendicular to the CN_x MWNT axis.

B.3 Glass transition temperature of the CN_x MWNT / PS nanocomposites.

Differential Scanning Calorimetry permits to define the influence of a-CN_x and PS-g-CN_x on the glass transition temperature of the nanocomposites using PS as a matrix. The results obtained are shown on Figure 65.

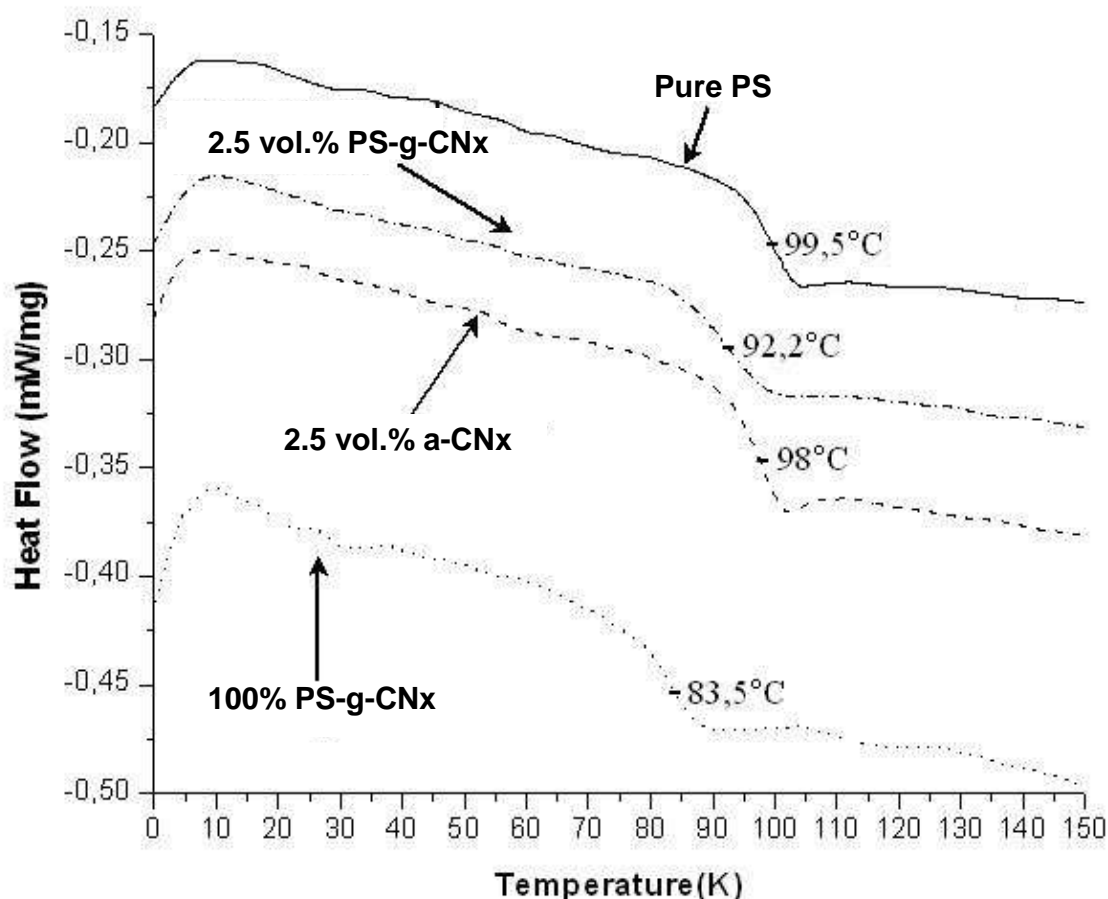


Figure 65 : Glassy transition temperatures determined by DSC of the PS matrix, a 2.5 vol. % a-CN_x / PS nanocomposite, a 2.5 vol. % PS-g-CN_x / PS nanocomposite, pure PS-g-CN_x.

Pure PS exhibits a glass transition at 99.5°C, in agreement with values reported in the literature [192]. Nanocomposites with as high as 2.5 vol. % of a-CN_x do not exhibit any significant change in the matrix glass transition: T_g = 98°C. Nevertheless polystyrene grafted on CN_x MWNTs surfaces have a lower glass transition temperature: T_g of pure PS-g-CN_x is found to be 83.5°C. (cf. Figure 65). C.Buenviaje [192] demonstrated that the polystyrene glass transition is constant for molecular weight (M_n) over 1.10⁵. Below this value, the glass transition temperature starts to decrease, following an exponential tendency

(C.f. Figure 66), (in fact the empirical relationship is often given as $T_g = T_{g\infty} - k/M_w$, where k is a constant).

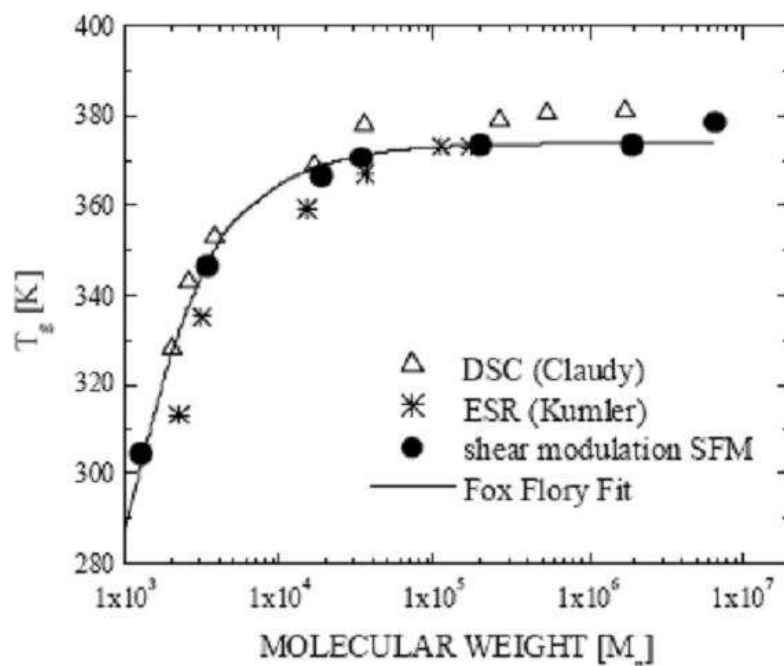


Figure 66: Glass transition temperature of polystyrene against its molecular weight [192].

It means that the low glass transition temperature we observed for 100 % PS-g-CN_x results from the polystyrene molecular weight. From the exponential dependence of T_g on the molecular weight, we conclude that the molecular weight of the polystyrene we grafted on the external layer of the CN_x MWNTs is about 10^4 g.mol⁻¹. Moreover, K. Matyjaszewski [97], showed that ATRP grown polystyrene generally have low molecular weight, which is consistent with the value found in this work.

Moreover, the glass transition phenomenon is representative of the thermal activation of the macromolecular mobility; it means that long macromolecular chain movements are possible above this temperature. We mentioned previously that for molecular weights below 10^4 , the glass transition temperature highly depends on the molecular weight [192]. As a consequence, for low molecular weights, a high polydispersity may result in an increase of the glass transition temperature range. Because the DSC thermogram shows that the glass transition temperature range of 100 % PS-g-CN_x is not wider than for pure polystyrene, we think that the grafted polystyrene has a rather low polydispersity. These results are in agreement with those of K. Matyjaszewski

[97], who confirmed that the ATRP synthesis permits to reach a very low polydispersity, because the macromolecular chains grow with a controlled process at very low speed (12 hours: $M_n < 2 \cdot 10^4$).

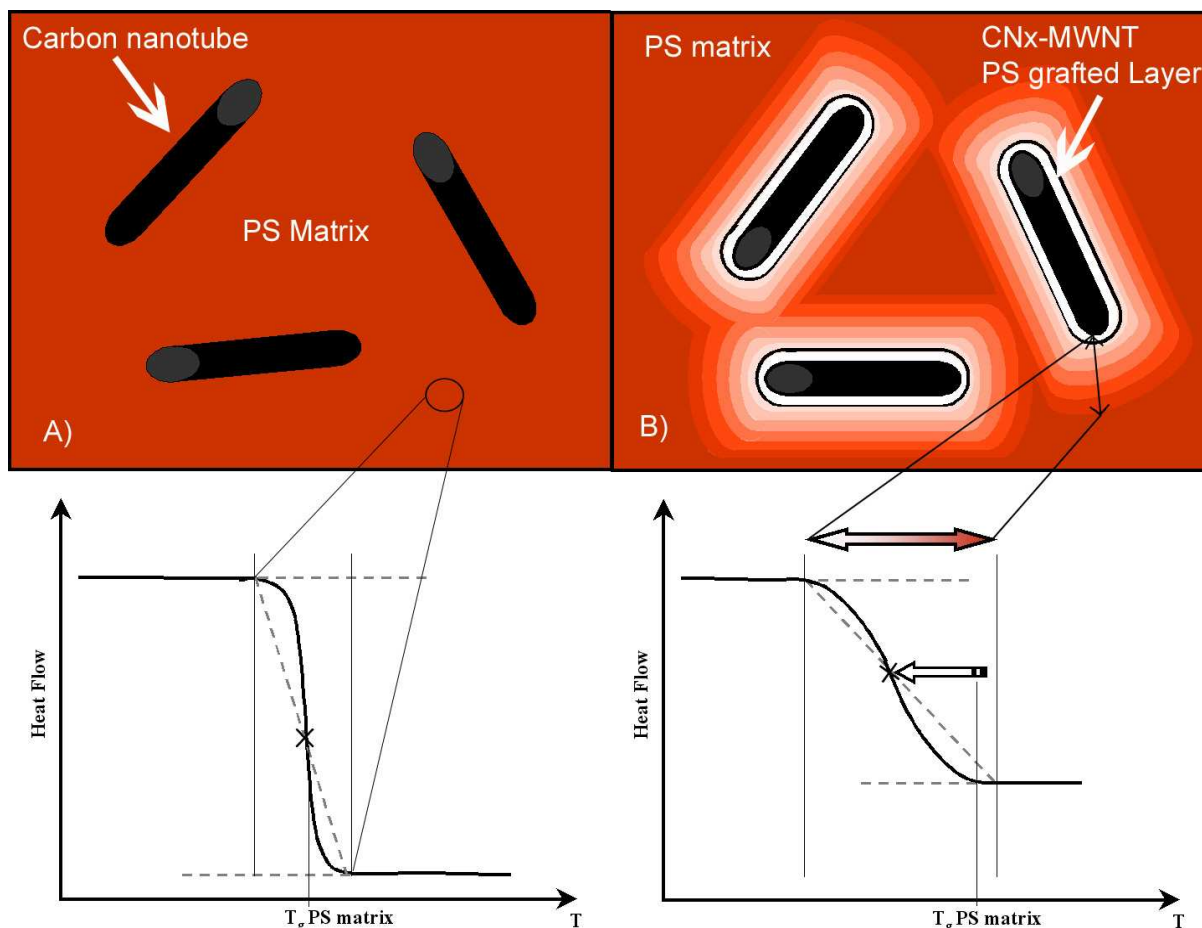


Figure 67: A) For the composites with a-CNx, the matrix have the same glass transition than pure PS; B) For the composites with PS-g-CNx the PS matrix next to the PS grafted layer ($T_g < T_g$ pure PS) has a lower glass transition: the low molecular weight PS grafted layer act as a plasticizer.

Finally nanocomposites with 2.5% vol. of PS-g-CNx present a glass transition temperature shifted down to 92°C and the transition ranges from 80°C to 99°C (Cf. Figure 65). The transition temperature of composites with 2.5 vol. % of a-CNx ranges from 90°C to 105°C. It should mean that 2.5 vol. % wt. of PS-g-CNx modified the mobility of the PS matrix.

Figure 67 depicts what should happen when PS-g-CNx or a-CNx are introduced in a PS matrix. As mentioned previously, there is no change of the molecular mobility at the interface between a-CNx and the PS matrix. As a consequence

the DSC thermogram exhibits a narrow transition that corresponds to the pure PS matrix glass transition (Fig. 9A).

In Figure 67 B), we assume that the PS grafted layer acts as a plasticizer so that, the PS matrix near the PS grafted layer should have a lower glass transition, whereas the PS matrix far from the PS grafted layer should not be affected. Therefore, as shown in Figure 67 B), this gradient of molecular mobility should be observed on the DSC thermogram as a wide transition. This transition should start from the lower temperature of the PS grafted layer glass transition that corresponds to the shortest molecules, and should rise up to the temperature of the bulk PS matrix glass transition.

This comment is consistent with our data. Nevertheless, for PS-g-CN_x we observed that the glass transition temperature range is overall shifted to lower temperatures (80°C to 99°C) whenever bulk PS glass transition ranges from 90°C to 105°C. This means that the average distance between carbon nanotubes is smaller than the interphase thickness, which in turn indicates that PS-g-CN_x are rather well dispersed.

B.4 Conclusion about the morphology and adhesion of CN_x / Polymer composites

It is difficult to have quantitative information on the nanotube dispersion. Nevertheless, grafting a PS layer onto CN_x MWNTs seems to improve the dispersion of the CN_x MWNTs in both matrices. It is also noteworthy that PS grafted CN_x MWNTs exhibit a better adhesion to the matrix. Indeed, the chemical nanotube functionalization permits to prevent the pull-out phenomenon of carbon nanotubes.

In a structured polymer matrix such as PSBS, the introduction of carbon nanotubes has different effects. It was shown that CN_x MWNTs might have local preferential affinities with a part of the block copolymer, which could originate from the nitrogen dopants atoms. Thus the as produced nanotubes generate a kind of disorder within the hexagonal packed structure of the PSBS. On the other hand, PS grafted CN_x MWNTs tend to preserve the hexagonal packed structure. We observed that small tubes can integrate the PS blocks within the hexagonal packed structure, whereas large tubes cross the matrix and induced a preferential orientation of the PS cylinders (with their axis either parallel or perpendicular to the nanotube axis).

Finally, DSC analysis has permitted to obtain more information about the thermal behavior of the interface PS / CN_x MWNTs. Moreover, this analysis has permitted to highlight the molecular characteristics of the PS-grafted layer. Indeed, it has been shown that its molecular weight is lower than $10^{-4} M_n$, and consequently it acts as a plasticizer in a matrix of the same nature (PS).

Part C Electrical properties of the CNx MWNT / polymer composites

The literature presents a massive number of references of nanocomposite using MWNTs as electric conductive fillers. The percolation threshold (p_c), that represents the appearance of a continuous conductive nanotube network through the matrix, is found to vary significantly possibly due to the preparation method. Below the percolation threshold, these nanocomposites act as dielectric materials. They exhibit a capacitive behavior, where the conductivity is a function of the AC frequency [193]. Above the percolation threshold, the real conductivity increases as the fraction of nanotubes is increased. In this context we would mention the work by J.N. Coleman [139] who found $p_c = 8.4\%$ in poly(p-phenylenevinyle-co-2,5-dioxy-m-phenylenevinylene). More recently, dispersing SWNT in poly(butylene terephthalate) using in-situ poly condensation [194] led to a low p_c of 0.2 wt.% of filler. Depending on the matrix used (i.e. thermoplastic or thermoset), the percolation network does not reach the same p_c [51, 53, 54]. Some papers show results obtained from a Poly-epoxy matrix [53, 54]; the authors show that depending on the kind of nanotubes and on the process involved in the fabrication of nanocomposites, the percolation threshold could dramatically change (ranging from 0.0025 wt.% to 0.3 wt.%). Other works discussed on the effect of the chemical treatment of the MWNT surface. It was observed that depending on the intensity of the chemical treatment (Strength of the acid treatment), the percolation threshold in polyepoxy varied (0.01 vol.% to 0.06 vol.%) [146]. The literature also reports various examples that illustrate the importance of the process and the matrix used in the synthesis of MWNT polymer in nanocomposites percolation threshold.

The semiconductor or conductor behavior of MWNTs depends on their chirality, diameter, and degree of crystallinity [26]. It has been reported elsewhere that nitrogen-doped carbon nanotubes (CNx MWNTs) exhibit unusual electrical

properties. By Using a Carbon-Nitrogen gas pyrolysis over transition metal atoms such as Fe, Cu or Ni the generated MWNTs produced contain nitrogen atoms that substitute carbon atoms in the graphitic network. The presence of nitrogen in the carbon layers tend to inject electrons in the conduction band and as a consequence the tubes could display a metallic behavior [136]. CNx MWNTs are the fillers used in this work.

In this section we present results related to the electric behavior of numerous CNx MWNTs / polymer composites. First, we realized dielectric analyses of polystyrene (PS) / CNx MWNTs nanocomposites using as produced tubes. This system was studied and compared with other results found in the literature. Subsequently, we introduced in the PS matrix, polystyrene grafted CNx MWNTs. Results demonstrated very dissimilar electrical behavior. For example, studies revealed that PS grafted layer tend to isolate CNx MWNTs, thus frustrating the electrical conductive percolating route.

Finally PSBS was used as a matrix. This polymer has the particularity to be composed of two covalently linked blocks. Moreover, one part is a thermoplastic polymer, whereas the other phase is an elastomer with glass transition temperatures about -90°C . Comparing the results obtained for both matrices, we expect an electrical percolation change (percolation threshold, critical exponent etc...). As well as for PS matrix, we introduced PS grafted CNx MWNT in the PSBS matrix. This ultimate nanocomposite allowed us to understand the effects of using grafted CNx MWNTs.

C.1 Electrical behavior of CNx MWNT / polymer nanocomposites

C.1.1 Nanocomposites using as produced CNx MWNTs

The complex electrical conductivity $\sigma(\omega)$ was measured at room temperature. Figure 68(a-b) presents the results obtained for nanocomposites with as produced CNx nanotubes as electric conductive filler on PSBS (Figure 68 a.) or PS (Figure 68b.). Non percolating materials have a typical dielectric response where the complex conductivity modulus $\sigma(\omega)$ is a function of the frequency: the AC current increases with the frequency from 1.10^{-13} S.m⁻¹ at 10 mHz to 1.10^{-5} S.m⁻¹ at 1MHz.

Moreover, for those materials, $\sigma(\omega)$ increases with the volume fraction of CNx MWNTs. This phenomenon is due to the capacitive effect of CNx MWNTs in the matrix. Each tube acts as an isopotential metallic filler, and locally forms a nano-capacitance with its neighbors. As a consequence, the higher the CNx-MWNT volume fraction is the lower the distance between metallic particles.

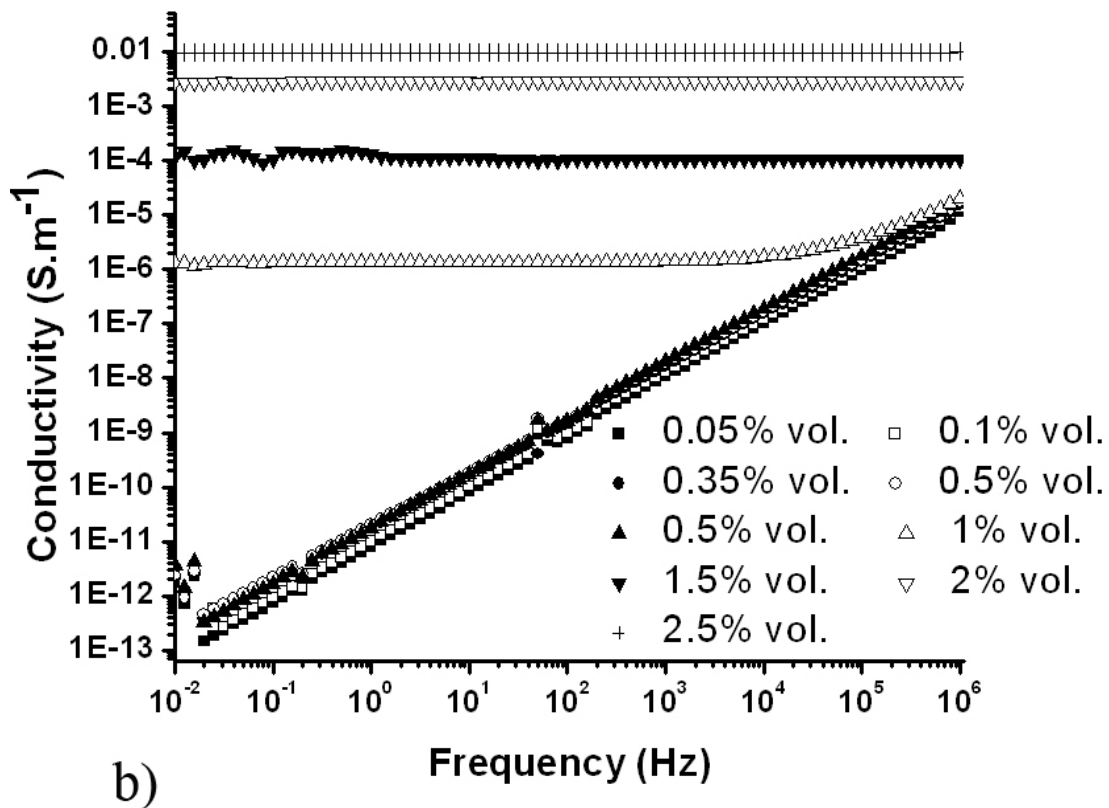
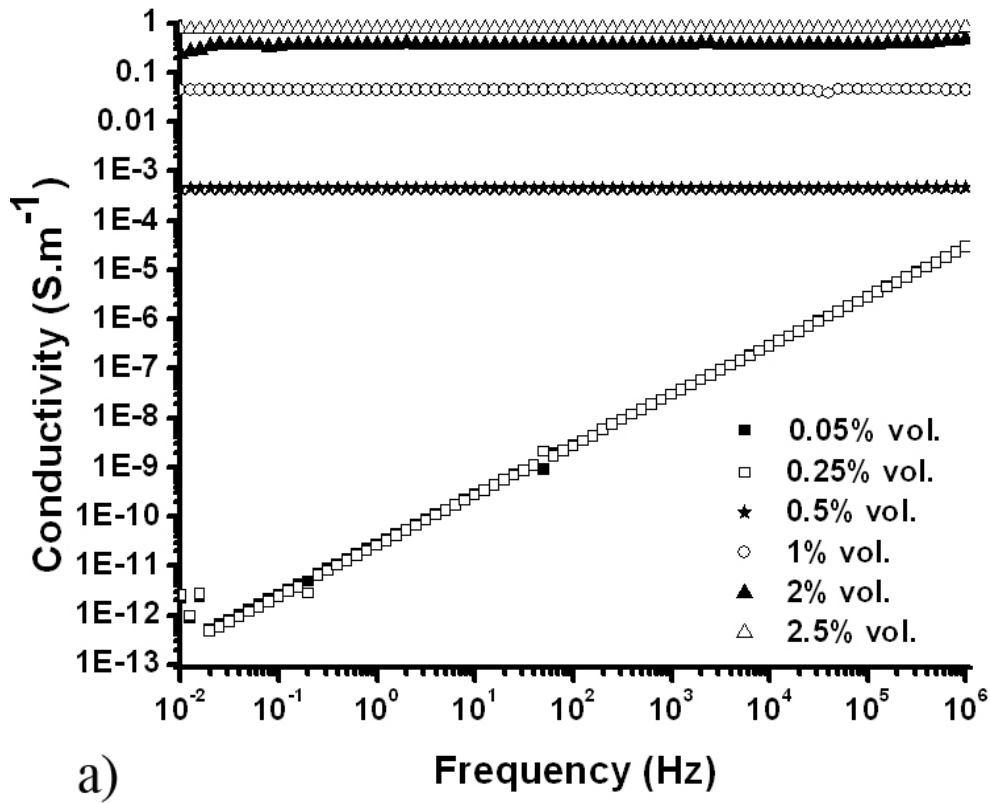


Figure 68 : Complex conductivity modulus $\sigma(\omega)$ of nanocomposites containing a-CN_x at different volume fractions: a) PS matrix and b) PSBS matrix.

Above a critical volume fraction (p_c), we observed the appearance of a conductivity plateau, independent of the frequency. For both matrices, it is observed a dramatic change in the conductivity, of about ten orders of magnitude. Above p_c , the conductivity increases with the volume fraction of CNx MWNT. This phenomenon, called percolation, is due to the appearance of a continuous CNx MWNT conductive network within the matrix that controls the conductivity. Percolation theory allows us to describe the insulator-conductive transition of the materials synthesized. The scaling law that is the resulting mathematical equation to describe a percolating system is given by: $\frac{\sigma}{\sigma_0} = (p - p_c)^t$ for $p > p_c$. σ_0 is a constant, p_c is the percolation threshold, and t is the critical exponent which describes how the system reaches the saturation in conductivity [140]. We could point out that above a critical frequency (ω_c), the conduction starts to be frequency dependent. As we demonstrated before, the continuous plateau is representative of the ohmic conduction due to a continuous network of nanotubes embedded within the matrix. However, for low volume fractions of nanotubes, many isolated nanotubes are still acting as nanocapacitors. As a consequence, for a given frequency the capacitive transport effect (frequency dependent) starts to be more important than the ohmic transport [54, 195].

Figure 69 (a-b) represents the modulus of the complex conductivity obtained at 1Hz for a-CNx nanocomposites using a Polystyrene matrix (Figure 69 a.) and a poly(butadiene-co-styrene) matrix (Figure 69 b.), versus the volume fraction of filler. The fitted scale law reports different percolation behaviors when using a PS matrix or a PSBS matrix. For the PS matrix, the percolation threshold was found at 0.4 vol.% with a critical exponent $t = 2.44$; whereas for the PSBS matrix it was found that $p_c = 0.9$ vol.% and $t = 3.2$. The low value of p_c can be attributed to the high aspect ratio of the CNx MWNTs that allows the formation of a conductive network at low volume fractions of filler. However, the difference observed between the two percolation thresholds comparing the two different matrices (using the same nano-composite synthesis process), suggests that the physico-chemical interactions between the matrix and the filler influence the dispersion of CNx MWNTs.

Previous works reported that nanotubes would disperse better in phenylic solvents such as benzene or toluene than in aliphatic or highly polar solvents. Therefore we believe that butadiene does not ensure a good dispersion of CNx MWNT and pure styrene would disperse better CNx MWNTs.

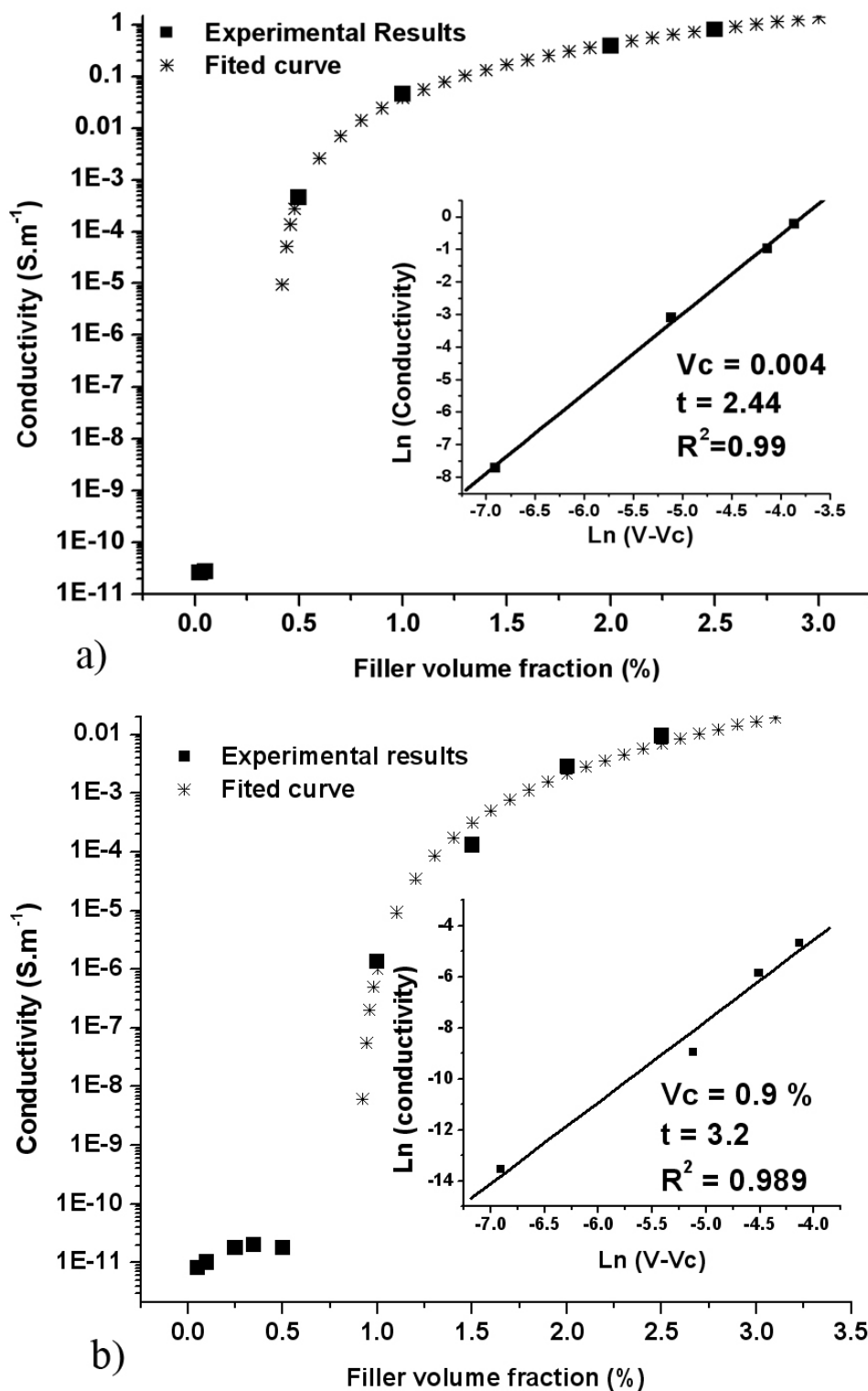


Figure 69 : Experimental conductivity results and fitted scaling law for a-CNx polymer nano-composite a) with PS matrix and b) with PSBS matrix.

Moreover, in a conductive network fiber dead branches do not participate in the conductivity. It has been reported a double percolating phenomenon, where MWNTs tend to preferentially segregate from a polymer A to another (named B) [175]. In this paper, two conditions are necessary to reach the bulk electric percolation: percolation of MWNTs in the polymer A, and percolation of the polymer A in the phase B. If CNx MWNTs tend to fill the polystyrene phase preferentially in the PSBS block copolymer; we could imagine that in this system (matrix PSBS), the quantity of dead branches increases and rises up the percolation threshold.

On the other hand, the literature [140, 146, 147] reported that the theoretical critical exponent ranges between 1.6 – 2.0. However, published experimental results show critical exponents varying between 1.2 to 3.1. Some publications mention that the curvature of MWNTs within the matrix has an influence on the critical exponent [148]. It was demonstrated theoretically for a random tube network that if the nanotubes are very twisted, the critical exponent increases because MWNTs tend to have a sphere-like structure. Furthermore, it could be extrapolated that MWNTs are apparently shorter, and thus the aspect ratio is smaller. Considering that CNx MWNTs have a lower dispersity in the polybutadiene phase, it is possible that they tend to twist in order to keep in the PS phase. As a consequence, this hypothesis could justify the higher percolation threshold we found using PSBS matrix.

C.1.2 Nanocomposites using PS-g-CNx MWNTs

In a similar way, PS-g-CNx were introduced in both matrices: PS and PSBS. Grafting polystyrene chains on the external layer of CNx MWNT improves the compatibility of the filler with the matrix, and thus should enhance its dispersion.

PS-g-CNx nanocomposites materials (with either PS or PSBS matrices) were submitted to complex electric conductivity measurements. Results obtained (C.f. Figure 70) demonstrated very dissimilar electric behaviors of those materials. PS-g-CNx / PS nanocomposites present a percolation threshold at 1 vol.% of filler and at 2.5 vol.%, the materials exhibit a plateau of conductivity at $1 \cdot 10^{-6} \text{ S} \cdot \text{m}^{-1}$. In addition, PS-g-CNx / PSBS samples reveal a percolation threshold between 1-2.5 vol.% of filler.

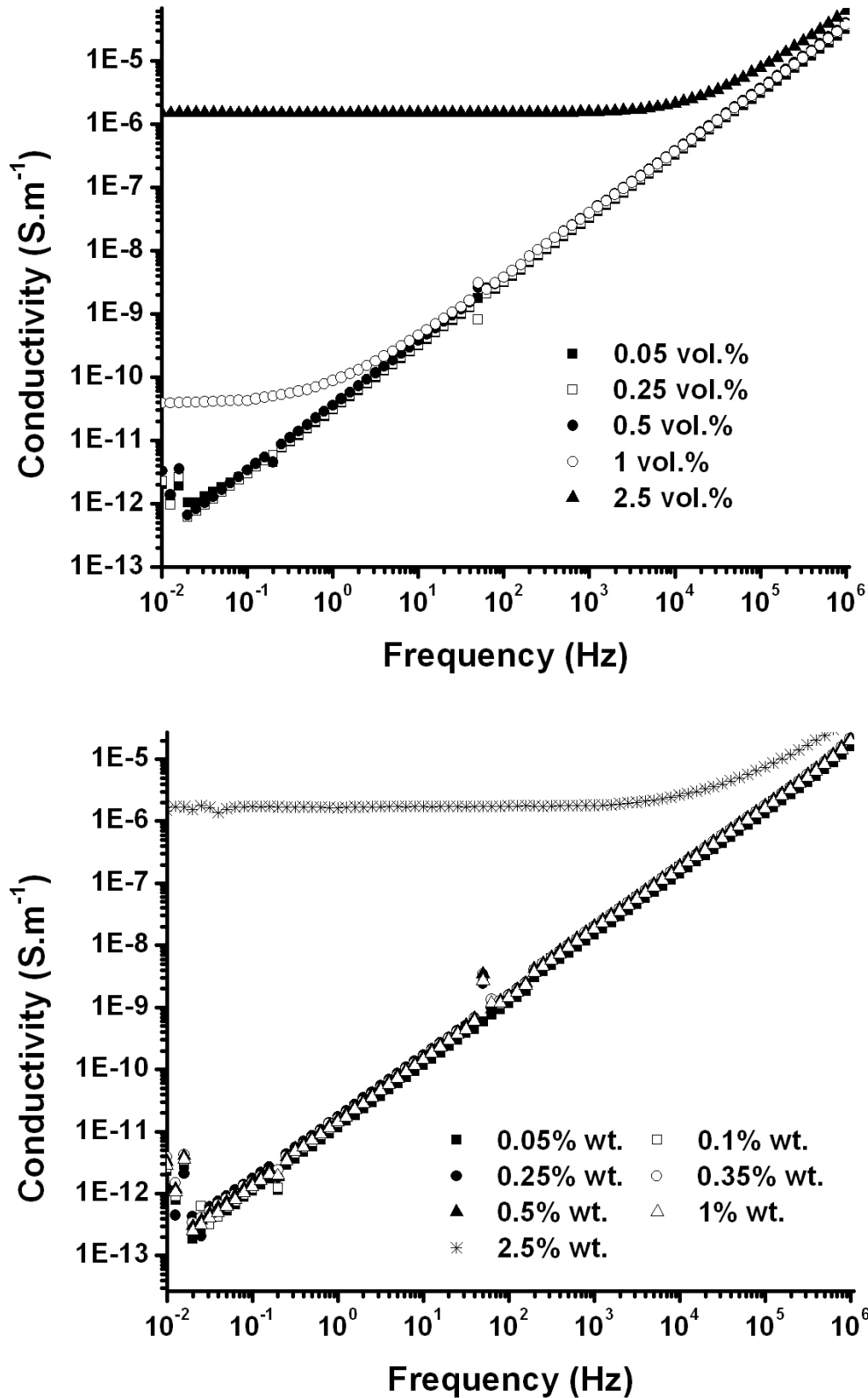


Figure 70 : Complex conductivity modulus of the Ps-g-CNx nano-composites against the frequency at different volume fractions of filler; a) PS matrix, b) PSBS matrix.

Compared to data obtained for a-CN_x nanocomposites, it appears that the percolation threshold was shifted towards higher concentrations of nanotubes after grafting the nanotubes with PS, i.e. from 0.45 vol.% ungrafted tubes to 1 vol.% grafted tubes in a PS matrix, and from 1 vol.% ungrafted tubes to almost 2.5 vol.% grafted tubes in a PSBS matrix. We believe that even if dispersion was improved by grafting polystyrene on the CN_x MWNT surface, fillers were isolated from each other by an insulating polymer. S. Li [196] reported that the grafting of chains with different molecular weights on the surface of MWNTs increases the solubility of MWNTs and as a consequence the conductivity of the nano-composites decreases. However, this work [196] does not mention the concentration of molecules by unit surface, and the electrical conductivity starts to decrease for grafted chains above 10 monomers long. In our work, the molecular weight of the grafted polymer chains seems to be high enough to inhibit the electrical conductivity.

However, in order to explain the presence of electrical percolation thresholds even if nanotubes are coated with an insulating layer, we should discuss the efficiency of the chemical reaction. We propose the existence of two types of CN_x-MWNTs. In the first type, all the nanotubes are completely coated, whereas in the second kind, the nanotubes did not participate in the in-situ polymerization and are not coated at all. This means that the first type of CN_x-MWNTs would not participate in the electrical conduction, whereas the second type acts like a-CN_x. It was measured that the fraction of a-CN_x will percolate in the PS matrix at 0.4 vol.%. In the case of PS-g-CN_x / PS nano-composites, the electrical percolation threshold is observed at 1 vol.%. If we consider a double CN_x MWNT population, 60% of the CN_x-MWNTs are insulating (grafted), and 40% are conductive CN_x MWNTs (ungrafted). However, the nano-composite using 2.5 vol.% of PS-g-CN_x exhibits a conductivity of 1.10^{-6} S.m⁻¹. Following the previous hypothesis, 2.5 vol.% of PS-g-CN_x correspond in fact to only 1.5 vol.% conductive CN_x MWNTs. From the results obtained on a-CN_x in a PS matrix, we should reach, with 1.5 vol.% conductive CN_x MWNTs, a conductivity of 0.1 S.m⁻¹. This is not in agreement with the observed conductivity of the PS-g-CN_x / PS nano-composites. Thus, the hypothesis of a double population (insulator, metallic) has to be rejected. Furthermore, the hypothesis of a double

population did not seem to be in agreement with previous Transmission Electron Microscopy observations because all the nanotubes we observed were coated with a PS layer. Alternatively, it is possible that the polymer layer is not perfectly homogeneous and its thickness varies along the tubes. Thus, there would be a dispersion of contact resistances: from an infinite resistance (contact between two PS-coated portions of nanotubes) to a given value (contact between two uncoated portions of nanotubes). Because the distance between tubes is higher when they are polymer grafted, the contact resistance has to increase. This could explain the low conductivity value observed for 2.5 vol.% PS-g-CN_x. Furthermore, the hypothesis of a contact resistance distribution should justify an increase of the percolation threshold we observed. Indeed, part of the nanotubes would possess an infinite contact resistance and as a consequence would act as insulator, thus the volume fraction of CN_x MWNTs has to be higher in order to reach the percolation threshold.

C.2 Conclusion

In this section, we showed that CN_x MWNTs behave as good electrical fillers in a polymer matrix. They permit to reach low percolation thresholds (0.4 vol.% in PS and 0.9 vol.% in PSBS) above which the conductivity increases with a power scaling law. It is also demonstrated that the physico-chemical nature of the matrix plays an important role in the dispersion of CN_x MWNTs in the polymer. Indeed different percolation thresholds were observed for two different matrices. However, it is shown that a coating of polymer chains on the external layer of CN_x MWNTs dramatically lowers those conductive properties by insulating the nanotubes. In this case it should be interesting to simulate the electric behavior of a 3D network using a distribution of contact resistances to represent the inhomogeneity of the contacts between the PS-g- CN_x .

Part D Mechanical properties of the CN_x MWNT polymer nanocomposites

In this part, we will discuss the effect of carbon nanotubes and polymer grafted carbon nanotubes on the mechanical properties of polymers. In order to analyze the nanocomposites we synthesized we used DMA, compression test and tensile test. For an easier understanding of the text, we will use the abbreviation a-CN_x for the as received CN_x MWNTs and PS-g-CN_x for Ps grafted CN_x MWNTs.

D.1 Nanocomposites using PS matrix: mechanical properties

D.1.1 Compression tensile test: elastic mechanical behavior

D.1.1.1 Experimental Results

Data displayed in Table 6 are the experimental Young modulus obtained from compression tensile tests at room temperature. The results obtained for nanocomposites reinforced by a-CN_x in a PS matrix are consistent with those reported by the literature [125, 137]. Below the glass transition temperature, with 2.5 vol.% of a-CN_x, we observed an increase of 20% of the Young modulus (PS = 2.02 GPa; 2.5 vol. % a-CN_x composite = 2.51 GPa).

The results obtained with nanocomposites that use PS-g-CN_x, and with nanocomposites using a-CN_x, are quite different. For 2.5 vol.% of filler, we observed an increase of 33% of the elastic shear modulus (PS = 2.02 GPa ; 2.5 vol. % PS-g-CN_x = 2.71 GPa).

Material	Young Modulus (GPa)
PS	2.02
0.05 vol.% a-CN _x	2.32
0.25 vol.% a-CN _x	2.37
0.5 vol.% a-CN _x	2.04
2.5 vol.% a-CN _x	2.51
0.05 vol.% PS-g-CN _x	2.04
0.25 vol.% PS-g-CN _x	2.15
0.5 vol.% PS-g-CN _x	2.25
1 vol.% PS-g-CN _x	2.62
2.5 vol.% PS-g-CN _x	2.72

Table 6 : Experimental results obtained during compression tensile test at ambient temperature for a-CN_x and PS-g-CN_x nanocomposites using a PS matrix

The literature reports numerous of references that demonstrate a reinforcement of polymers by introducing MWNTs or SWNTs [125, 137, 175, 197, 198]. For as produced MWNT, it is reported that the reinforcement effect is largely supported by the interface between matrix and filler. Indeed, it has been shown that the high aspect ratio of MWNT, and as a consequence its very high surface contact permits to reach a better mechanical reinforcement compared to carbon black fillers [125, 175]. Nevertheless, experimental results obtained are weaker than those expected by theoretical calculations. G.M. Odegard [157], using molecular dynamics and an equivalent-continuum model, surmised an increase of 300% of the elastic modulus for 5% of randomly dispersed long carbon nanotubes. Many factors can explain the gap between experimental results and theoretical calculations.

The first argument points out the bad dispersion of carbon nanotubes. Some works confirmed that aggregates tend to minimize the effect of carbon nanotubes mechanical properties enhancement [125, 165]. It has been demonstrated that nanotubes tend to aggregate due to van der Waals forces. It results in a poor CN_x MWNT / matrix contact area, which minimizes load transfer. We can point out that the reinforcement is slightly higher for PS-g-CN_x. We think that the better dispersion of PS-g-CN_x, as previously observed by SEM and TEM Microscopy (Part B: morphology of the CN_x MWNT composites) permits to increase the matrix / filler contact area. Furthermore it is believed that the load transfer could be increased by a stronger interface between the matrix

and the filler. As a consequence, the covalent bounds of PS on the external layer of CN_x MWNTs certainly improve the compatibility of the filler with the matrix.

On the other hand, the nanotubes we used are nitrogen doped (CN_x MWNTs). It was published that nitrogen atoms induce defects in the main carbon structure of the CN_x MWNTs [45], which most likely tend to lower the longitudinal Young's modulus of the CN_x MWNTs. Theoretical calculations conjecture that CN_x MWNT longitudinal modulus ranges from 700 to 800 GPa [48]. Then, we think that the effective modulus of randomly dispersed CN_x MWNTs should be lower than that of classical MWNTs and consequently lowers the mechanical reinforcement too.

To summarize, the low reinforcement of the a-CN_x and PS-g-CN_x should be attributed to:

- A low dispersion of the nanotubes
- Longitudinal elastic modulus of the CN_x MWNTs is lower than conventional carbon MWNTs

Nevertheless, it should be considered that the polymer grafting permits to slightly improve the reinforcement because of a better dispersion.

D.1.1.2 Comparison with the Halpin Kardos Model

In order to fit the experimental Young modulus we obtained for PS-g-CN_x composites, we used the Halpin Kardos model (HK equation). Halpin Kardos approach [170], reformulates the Halpin-Tsai equation considering four layers oriented at 0°, +45°, 90°, -45°. Nevertheless this model is not perfectly adapted to our system, since the authors considered that fillers are straight rigid fibers, and nanotubes have a low flexion modulus (≈ 20 GPa).

If we use the CNT set of parameters required by the HK equation, we get for the nanocomposites, Young modulus values much higher than the experimental data. In order to further analyze the reinforcement mechanisms in our materials, we tried two different ways: (i) we keep the CNT elastic constants given by the literature, and consider the shape factor as adjustable to fit our experimental

data; or (ii) we keep the average shape factor (roughly determined from our observations) and consider the longitudinal modulus as adjustable.

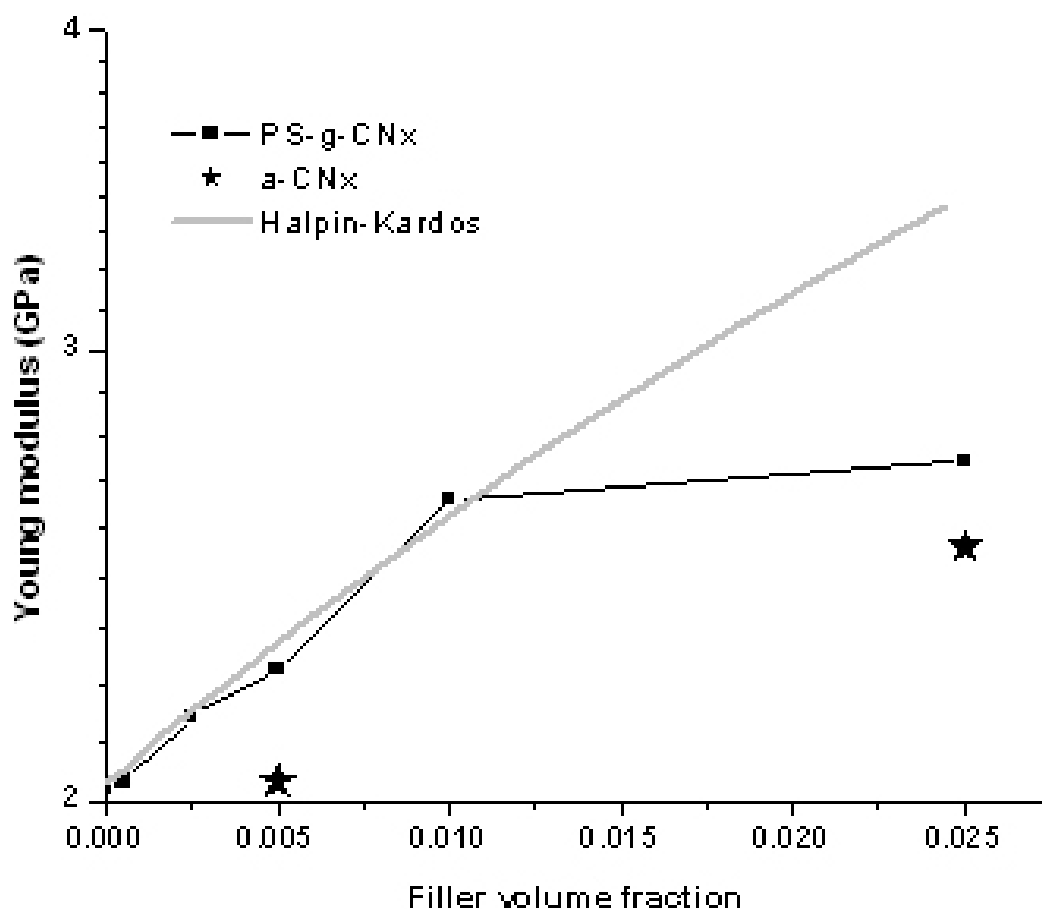


Figure 71: Young modulus experimental results for a-CNx nanocomposites: (-★-); PS-g-CNx nanocomposites (-■-); theoretical results calculated from Halpin Kardos theory (—).

Thus, as a first attempt, we decided to use (i) a theoretical longitudinal modulus of 750 GPa (according to the literature, [48]) and (ii) the nanotube aspect ratio (f) as a free parameter. We should mention that the volume fraction of grafted carbon nanotubes we used in the calculation is the volume fraction of nanotubes without the grafted polymer. Indeed, since the PS matrix has the same properties than the grafted layer, we should consider that the reinforcement effect is mainly supported by the CN_x MWNTs themselves.

Figure 71 displays the results we obtained. We reached the best fit of the PS-g-CNx composite experimental results by using the aspect ratio: $f = 80$. This aspect ratio seems to be very small compared to the real one. Indeed, the aspect ratio is the ratio of the tube length by the tube diameter. The HK model

fit well with experimental results for nanotubes concentrations up to 1 vol.%. On the contrary, we can observe at 2.5 vol.% of PS-g-CN_x that the material presents a modulus far from those calculated with the Halpin Kardos model. It has been shown that for high volume fractions, CN_x MWNTs might "saturate" the matrix. Y. Wang et al. [163] reported, for fraction above 1 vol. % in a polyethylene matrix, similar results: a high volume fraction of MWNTs leads to a decrease of the mechanical properties of the nanotube composite. They attribute this phenomenon to the apparition of aggregates, observed by SEM. In this case, the tubes cannot be considered as perfectly dispersed, and consequently they do not follow the hypothesis of Halpin Kardos where tubes are completely embedded in the matrix. This phenomenon can lower the load transfer and thus explains the differences between calculations and experiments observations.

Concerning the aspect ratio we obtained ($f = 80$), we have shown in "Part B" that a-CN_x MWNTs have an average length of 20 μm and an average diameter of 50 nm, which corresponds to an aspect ratio of about 400. As a consequence, the low aspect ratio we determined by fitting experimental data with the HK equation must be representative of the high waviness of the CN_x MWNTs within the matrix. Nonetheless this result is far from the expected one to explain the mechanical reinforcement of our composites.

The second way to fit experimental data consists in taking the CN_x Young modulus as an adjustable parameter accounting with the true shape factor. We obtained the best fit by using an aspect ratio of 400, and a longitudinal nanotube modulus of 240 GPa. It is clear that the very high longitudinal modulus value of 750 GPa cannot be used since the nanotubes, when dispersed in a polymeric matrix, are far to be perfectly stretched [199]. For example, J.N. Coleman [122], using a Krenchel's rule of mixture to model his experimental results, showed that catalytically grown MWNTs dispersed in chlorinated polypropylene have an effective modulus of 191 GPa what is consistent with the fitted modulus we obtained.

To conclude, both HK fits we have done are not representative of the system we studied. Indeed, the first case has permitted to highlight that the carbon nanotubes in a polymeric matrix are twisted which results in a lower aspect ratio

factor. Thus, one twisted nanotube appears to be equivalent to a set of straight segments, independent each from each other.

The second case confirms that the nanotubes cannot be considered as straight rigid fibers. Therefore it is necessary to take into account the low flexion modulus of the carbon nanotubes in the calculation in order to describe properly our system. Thus, the curvature of the carbon nanotubes leads to a weaker reinforcing effect as compared to those expected by theoretical calculation [157].

D.1.2 Dynamic Mechanical analysis: above the glass transition temperature

As recalled in the chapter III, the drastic dependence of the thickness sample (a) on its stiffness (b) in torsion mode ($b \sim a^3$) leads to a strong uncertainty on shear modulus measurements. In order to correct this uncertainty in the calculation of the conservative modulus induced by the measurement of the samples thickness (≈ 0.5 mm), we chose to calibrate the DMA curves from tensile test data. All the results are presented in Figure 72 and Figure 73.

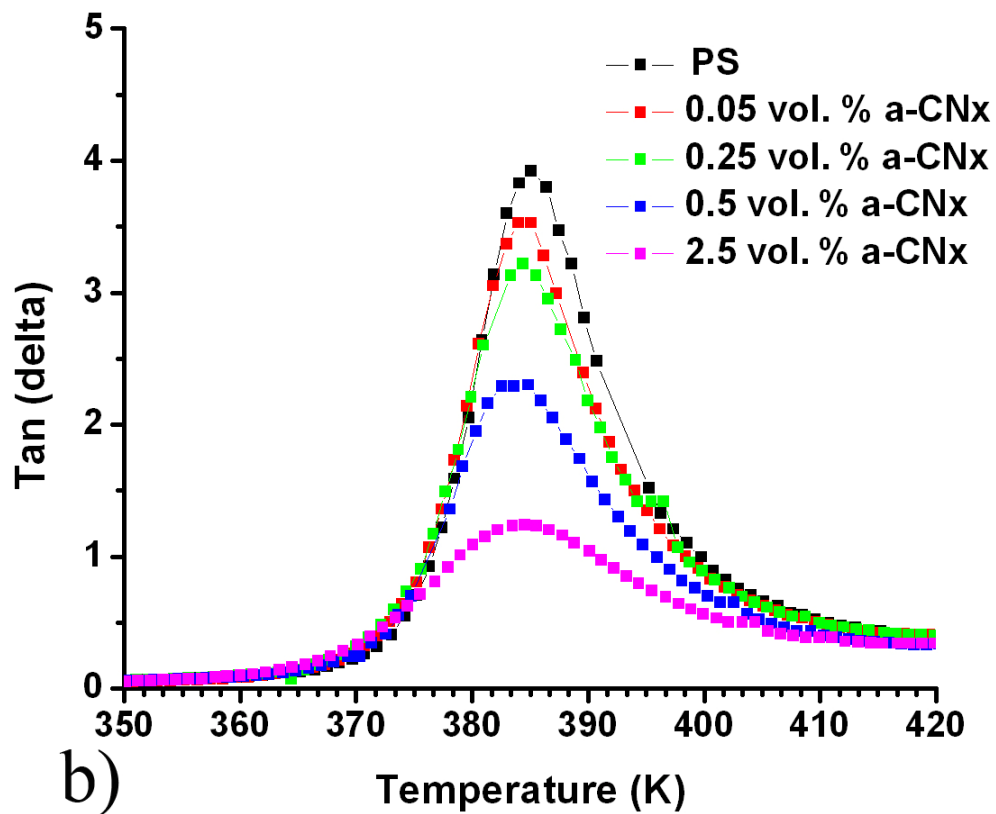
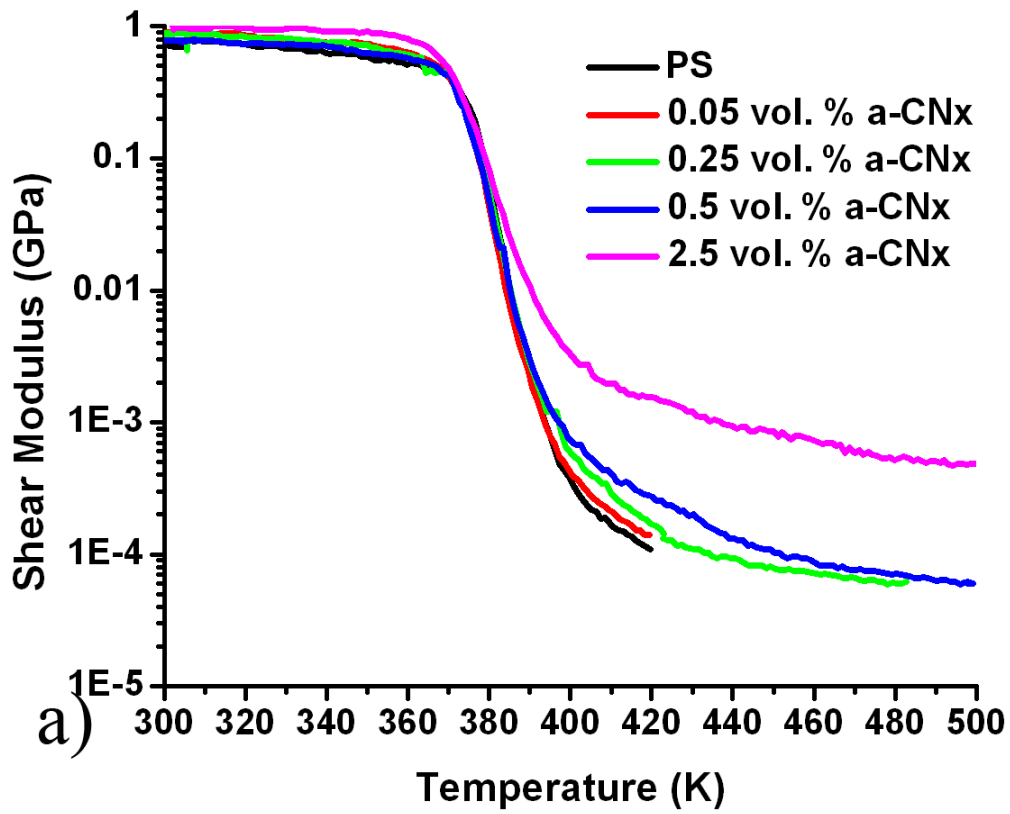


Figure 72: DMA results for the a-CNx / PS composites, a) storage shear modulus as a function of the temperature and b) tangent of the loss angle as a function of the temperature

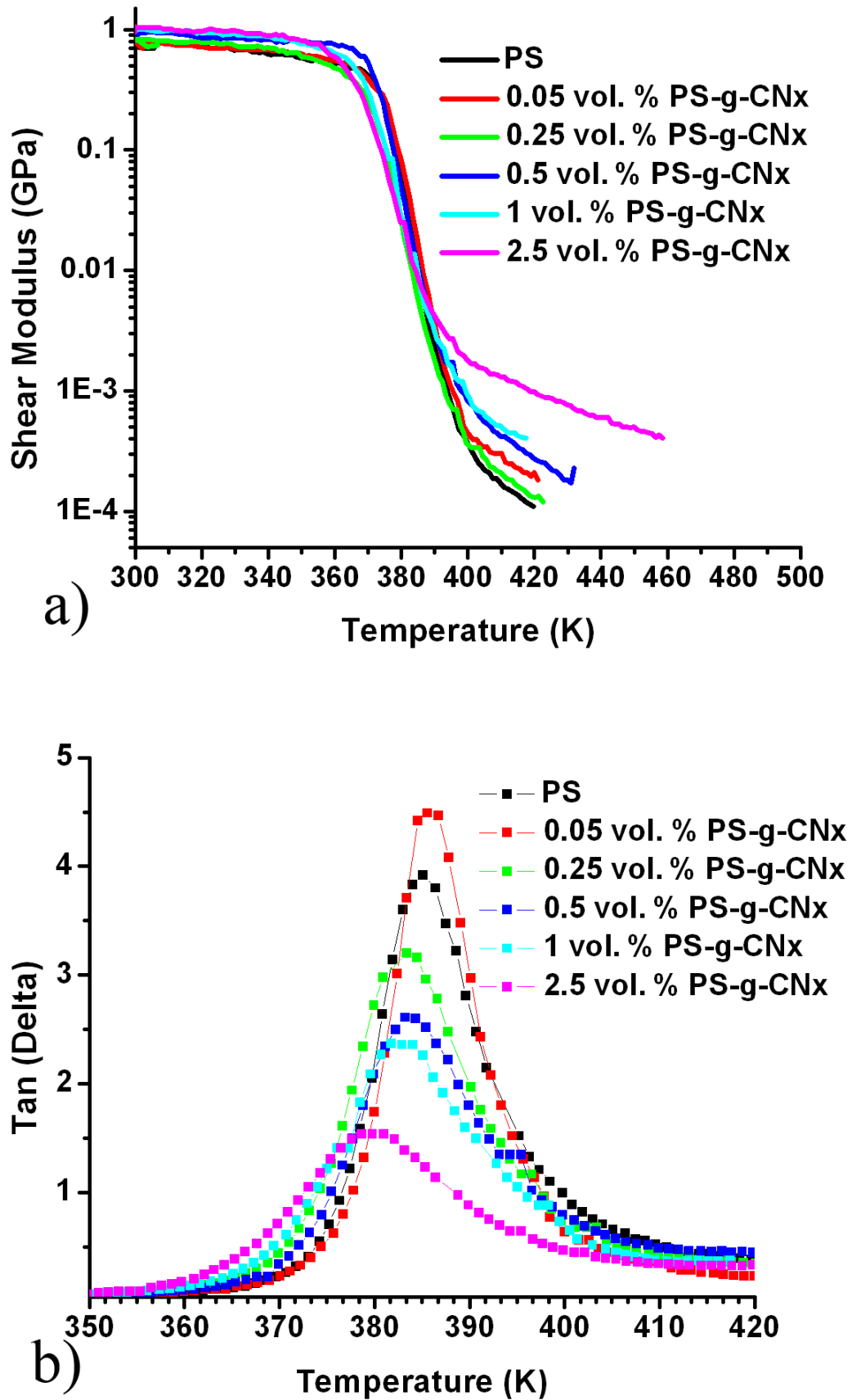


Figure 73: DMA results for the PS-g-CNx / PS composites, a) storage shear modulus as a function of the temperature and b) tangent of the loss angle as a function of the temperature

D.1.2.1 α Transition temperature

Figure 72 b. and Figure 73 b. show $\tan\delta$ as a function of the temperature. Both composites exhibit a decrease of $\tan\delta$ at increasing volume fraction of CN_x MWNTs. a-CN_x (0 to 2.5 vol.% of CN_x MWNTs) nanocomposites exhibit a relative stability of T α temperature: 384 K – 385 K; in agreement with previous measurements of T_g by DSC (C.f. Figure 65). However, some papers have shown that the use of carbon nanotubes could increase the $\tan\delta$ peak temperature [143, 152]. This phenomenon is explained by the limitation of the molecular mobility near the nanofillers surface. Our results do not fit these predictions.

Results obtained for PS-g-CN_x / PS nanocomposites seem interesting. Contrarily to the theory of limited macromolecular mobility near the surface of nanofillers, we observed a shift of T α toward the lower temperatures when increasing the quantity of PS-g-CN_x (PS T α = 385 K, 2.5 vol. % PS-g-CN_x T α = 379,8 K). This result is in accordance with the DSC experiments we exposed in Figure 65, and is representative of an increase of the molecular mobility.

Nevertheless, the position and the broadness of the $\tan\delta$ peak for 2.5 vol.% PS-g-CN_x (shifted toward lower temperatures) should mean that most of the PS matrix has a higher molecular mobility than the original PS. It could mean that most parts of the matrix are in contact or very close to the chemically modified CN_x MWNTs. As a consequence and as well as we commented previously with DSC experiments, it might be a proof that PS-g-CN_x are rather well dispersed.

D.1.2.2 Pseudo plateau characteristics

Above the glass transition temperature, the storage shear modulus of both nanocomposites has different evolutions. In Figure 72 a), we can observe that by increasing the quantity of a-CN_x we increase the temperature T_d, at which the material starts to flow. Therefore, above 0.25 vol. % of a-CN_x the material never flows up to 500 K (maximum temperature reached in these experiments); whereas pure PS flows at 420 K. On the other hand PS-g-CN_x nanocomposites reveal a weaker flowing thermal resistance (cf. Figure 73 b). Most of the PS-g-

CNx composites have a flowing temperature that corresponds to pure PS (420 K). Nevertheless, we can point out that the flowing temperature of composites with 2.5 vol. % of PS-g-CNx starts to increase ($T_d = 460$ K).

Rheological analysis of liquid polymer filled with MWNTs demonstrated that above a given volume fraction of carbon nanotubes (the percolation threshold) a solid-liquid transition is observed [124, 175] comparable to the gelation of a viscoelastic liquid; extensively described by Winter et al. [200]. O. Meincke and co-workers [175] assume that this phenomenon is due to a mechanical percolating network, formed by interlocked tubes. Moreover, F. Dalmas et al. [70] have shown, that nanotubes dispersed in a poly(styrene-co-butyl acrylate) can form a mechanical percolating network when the nanotubes are entangled. They also reported that a simple contact (C.f. Figure 74) between nanotubes is not sufficient to increase the flowing temperature of the nanocomposites.

In the case of PS-g-CNx composites, the grafted polymer layer has a temperature dependent behavior. Above its glass transition temperature (lower than that of the pure PS matrix) the viscosity near the tube surface decreases allowing the nanocomposite to flow more easily than for a-CNx. It is interesting to compare these results with previous works done on electrical behavior of the same nanocomposites (Part C: electrical properties of nanotubes composites). We demonstrated that the grafting electrically isolate the CN_x MWNTs from each other. However, the appearance of an electrical percolation threshold for higher volume fractions of PS-g-CNx permits to prove that not all the tube surfaces are well coated by the polymer. This can explain why the temperature at which composites with 2.5 vol.% of PS-g-CNx start to flow, is higher than for lower fractions PS-g-CNx. As mentioned above, the increase of the flowing temperature is an indicator of the presence of a mechanical percolating network. As we observed with electrical properties of the composites, imperfectly coated tubes should have direct CN_x MWNTs surface contacts, which mechanical properties are almost temperature independent. Thus, it explains why for high volume fractions of PS-g-CNx, we observed an increase of the flow temperature.

Furthermore, we have mentioned that PS-grafted CNx over 1 vol. % tend to "saturate" the matrix and start to aggregate [36]. We should think that aggregates are composed of highly entangled tubes that are more difficult to

separate. Consequently the composite require higher temperatures (more energy) to flow.

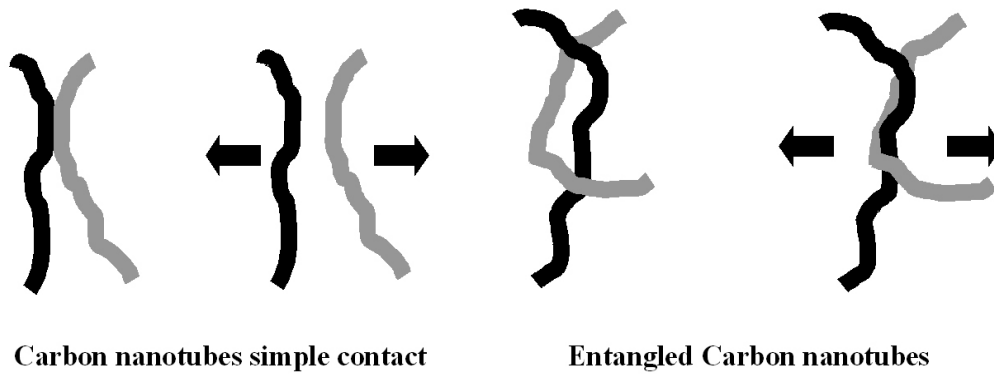


Figure 74: representation of the possible contacts behavior between carbon nanotubes: a) schema of simple contact; b) schema of entangled contact [70]

D.1.2.3 Pseudo plateau characteristics: storage modulus

From DMA experiments, storage shear modulus of the different materials at 420K, are plotted versus the filler volume fraction. They are compared with the Halpin Kardos model using the same parameters as those obtained for composites below the glass transition (i.e. Young modulus of the fiber: 750 GPa, and the aspect ratio $f = 80$). All the results are shown in Figure 75.

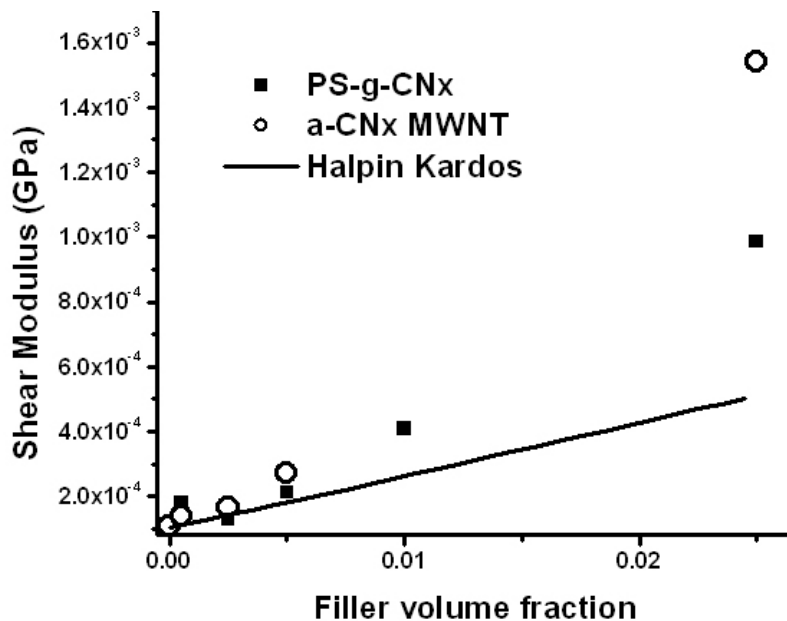


Figure 75: Experimental shear storage modulus at 420 K of PS filled with a-CNx MWNTs (...O...) or PS-g-CNx MWNTs (- ■ -), and shear modulus from Halpin Kardos calculation (—).

Here again, above T_g the mechanical behavior for a-CN_x composites and for PS-g-CN_x composites is different. Storage shear modulus of both CN_x MWNTs composites, with volume fractions less than 0.5 vol. %, are in good agreement with the theoretical prediction from the Halpin Kardos model. For higher volume fractions, both composite exhibit a stronger modulus than predicted by the HK equation. PS-g-CN_x composites are less stiff than a-CN_x MWNTs composites. Figure 76 represents homogeneously dispersed MWNTs in the matrix without any interaction. As a consequence it seems consistent to conclude that the Halpin Kardos model corroborate experimental results for $T > T_g$ when the volume fraction of filler is below the percolation threshold.

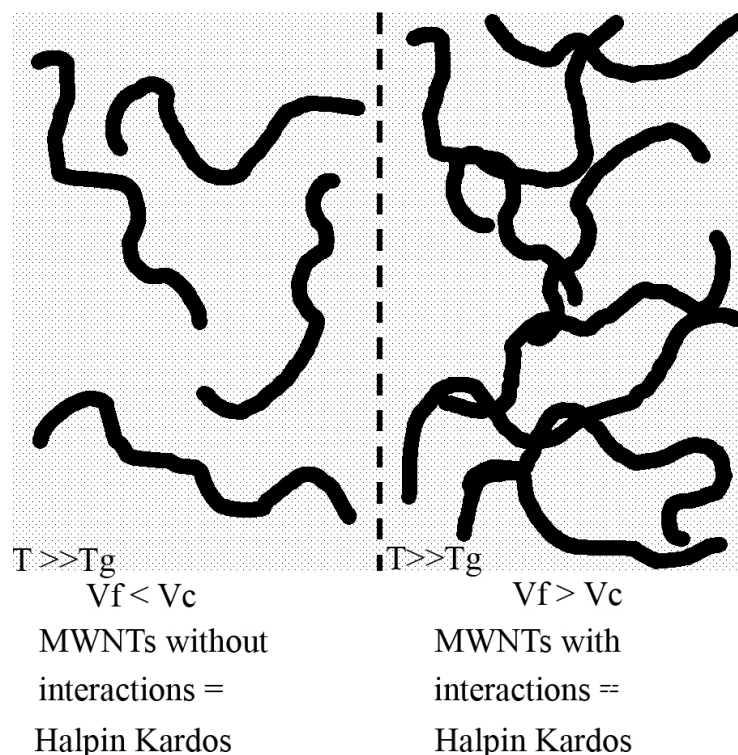


Figure 76: $T \gg T_g$ matrix; when the filler volume fraction lower than the percolation threshold the tubes do not have any interaction and may be modeled by the Halpin Kardos model. For volume fraction of filler higher than the percolation threshold, the interaction between tubes should be considered as strong interaction compared to the shear modulus of the matrix.

These deviations of the mechanical behavior are in agreement with the previous discussion about entangled fibers (C.f Figure 76), thus corroborating the results obtained on the flowing temperatures. Indeed, the mechanical interactions between a-CN_x MWNTs have to be considered as strong interactions as compared to the matrix shear modulus when the volume fraction of a-CN_x MWNTs is above the percolation threshold. So, the Halpin Kardos model is no

more adapted to describe the modulus evolution of the composites. Furthermore, as we observed in the previous paragraph, the PS grafted layer permits the sliding of some interlocked nanotubes and consequently shifts toward higher volume fraction of filler the mechanical percolation threshold.

D.1.3 Large strain deformation

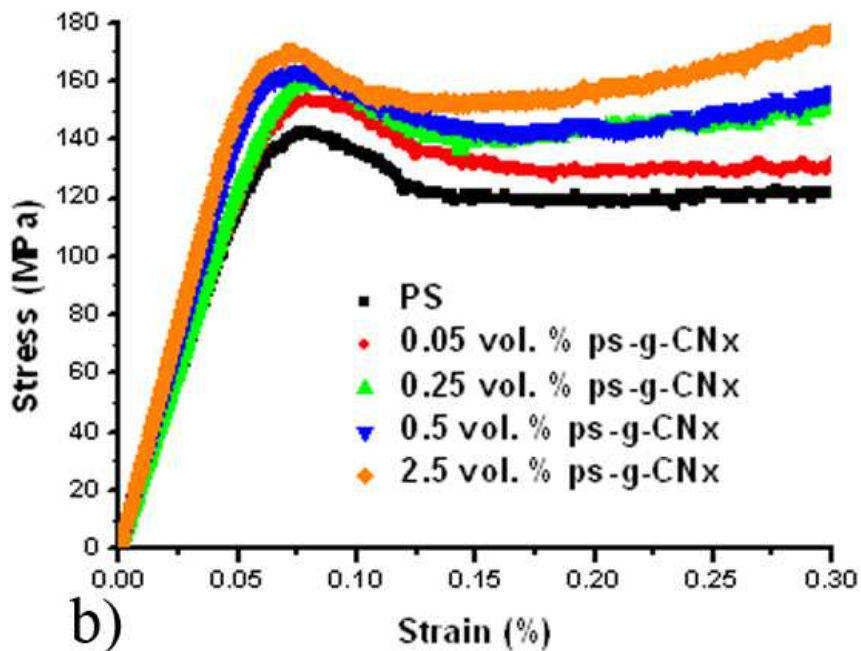
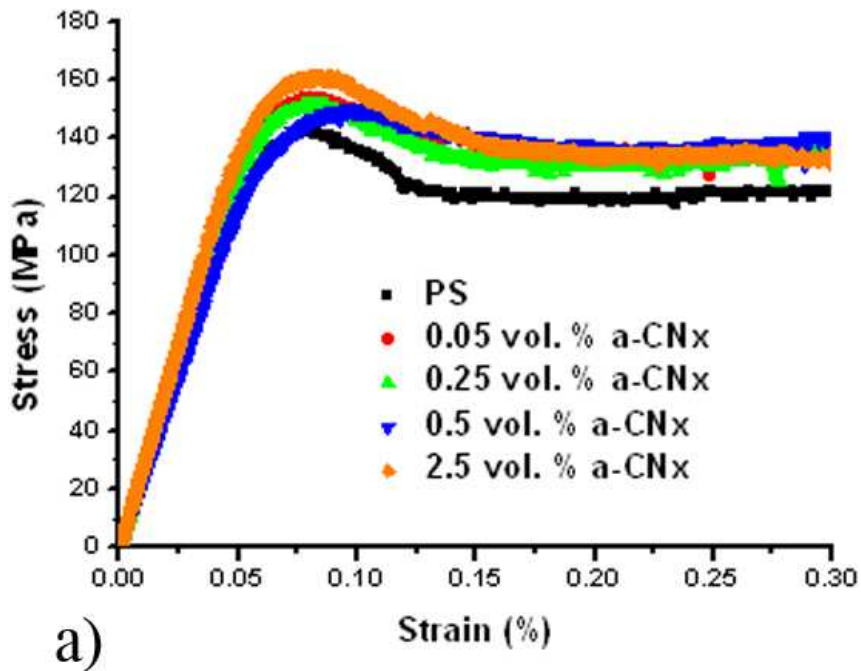


Figure 77: Compression tensile test curves of: a) a-CNx, b) PS-g-CNx.

As shown in Figure 77 and Table 7, it is noteworthy that the addition of CNx MWNTs increases the yield stress in both cases. For nanocomposites with 2.5 vol.% of a-CNx the yield stress increases by 12% , whereas it increases by 19% with 2.5 vol.% of PS-g-CNx. At higher strain, i.e. in the steady state region, experimental curves (Figure 77) exhibit two different behaviors for as produced tubes and for grafted tubes. For as produced tubes, stress appears to be constant, whereas, for grafted tubes at increasing the nanotubes fraction, a hardening phenomenon appears very clearly.

Material	Yield Stress (MPa)	Yield strain (%)	Stress at 27.5% strain (MPa)
PS	142	7.9	122.1
0.05% a-CNx	154	8.1	135
0.25% a-CNx	151	7.9	132
0.5% a-CNx	150	9.7	138
2.5% a-CNx	160	7.9	133.5
0.05% PS-g-CNx	153	8.1	130
0.25% PS-g-CNx	160	8.2	148.5
0.5% PS-g-CNx	162	7.4	153
2.5% PS-g-CNx	169,5	6.9	171

Table 7: Experimental results obtained during compression tensile test for a-CNx and PS-g-CNx with a PS matrix, respectively Yield stress, Yield strain, and stress at 27.5 % strain.

These results confirm the previous dynamic mechanical analysis results we presented previously: grafted CNx MWNTs are better dispersed because they have a better physical-chemical compatibility with the matrix. Thus, it permits to increase the load transfer, and as a consequence the yield stress increases. This hypothesis was confirmed by a theoretical study [158] where individual tubes (equivalent to highly dispersed tubes) are more efficient to reinforce polymer matrices than aggregated tubes.

Concerning the steady state, the hardening is a complex phenomenon that is still being investigated. Generally it is attributed to the limit where the inter-crossed polymer chains are highly stretched and consequently the strain against stress increases rapidly. In a composite material using rigid fillers, the plastic deformation corresponds to the matrix deformation. It is reported that the

main reinforcement phenomenon for as produced nanotubes is due to local shear stress at the interface nanotubes matrix [154]. As mention previously the addition of a-CNx does not have any effect on the PS matrix plastic deformation. It probably means that at these deformations the interface a-CNx / PS is broken and consequently the matrix/nanotube load transfer is not efficient any more. It means that in the case of as-produced CNx MWNTs the activation of pull out phenomenon appears at the matrix yield stress, and it permits to release internal stress by sliding nanotubes through the matrix.

On the contrary, we believe that the polymer grafting permits to preserve the interface even for high strain. V. Favier [201], has shown that a hard coupling between the filler and the matrix permits to increase the reinforcement at high strain due to the physically intercrossed polymer chains that still interacting we the filler until the fracture. The hardening behavior we observed, confirms that PS-g-CNx are chemically bound to polystyrene and moreover we believe that the grafting limits the pull out phenomenon. This behavior is in agreement with TEM analysis we did where we showed that PS-g-CNx do not slide (pull-out) in the matrix.

D.2 Nanocomposites using SBS matrix

D.2.1 Dynamic Mechanical analysis

Dynamic mechanical analysis was used to analyze the viscoelastic behavior of nanocomposites we synthesized using PSBS matrix. Shear modulus and $\tan\delta$ are represented as a function of the temperature in Figure 78u and Figure 79. Results were normalized to 1GPa below the glass transition temperature in order to correct the uncertainty induced by sample dimensions measurements. By the way we cannot do any comments on the effect of CNx MWNTs in a PSBS matrix for experiments below T_g . However we should expect a behavior similar to that of composites using PS matrix below T_g . Indeed, introduced in a stiff matrix, nanotubes should increase the modulus following mean field approach.

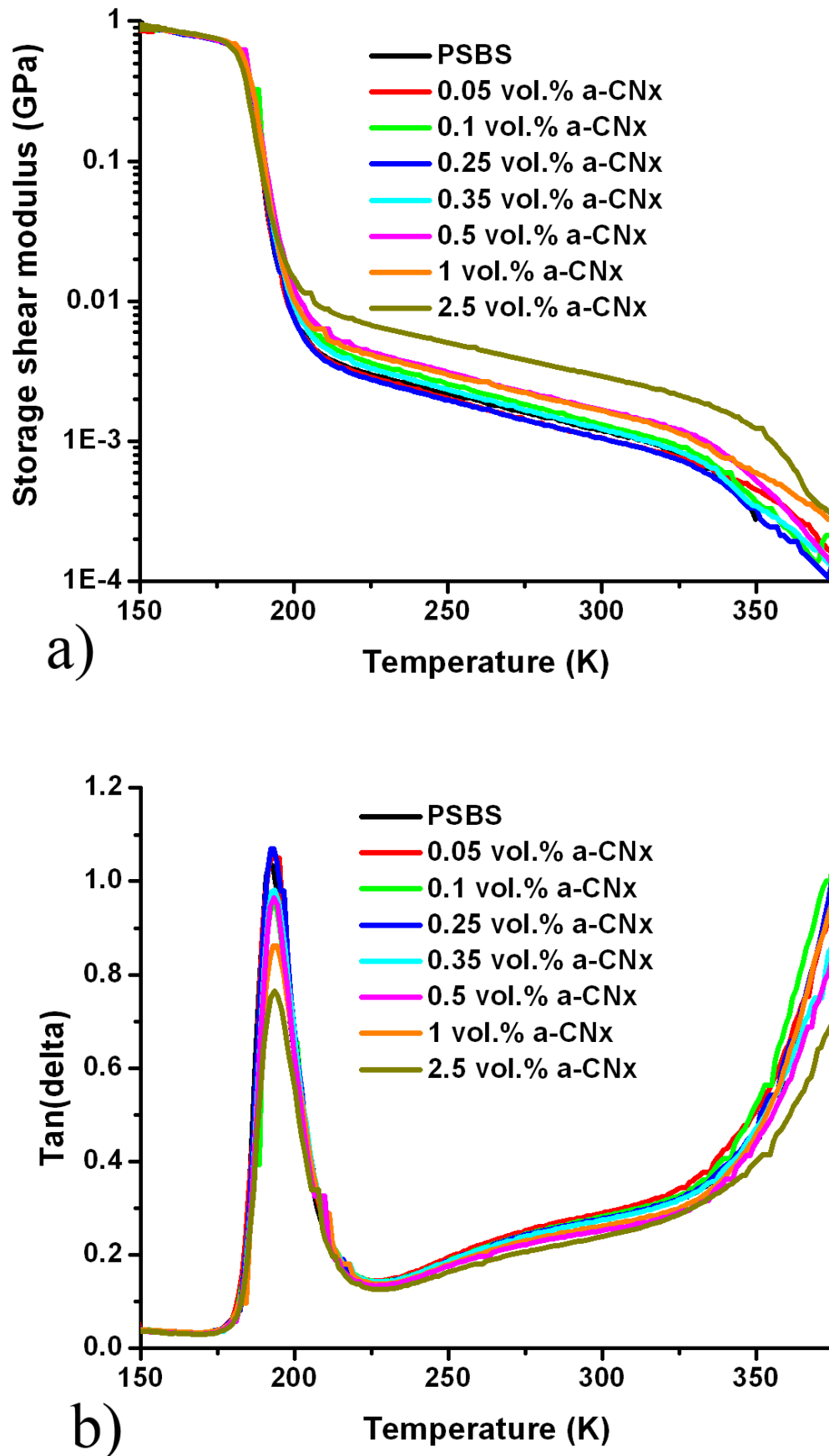


Figure 78: DMA results for the a-CNx / PSBS composites, a) storage shear modulus as a function of the temperature and b) tangent of the loss angle as a function of the temperature

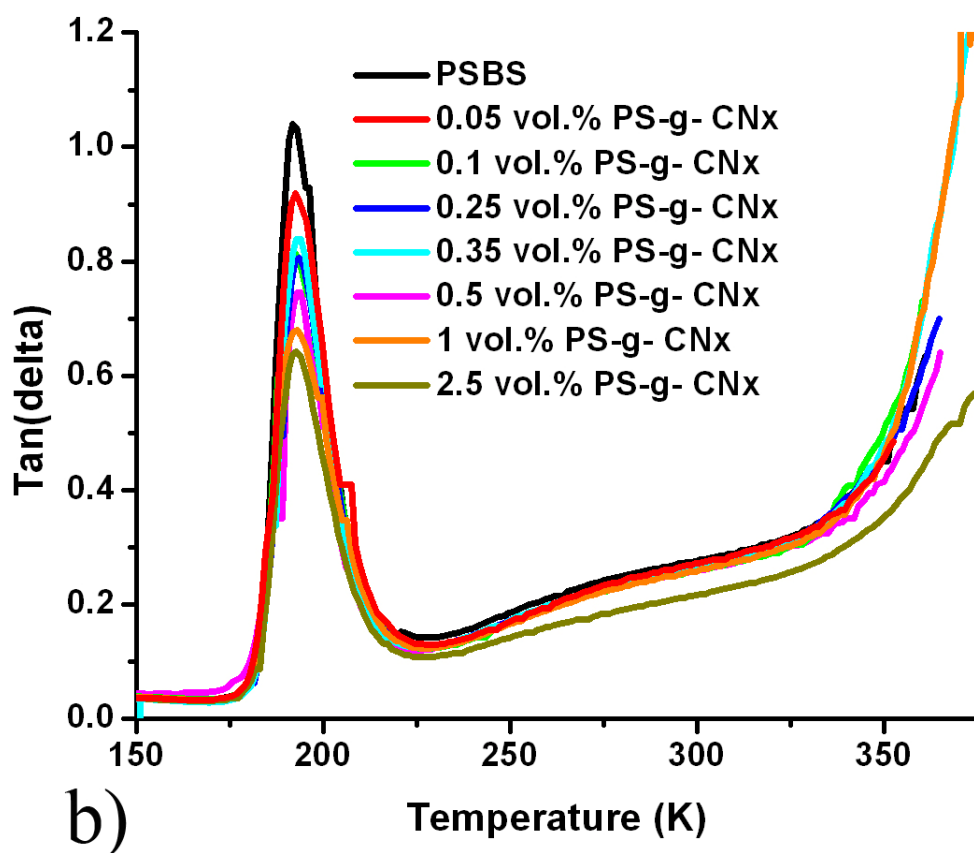
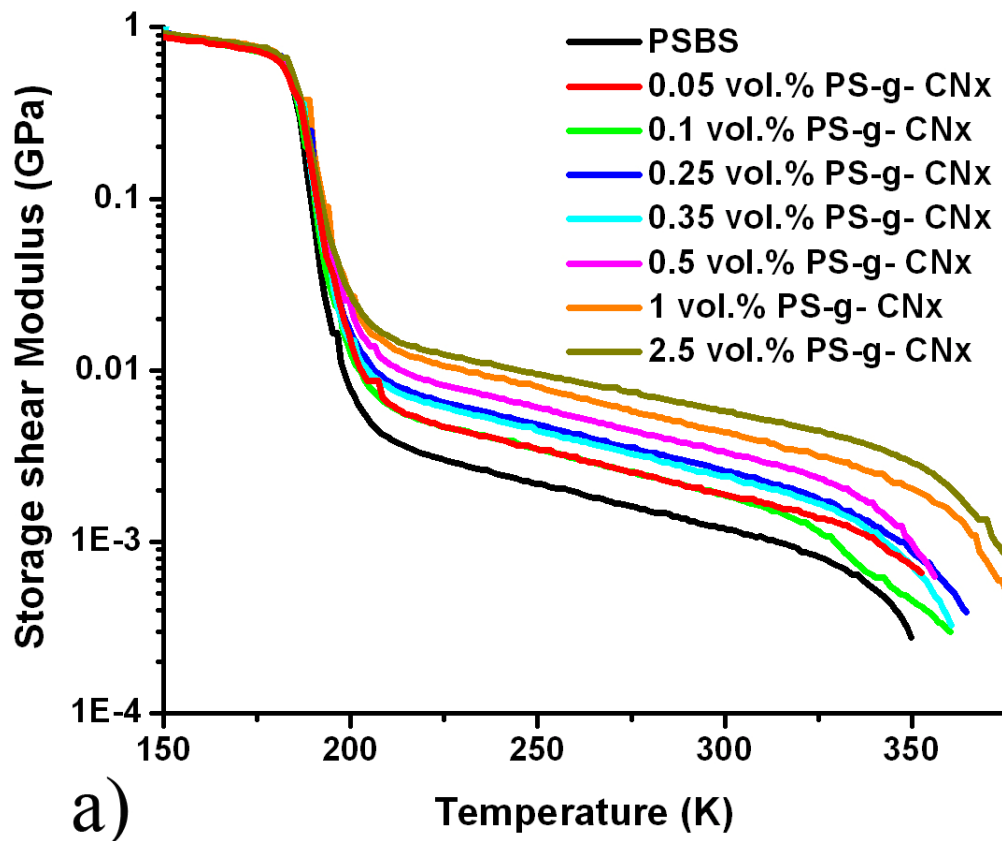


Figure 79: DMA results for the PS-g-CNx / PSBS composites, a) storage shear modulus versus temperature and b) tangent of the loss angle versus temperature

D.2.1.1 α Transition temperature

Regarding the evolution of $\tan\delta$, as for composites using PS matrices, we can conclude that the introduction of CN_x MWNT and PS-g- CN_x do not have effect on the α -relaxation temperature. DSC experiments did confirm this result: the polybutadiene glass transition occurs at -93°C for all composites.

It has previously been shown that there is no change in the glass transition temperature for a- CN_x / PS composites when increasing the volume fraction of filler. In this case (PSBS matrix), we observe a similar phenomenon, thus confirming that there is no loss of molecular mobility on the surface of a- CN_x for both polymeric matrices. For PS-g- CN_x / PSBS composites there is no effect of the grafting on the polybutadiene glass transition. Indeed, PSBS we used is a block copolymer and each block has its own glass transition. Moreover PS and PB are well known to be immiscible. Therefore, the grafting on the nanotubes surface does not disturb the macromolecular mobility of PB blocks.

D.2.1.2 Storage shear modulus

Both composites (a- CN_x and PS-g- CN_x) present an increase of the shear modulus when increasing the filler volume fraction. For 2.5 vol.% of a- CN_x at room temperature the modulus of the original matrix is increased by about 2.5. For PS-g- CN_x , the increase is even higher: at 0.05% volume of filler, the shear modulus increases by a factor 2 the modulus of pure PSBS, whereas for a- CN_x the increase was of few percents. For 2.5 vol.% of PS-g- CN_x , at room temperature, the increase is more than 5 the modulus of PSBS.

To explain the differences between these materials we need to recall some results from Part B: Morphology of the composites. In Figure 80 we observe a micrograph of the PSBS matrix when adding a- CN_x .

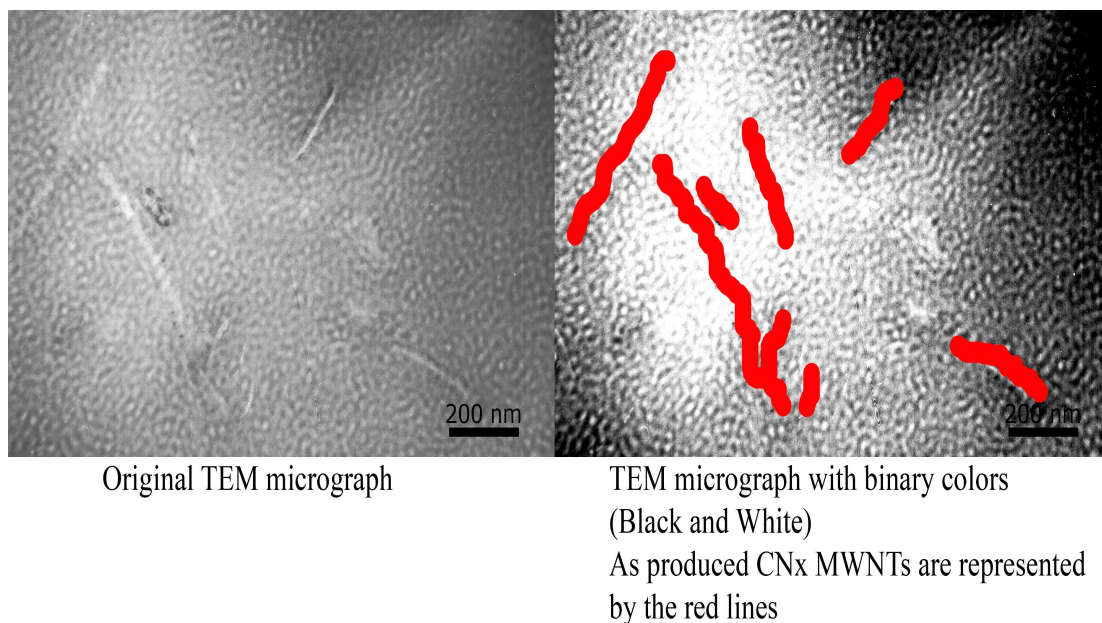


Figure 80: SEM micrograph of the a-CN_x in PSBS; a) original SEM micrograph and, b) treated micrograph to highlight the disorder in the PSBS matrix

As shown previously, the introduction of a-CN_x in PSBS induces disorder in the hexagonal packed structure: the PSBS has a more chaotic structure. From Figure 80, we can assume that most of the CN_x MWNTs are larger than the matrix heterogeneity. Therefore, we should consider that the matrix mechanical properties are uniform along the nanotubes surface. As a consequence the system could be considered as homogenous polymer filled by nanotubes. Then, the a-CN_x composites might be described using the mean field approach, and consequently the results should be described by using the Halpin Kardos model. Thus it explains why we observe a low reinforcement for low concentrations of as produced nanotubes.

On the other hand, we have commented that the introduction of few percents of PS-g-CN_x results in a strong reinforcement of the PSBS matrix. Indeed the morphology of the PSBS matrix is not disturbed when adding PS-g-CN_x. Contrarily to composites reinforced by a-CN_x, by using PS-g-CN_x the hexagonal packed structure is preserved. As shown in Figure 81, The PS domains are longer than 400 nm. Thus, in this system, we cannot consider that the heterogeneities of the matrix are very small as compared to the nanotubes dimensions. As shown in Figure 81, we believe that the PS-g-CN_x allow the interconnection of the matrix PS domains; thus affecting the mechanical properties.

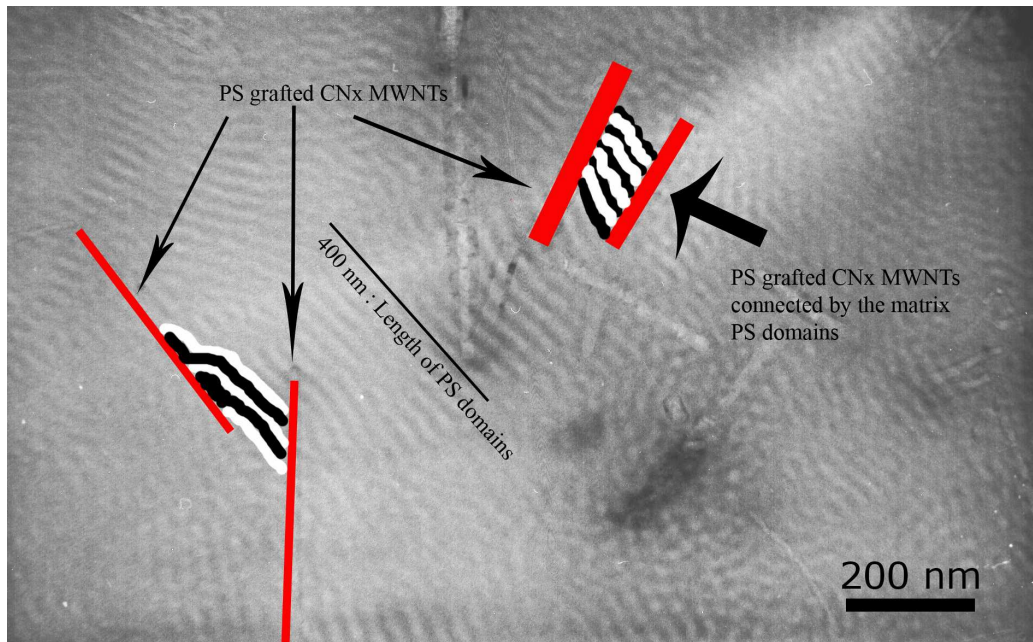


Figure 81: TEM micrograph that represents the hexagonal packed structure preserved when using PS-g-CNx and how PS-g-CNx link the matrix PS domains.

In order to understand the mechanical reinforcement when using PS-g-CNx, it is necessary to consider a local effect of the nanotubes within the matrix. We believe that the strong reinforcement we observed by using PS-g-CNx is representative of a mechanical percolating network obtained by connecting the matrix PS domains. We can note that we obtained a very low percolation threshold (less than 0.05 vol. %).

D.2.2 Tensile test

Tensile test is a useful technique that permitted to confirm and complete previous results obtained with dynamic mechanical analysis. Figure 84 presents the more representative tensile test curve we obtained for each composite.

D.2.2.1 Linear Viscoelastic behavior

In Table 8 it is reported the Young modulus for both composites (PS-g-CNx and a-CNx) at different filler volume fraction. This data are the average value measured on five materials.

Volume fraction of filler	Young modulus (MPa)	
	a-CN _x MWNTs	PS-g-CN _x MWNTs
0.05%	1.53	2.44
0.10%	1.69	2.72
0.25%	1.43	2.93
0.35%	1.84	4.01
0.50%	1.96	4.87
1%	2.46	8.79
2.50%	4.03	13.68

Table 8: Average Young modulus for a-CN_x and PS-g-CN_x composites.

For a-CN_x composites with 2.5 vol. % of fillers we observe an increase by about 3 of the Young modulus, which allows to confirm the DMA data. We can observe that the Young modulus for 2.5 vol.% PS-g-CN_x / PSBS composite increases by about 6 which is consistent with DMA data. As we observed with DMA data, the enhancement in the mechanical properties for PS-g-CN_x composites is stronger than those of a-CN_x composites; particularly for low volume fraction of filler (PSBS modulus = 1.4 MPa, 0.05 vol. % a-CN_x modulus = 1.53 MPa, 0.05 vol. % PS-g-CN_x = 2.44 MPa).

D.2.2.1.1 a-CN_x

From previous discussion on DMA data, we concluded that the nanotubes in a-CN_x MWNTs composites can be considered as totally embedded in the PSBS matrix, without nanotube/nanotube interaction. As consequence, as we did with PS matrix composites, we decided to model the behavior using the Halpin-Kardos equations.

Young modulus of the matrix was chosen equal to 1.4 MPa (experimental data obtained for pure PSBS Young modulus). According to PS matrix composite experiments, the longitudinal modulus of the CN_x MWNTs was chosen at 750 GPa, and we decided to use the aspect ratio factor as a free parameter.

Figure 82 shows the experimental Young modulus obtained for a-CN_x and the Halpin Kardos calculated Young modulus as a function of the filler volume fraction.

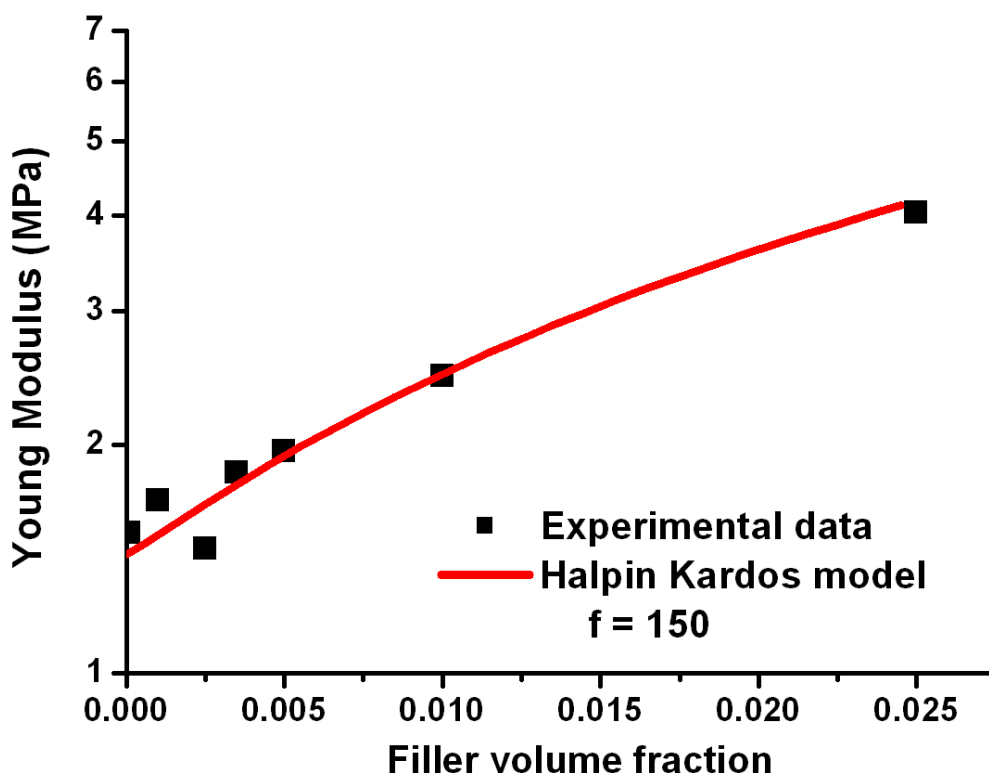


Figure 82: Experimental measured Young modulus of a-CNx / PSBS (-■ -), Prediction of Halpin Kardos mean field approach: $f = 150$ (—),

As we observed previously with the PS matrix, the aspect ratio that permits to fit the experimental results is low ($f = 150$). In order to explain this low value compared to the expected value of about 400 [157], it is necessary to take into account the flexibility of the nanotubes. As we have shown for the PS matrix; the effective longitudinal modulus must be calculated from an average value of the fiber shear modulus (≈ 20 GPa) and the longitudinal fiber modulus, what leads to a weaker reinforcement. Moreover, we should take into account that the aggregates lower the contact area between the matrix and fillers, thus resulting in a lower load transfer.

D.2.2.1.2 PS-g-CNx

Previously we have shown that the PS-g-CNx, when introduced in a PSBS matrix, are able to link together the PS domains and consequently form a rigid network. At the percolation threshold, we expect the existence of a path that would have the mechanical properties of pure PS. Regarding the percolation theory, Ouali et al. in the study of polymer blend [172] have modified the Takayanagi series parallel model [173] by introducing the percolation concept to

mechanical properties of polymers. They demonstrated that the appearance of the percolating continuous paths of rigid phase against the volume fraction filler will follow an exponential scale law and thus mechanical properties of the composite too.

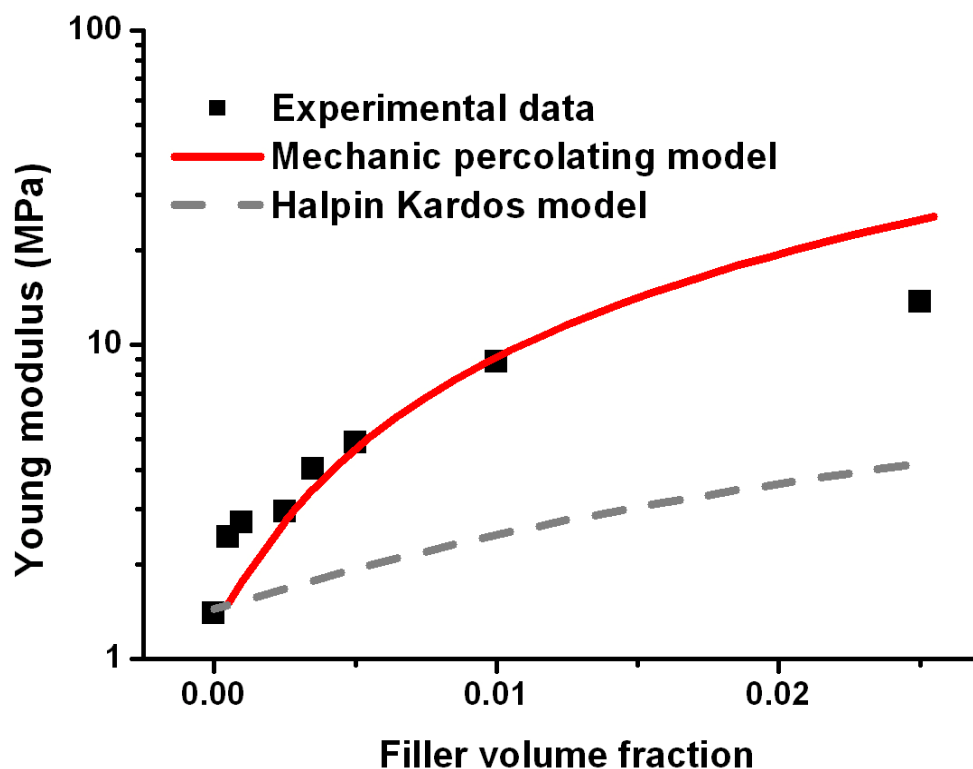


Figure 83: Modulus of PSBS composites as a function of the filler volume fraction: Young Modulus of PS-g-CN_x / PSBS composites (- ■ -), (—) Mechanical percolating model and (- - -) Halpin-Kardos Model.

In Figure 83, the graph represents the evolution of the Young modulus of the PS-g-CN_x nanocomposites as a function of the filler volume fraction.

The jump in mechanical properties even for low volume fraction of PS-g-CN_x indicates that the mechanical percolation is yet reached at 0.1% volume of PS-g-CN_x. Thus we plotted data from the modified series parallel Takayanagi model using $E_s = 1.4$ MPa, $E_r = 2$ GPa (polystyrene Young modulus), $P_c < 0.1$ vol.%, and the critical exponent β was used as a free parameter. The better fit was obtained for $\beta = 1.2$.

Firstly, it must be pointed out that the mean field approach (using the same parameters than those used for a-CN_x composites) does not give a good fit of our experimental results: the nanotubes can not be considered without

interactions between each other. We should have imagined that the reinforcement increase is essentially due to a more important volume fraction of filler. Indeed, in this work we only considered the volume fraction of CNx MWNTs whereas we introduced CNx MWNTs covered by PS. If we consider a more important volume fraction of filler, we cannot explain the drastic reinforcement for few percents of CNx MWNTs by using the mean field approach. Thus, it suggests that the mechanical percolating network gives a good definition of PS-g-CNx composites using PSBS matrix.

Concerning the mechanical percolation fit, as we mentioned before, the very low percolation threshold can be attributed to the peculiar microstructure obtained with the PSBS matrix. Nan [202] reported that for randomly long straight fibers with an aspect ratio of 300, the percolation threshold should be of about 0.3% vol. of filler. The presence of long PS cylinders, within the PSBS matrix, permits to link nanotubes even if there are not in contact. Therefore for very low volume fraction of fillers we observe the appearance of continuous PS paths through the PSBS matrix that lead to a radical increase of the modulus.

Concerning the critical exponent (β), de Gennes [142] reported that it should be of about 1.8. Indeed, it was demonstrated that only the backbone of the connected fillers sustains the stress propagation of the percolating paths. Else, the critical exponent is higher than the theoretical one due to the presence of dead branches which do not participate to the reinforcement mechanism. Nevertheless, the critical exponent we obtained ($\beta = 1.2$) is lower than the one predicted by de Gennes. Indeed, we have shown that the microstructure of the matrix allows connecting nanotubes that are not directly in contact. Thus, as shown in Figure 81, the nanotubes that belong to dead arms are now connected to the backbone via the matrix long PS domains. As a consequence, the quantity of dead arms will be lowered what could explain the low critical exponent we obtained.

Finally, we can observe that for 2.5 vol. % of PS-g-CNx the experimental modulus we measured is lower than the predicted one. As we have shown previously [163], the nanotubes aggregate for concentrations up to 1 vol. %, thus lowering the increase of percolating paths quantity.

D.2.2.2 Large strain deformation

Figure 84 a) and b) represent the more representative tensile test curve at room temperature for a-CNx composites and PS-g-CNx composites. Regarding yield stress and fracture strain of both composites, we can note drastic differences between composites using a-CNx and PS-g-CNx. Both materials present a linear increase of the stress against strain, which is representative of the linear viscoelastic domain. Thus, stress reaches a maximum (yield stress), before a stiffening of the composites that belong to the "plastic" domain.

In the case of a-CNx composites (Figure 84 a.), and for low volume fractions of fillers, the reinforcement is weak: we observed a yield stress increase of 11% for 0.25 vol.% of CNx MWNT. At higher volume fraction of fillers the reinforcement effect is noteworthy. We obtained a yield stress increase by 80% for 2.5 vol. % of a-CNx. On the other hand, for 0.05 vol. % fraction of a-CNx, the strain at break is more than 200%, whereas for 2.5 vol. % of a-CNx the fracture occurs at 75%.

The tensile test results of PS-g-CNx are presented in Figure 84 b. A strong yield stress increase is observed even for the lower filler volume fraction: yield stress enhancement of 65 % with 0.05 vol.% of PS-g-CNx. For higher fillers volume fractions the increase is much more important: 2.5 vol. % PS-g-CNx = 450% enhancement. The strain fracture for only 0.05 vol. % of grafted filler is about 150%, and for 2.5 vol. % of PS-g-CNx we reach a minimum of 15%.

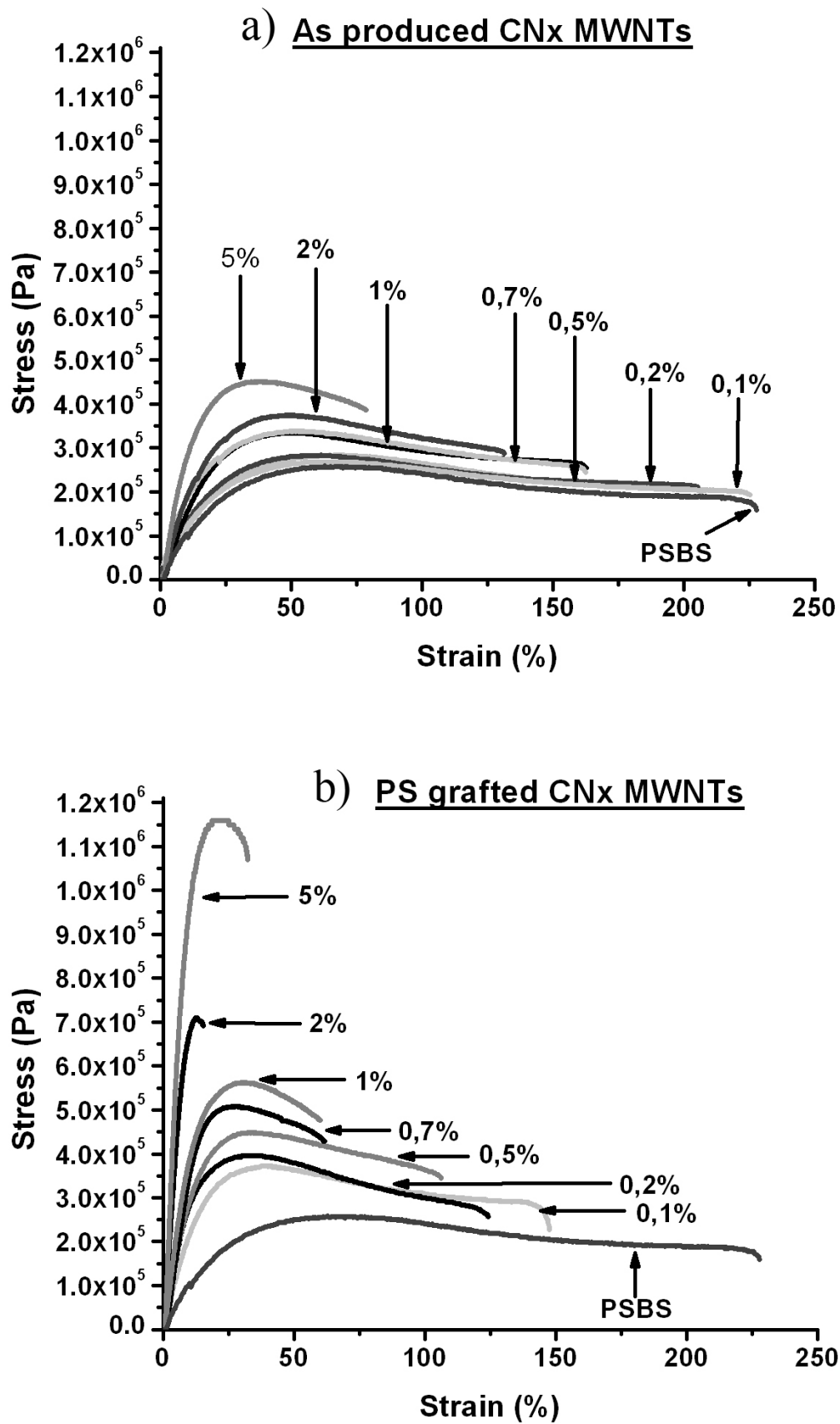


Figure 84: Room temperature tensile test of CNx MWNT composites using a PSBS matrix, a) a-CNx composites, b) PS-g-CNx composites.

Concerning a-CNx, we believe that the increase of the yield stress is representative of the carbon nanotube reinforcement due to the matrix/filler load transfer. As mentioned previously, it is reported that the main reinforcement phenomenon for as produced nanotubes is due to local shear stress at the interface nanotubes matrix [154], thus at increasing the filler volume fraction we increase the filler/matrix interface area and consequently the reinforcement.

Concerning fracture properties of our materials, as shown previously, a-CNx MWTs are pulled out of the matrix during breaking. In the viscoplastic regime, decohesion at the filler/matrix interface is responsible for the loss of ductile properties at increasing fillers volume fraction. Indeed, the defects at the interface matrix/filler result in stress concentrations that damage the material and consequently lead to the fracture [201].

PS-g-CNx have a very different mechanical behavior. In this case, we have demonstrated previously that the reinforcement is supported a percolating rigid network (matrix+PS grafted nanotubes). V. Favier [201] has demonstrated for this kind of system, the reinforcement results from the filler/matrix load transfer and the filler/filler interaction (rigid network cooperation). The effect of the filler/matrix load transfer was described above with the case of a-CNx composites. Thus, it means that the filler/filler interactions have a strong impact on the matrix mechanical properties.

The composite fracture is largely affected by the polymer grafting on the CNx MWNTs. At increasing the volume fraction of filler, the matrix is more brittle. We believe that the rupture of the rigid network cause numerous of defects that result in a rapid propagation of the fracture through the matrix.

D.3 Conclusions

In this part, we have shown that the introduction of a-CNx in polymer matrix results in a low increase of the matrix elastic properties. Nevertheless, we have seen that the grafting of polystyrene on the external layer of carbon nanotubes has permitted to enhance the reinforcement of the composites. We have attributed this phenomenon to the better matrix/filler interface and the better dispersion of the nanotubes within the matrix. The special case of nano-structured PSBS matrix has demonstrated that the nanotube polymer grafting can lead to a strong reinforcement due to existence of a strong nanotube rigid network, where nanotubes are linked by the rigid polystyrene domains.

Interestingly, we have shown that a-CNx are not able to efficiently reinforce a polymer matrix at high strain whereas the PS-g-CNx do. It permits to prove that the grafting of polymer on the nanotubes is an efficient process to strongly enhance the matrix/filler interaction.

Chapter V

Conclusions and perspectives

Part A Conclusions

This PhD thesis presented the analysis of CNx MWNTs / polymer composites. The methodology of this work relies on the synthesis, chemical analyses and description of the microstructure morphology of the different nanocomposites in order to understand their macro physical properties (mechanical and electrical properties). A complex process was established to obtain new carbon nanotubes polymer composites. It was demonstrated that the grafting of polymer on the carbon nanotube surface largely influence the physical properties of the composite.

A.1 synthesis of polystyrene grafted CNx MWNTs

It was demonstrated that free radical chemical addition, which respects the anti Markovitch rule, is able to chemically modify the CNx MWNT surface. TGA analysis confirmed a high efficiency of the aromatic ring grafting. This chemical group permitted the synthesis of an ATRP macroinitiator on the surface of the CNx MWNTs. This ATRP “grafting from” approach was able to completely coat the surface of the CNx MWNTs. Indeed, the tubes were homogenously (coated) with an amorphous layer of PS (3-5 nm thick). HRTEM also confirmed that the main body of the nanotubes remained almost intact after the different chemical treatments. It might confirm that chemical modifications are less destructive than acid treatment processes.

A.2 Morphology and adhesion of the CNx MWNTs composites

Interestingly, we observed changes in the dispersion and adhesion of the CNx MWNTs after polystyrene grafting within both polymer matrices. Indeed, SEM

observations gave some evidence of a better dispersion of the PS-CN_x compared to a-CN_x. Moreover it is noteworthy that the filler / matrix adhesion was improved when using PS-g-CN_x compared to a-CN_x. Indeed, grafting of polystyrene on CN_x MWNTs avoids the pull-out phenomenon when the composites are submitted to a mechanical stress.

Further TEM analyses of the PSBS / CN_x MWNTs composites demonstrated a peculiar morphologic behavior. Indeed the a-CN_x introduce disorder in the hexagonal packed structure of the PSBS, whereas PS-g-CN_x tend to preserve it. We concluded that the nitrogen dopant atoms of the a-CN_x might punctually increase the cohesive forces with the PS blocks and as a consequence locally disturb the hexagonal structure (≈ 100 nm).

On the other hand, the homogenous grafted polystyrene layers of PS-g-CN_x continuously interact with the PS blocks of the PSBS matrix. Thus, we observed that small tubes have a special orientation since they are embedded in the PS cylinders of the hexagonal packed structure. On the contrary, the biggest tubes only cross the matrix without largely disturbing the hexagonal packed structure. It is however noted that the PS cylinders have a preferential orientation close to the PS-g-CN_x, being either parallel or perpendicular to them.

A.3 Electrical properties of CN_x MWNT polymer composites

In this part, we showed that CN_x MWNTs behave as good electrical fillers in a polymer matrix. They permit to reach a low percolation threshold (0.4 vol.% in PS and 0.9 vol.% in PSBS) above which the conductivity increases following a power scaling law. It is also demonstrated that the physical-chemical nature of the matrix plays an important role in the dispersion of CN_x-MWNTs. As a matter of fact, different percolation thresholds were observed for the two different matrices. Moreover, the scaling law presents different critical exponents depending on the matrix used ($t = 2.4$ for PS, and $t = 3.2$ for PSBS). It might signify that the waviness of the CN_x MWNTs changes due to the different physical-chemical interactions between the matrix and the CN_x MWNTs surface.

However, it is shown that the grafting polymer chains on the external layer of CNx MWNTs dramatically lowered those conductive properties by isolating them each others. The presence of a percolating threshold for the nanocomposites containing PS-g-CNx was discussed. It may be explained by a distribution of contact resistances between nanotubes, probably originating from a grafted PS layer with a non uniform thickness.

A.4 Mechanical properties of the CNx MWNT polymer composites

Our results confirmed those published by the literature. Indeed the introduction of carbon nanotubes in a polymer matrix increases its elastic modulus. By using a-CNx the PS Young's modulus was increased by 20 % for 2.5 vol.% of filler, whereas PS-g-CNx composites present an increase of 33.5% for 2.5 vol.% of fillers. On one hand we concluded that the better dispersion of the PS-g-CNx within the matrix compared to the a-CNx permitted to increase the surface contact area between matrix and filler. On the other hand, the polymer grafted layer permitted to reach a better matrix / filler interfacial adhesion and as a consequence increase the load transfer. This phenomenon was highlighted with the results obtained for large strain compression test. Indeed, the hardening of the materials containing PS-g-CNx confirmed drastic changes at the nanotube / matrix interface.

To summarize, the effects of the low molecular weight PS coating of nanotubes, are, (i) a better dispersion in a PS matrix, (ii) a better load transfer from the matrix towards the nanotubes at room temperature, (iii) a drastic decrease of the electrical conductivity of the composites due to the insulator behavior of PS and (iv) at temperature close to Tg of PS (around 100°C), a lubricant effect due to the low Tg (resulting to the low molecular weight of the PS coating). This later effect decreases the temperature at which composites start to creep. All of these effects confirm that the PS coating has been successfully performed, which in turn opens to various applications.

Part B Further works and perspectives

B.1 Carbon nanotubes chemical modification

Further works on the ATRP “grafting from” kinetic should be interesting in order to identify the effect of the polymer chain sizes on the dispersion. Furthermore, it would be interesting to observe the impact of the grafted polystyrene layer thickness on the carbon nanotube electrical contact resistance. Complementary EPR analyses should be a way to define the reaction kinetic variable.

The use of a living controlled free radical polymerization process could allow the synthesis of grafted block copolymers. We expect that this kind of material would provide new composites morphologies.

We have shown that it was possible to open the carbon π double bond of the carbon nanotubes. As a consequence, we expect that it is possible to link nanotubes by strong carbon-carbon covalent bonds.

B.2 Morphology of PS grafted carbon nanotubes

We observed that small grafted PS-g-CN_x tend to integrate preferentially a part of the structured PSBS. We suggest to confirm this result by using polymer grafted double walled carbon nanotubes. Indeed, we believed that their small diameter will permit to selectively disperse them in a specific phase of the structured polymer.

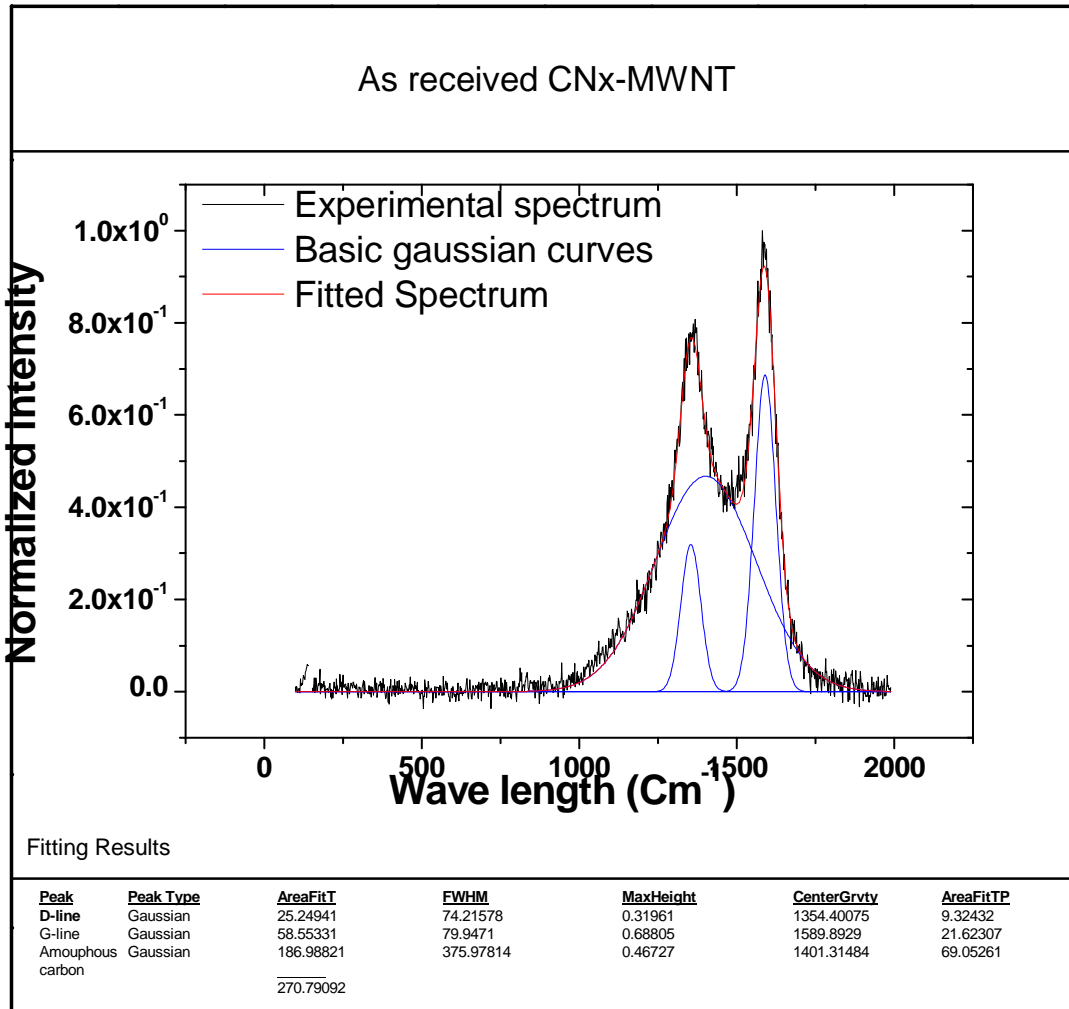
B.3 Electrical behavior of polymer grafted carbon nanotubes

Previous works [148], using numerical simulations have largely described the effect of the tube waviness on the electrical percolation threshold and the scaling low critical exponent. But it was considered a constant nanotube electrical contact resistance. We have seen that the polymer grafting seems to dramatically increase this resistance. Nevertheless, we demonstrated that the polymer grafted layer leads to a continuous distribution of contact resistances. As a consequence, to confirm our hypothesis, it should be interesting to simulate the electrical properties of carbon nanotube networks considering such a distribution. We suggest to use a log normal distribution in order to take into account that the contact resistances varie over several decades ($\approx 1.10^{16}$ ohms to some ohms)

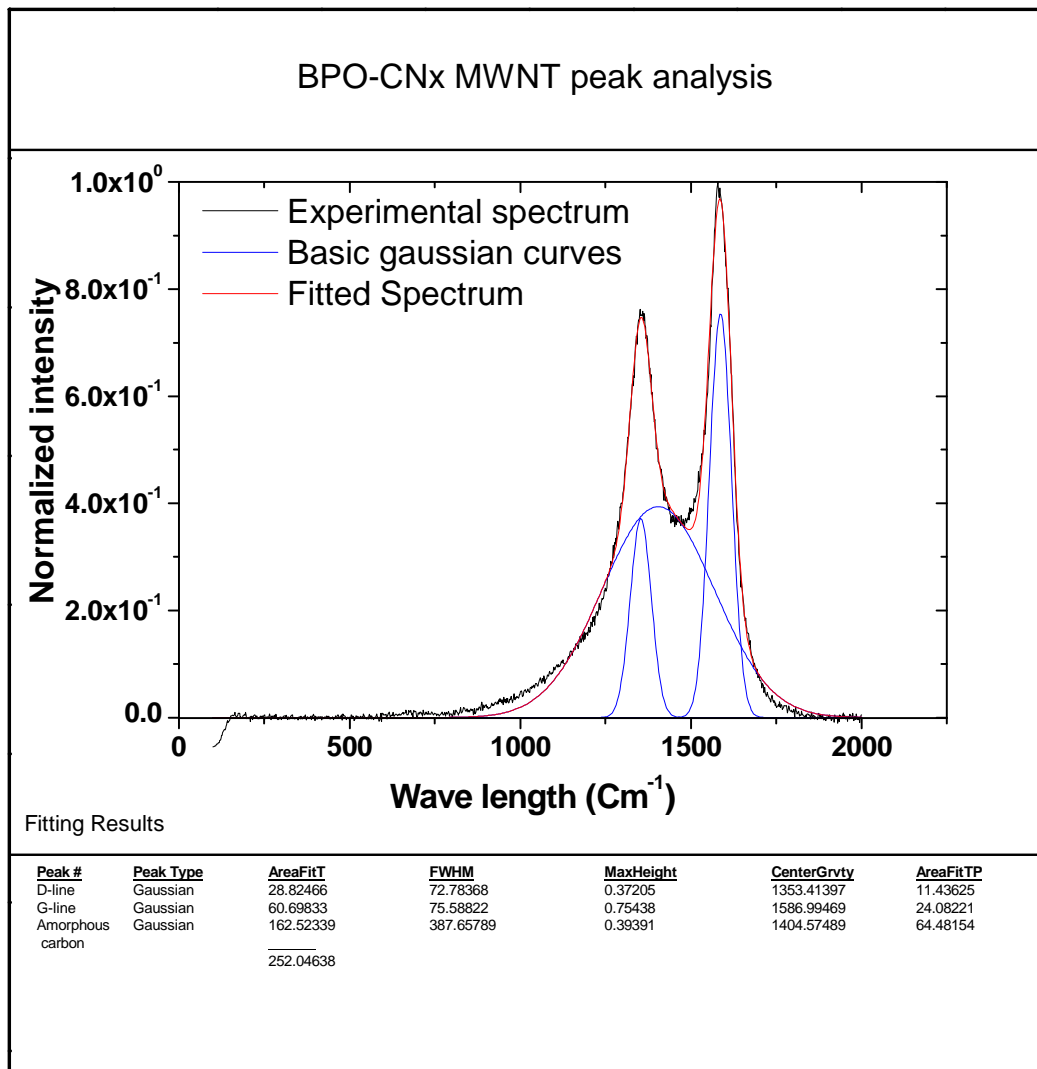
B.4 Mechanic properties of polymer carbon nanotubes composites

It would be interesting to perform further studies under large stress-strain condition. Indeed, the results we obtained have demonstrated the role of nanotube/filler interface; nevertheless we have no information about the mechanism involved in the hardening observed for PS grafted nanotubes for large deformations, and more generally on the damage effect such as decohesion, on the macroscopic behavior.

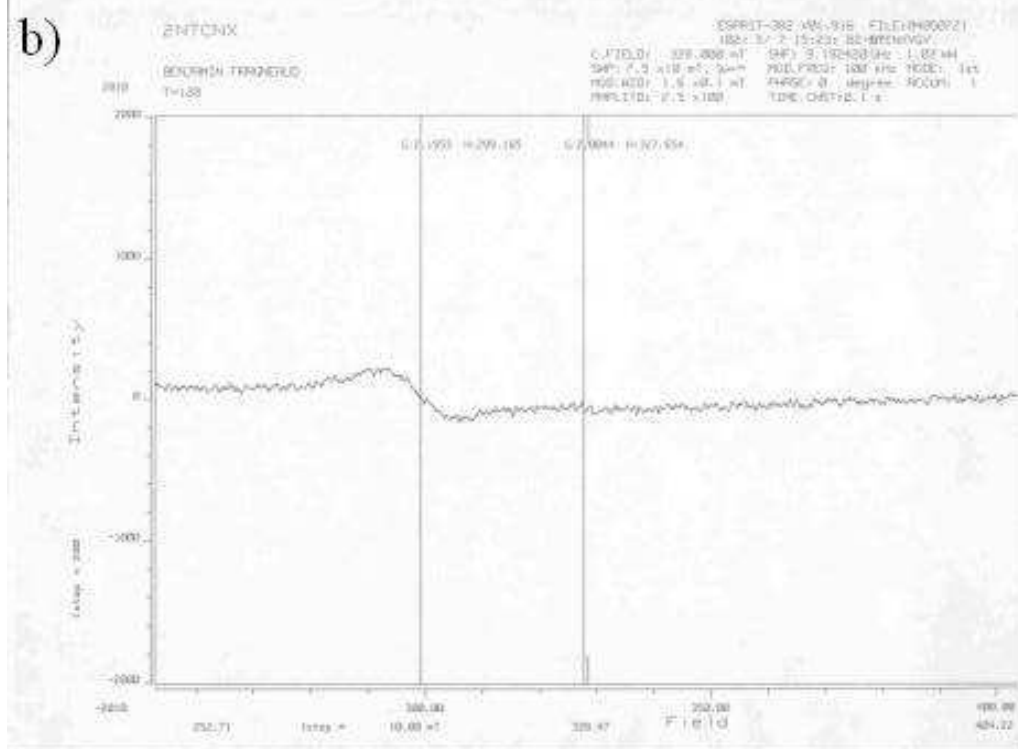
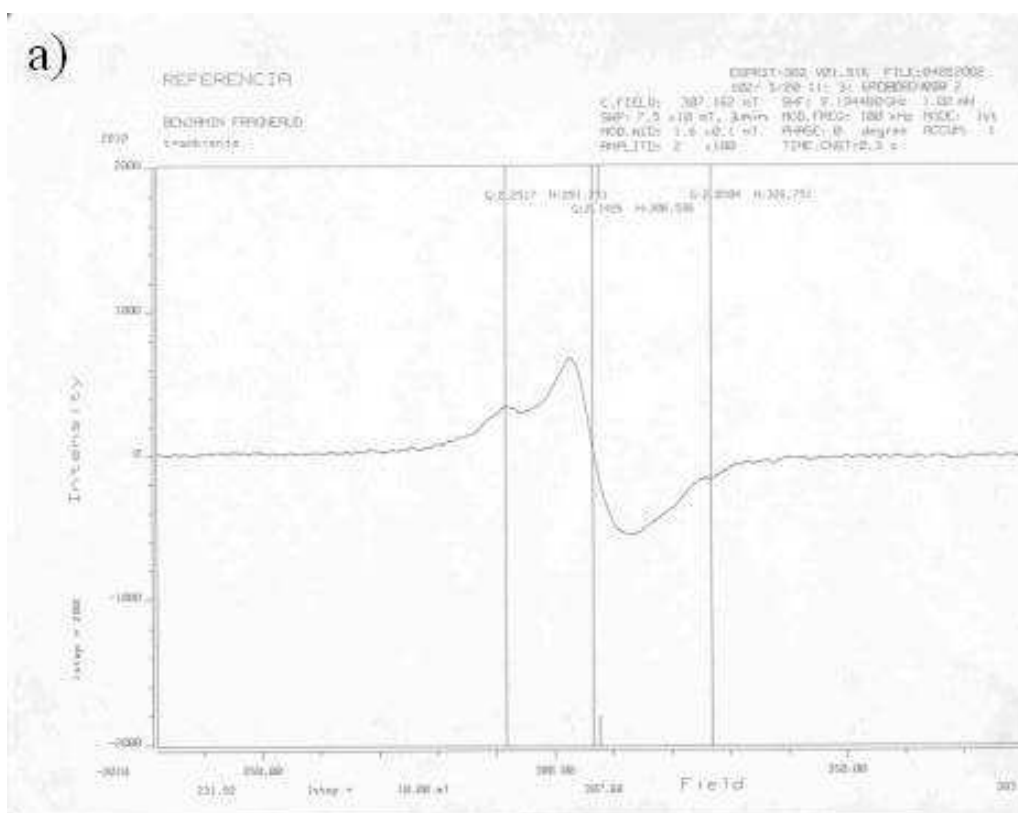
Annex I.a



Annex I.b



Annex II



Bibliography

- [1] **S. Iijima**
Helical microtubulus of graphitic carbon, Nature, (1991) vol. 354: p. 56-58
- [2] **H. W. Kroto, J. R. Heath, S. O'Brien, R. F. Curl and R. E. Smalley**
C60: Buckminsterfullerene, Nature, (1985) vol. 318: p. 162-163
- [3] **M. Ge and K. Sattler**
Scanning tunnelling microscopy of single shell nanotube of carbon, Appl. Phys. Lett., (1994) vol. 65: p. 2284
- [4] **N. Hamada, S. Sawada and A. Oshiyama**
New one dimensional conductors: graphitic microtubules, Phys. Rev. Lett., (1992) vol. 68: p. 1579-1581
- [5] **R. Saito, M. Fujita, G. Dresselhaus and M. S. Dresselhaus**
Electronic structure of chiral graphene tubules, Appl. Phys. Lett., (1992) vol. 60: p. 2204-2206
- [6] **M. Treacy, T. W. Ebbesen and J. M. Gibson**
Execeptionally high Young's Modulus Iberved for individual carbon nanotubes, Nature, (1996) vol. 381: p. 678-680
- [7] **E. W. Wong, P. E. Sheehan and C. M. Lieber**
Nanobeam Mechanics: Elasticity, Strength, and toughness of nanorods and nanotubes, Science, (1997) vol. 277: p. 1971-1975
- [8] **M. R. Falvo, G. J. Clary, R. M. Taylor, V. Chi, F. P. Brooks, S. Washburn and R. Superfine**
Bending and buckling of carbon nanotubes under large strain, Nature, (1997) vol. 389: p. 582-584
- [9] **T. W. Ebbesen and P. M. Ajayan**
Large-scale synthesis of carbon nanotubes, Nature, (1992) vol. 361: p. 333
- [10] **T. Guo, P. Nikolaev, A. G. Rinzler, D. Tomanek, D. T. Colbert and R. E. Samlley**
Self.assembly of tubular fullerenes, J.Phys. Chem., (1995) vol. 99: p. 10694-10697
- [11] **M. Terrones**
PhD, (1997) Univ Sussex
- [12] **W. K. Hsu, J. P. Hare, M. Terrones, H. W. Kroto, D. R. M. Walton and P. J. F. Harris**
Condensed-phase nanotubes, Nature, (1995) vol. 377: p. 687

- [13] **D. Laplaze, P. Bernier, W. K. Maser, G. Flamant, T. Guillard and A. Loiseau**
Carbon nanotubes: the solar approach, Carbon, (1998) vol. 36: p. 685-688
- [14] **R. Kamalakaran, M. Terrones, T. Seeger, P. Kohler-Redlich and M. Ruhle**
Synthesis of thick crystalline nanotube arrays by spray pyrolysis, Appl. Phys. Lett., (2000) vol. 77: p. 3385-3387
- [15] **X. K. Wang, X. W. Lin, V. P. Dravid, J. B. Katterson and R. P. H. Chang**
Carbon nanotubes produced in hydrogen arc discharge, Appl. Phys. Lett., (1995) vol. 66: p. 2430
- [16] **L. Dong, J. Jiao and C. L. Mosher**
Growth of carbon nanotubes with controlled morphologies, Mat. Res. Soc. Symp. Proc., (2002) vol. 728: p. S.8.21.1
- [17] **R. T. K. Baker and P. S. Harris**
The formation of filament carbon, Chem. Phys. Carbon, (1978) vol. 14: p. 83
- [18] **T. Baird and J. R. Fryer**
Carbon formation on iron and nickel foils by hydrocarbon pyrolysis-reactions at 700 °C, Carbon, (1974) vol. 12: p. 591-603
- [19] **G. Tibbets**
Carbon fibers produced by pyrolysis of natural gas in stainless steel tubes, Appl Phys. Lett., (1983) vol. 42: p. 666-667
- [20] **H. M. Cheng, F. Li, G. Su, H. Y. Pan, L. L. He, X. Sun and M. S. Dresselhaus**
Large-scale and low cost synthesis of single walled carbon nanotubes by catalytic pyrolysis of hydrocarbons, Appl. Phys. Lett., (1998) vol. 72: p. 3282-84
- [21] **M. Terrones**
Science and technology of the twenty-first century: synthesis, properties and applications of carbon nanotubes, Annu. Rev. Res., (2003) vol. 33: p. 419-501
- [22] **G. Baumgartner, M. Garrard, L. Zuppirolo, W. Bacsa, W. A. d. Heer and L. Forro**
Hall effect and magnetoresistance of carbon nanotube films, Phys. Rev. B, (1997) vol. 55: p. 6704-6707
- [23] **W. A. D. Heer, W. S. Bacsa, A. Chatelain, T. Gerfin, R. Humphrey-Baker, L. Forro and D. Ugarte**
Aligned carbon nanotubes films: production and optical and electronics properties, Science, (1995) vol. 268: p. 845-847
- [24] **W. A. D. Heer, A. Chatelain and D. Ugarte**
A carbon nanotube field-emission electron source, Science, (1995) vol. 270: p. 1179-1180
- [25] **M. Terrones, W. K. Hsu, A. Schilder, H. Terrones, N. Grobert, J. P. Hare, Y. Q. Zhu, M. Schwoerer, K. Prassides, H. W. Kroto and D. R. M. Walton**

Novel nanotubes and encapsulated nanowires, Appl. Phys. A., (1998) vol. 66: p. 307-317

[26] **H. Dai, E. W. Wong and C. M. Lieber**

Probing electrical transport in nanomaterials: conductivity of individual carbon nanotubes, Science, (1996) vol. 272: p. 523-526

[27] **M. Terrones, W. K. Hsu, J. P. Hare, H. W. Kroto, H. Terrones and D. R. M. Walton**

Graphitic structures: from planar to spheres, toroids and helices, Philos. Trans. R. Soc. London Ser. A., (1996) vol. 354: p. 2025-2054

[28] **H. Terrones, M. Terrones, E. Hernandez, N. Grobert, J. C. Charlier and P. M. Ajayan**

New metallic allotropes of planar tubular carbon, Phys. Rev. Lett., (2000) vol. 84: p. 1716-1719

[29] **M. F. Yu, B. S. Files, S. Arepalli and R. S. Ruoff**

Tensile loading of ropes of single wall carbon nanotubes and their mechanical properties, Phys. Rev. Lett., (2000) vol. 84: p. 5552-5555

[30] **G. Overney, W. Zhong and D. Tomanek**

Structural rigidity and low frequency vibrational modes of long carbon tubules, Z. Phys. D., (1993) vol. 27: p. 93-96

[31] **D. H. Robertson, D. W. Brenner and J. W. Mintmire**

Energetics of nanoscale graphitic tubules, Phys. Rev. B., (1992) vol. 45: p. 12592-12595

[32] **J. Tersoff**

Energies of fullerenes, Phys. Rev. B., (1992) vol. 46: p. 15546-15549

[33] **A. Krishnan, E. Dujardin, T. W. Ebbesen, P. N. Yianilos and M. M. J. Treacy**

Young's modulus of single-walled nanotubes, Phys. Rev. B, (1998) vol. 58: p. 14013-019

[34] **Z. Pan, S. Xie, L. LU, B. Chang, L. Sun, W. Zhou, G. Wang and D. Zhang**

Tensile tests of ropes of very long aligned multiwall carbon nanotubes Appl. Phys. Lett., (1999) vol. 74: p. 3152-3154

[35] **D. A. Walter, L. M. Ericson, M. J. Casavant, J. Liu, D. T. Colbert, K. A. Smith and R. E. Smalley**

Elastic strain of freely suspended single-wall carbon nanotube ropes, Appl. Phys. Lett., (2004) vol. 74: p. 3803-3805

[36] **P. Poncharal, Z. L. Wang, D. Ugarte and W. d. Heer**

Electrostatic deflections and electrochemical resonances of carbon nanotubes, Science, (1999) vol. 283: p. 1513-1516

- [37] **J. P. Salvetat, A. J. Kulik, J. M. Bonard, G. Andrew, D. Briggs, T. Stockli, K. Méténier, S. Bonnamy, F. Béguin, N. A. Burnham and L. Forró**
Elastic Modulus of Ordered and Disordered Multiwalled Carbon Nanotubes, *Advanced Material*, (1999) vol. 11: p. 161-165
- [38] **J. P. Salvetat, G. Andrew, D. Briggs, J. M. Bonard, R. R. Bacsá, A. J. Kulik, T. Stockli, N. A. Burnham and L. Forró**
Elastic and Shear Moduli of Single-Walled Carbon Nanotube Ropes, *Phys. Rev. Lett.*, (1999) vol. 82: p. 944-947
- [39] **M. Yu, O. Lourie, M. J. Dyer, K. Moloni, T. F. Kelly and R. S. Ruoff**
Strength and Breaking Mechanism of Multiwalled Carbon Nanotubes Under Tensile Load, *Science*, (2000) vol. 287: p. 637-640
- [40] **H. W. Zhu, C. L. Xu, D. H. Wu, B. Q. Wei, R. Vajtai and P. M. Ajayan**
Direct Synthesis of Long Single-Walled Carbon Nanotube Strands, *Science*, (2002) vol. 296: p. 884-886
- [41] **B. G. Demczyk, Y. M. Wang, J. Cumings, M. Hetman, W. Han, A. Zettl and R. O. Ritchie**
Direct mechanical measurement of the tensile strength and elastic modulus of multiwalled carbon nanotubes, *Mat. sci., Eng. A*, (2002) vol. 334: p. 173-178
- [42] **H. Qi, K. Teo, K. Lau, M. Boyce, W. Milne, J. Robertson and K. Gleason**
J. Mech. Phys. Sol., (2003) vol. 51: p. 2213-2237
- [43] **M. Terrones, R. Kamalakaran, T. Seeger and M. Ruhle**
Novel nanoscale gas containers: encapsulation of N₂ in CN_x nanotubes, *Chem Com*, (2000) vol. p. 2335-2336
- [44] **M. Terrones, N. Grobert, H. Terrones, P. M. Ajayan, F. Banhart, X. Blase, D. L. Carroll, R. Czrew, B. Foley and J. C. Charlier**
Doping and connecting carbon nanotubes, *Mol. Cryst. Liq. Cryst.*, (2002) vol. 387: p. 275-286
- [45] **M. Terrones, A. Joriot, M. Endo, A. M. Rao, Y. A. Kim, T. Hayashi, H. Terrones, J. C. Charlier, G. Dresselhaus and M. S. Dresselhaus**
New direction in nanotube science, *Material Today*, (2004) vol. p. 30-45
- [46] **J. V. Zanchetta and A. Marchand**
Electronic properties of nitrogen doped carbons, *Carbon*, (1965) vol. 3: p. 332
- [47] **J. Maultzsch and e. al**
Appl. Phys. Lett., (2002) vol. 81: p. 2647
- [48] **E. Hernandez, C. Goze, P. Bernier and A. Rubio**
Elastic Properties of C and B_xC_yN_z Composite Nanotubes, *Phys. Rev. Lett.*, (1998) vol. 80: p. 4502
- [49] **R. Gao, Z. L. Wang, Z. Bai, W. A. d. Heer, L. Dai and M. Gao**

Nanomechanics of Individual Carbon Nanotubes from Pyrolytically Grown Arrays, Phys. Rev. Lett., (2000) vol. 85: p. 622

[50] **A. Seiji and Y. Nakayama**

Mechanical and Electrical properties of Multiwall Nanotube under Interlayer Sliding, 2-J. Surf. Sci. Nanotech., (2005) vol. 3: p. 86-93

[51] **P. Potschke, S. M. Dudkin and I. Alig**

Dielectric spectroscopy on melt processed polycarbonate—multiwalled carbon nanotube composites, Polymer, (2003) vol. 44: p. 5023

[52] **M. K. Seo and S. J. Park**

Electrical resistivity and rheological behaviors of carbon nanotubes-filled polypropylene composites, Chem. Phys. Lett., (2004) vol. 395: p. 44-48

[53] **J. K. W. Sandler, J. E. Kirk, I. A. Kinloch, M. S. P. Shaffer and A. H. Windle**

Ultra-low electrical percolation threshold in carbon-nanotube-epoxy composites, Polymer, (2003) vol. 44: p. 5893-5899

[54] **S. Barrau, P. Demont, A. Peignet, C. Laurent and C. Lacabanne**

DC and AC conductivity of carbon nanotubes-polyepoxy composites, Macromol., (2003) vol. 36: p. 5187-5194

[55] **B. Fragneaud, K. Masenelli-Varlot, J. Y. Cavallé, A. Gonzalez-Montiel and M. Terrones**

Efficient coating of N-doped carbon nanotubes with polystyrene using atomic transfer radical polymerization, Chem. Phys. Lett., (2006) vol. 419: p. 567-573

[56] **J. Chen, M. A. Hamon, H. Hu, Y. Chen, A. M. Rao, P. C. Eklund and R. C. Haddon**

Science, (1998) vol. 282: p. 95

[57] **P. Liu**

Modifications of carbon nanotubes with polymers, European Polymer Journal, (2005) vol. 41: p. 2693-2703

[58] **S. S. Wong, S. Banerjee and M. G. C. Kahn**

Carbon nanotube functionalization (Rational chemical strategies for carbon nanotube functionalization), e. Chem. Eur. J., (2003) vol. 9: p. 1898-1908

[59] **M. Burghard and K. Balasubramanian**

Chemically functionalized carbon nanotubes, small, (2005) vol. 1: p. 180-192

[60] **S. Banerjee, T. Hemraj-Benny and S. S. Wong**

Covalent surface chemistry of single walled carbon nanotubes, Advanced Material, (2005) vol. 17: p. 17-29

[61] **H. W. Goh, S. H. Goh, G. Q. Xu, K. P. Pramoda and W. D. Zhang**

Dynamic mechanical behavior of in situ functionalized multi-walled carbon nanotubes/phenoxy resin composite, Chem. Phys. Lett., (2003) vol. 373: p. 277-283

- [62] **S. Niyogi, M. A. Hamon, H. Hu, B. Zhao, P. Bhowmik, R. Sen, M. E. Itkis and R. C. Haddon**
Chemistry of single-walled carbon nanotubes, Acc. Chem. Res., (2002) vol. 35: p. 1105
- [63] **X. Y. Gong, J. Liu, S. Baskaran, R. D. Voise and J. S. Young**
Surfactant-assisted processing of carbon nanotube/polymer composites, Chem. Mater., (2000) vol. 12: p. 1049-1052
- [64] **D. E. Hill, Y. Lin, A. M. Rao, L. F. Allard and Y. P. Sun**
Functionalization of carbon nanotubes with polystyrene, Macromol., (2002) vol. 35: p. 9466-94671
- [65] **G. S. Duesberg, S. Roth, P. Downes, A. Minett, R. Graupner, L. Ley and N. Nicoloso**
Modification of single walled carbon nanotubes by hydrothermal treatment, Chem. Mater., (2003) vol. 15: p. 3314
- [66] **K. S. Coleman, S. R. Bailey, S. Fodgen and M. L. H. Green**
Functionalization of single-walled carbon nanotubes via Bingel reaction, J. Am. Chem. Soc., (2003) vol. 125: p. 8722-8723
- [67] **C. A. Dyke and J. M. Tour**
Solvent-free functionalization of carbon nanotubes, J. Am. Chem Soc., (2003) vol. 125: p. 1156
- [68] **M. O'Connell, P. Boul, L. M. Ericson, C. Huffman, Y. Wang, E. Haroz, C. Kuper, J. Tour, K. D. Ausman and R. E. Smalley**
Amino acid functionalisation of water soluble carbon nanotubes, Chem. Phys. Lett., (2001) vol. 342: p. 265
- [69] **Z. J. Guo, P. J. Sadler and S. C. Tsang**
Immobilization and Visualization of DNA and Proteins on Carbon Nanotubes, Adv. Material, (1998) vol. 10: p. 701-703
- [70] **F. Dalmas, L. Chazeau, C. Gauthier, K. Masenelli-Varlot, R. Dendievel, J. Y. Cavallé and L. Forró**
Multiwalled carbon nanotube/polymer nanocomposites: processing and properties, J. of Polym. Sci.: Part B Polym. Phys., (2005) vol. 43: p. 1186-1197
- [71] **Z. Chen, W. Thiel and A. Hirsch**
Dependence reactivity of the curvature of single walled nanotube (SWNT), Chem. Phys. Chem., (2003) vol. 4: p. 93
- [72] **J. Chen, M. A. Hamon, H. Hu, Y. Chen, A. M. Rao, P. C. Eklund and R. C. Haddon**
Solution Properties of Single-Walled Carbon Nanotubes, Science, (1998) vol. 282: p. 95-98

[73] **P. M. Ajayan, T. W. Ebbesen, T. I. Ichihashi, S. Iijima, K. Tanigaki and H. Hiura**

Opening carbon nanotubes with oxygen and implications for filling, Nature, (1993) vol. 361: p. 333-334

[74] **H. Hiura, T. W. Ebbesen and K. Tanigaki**

Opening and purification of carbon nanotubes in high yields, Advanced Material, (1995) vol. 7: p. 275-276

[75] **J. Liu, A. G. Rinzler, H. Dai, J. H. Hafner, R. K. Bradley, P. J. Boul, Y. S. Shon, A. Lu, T. Iverson, K. Shelimov, C. B. Huffman, F. Rodriguez-Macias, Y. S. Shon, T. R. Lee, D. T. Colbert and R. E. Smalley**

Fullerene Pipes, Science, (1998) vol. 280: p. 1253-1256

[76] **N. W. S. Kam, T. C. Jessop, P. A. Wender and H. Dai**

Nanotube Molecular Transporters: Internalization of Carbon Nanotube-Protein Conjugates into Mammalian Cells, J. Am. Chem. Soc., (2004) vol. 126: p. 6850-6851

[77] **Y.-P. Sun, K. Fu, Y. Lin and W. Huang**

Functionalized carbon nanotubes: properties and applications, Acc. Chem. Res., (2002) vol. 35: p. 1096-1104

[78] **M. A. Hamon, H. Hui, P. Bhowmik, H. M. E. Itkis and R. C. Haddon**

Ester-functionalized soluble single-walled carbon nanotubes, Appl. Phys. A: Mater. Sci. Process, (2002) vol. 74: p. 333-338

[79] **L. W. Qu, R. B. Martin, W. Huang, K. Fu, D. Zweifel, Y. Lin, Y.-P. Sun, C. E. Bunker, B. A. Harruf, J. R. Gord and L. F. Allard**

Interactions of functionalized carbon nanotubes with tethered pyrenes in solution, J. Chem. Phys., (2002) vol. 117: p. 8089-8094

[80] **B. R. Azamian, K. S. Coleman, J. J. Davis, N. Hanson and M. L. H. Green**

Directly observed covalent coupling of quantum dots to single-wall carbon nanotubes, Chem. Commun., (2002) vol. 2: p. 195

[81] **A. Garg and S. B. Sinnott**

Effect of chemical functionalization on the mechanical properties of carbon nanotubes, Chem. Phys. Lett., (1998) vol. 295: p. 273

[82] **O. Gulseren, T. Yildirim and S. Ciraci**

Systematic ab initio study of curvature effects in carbon nanotubes, Phys. Rev. B., (2002) vol. 65: p. 153405-153408

[83] **K. D. Asuman, H. W. Rohrs, M. F. Yu and R. Rufo**

Nanotechnology, (1999) vol. 10: p. 258-62

[84] **V. N. Khabashesku, W. E. Billups and J. L. Margrave**

Fluorination of Single-Wall Carbon Nanotubes and Subsequent Derivatization Reactions, Acc. Chem. Res., (2002) vol. 35: p. 1087

- [85] **P. J. Boul, J. Liu, E. T. Mickelson, C. B. Huffman, L. M. Ericson, I. W. Chiang, K. A. Smith, D. T. Colbert, J. L. Margrave and R. E. Smalley**
Reversible Sidewall Functionalization of Buckytubes, Chem. Phys. Lett., (1999) vol. 310: p. 367-372
- [86] **X. Lu, L. Zhang, X. XU, N. Wang and Q. Zhang**
Can the Sidewalls of Single-Wall Carbon Nanotubes Be Ozonized?, J. Phys. Chem. B., (2002) vol. 106: p. 2136
- [87] **X. Lu, F. Tian, X. XU, N. Wang and Q. Zhang**
A Theoretical Exploration of the 1,3-Dipolar Cycloadditions onto the Sidewalls of (n,n) Armchair Single-Wall Carbon Nanotubes, J. Am. Chem Soc., (2003) vol. 125: p. 10459-10464
- [88] **J. E. Riggs, Z. X. Guo, D. L. Carroll and Y.-P. Sun**
Strong Luminescence of Solubilized Carbon Nanotubes, J. Am. Chem Soc., (2000) vol. 122: p. 5879-5880
- [89] **D. E. Hill, Y. Lin, L. F. Allard and Y. P. Sun**
Solubilization of Carbon Nanotubes via Polymer Attachment, Nanosci., (2002) vol. 1: p. 213-221
- [90] **M. Sano, A. Kamino, J. Okamura and S. Shinkai**
Self-Organization of PEO-graft-Single-Walled Carbon Nanotubes in Solutions and Langmuir-Blodgett Films, Langmuir, (2001) vol. 17: p. 5125-5128
- [91] **Y. Lin, B. Hou, K. A. S. Fernando, P. Liu, L. F. Allard, Y. P. Sun and Z. B.**
Polymeric carbon nanocomposites from carbon nanotubes functionalized with matrix polymer, Macromol., (2003) vol. 36: p. 7199-7204
- [92] **X. D. Lou, C. Detrembleur, V. Sciannamea, C. Pagnouille and R. Jerome**
Grafting of alkoxyamine end-capped (co) polymers onto multi-walled carbon nanotubes Polymer, (2004) vol. 45: p. 6097-6102
- [93] **H. Kong, C. Gao and Y. Yan**
Functionalization of multiwalled carbon nanotubes by atom transfer radical polymerization and defunctionalization of the products, Macrom., (2004) vol. 37: p. 4022-4030
- [94] **H. Kong, H. Gao and D. Y. Yan**
Constructing amphiphilic polymer brushes on the convex surfaces of multi-walled carbon nanotubes by in situ atom transfer radical polymerization, J. Mater. Chem., (2004) vol. 14: p. 1401-1405
- [95] **K. R. Yoon, W. J. Kim and I. S. Choi**
Functionalization of Shortened Single-Walled Carbon Nanotubes with Poly(p-dioxanone) by Grafting-From Approach, Macromol. Chem. Phys, (2004) vol. 205: p. 1218-1221

- [96] **K. Jiang, A. Eitan, L. S. Schadler, P. M. Ajayan, R. W. Siegel, N. Grobert, M. Mayne, M. Reyes-Reyes, H. Terrones and M. Terrones**
Selective attachment of gold nanoparticles to nitrogen doped carbon nanotubes, Nano. Lett., (2003) vol. 3: p. 275-277
- [97] **K. Matyjaszewski and J. Xia**
Atom transfer radical polymerization, Chem. Rev., (2001) vol. 101: p. 2921-2990
- [98] **P. T. E. Von Werne T.**
J. Am. Chem. Soc., (1999) vol. 121: p. 7409
- [99] **H. Bottcher, M. L. Hallensleben, S. Nub and H. Wurm**
ATRP grafting from silica surface to create first and second generation of grafts, Polym. Bull., (2000) vol. 44: p. 223-229
- [100] **J. Pyun, K. Matyjaszewski, T. Kowalewski, D. Savin, G. Patterson, G. Kickelbick and N. Huesing**
Synthesis of Well-Defined Block Copolymers Tethered to Polysilsesquioxane Nanoparticles and Their Nanoscale Morphology on Surfaces, J. Am. Chem. Soc., (2001) vol. 123: p. 9445-9446
- [101] **M. Kato, M. Kamigaito and T. Higashimura**
Polymerization of methyl methacrylate with the carbon tetrachloride/dichlorotris-(triphenylphosphine)ruthenium(II)/methylaluminium bis(2,6-di-tert-butylphenoxide) initiating system: possibility of living radical polymerization, Macromol., (1995) vol. 28: p. 1721-1723
- [102] **J. S. Wang and K. Matyjaszewski**
Controlled/"living" radical polymerization. Atom Transfer Radical Polymerization in the presence of transition-metal complexes, J. Am. Chem. Soc., (1995) vol. 117: p. 5614-5615
- [103] **T. Ando, M. Kamigaito and M. Sawamoto**
Design of initiators for living radical polymerization of methyl methacrylate mediated by ruthenium(II) complex, Tetrahedron, (1997) vol. 53: p. 15445-15448
- [104] **A. Neumann, H. Keul and H. Hocker**
Atom transfer radical polymerization (ATRP) of styrene and methyl methacrylate with , -dichlorotoluene as initiator; a kinetic study, Macromol. Chem. Phys., (2000) vol. 201: p. 980-984
- [105] **H. C. Brown and R. S. Fletcher**
Chemical Effects of Steric Strains. I. The Effect of Structure upon the Hydrolysis of Tertiary Aliphatic Chlorides, J. Am. Chem. Soc., (1949) vol. 71: p. 1845-1854
- [106] **H. Mayr, M. Roth and R. Faust**
Examination of models for carbocationic polymerization : Influence of chain length on carbocation reactivities, Macromol., (1996) vol. 29: p. 6110-6113
- [107] **C. Granel, P. Dubois, R. Jerome and P. Teyssie**

Controlled radical polymerization of methyl methacrylate in the presence of bis(ortho-chelated) arylnickel (II) complex with different activated alkyl halides, *Macromol.*, (1996) vol. 29: p. 8576-8582

[108] **T. Nishikawa, M. Kamigaito and M. Sawamoto**

Living radical polymerization in Water and alcohols : Suspension polymerization of methyl methacrylate with RuCl₂(PPh₃)₃ complex, *Macromol.*, (1999) vol. 32: p. 2204-2209

[109] **K. Matyjaszewski, S. M. Jo, H. J. Paik and S. G. Gaynor**

Synthesis of Well-Defined Polyacrylonitrile by Atom Transfer Radical Polymerization, *Macromol.*, (1997) vol. 30: p. 6398

[110] **K. Matyjaszewski, M. Wei, J. Xia and N. E. Dermott**

Controlled/"Living" Radical Polymerization of Styrene and Methyl Methacrylate Catalyzed by Iron Complexes, *Macromol.*, (1997) vol. 30: p. 8161-8164

[111] **M. Matsuyama, M. Kamigaito and M. Sawamoto**

Sulfonyl chlorides as initiators for the ruthenium-mediated living radical polymerization of methyl methacrylate, *J. Polym. Sci. Part. A: Polym. Chem.*, (1996) vol. 34: p. 3585

[112] **V. Percec, H. J. Kim and B. Barboiu**

Scope and Limitations of Functional Sulfonyl Chlorides as Initiators for Metal-Catalyzed "Living" Radical Polymerization of Styrene and Methacrylates, *Macromol.*, (1997) vol. 30: p. 8526-8528

[113] **A. Goto and T. Fukuda**

Determination of the activation rate constants of alkyl halide initiators for atom transfer radical polymerization, *macromol. Rapid Com.*, (1999) vol. 20: p. 633-636

[114] **K. Matyjaszewski, H. J. Paik, P. Zhou and S. J. Diamanti**

Determination of Activation and Deactivation Rate Constants of Model Compounds in Atom Transfer Radical Polymerization, *Macromol.*, (2001) vol. 34: p. 5125

[115] **R. Tatemoto and M. Oka**

Contemporary topics in Polymer science, (1984), 4, W. J. Bailey

[116] **T. Ando, M. Kamigaito and M. Sawamoto**

Iron(II) Chloride Complex for Living Radical Polymerization of Methyl Methacrylate, *Macromol.*, (1997) vol. 30: p. 4507-4510

[117] **V. Percec, B. Barboiu, A. Neumann, J. C. Ronda and M. Zhao**

Metal-Catalyzed "Living" Radical Polymerization of Styrene Initiated with Arenesulfonyl Chlorides. From Heterogeneous to Homogeneous Catalysis, *Macromol.*, (1996) vol. 29: p. 3665-3668

[118] **P. Lecomte, I. Drapier, P. Dubois, P. Teyssié and R. Jérôme**

Controlled Radical Polymerization of Methyl Methacrylate in the Presence of Palladium Acetate, Triphenylphosphine, and Carbon Tetrachloride, *macromol.*, (1997) vol. 30: p. 7631-7633

[119] **T. Otsu, T. Tasaki and M. Yoshioka**
Chem. Express, (1990) vol. 5: p. 801

[120] **T. E. Patten and K. Matyjaszewski**
Copper(I)-Catalyzed Atom Transfer Radical Polymerizations, *Acc Chem. Res.*, (1999) vol. 32: p. 895

[121] **J. Xia, X. Zhang and K. Matyjaszewski**
The effect of ligands on copper-mediated atom transfer radical polymerization, *ACS Symp. Ser.*, (2000) vol. 760: p. 207-223

[122] **J. N. Coleman, M. Cadek, R. Blake, V. Nicolosi, K. P. Ryan, C. Belton, A. Fonseca, J. B. Nagy, Y. K. Gun'ko and W. J. Blau**
High-performance nanotube-reinforced plastics understanding the mechanism of strength increase, *Adv. Funct. Mater.*, (2004) vol. 14: p. 791-798

[123] **X. Li, H. Gao, W. A. Scrivens, D. Fei, X. Xu, M. A. Sutton, A. P. Reynolds and M. L. Myrick**
nanomechanical characterization of single-walled carbon nanotube reinforced epoxy composites, *Nanotechnology*, (2004) vol. 15: p. 1416-1423

[124] **Y. S. Song and J. R. Youn**
Properties of epoxy nanocomposites filled with carbon nanomaterials, *e-Polymers*, (2004) vol. 80: p. 1-11

[125] **N. H. Tai, M. K. Yeh and J. H. Liu**
Enhancement of the mechanical properties of carbon nanotube/phenolic composites using a carbon nanotube network as the reinforcement, *carbon*, (2004) vol. 42: p. 2735-2777

[126] **M. Girard**
(2003) Université Laval

[127] **P. J. Flory**
J. Chem. Phys., (1942) vol. 10: p. 51-61

[128] **M. L. Huggins**
Theory of Solutions of High Polymers, *J. Am. Chem. Phys.*, (1942) vol. 64: p. 1712-1719

[129] **P. J. Flory**
Principles of polymer Chemistry, (1953), C. U. P. N. York

[130] **I. W. Hamley**
Structure and flow behaviour of block copolymers, *J. Phys. Condens. Matter.*, (2001) vol. 13: p. R643-R671

- [131] **M. W. Matsen and F. S. Bates**
Unifying Weak- and Strong-Segregation Block Copolymer Theories, *Macromol.*, (1996) vol. 29: p. 1091-1098
- [132] **M. W. Matsen and M. Schick**
Stable and unstable phases of a diblock copolymer melt, *Phys. Rev. Lett.*, (1994) vol. 72: p. 2660
- [133] **M. Wong, M. Paramsothy, X. J. Xu, Y. Ren, S. Li and K. Liao**
Physical interactions at carbon nanotube-polymer interface, *Polymer*, (2003) vol. 44: p. 7757-7764
- [134] **K. Liao and S. Li**
Interfacial characteristics of a carbon nanotube-polystyrene composite system, *Appl. Phys. Lett.*, (2001) vol. 79: p. 4225-4227
- [135] **H. D. Wagner, O. Lourie, Y. Feldman and R. Tenne**
Stress-induced fragmentation of multiwall carbon nanotubes in a polymer matrix, *Appl. Phys. Lett.*, (1998) vol. 72: p. 188-190
- [136] **R. Czerw, M. Terrones, J.-C. Charlier, W. Blase, B. Foley, R. Kamalakaran, N. Grobert, H. Terrones, D. Tekleab, P. M. Ajayan, W. Blau, M. Ruhle and D. L. Carroll**
Nano Lett., (2001) vol. p.
- [137] **Y. Breton, G. Désarmot, J. P. Salvetat, S. Delpeux, C. Sinturel, F. Béguin and S. Bonnamy**
Mechanical properties of multiwall carbon nanotubes/epoxy composites: influence of network morphology, *Carbon*, (2004) vol. 42: p. 1027-1030
- [138] **G. L. Hwang, Y.-T. Shieh and K. C. Hwang**
Efficient load transfer to polymer-grafted multiwalled carbon nanotubes in polymer composites, *Adv. Funct. Mater.*, (2004) vol. 14: p. 487-491
- [139] **J. N. Coleman, S. Curran, A. B. Dalton, A. P. Davey, B. McCarthy, W. Blau and R. C. Barklie**
Percolation-dominated conductivity in a conjugated-polymer-carbon-nanotube composite, *Physical Review B.*, (1998) vol. 58: p. R7492-R7492
- [140] **Stauffer**
Introduction to percolation theory, (1991), T. F. London
- [141] **A. Lesne**
Renormalization methods: critical phenomena, chaos, fractal structures, (1998), J. W. sons
- [142] **P. G. d. Gennes**
On a relation between percolation theory and the elasticity of gels, *J. Phys. Letters*, (1976) vol. 37: p. L1-2

- [143] **Y. T. Sung, C. K. Kum, H. S. Lee, N. S. Byon, H. G. Yoon and W. N. Kim**
Dynamic mechanical and morphological properties of polycarbonate/multi-walled carbon nanotub composites, Polymer, (2005) vol. 46: p. 5656-5661
- [144] **V. Favier, R. Dendievel, G. Canova, J. Y. Cavallé and P. Gilormini**
Simulation and modeling of three-dimensional percolating structures: Case of a latex matrix reinforced by a network of cellulose fibers, Acta Mater, (1997) vol. 45: p. 1557-1565
- [145] **Y. B. Yi, L. Berhan and A. M. Sastry**
Statistical geometry of random fibrous networks, revisited: Waviness, dimensionality, and percolation, J. Appl. Phys., (2004) vol. 96: p. 1318-1327
- [146] **Y. J. Kim, T. S. Shin, H. D. Choi, J. H. Kwon, Y.-C. Chung and H. G. Yoon**
Electrical conductivity of chemically modified multiwalled carbon nanotube/epoxy composites, carbon, (2005) vol. 43: p. 23-30
- [147] **M. Weber and M. R. Kamal**
Estimation of the volume resistivity of electrically conductive composites, Polym. Comp., (1997) vol. 18: p. 711-725
- [148] **F. Dalmas**
PhD, *Composites à matrice polymère et nano-renforts flexibles: propriétés mécaniques et électriques*, (2005) INSA de Lyon
- [149] **L. Flandin**
PhD, *Etude expérimentale et modélisation microstructurale de l'évolution des propriétés électriques d'un matériau composite*, (1992) Université Joseph Fourier
- [150] **O. Breuer and U. Sundararaj**
Big returns from small fibers: a review of polymer/carbon nanotube composites, Polymer composites, (2004) vol. 25: p. 630-645
- [151] **X. Jiang, Y. Bin and M. Matsuo**
Electrical properties of polyimide-carbon nanotubes composites fabricated by in situ polymerization, Polymer, (2005) vol. 46: p. 7418-7424
- [152] **C. Velasco-Santos, A. L. Martínez-Hernández, F. Fisher, R. Ruoff and V. M. Castaño**
Dynamical-mechanical and thermal analysis of carbon nanotube-methyl.ethyl methacrylate nanocomposites, J. Phys. D: Appl. Phys., (2003) vol. 36: p. 1423-1428
- [153] **X. Xu, M. M. Thwe, C. Shearwood and K. Liao**
Mechanical properties and interfacial characteristics of carbon-nanotube-reinforced epoxy thin films, Appl. Phys. Lett., (2002) vol. 81: p. 2833-2835
- [154] **X. Zhang, T. Liu, T. V. Sreekumar, S. Kumar, X. Hu and K. Smith**
Gel spinning of PVA/SWNT composites fiber, Polymer, (2004) vol. 45: p. 8801-8807

- [155] **M. Cadek, J. N. Coleman, V. Barron, K. Hedicke and W. J. Blau**
Morphological and mechanical properties of carbon-nanotube-reinforced semicrystalline and amorphous polymer composites, Appl. Phys. Lett., (2002) vol. 81: p. 5123-5125
- [156] **B. Safadi, R. Andrews and E. A. Grulke**
Multiwalled carbon nanotube polymer composites: synthesis and characterization of thin films, J. of Appl. Polym. Sci., (2002) vol. 84: p. 2660-2669
- [157] **G. M. Odegard, T. S. Gates, K. E. Wise, C. Park and E. J. Siochi**
Constitutive modeling of nanotube-reinforced polymer composites, Composites Science and Technology, (2003) vol. 63: p. 1671-1687
- [158] **J. Gou, Z. Liang, C. Zhang and B. Wang**
Computational analysis of effect of single-walled carbon nanotubes rope on molecular interaction and load transfer of nanocomposites, Composites: part B, (2005) vol. 36: p. 524-533
- [159] **E. Chabert**
PhD, *Propriétés mécaniques de nanocomposites à matrice polymère: approche expérimentale et modélisation*, (2002) INSA Lyon
- [160] **L. Chazeau**
PhD, *Etude de nanocomposites à renfort cellulosique et matrice poly(chlorure de vinyle): mise en oeuvre, étude structurale, comportement mécanique*, (1998) université Joseph Fourier-Grenoble 1
- [161] **E. F. Oleinik**
Prog. Coll. Polym. Sci., (1989) vol. 80: p. 140-150
- [162] **B. Pukánszky**
Interfaces and interphases in multicomponent materials: past, present future, European Polymer Journal, (2005) vol. 41: p. 645-662
- [163] **Y. Wang, R. Cheng, L. Liang and Y. Wang**
Study on the preparation and characterization of ultra-high molecular weight polyethylene-carbon nanotubes composite fiber, composites Science and Technology, (2005) vol. 2005: p. 793-795
- [164] **T. Takahashi, K. Yonetake, K. Koyama and T. Kituchi**
Macromol. Rapid Com., (2003) vol. 24: p. 763-767
- [165] **L. Valentini, J. Biagiotti, J. M. Kenny and M. A. L. Manchado**
Physical and mechanical behavior of single-walled carbon nanotube/polypropylene/ethylene-propylene-diene rubber nanocomposites, J. of Appl. Polym. Sci., (2003) vol. 89: p. 2657-2663
- [166] **A. Wall, J. N. Coleman and M. S. Ferreira**
Physical mechanism for the mechanical reinforcement in nanotube-polymer composite materials, Physical Review B., (2005) vol. 71: p. 125421

- [167] **Y. C. Zhang and W. Wang**
Thermal effects on interfacial stress transfer characteristics of carbon nanotubes/polymer composites, Int. J. of Sol. and Struc., (2005) vol. 42: p. 5399-5412
- [168] **E. H. Kerner**
Proceedings of the Physical Society: Section B, (1956) vol. 69: p. 808-813
- [169] **J. C. Halpin and S. W. Tsai**
Effects of environmental factors on composites materials, (1969), AFPIL-Tr
- [170] **J. C. Halpin and J. L. Kardos**
Moduli of Crystalline Polymers Employing Composite Theory, J. Appl. Phys., (1972) vol. 43: p. 2235-2241
- [171] **L. E. Holman and H. Leuenberger**
The relationship between solid fraction and mechanical properties of compacts — the percolation theory model approach, Int. J. Pharmaceutics, (1988) vol. 46: p. 35-44
- [172] **N. Ouali, J. Y. Cavallé and J. Perez**
Elastic, Viscoelastic and Plastic Behavior of Multiphase Polymer Blends, Plast. Rubber and Composites Proc. and Appl., (1991) vol. 16: p. 55-60
- [173] **M. Takayanagi, S. Uemura and S. Muinami**
J. Polym. Sci: C., (1964) vol. 5: p. 113
- [174] **J. Kolarik**
Simultaneous prediction of the modulus, tensile strength and gas permeability of binary polymer blends, Eur. Polym. J., (1997) vol. 34: p. 585-590
- [175] **O. Meincke, D. Kaempfer, H. Weickmann, C. Friedrich, M. Vathauer and H. Warth**
Mechanical properties and electrical conductivity of carbon-nanotube filled polyamide-6 its blends with acrylonitrile/butadiene/styrene, Polymer, (2004) vol. 45: p. 739-748
- [176] **M. Terrones**
Synthetic routes to nanoscale BxCyNz architectures, Carbon, (2002) vol. 40: p. 1665-1684
- [177] **M. D. Gomez**
(2006) Advanced Material, IPICYT
- [178] **Y. Ying, R. S. Saini, F. Liang, A. K. Sadana and W. E. Billups**
Functionalization of Carbon Nanotubes by Free Radicals, Organic Letter, (2003) vol. 5: p. 1471-1473
- [179] **K. Varlot**
Ph-D thesis, (1998) Ecole Centrale de Lyon, France

- [180] **Z. L. Wang, R. P. Gao, P. Poncharal, W. A. d. Heer, Z. R. Dai and Z. W. Pan**
Mechanical and electrostatic properties of carbon nanotubes and nanowires, Mater. Sci. Eng. C, (2001) vol. 16: p. 3-10
- [181] **L. Langer, J. P. Heremans, V. Bayot, J.-P. Issi, L. Stockman, C. V. Haesendonck, Y. Bruynseraede and C. H. Olk**
Electrical measurements on submicronic synthetic conductors : Carbon nanotubes, Synthetic Metals, (1995) vol. 70: p. 1393-1396
- [182] **C. Y. Wei, D. Srivastava and K. J. Cho**
Thermal Expansion and Diffusion Coefficients of Carbon Nanotube-Polymer Composites, NanoLetters, (2002) vol. 2: p. 647-650
- [183] **J. Zhao, J. P. Lu, J. Han and C. K. Yang**
Noncovalent functionalization of carbon nanotubes by aromatic organic molecules, Appl. Phys. Lett., (2003) vol. 82: p. 3746-3748
- [184] **M. S. P. Shaffer and K. Koziol**
Polystyrene grafted multi-walled carbon nanotubes, Chem. Commun., (2002) vol. p. 2074-2075
- [185] **D. Baskaran, J. W. Mays and M. S. Bratcher**
Polymer-Grafted Multiwalled Carbon Nanotubes through Surface-Initiated Polymerization, Angewandte Chem. Int. Ed., (2004) vol. 43: p. 2138-2142
- [186] **Q. Shuhui, Q. Dongpi and W. T. Ford**
Functionalization of Single-Walled Carbon Nanotubes with Polystyrene via Grafting to and Grafting from Methods, Macrom., (2004) vol. 37: p. 752-757
- [187] **Z. L. Yao, N. Braidy, G. A. Botton and A. Adronov**
Polymerization from the Surface of Single-Walled Carbon Nanotubes - Preparation and Characterization of Nanocomposites, J. Am. Chem Soc., (2003) vol. 125: p. 16015-16024
- [188] **M.-. Canonico, G. B. Adams, C. Poweleit, J. Menendez, J. B. Harris, H. P. v. d. Meulen, J. M. Calleja and J. Rubio**
Characterization of carbon nanotubes using Raman excitation profiles, Physical Review B., (2002) vol. 65: p. 201402R
- [189] **X. Zhao, Y. Ando, L. C. Qin, H. Kataura, Y. Maniwa and R. Saito**
Multiple splitting modes from individual multiwalled carbon nanotubes, Appl. Phys. Lett., (2002) vol. 81: p. 2550-2552
- [190] **R. Andrews and M. C. Weisenberger**
Carbon nanotube polymer composites, Current Opinion in Solid State and Material Science, (2004) vol. 8: p. 31-37
- [191] **G. Holden, M. R. Legge, R. P. Quirk and H. E. Schroeder**
Thermoplastic elastomer, (1996), H. Publisher

- [192] **C. Buenviaje, F. Dinelli and R. M. Overney**
Glass transition measurement of ultrathin polystyrene films, (2000) vol. p.
- [193] **M. Wu, G. A. Snook, V. Gupta, M. Shaffer, D. J. Fray and G. Z. Chen**
Electrochemical fabrication and capacitance of composite films of carbon nanotubes and polyaniline, *J. of Mat. Chem.*, (2005) vol. 15: p. 2297-2303
- [194] **A. Nogales, G. Broza, Z. Roslaniec, K. Schulte, I. Sics, B. S. Hsiao, A. Sanz, M. C. Garcia-gutierrez, D. R. Rueda, C. Domingo and T. A. Ezquerra**
Low percolation threshold in nanocomposites based on oxidized single wall carbon nanotubes and poly(butylene terephthalate), *Macromol.*, (2004) vol. 37: p. 7669-7672
- [195] **J. C. Dyre and T. B. Schroder**
Universality of ac conduction in disordered solids, *Rev. Mod. Phys.*, (2000) vol. 72: p. 873
- [196] **S. Li, Y. Qin, J. Shi, Z.-X. Guo, Y. Li and D. Zhu**
Electrical Properties of Soluble Carbon Nanotube/Polymer Composite Films, *Chem. Mater.*, (2005) vol. 17: p. 130-135
- [197] **T. Liu, I. Y. Phang, L. Shen, S. Y. Chow and W. D. Zhang**
Morphology and Mechanical Properties of Multiwalled Carbon Nanotubes Reinforced Nylon-6 Composites, *Macromol.*, (2004) vol. 37: p. 7214-7222
- [198] **J. Yang, J. Hu, C. Wang, Y. Qin and Z. Guo**
Fabrication and characterization of soluble multi-walled carbon nanotubes reinforced P(MMA-co-EMA) composites, *Macromol. Mater. Eng.*, (2004) vol. 289: p. 828-832
- [199] **F. Dalmás**
PhD, (2005) INSA de Lyon
- [200] **B. Ewen, D. Richter, D. Shiga, H. H. Winter and M. Mours**
Advance in polymer science, (1997), B. Springer
- [201] **V. Favier**
PhD, *Etude de nouveaux matériaux composites obtenus à partir de latex filmogènes et de whiskers de cellulose: effet de percolation mécanique*, (1995) Institut National Polytechnique de Grenoble
- [202] **C. W. Nan**
Theoretical approach to the coupled thermal-electrical-mechanical properties of inhomogeneous media, *Phys. Rev. B*, (1994) vol. 49: p. 12619–12624